Interpretation of DC and IP Time-Domain Data Observed on a Copper Deposit in Turkey Using a Newly Developed 2D Finite Element Inversion With Unstructured Meshes

Inaugural-Dissertation

zur
Erlangung des Doktorgrades
der Mathematisch-Naturwissenschaftlichen Fakultät
der Universität zu Köln

vorgelegt von
Juliane Adrian
aus Düren

Köln, 2017

Gutachter:	Prof. Dr. B. Tezkan Prof. Dr. A. Hördt
Tag der mündlichen Prüfung:	2. Mai 2017

Abstract

Within the framework of this thesis, a new two-dimensional inversion algorithm for direct current (DC) resistivity and time-domain induced polarization (IP) data was developed. The algorithm consists of a novel composition of finite element forward calculation and a smoothness constrained local regularization inversion approach including error weighting and a non-linear IP chargeability inversion. All forward an inverse calculations are conducted on unstructured triangular meshes. The advantage of employing an unstructured mesh over the use of structured grids is that complicated surface topography can easily be implemented and complex subsurface structures can be reproduced better. This is among other things due to flexibility and because local mesh refinement is possible without globally increasing the number of elements significantly.

An IP perturbation model is implemented that explains the effect of chargeable material by an increase of effective resistivity. Consequently, the inversion is conducted in two steps. The first step is a non-linear DC inversion recovering a resistivity model that corresponds to the effective resistivity and explains the measured DC data within the error bounds. In the second step, a chargeability model is derived by non-linear IP inversion.

The employment of unstructured grids pleads for special smoothness constraints because model elements are not arranged in a regular manner and are oriented arbitrarily. Therefore, three types of smoothness matrices are examined that approximate first order derivatives in the triangular mesh. Furthermore, a measure of the depth of investigation is presented that is based on the normalized coverage which is a cumulative sensitivity. A coverage threshold applicable for 2D models is derived by the coverage value of a homogeneous model that corresponds to the depth of investigation according to a rule of thumb.

The accuracy of the implemented forward algorithm is verified by modeling of 1D and 2D models and comparison to analytical solutions. By inversion of synthetic data, it is assessed whether the algorithm can reproduce the original models. Reliability is also checked by comparison of the forward and inverse modeling of synthetic data with established algorithms.

The new algorithm was successfully applied to DC and time-domain IP field data acquired on a copper ore deposit in Elbistan, Turkey. Due to the state of the ore deposit, which is mainly disseminated, it was expected that the presence of the metallic particles does not produce a prominent resistivity anomaly. Thus, the deposit is difficult to detect with the DC resistivity method alone. However, the assumed sulfide content leads to strong induced polarization effects. These assumptions are confirmed by the resistivity and chargeability models obtained by inversion with the new algorithm. As expected, highly chargeable structures with more than 100 mV/V are recovered that are associated with the ore deposit, while the outline is not clearly distinguishable in the resistivity models. Comparison with inversion results obtained by other algorithms and a near surface resistivity model derived from Radiomagnetotelluric data confirm the resistivity and chargeability results of the new algorithm.

Zusammenfassung

Im Rahmen der vorliegenden Arbeit wurde ein neuer zweidimensionaler Inversionsalgorithmus für Daten der Gleichstromgeoelektrik (DC) und induzierten Polarisation (IP) im Zeitbereich entwickelt. Der Algorithmus besteht aus einer neuen Zusammenstellung aus Vorwärtsrechnung mittels der Methode der Finiten Elemente und einer Inversion mit einer lokalen Regularisierung zur Glättung des Modells. Der Inversionsalgorithmus beinhaltet außerdem eine Fehlerwichtung und eine nicht-lineare IP Inversion der Aufladbarkeit. Sowohl die Vorwärtsrechnung als auch die Inversion werden auf unstrukturierten Dreiecksgittern durchgeführt. Der Vorteil von unstrukturierten Gittern gegenüber strukturierten Gittern ist, dass komplizierte Topographie der Erdoberfläche und komplexe Untergrundstrukturen besser nachempfunden werden können. Dies ist unter anderem auf höhere Flexibilität zurückzuführen und darauf, dass lokale Verfeinerungen des Gitters möglich sind ohne global gesehen die Anzahl an Gitter-Elementen wesentlich zu erhöhen.

Das implementierte IP Perturbationsmodell verbindet den Effekt eines aufladbaren Materials mit einer Erhöhung des effektiven spezifischen Widerstands. Somit kann die Inversion in zwei Schritte aufgeteilt werden. Den ersten Schritt bildet eine nicht-lineare DC Inversion, welche in einem Widerstandsmodell resultiert, welches dem effektiven spezifischen Widerstand entspricht und welches die gemessen DC Daten im Rahmen der Fehlergrenzen erklärt. Im zweiten Schritt wird ein Aufladbarkeitsmodell durch eine nicht-lineare IP Inversion abgeleitet.

Bei Verwendung von unstrukturierten Gittern werden spezielle Glättungsbedingungen benötigt, da die Gitterelemente nicht nach einen regelmäßigen Schema angeordnet und zufällig ausgerichtet sind. Aus diesem Grund werden drei Arten von Glättungsmatrizen untersucht, welche die räumlichen partiellen Ableitungen innerhalb der Dreiecksgitter approximieren. Außerdem wird ein Maß zur Abschätzung der Erkundungstiefe vorgestellt, welches auf der normierten Coverage (Überdeckung), also einer kumulativen Sensitivität, beruht. Ein Schwellenwert der Coverage, welcher auf 2D Modellen anwendbar ist, wird abgeleitet von dem Wert der Coverage eines homogenen Halbraums, welcher in der Tiefe vorzufinden ist, die der Erkundungstiefe nach einer Faustformel entspricht.

Die Genauigkeit der implementierten Vorwärtsrechnung wird durch Modellierungen von 1D und 2D Modellen und dem Vergleich mit analytischen Lösungen überprüft. Durch Inversion von synthetischen Daten wird getestet ob der Algorithmus in der Lage ist die Ursprungsmodelle zu reproduzieren. Die Verlässlichkeit des neuen Algorithmus wird zudem durch Vergleich der Ergebnisse von Vorwärtsrechnung und Inversion synthetischer Daten mit bereits bestehenden Algorithmen getestet.

Der neu entwickelte Inversionsalgorithmus wird schließlich erfolgreich auf DC und Zeitbereichs-IP Daten angewendet, welche auf einer Kupfererz-Lagerstätte nahe Elbistan in der Türkei gemessen wurden. Aufgrund des hauptsächlich als feinverwachsenes Material auftretenden Erzes, wird erwartet, dass die Anwesenheit der metallischen Partikel keine auffälligen Anomalien in den Widerstandsdaten hervorruft. Somit ist es schwierig die Lagerstätte allein mit der DC Methode zu untersuchen. Der vermutete Sulfidgehalt führt jedoch zu starken IP Effekten. Diese

Annahmen spiegeln sich in den Inversionsergebnissen des neuen Algorithmus wider. Wie erwartet ergeben sich Strukturen in den Aufladbarkeitsmodellen mit Werten von über 100 mV/V, welche mit der Erzlagerstätte in Verbindung gebracht werden. Die Form der Lagerstätte kann hingegen nicht eindeutig aus den Widerstandsmodellen abgeleitet werden. Vergleich mit Inversionsergebnissen etablierter Algorithmen sowie einem oberflächennahen Widerstandsmodell, welches mit der Radiomagnetotellurik Methode bestimmt wurde, bestätigen die mit dem neuen Algorithmus erhaltenen Widerstands- und Aufladbarkeitsmodelle.

Contents

1. Introduction **1**
1.1. Guideline of the Thesis 4
1.2. Preliminary Notes 5

2. Applied Geophysical Methods **7**
2.1. Electrical Resistivity 7
2.2. Direct Current Resistivity Method 8
2.2.1. Potential in Homogeneous Media 9
2.2.2. Potential in Inhomogeneous Media 12
2.2.3. Field Setup and Apparent Resistivity 13
2.3. Induced Polarization Method 17
2.3.1. Time-Domain IP measurements 18
2.3.2. Frequency-Domain Measurements 20
2.3.3. Mathematical Formulation after Seigel 22

3. Forward Modeling of DC and TDIP Data **25**
3.1. Basic Equations 25
3.1.1. Fourier Cosine Transformation 26
3.1.2. Singularity Removal 27
3.1.3. Boundary Conditions 27
3.2. Finite Element Method 28
3.2.1. Solving the System of Linear Equations 31
3.2.2. Calculation of Synthetic Data for Multi-electrode setups . . . 31
3.3. Mesh 32
3.4. Incorporation of IP in the DC Forward Modeling Algorithm 35
3.5. Modeling Examples: Verification of `ResIPIn2D` 36
3.5.1. Homogeneous Half-Space 36
3.5.2. Two Horizontal Layers 37
3.5.3. Vertical Contact 39
3.5.4. Buried Block 41
3.5.5. IP Example 43
3.5.6. Conclusions 45

4. Smoothness Constrained Regularization Inversion of DC and TDIP Data **47**
4.1. Non-linear Inversion Strategies 48
4.1.1. Error Weighting 48
4.1.2. Newton-Type Methods 49
4.1.3. Regularization Methods 50

4.2. Sensitivity (Jacobian Matrix) . . . 52
4.2.1. Derivation of Sensitivity by the Reciprocity Principle . . . 52
4.3. TDIP Two-step Inversion Approach . . . 54
4.3.1. Non-linear Chargeability Inversion . . . 54
4.3.2. Practical Considerations . . . 55
4.3.3. Implementation in `ResIPIn2D` . . . 55
4.4. Regularization Parameter and Step-length of Model Update . . . 58
4.5. Inversion Mesh . . . 60
4.6. Parameterization . . . 61
4.7. Smoothness Constraint Matrix . . . 62
4.8. Depth of Investigation . . . 65
4.8.1. Rule of Thumb . . . 65
4.8.2. Coverage . . . 65
4.8.3. DOI index . . . 67
4.8.4. Features of `BERT` and `Res2DInv` . . . 68

5. Inversion of Synthetic Data 71
5.1. Resolution of Chargeability Dependent on Resistivity Model? . . . 71
5.2. Comparison of Smoothness Constraints and Regularization Parameters 73
5.3. Influence of Initial Model . . . 80
5.4. Resolution of the lower boundary of a model block . . . 81
5.4.1. Lower Boundary of Resistivity Anomaly . . . 82
5.4.2. Lower Boundary of Highly Chargeable Model Block . . . 87
5.4.3. Comparison of Inversion Results with other Algorithms . . . 89
5.5. Conclusions . . . 91

6. Consideration of Topography Effects 93
6.1. Topography Effects of Hill and Valley Examples . . . 94
6.2. Handling Topography Effects in Interpretation . . . 102
6.2.1. Topography Correction . . . 102
6.2.2. Incorporation of Topography into Inversion Mesh . . . 104
6.2.3. Comments and Recommendations . . . 104
6.3. Inversion of Synthetic Data Under Consideration of Topography Effects 107
6.3.1. Circular Body Buried Beneath a Hill Structure . . . 107
6.3.2. Rectangular Block Buried Beneath a Valley Topography . . . 115
6.3.3. Comparison with other algorithms . . . 120
6.3.4. Conclusions . . . 122

7. Inversion of Field Data 125
7.1. Survey on a Copper Ore Deposit in Elbistan, Turkey . . . 128
7.1.1. Geological Background . . . 128
7.1.2. The Survey Area . . . 131
7.1.3. Geophysical Data Acquisition . . . 132
7.1.4. Topography Influence . . . 136
7.1.5. Measured Data and Error Estimation . . . 138
7.1.6. Inversion Results . . . 141
7.1.7. Comparison of the Inversion Results . . . 150

7.1.8. Summary and Interpretation 152

8. Discussion and Conclusions **155**

Bibliography **159**

A. Appendix Geophysical Methods **185**

B. Appendix Forward Calculation **189**
B.1. Wavenumbers and weights used in the FCT 189
B.2. Element Matrices 189
B.3. Electrode Protocols 192
B.4. Appendix Inversion of Synthetic Data 196

C. Appendix Survey Results **197**
C.1. Topography Influence 197
C.2. Inversion Results 199

1. Introduction

The focus of this thesis lies on the development of an algorithm for evaluation of geoelectrical data which can be applied on various geophysical issues, in particular for mineral exploration purposes.

Mineral exploration is an important task that serves to investigate the characteristics, such as size and shape, of a mineral deposit prior to the exploitation. The application of geophysical methods serves the nondestructive characterization of the subsurface. If applied covering a large area, it is a powerful tool to define outlines of a potential mineral deposit and suggest promising locations for boreholes or excavations.
Generally, applied geophysical methods serve to investigate physical parameters of the earth's subsurface. The applied method depends on the physical property of interest. To achieve the most reliable result, it is preferable to apply several methods simultaneously. Geoelectrical and electromagnetic methods investigate the electrical conductivity or the reciprocal, the electrical resistivity. The direct current (DC) resistivity method is widely spread and has been applied for many decades. A direct current is injected in the subsurface by galvanic coupled electrodes while simultaneously recording electrical potential differences between predefined points. It is employed in a wide field of near-surface applications, such as hydrological (Wilson et al., 2006), environmental (Yogeshwar et al., 2012), archaeological (Griffiths and Barker, 1994) and mineral exploration (Oldenburg et al., 1997) issues.
In mineral exploration, the DC method is commonly combined with the induced polarization (IP) method (Pelton et al., 1978). The advantage of using IP in addition to pure DC is that the resistivity signature caused e.g. by disseminated material is hard to detect whereas the chargeability signature resolved by the IP method might be strong and rather independent from the geometry of the resistivity structure. In this case, the DC method gives an overview of the general geology while the IP method provides information about a potential ore deposit (Spitzer and Chouteau, 2003). The IP method is strongly associated with the DC method. It makes use of polarization effects in a low-frequency range that are analogous to a capacitor like reversible storage of energy (Revil et al., 2012). In frequency-domain (FD), mostly a phase shift between transmitter signal and measured voltage is investigated, which is dependent on the transmitter frequency. A special variation of FDIP is the spectral induced polarization (SIP) where several frequencies are employed. Time-domain (TD) applications make use of the voltage decay after transmitter turn-off. Besides information about the subsurface resistivity distribution, the IP method offers the determination of further properties. The most important property is the chargeability which is related to the ability of the subsurface to store energy. Several IP models exist that describe the instant voltage drop and the voltage decay curve after transmitter turn-off. In the model according to Seigel (1959), the effect of the

presence of chargeable material results in an increase of effective resistivity. Other models are e.g. the Cole-Cole model (Pelton, 1977) or the model by Dias (1968) just to name a few. They describe a complex resistivity, which is dependent on the frequency by introducing further parameters, such as the relaxation time and a frequency exponent that allow conclusions about the texture of the polarizable material. They are represented by an equivalent circuit including a capacitor. Dias (2000) provides an overview of the most commonly used IP models.
Besides mineral exploration (Pelton et al., 1978; Seigel et al., 1997; Vanhala and Peltoniemi, 1992), the IP method is also employed for environmental issues, e.g. characterization of contamination of the subsurface (Yuval and Oldenburg, 1996; Kemna et al., 2004), hydrogeological aspects (Kemna et al., 2002; Hördt et al., 2007) or investigation of porous rocks and sediments in field surveys (Kemna, 2000; Titov et al., 2004) or laboratory experiments (Zimmermann et al., 2008; Bairlein et al., 2014). A review about recent developments of the DC and the IP method is given in Loke et al. (2013), Revil et al. (2012) and Kemna et al. (2012).

For most geophysical problems, the direct reconstruction of the underlying physical model from acquired data is not possible because the problem is non-linear. Therefore, it is necessary to solve an inverse problem. For several decades, the application and analysis of the DC method were one-dimensional. In the 1990s, multi-electrode arrays and multi-channel devices were developed and became popular. Nowadays, multi-dimensional applications of DC and IP are standard due to developments in instrumentation and inversion techniques in the last three decades whereupon it is most popular in 2 dimensions (Loke et al., 2013). But, also 3-dimensional (e.g. Loke and Barker, 1996a; Günther et al., 2006; Li and Oldenburg, 2000) and 4-dimensional (e.g. Kim et al., 2009; Karaoulis et al., 2013) applications and algorithms were developed.

The basis of each inversion algorithm is the implemented forward calculation, which serves to create synthetic data for a given subsurface model. In TDIP, commonly the model according to Seigel (1959) is employed, e.g. in the algorithms by Oldenburg and Li (1994), Loke and Barker (1996b) or Karaoulis et al. (2013). Then, the synthetic IP datum "apparent chargeability" is derived from DC forward calculation. In general, most geophysical forward calculations make use of the finite difference (FD) approach (Mufti, 1976; Dey and Morrison, 1979) or the finite element (FE) method (Coggon, 1971). Besides the work of Coggon (1971), further basics of using the FE method for DC problems are presented by Pridmore et al. (1981), Queralt et al. (1991) and Li and Spitzer (2002).
Moreover, Queralt et al. (1991) describe the application of a Fourier-cosine transformation of the electrical potential from 3 dimensions into the 2.5-dimensional wavenumber domain. Like this, the dependence of the potential on the y-direction is circumvented, and the sought potential can, therefore, be determined by a 2-dimensional forward calculation. The forward problem is to be solved under consideration of boundary conditions that restrict the potential at the boundaries of the computational domain, such as the Neumann boundary condition or mixed boundary conditions (Dey and Morrison, 1979).
In FE and FD methods, the computational area is discretized into a grid consisting of mesh elements and nodes. The introduction of boundary elements (Okabe, 1981;

Queralt et al., 1991) at the outer mesh boundaries facilitates the incorporation of boundary conditions. Every DC forward problem is eventually reduced to a sparse linear system of equation that is to be solved with respect to the electrical potential. An overview over efficient solvers is given in Spitzer and Wurmstich (1999).
While the FD approach is usually applied on structured rectangular grids, the FE method is suited for the use of unstructured triangular meshes in 2D or tetrahedral grids in 3D (Günther et al., 2006). The advantage of unstructured meshes over structured grids is that local refinement is achieved where accuracy is needed without increasing the number of mesh elements significantly. On the contrary, refining a structured mesh naturally results in a refinement on global scales. Furthermore, unstructured meshes are best suited for the incorporation of surface topography or complex subsurface structures. However, several existing algorithms, such as Sasaki (1994) or Loke and Barker (1996b), apply FE forward calculations on triangular meshes, but the inversion procedure itself is conducted on a mesh that is bound to rectangular model elements.

In the direct vicinity of point current sources, a singularity exists. Therefore, a separation of potentials (Coggon, 1971) is applied, which is also referred to as singularity removal technique (Lowry et al., 1989; Zhao and Yedlin, 1996). Thereby, the potential is split into a primary part, that is the analytical solution for a homogeneous half-space with e.g. the resistivity at the considered current electrode, and a secondary potential which is the effect of all deviations of the original resistivity model from the homogeneous model. The secondary potential is the result of solving the FE equations. However, the singularity removal technique can only be applied for flat-surface models because the analytical solution is not valid for surface topography models. In this case, the total potential is determined by solution of the system of linear equations.
DC topography studies were e.g. performed in 2D by Coggon (1971) and Fox et al. (1980) and in 3D by Holcombe and Jiracek (1984) and Sasaki (1994). However, these studies do not benefit from the advantages of unstructured meshes because structured grids were applied. Rücker et al. (2006) use an unstructured tetrahedral grid for 3D DC modeling including surface topography.
A method to correct field data for topography effects was presented by Fox et al. (1980). Then, inversion of the corrected data can be conducted with a flat surface mesh. However, the topography effects are not completely removed by the proposed method. According to Tong and Yang (1990) a direct incorporation of surface topography into the inversion mesh is more sufficient.

Oldenburg and Li (1994) proposed three TDIP inversion approaches. All of them are based on the IP perturbation model according to Seigel (1959), and they recover a resistivity and a chargeability model after two inversion steps. The first step is always a pure DC inversion recovering a resistivity model. The second step serves to recover a chargeability model. In the first method, the IP data is linearized, and a linear inverse problem is solved under the assumption that chargeability is small. In the second approach, a chargeability model is approximated after two resistivity inversions of perturbed resistivity models. The third method involves a non-linear chargeability inversion.

In a non-linear inversion, the non-linearity of the underlying problem is linearized,

and a sensitivity matrix is introduced that is denoted as Jacobian. The entries of the Jacobian contain partial derivatives of data-points with respect to model parameters. The most obvious way to determine those entries is the application of a small perturbation of all model parameters which is rather time-consuming. Another method makes use of the reciprocity of the electrical potential (Sasaki, 1989). Then, the DC-Jacobian can be obtained based on the forward calculation with little extra effort (Tripp et al., 1984). The IP-Jacobian used in the non-linear chargeability inversion step is a scaled version of the DC-Jacobian (Oldenburg and Li, 1994). Since the DC and IP problems are ill-posed, regularization techniques were introduced (e.g. Tikhonov and Arsenin, 1977) that serve to improve convergence and circumvent ambiguity. Smoothness constrained regularization techniques (Constable et al., 1987) enforce smooth model characteristics and consequently prefer smooth parameter transitions over rough models. These constraints are introduced by matrices that approximate the first or second order derivatives of parameter transitions. These constraints affect either locally neighboring parameters or act globally by forcing the parameters to stay close to the initial model.

The algorithm developed in the framework of this thesis applies a local smoothness constraint regularization approach for 2D inversion of DC and TDIP data including error weighting. The basis of the inversion algorithm is an FE DC forward calculation using unstructured triangular meshes. Also, the inversion procedures are conducted on an unstructured mesh enhancing the incorporation of surface topography. The IP chargeability is determined by a slightly modified version of the third method that was proposed by Oldenburg and Li (1994) which is a non-linear IP inversion subsequent to a non-linear DC inversion. In this approach, there is no need for the chargeability to be small. Therefore, strong chargeability anomalies can be resolved.

Part of this work was conducted within the framework of the project "Two-Dimensional Joint Interpretation of Radiomagnetotelluric, Direct Current Resistivity and Induced Polarization Data: an example from an ore exploration" funded by the German Federal Ministry of Education and Research (BMBF) and the Scientific and Technological Research Council of Turkey (TÜBITAK).

1.1. Guideline of the Thesis

Chapter 2 gives an introduction to the applied geophysical methods, namely the DC resistivity and the time-domain IP method. The concept of forward modeling by the finite element method is introduced in Chapter 3. After the illustration of the implemented features, the reliability of the newly developed 2D forward algorithm is assessed by comparison of modeling examples with analytical solutions and established algorithms. In Chapter 4, non-linear inversion strategies are explained, in particular, the applied smoothness constrained regularization technique and the two-step DC/TDIP inversion method. By inversion of synthetic datasets, presented in Chapter 5, the ability of the new inversion algorithm to reproduce original models is verified. At the same time, several computational and practical aspects regarding the applicability on field data are assessed. The importance of the consideration

of topography effects in forward and reverse modeling is discussed in Chapter 6. Modeling examples and comparison to established algorithms complete the Chapter. Chapter 7 deals with the application of the newly developed algorithm on field data acquired on a copper ore deposit in Turkey. As expected, a strong chargeability signature is resolved, that indicates the presence of an ore deposit with sulfide content. Eventually, a summary of the thesis including discussion of individual aspects is given in Chapter 8.

1.2. Preliminary Notes

The algorithm that was developed within the framework of this thesis is denoted as `ResIPIn2D` which is short for "(Res)istivity and (IP) (In)version in (2) (D)imensions". A user's manual will be provided with the algorithm after the submission of this thesis.

Several forward modeling and inversion results are compared to results obtained by established algorithms. Corresponding references will be given in the following and will not be repeated in this thesis:

- `DC2DInvRes`: Günther (2004)
- `BERT`: Rücker et al. (2006); Günther et al. (2006)
- `Res2DMod`: Loke (2002)
- `Res2DInv`: Loke and Barker (1996b), Loke and Dahlin (2002)

In all descriptions, vector quantities are indicated by an arrow superscript, e.g. $\vec{x}$, while matrices are presented by bold letters, such as $\mathbf{M}$.

2. Applied Geophysical Methods

The following chapter gives an introduction to the geophysical methods that are applied within the framework of this thesis. At first, the Direct Current (DC) Resistivity method is introduced (cf. Chapter 2.2). The most important field setups are shown, and the basic equations are given. Subsequently, the phenomenon of polarization effects is explained, and the Induced Polarization (IP) method is introduced (cf. Chapter 2.3).
Some physical quantities are summarized in Table A.1 that are important for the description of electrical and electromagnetic methods. The descriptions in this chapter follow Sumner (1976), Telford et al. (1990) and Reynolds (1997).

2.1. Electrical Resistivity

The surface effects prospected by electrical methods are produced by electrical current flow in the subsurface. The main electrical properties of rocks and minerals are natural electrical potentials, the dielectric constant and the electrical resistivity (or the inverse conductivity). The latter is most important for the electrical methods discussed in this thesis. The resistivity ρ is a property that is specific for a certain material. For a cylinder with length L, cross-section A and resistance R it is defined as

$$\rho = \frac{RA}{L} \ . \tag{2.1}$$

With a span of $10^{-5}\,\Omega$m (metallic minerals) to $10^{7}\,\Omega$m (dense, dry stones), the resistivity has one of the largest variabilities of all geophysical properties (Telford et al., 1990). Solely considering different rock types, sedimentary rocks have the lowest resistivity values, whereas metamorphic rocks have intermediate and volcanic rocks have the highest resistivity values. Resistivity values of several rock types and minerals that are present in the survey area in Turkey (cf. Chapter 7) are listed in Table A.2 in the Appendix.

There are several propagation types of electrical currents in earth materials that contribute to the resistivity, such as the electronic (ohmic), the electrolytic and the double layer conduction (Knödel et al., 1997; Telford et al., 1990):

Electronic Conduction

Generally, the charge transfer by free electrons is referred to as electronic conduction. It is the driving mechanism in metallic materials. In hard rocks, the electronic conductance is rather small. However, in rocks containing particles of metallic material, electronic conductance might occur.

Electrolytic Conduction

In wet, porous rocks the current is transported by ions through the electrolytic pore fluid. A connection between the pores and a certain portion of pore fluid is crucial. The empirical formula after Archie (1942) describes the resistivity ρ_s of a wet, porous and clay-free sediment in dependency on the porosity P (fraction of pore space per volume), the saturation S (fraction of pores filled with fluid) and the resistivity of the pore fluid ρ_{fl}:

$$\rho_s = aP^{-m}S^{-n}\rho_{fl} \ . \tag{2.2}$$

Here, a is a proportionality factor ($0.5 \leq a \leq 2.5$), m is the cementation exponent ($1.3 \leq m \leq 2.5$) and n is a saturation exponent ($n \approx 2$).

Double Layer Conduction

The double layer conduction is associated with an increased surface conductivity which is caused by an electric double layer at the interface between the rock matrix and the pore fluid. Due to negative surface charges of the rock, the ions solved in the pore fluid interact with the rock matrix. This results in an increased concentration of mobile ions towards the surface (Ward, 1990). This effect is strong when clay particles are present resulting in low resistivity values for clayey materials.

2.2. Direct Current Resistivity Method

The DC method is a widely spread geophysical method. It assesses the distribution of the resistivity within the subsurface by acquiring an electrical potential while injecting a direct current I into the ground. To derive the basic equations for the description of the DC method, we consider the electrostatic and electromagnetic theory. The very basic equations are Maxwell's equations and Ohm's law:

$$\text{Gauss' law} \quad \nabla \cdot \vec{D} = q \tag{2.3}$$

$$\text{Gauss' law for magnetic fields} \quad \nabla \cdot \vec{B} = 0 \tag{2.4}$$

$$\text{Faraday's law of induction} \quad \nabla \times \vec{E} = -\frac{\partial \vec{B}}{\partial t} \tag{2.5}$$

$$\text{Ampere's law} \quad \nabla \times \vec{H} = \vec{j} + \frac{\partial \vec{D}}{\partial t} \tag{2.6}$$

$$\text{Ohm's law} \quad \vec{j} = \sigma \vec{E} \tag{2.7}$$

The displacement field $\vec{D}$ is connected to the electrical field intensity $\vec{E}$ by the electrical permittivity ϵ:

$$\vec{D} = \epsilon \vec{E} \ . \tag{2.8}$$

The magnetic flux density $\vec{B}$ is connected to the magnetic field intensity $\vec{H}$ by the magnetic permeability μ:

$$\vec{B} = \mu \vec{H} \ . \tag{2.9}$$

Equations (2.3) through (2.7) describe the interaction of electromagnetic fields with matter and among each other. In particular, Gauss' law (Eq. 2.3) states that electrical charges are the sources of electrical fields, whereas magnetic fields are source free (Gauss' law for magnetic fields (Eq. 2.4)). After Faraday's law of induction (Eq. 2.5), the variation of a magnetic field causes a rotational electrical field which is proportional to the negative rate of change of $\vec{B}$. Ampere's law (Eq. 2.6) describes the generation of a magnetic field caused by electrical current including the displacement currents. Ohm's law (Eq. 2.7) connects the current density $\vec{j}$ with the electrical field intensity $\vec{E}$ by the conductivity σ.

Due to anisotropy, σ is generally considered as a tensor. That means that there are preferred or unprivileged directions of current flow due to pathways, e.g., caused by pressure in metamorphic or sedimentary rocks. However, the effect of anisotropy is not considered in this thesis because it would increase the degrees of freedom and therefore, a more complex regularization approach is needed. Consequently, σ (and the reciprocal ρ) is regarded as a scalar parameter in the following.

We consider the electrostatic approximation, i.e., we assume that the electromagnetic fields are not varying with time ($\frac{\partial}{\partial t} = 0$) and thus the electrical field is rotational-free ($\nabla \times \vec{E} = 0$). Under this assumption, the electrical field can be expressed as the negative gradient of an electrical potential Φ:

$$\vec{E} = -\nabla\Phi \ . \tag{2.10}$$

Consequently, Ohm's law becomes

$$\vec{j} = -\sigma\nabla\Phi \ . \tag{2.11}$$

We assume that there are no free charges in the subsurface, so the continuity (Eq. 2.3) demands

$$\nabla \cdot \vec{j} = 0 \ . \tag{2.12}$$

Combining Equations (2.11) and (2.12) yields

$$\nabla \cdot (\sigma\nabla\Phi) = 0 \ , \tag{2.13}$$

$$\Rightarrow \quad \nabla\sigma \cdot \nabla\Phi + \sigma\nabla^2\Phi = 0 \ . \tag{2.14}$$

When regarding the conductivity as an isotropic parameter, the gradient of σ is zero ($\nabla\sigma = 0$) and therefore

$$\nabla^2\Phi = 0 \ . \tag{2.15}$$

Equation (2.15) is generally referred to as Laplace equation. It is the basic equation of the DC method.

2.2.1. Potential in Homogeneous Media

We assume a homogeneous medium with constant resistivity $\rho = \rho_0$. A point current source buried in the subsurface is considered as it is common in the *mise-à-la-masse*

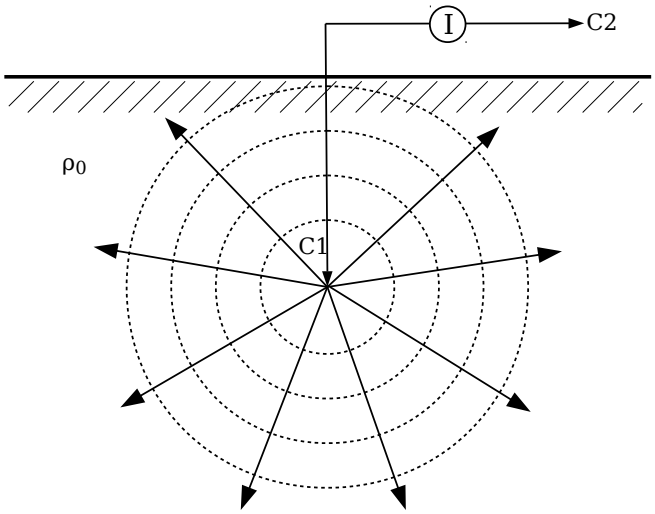

Figure 2.1.: *Current injected at a point source C_1 within a homogeneous half-space ($\rho = \rho_0$). Dashed lines display equipotential surfaces, arrows display current flow lines.*

method. Due to symmetry, the potential Φ is solely a function of the radial distances r to the source. The Laplace equation in spherical coordinates becomes

$$\nabla^2\Phi = \frac{\mathrm{d}^2\Phi}{\mathrm{d}r^2} + \frac{2}{r}\frac{\mathrm{d}\Phi}{\mathrm{d}r} = 0 \ . \tag{2.16}$$

Under the consideration that the potential vanishes in large distance $r \to \infty$, the solution of Equation (2.16) is

$$\Phi = \left(\frac{I\rho}{4\pi}\right)\frac{1}{r} \ . \tag{2.17}$$

Equation (2.17) is referred to as full-space solution. According to this equation, the current flow from the point current source is radial, and the equipotential surfaces are spherical and cross the current flow lines orthogonally as it is displayed in Figure 2.1.

Potential of a single current electrode at the surface

In most common DC field setups, the current injecting electrodes are located at the earth's surface, i.e., the earth-air interface. We assume the air to be a nonconductor ($\sigma = 0$) and the subsurface to be homogeneous ($\rho = \rho_0$). This setting is also referred to as homogeneous half-space. Considering the boundary condition[1] that the electrical field has no vertical component at the earth-air interface leads to the solution of Equation (2.16) in the form

$$\Phi = \left(\frac{I\rho}{2\pi}\right)\frac{1}{r} \ . \tag{2.18}$$

[1]Boundary conditions at interfaces between media with different resistivity are listed in chapter 2.2.2.

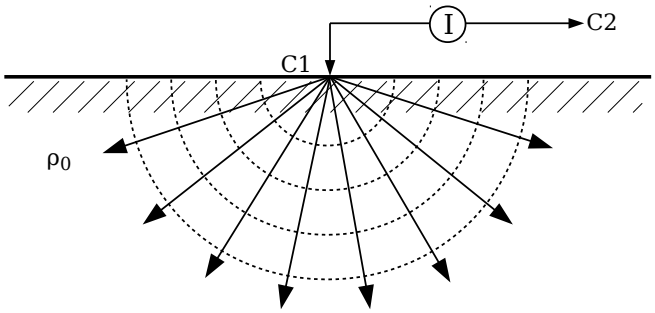

Figure 2.2.: *Current injected at a point source C_1 at the surface of a homogeneous half-space ($\rho = \rho_0$). Dashed lines display equipotential surfaces, arrows display current flow lines.*

Equation (2.18) is the half-space solution. This equation indicates that the current flows radially into the subsurface and the equipotential surfaces in the subsurface are half-spheres (cf. Figure 2.2).

Potential of two current electrodes at the surface

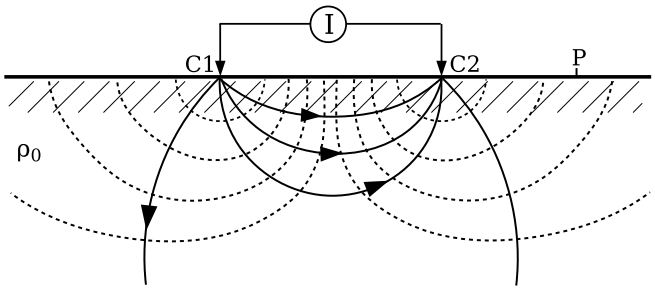

Figure 2.3.: *Currents I and $-I$ injected at point sources C_1 and C_2 located at the surface of a homogeneous half-space ($\rho = \rho_0$). Dashed lines display equipotential surfaces, arrows display current flow lines.*

If a second current injecting electrode is close to the first one, the effects superimpose. Figure 2.3 displays the current flow and equipotential surfaces produced by two current electrodes. The potential at a certain point P is a superposition of potential Φ_1 produced by C_1 and of the potential Φ_2 produced by C_2:

$$\Phi_1 - \Phi_2 = \frac{I\rho}{2\pi}\left(\frac{1}{r_1} - \frac{1}{r_2}\right) \ . \tag{2.19}$$

Here, r_1 and r_2 are the distances from point P to electrodes C_1 and C_2, respectively. The minus in the left hand term indicates that a positive current I is injected at electrode C_1 whereas the second electrode C_2 injects a current $-I$. This results in current flow from C_1 to C_2.

2.2.2. Potential in Inhomogeneous Media

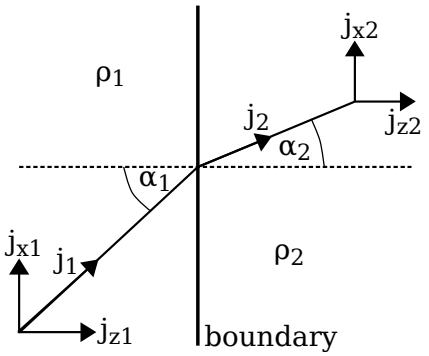

Figure 2.4.: *Current flow through a boundary between Medium 1 with resistivity ρ_1 and Medium 2 with resistivity $\rho_2 > \rho_1$ (redrawn after Telford et al. (1990)).*

In reality, the subsurface is rarely a perfect homogeneous half-space. It is rather inhomogeneous, but might be simplified as a layered half-space, as vertical contact or as anomalous bodies buried within a half-space, etc.. The behavior of electric field lines, electrical potential and current flow lines at interfaces between media with different resistivity underlies certain boundary conditions, such as

$$E_{x1} = E_{x2} \ , \tag{2.20}$$

$$\sigma_1 E_{z1} = \sigma_2 E_{z2} \ , \tag{2.21}$$

$$\Phi_1 = \Phi_2 \ . \tag{2.22}$$

As indicated in the schematic in Figure 2.4, the x-direction is parallel to the interface between Medium 1 (ρ_1) and Medium 2 (ρ_2), whereas the z-direction is perpendicular to the interface. Equation (2.20) states that the parallel components of the electrical field are continuous at the interface. Following Equation (2.21), the current flow j_z perpendicular to the interface is continuous. Furthermore, the electrical potential is continuous at the interface (Eq. 2.22). Using Ohm's law on Equation (2.20) yields

$$j_{x1}\rho_1 = j_{x2}\rho_2 \ , \tag{2.23}$$

$$\Rightarrow \frac{\tan\alpha_1}{\tan\alpha_2} = \frac{\rho_2}{\rho_1} = \frac{\sigma_1}{\sigma_2} \ . \tag{2.24}$$

Here, α_1 is the entrance angle of a current flow line approaching the interface in medium 1 and α_2 is the exit angle in medium 2. According to Equation (2.24), α_2 is dependent on the resistivity relation ρ_1/ρ_2 and the entrance angle. Therefore, a current flow line will be bent towards the perpendicular when $\rho_1 < \rho_2$ and vice versa.

The assumptions made above are simplifications of the rather inhomogeneous real earth subsurface. For example, we assumed that the resistivity is constant within a medium. Slow transitions of resistivity and anisotropy are neglected. Also, surface topography affects the propagation of the electrical fields and currents (see Chapter 6). Nevertheless, the simplification of a complex problem usually helps best to understand the basic principles.

2.2.3. Field Setup and Apparent Resistivity

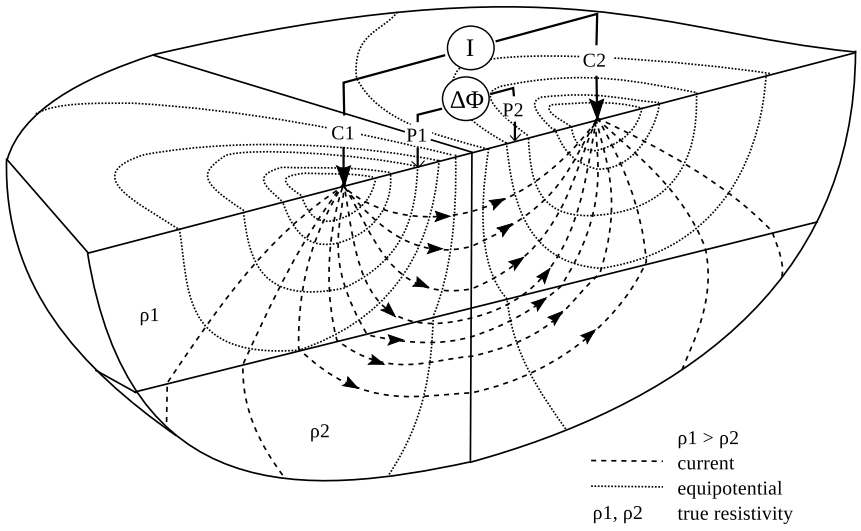

Figure 2.5.: *Principle of a 4-electrode setup (redrawn after Knödel et al. (1997)).*

In most common DC field setups 4 electrodes are involved as indicated in Figure 2.5: A direct current I is injected through current electrodes C_1 and C_2 while a potential difference $\Delta\Phi$ (or voltage $U = \Delta\Phi$) is measured by two potential electrodes P_1 and P_2. According to Equation (2.19), the potential difference is obtained by superposition of the potentials Φ_{11} and Φ_{21} that are measured at electrode P_1 and the potentials Φ_{12} and Φ_{22} that are measured at electrode P_2. The first subscript denotes the index of the current electrode and the second subscript the index of the potential electrode, respectively. The potential difference is

$$\Delta\Phi = (\Phi_{11} - \Phi_{21}) - (\Phi_{12} - \Phi_{22}) \ , \tag{2.25}$$

$$\Leftrightarrow \Delta\Phi = \frac{I\rho}{2\pi}\left[\left(\frac{1}{r_1} - \frac{1}{r_2}\right) - \left(\frac{1}{r_3} - \frac{1}{r_4}\right)\right] \ , \tag{2.26}$$

$$\Leftrightarrow \rho = \frac{\Delta\Phi}{I} 2\pi \left[\left(\frac{1}{r_1} - \frac{1}{r_2}\right) - \left(\frac{1}{r_3} - \frac{1}{r_4}\right)\right]^{-1} \ . \tag{2.27}$$

The distances between electrodes are denoted by r_i according to: $r_1 = \overline{C_1P_1}$, $r_2 = \overline{C_2P_1}$, $r_3 = \overline{C_1P_2}$ and $r_4 = \overline{C_2P_2}$. In case of a homogeneous subsurface with constant resistivity ρ_0, the resistivity ρ obtained by Equation (2.27) from a measured potential difference is equal to the real resistivity of the subsurface ($\rho = \rho_0$).

Note that the potentials are reciprocal. That means that the potential produced by current injection at point C_1 measured at P_1 is equal to the potential produced by current injection at point P_1 measured at C_1. This is of special interest for the forward calculation described in Chapter 3 since it simplifies and accelerates the calculations.

Apparent Resistivity

In the case of an inhomogeneous subsurface, the resistivity ρ calculated after Equation (2.27) is not equal to the real resistivity of the subsurface. Rather, it is a weighted average resistivity ρ_a that is influenced by the resistivity of all media that are passed through by the current flow. Introducing the apparent resistivity ρ_a into Equation (2.27) yields

$$\rho_a = \frac{\Delta\Phi}{I} \underbrace{2\pi \left[\left(\frac{1}{r_1} - \frac{1}{r_2} \right) - \left(\frac{1}{r_3} - \frac{1}{r_4} \right) \right]^{-1}}_{G} , \tag{2.28}$$

$$\Rightarrow \rho_a = \frac{\Delta\Phi}{I} G . \tag{2.29}$$

The real factor G is referred to as geometry factor.

Array Types

Commonly, several conventional DC arrays (or electrode setups) are applied (see Figure 2.6). Table 2.1 lists simplified formulations of G and the depth of investigation DOI_t corresponding to the presented electrode setups. The depth DOI_t is also referred to as pseudo-depth. Due to the symmetry of the arrays, different resolution characteristics regarding subsurface structures are achieved. Thus, the choice of array type strongly depends on the geological setting that is to be investigated. For best results, a combination of different array types is advisable (Dahlin and Zhou, 2004).

Dahlin and Zhou (2004) investigate the advantages and disadvantages concerning sensitivity, signal-to-noise ratio (S/N), depth of investigation, spatial resolution and anomaly effect for different DC arrays. The sensitivity patterns are displayed in Figure 2.7. Reddish colors represent positive signal contributions, bluish colors represent negative signal contributions. Dark regions denote higher sensitivity. The main results of their investigation are summarized in the following: The Wenner array offers a high S/N ratio and a large penetration depth, but the spatial resolution is rather poor. The Schlumberger array exhibits a large S/N ratio and an increased imaging resolution compared to the Wenner array. The Dipole-Dipole configuration has a high anomaly effect meaning that the signature caused by a resistivity anomaly is significantly larger than the effect caused by the background (Militzer et al., 1979). The depth resolution is moderate, despite a rather low S/N ratio. The Pole-Dipole array also offers only a low S/N ratio, but moderate anomaly effects and good spatial and imaging resolution. The Gradient array has similar spatial and image resolution as the Dipole-Dipole and Pole-Dipole configurations.

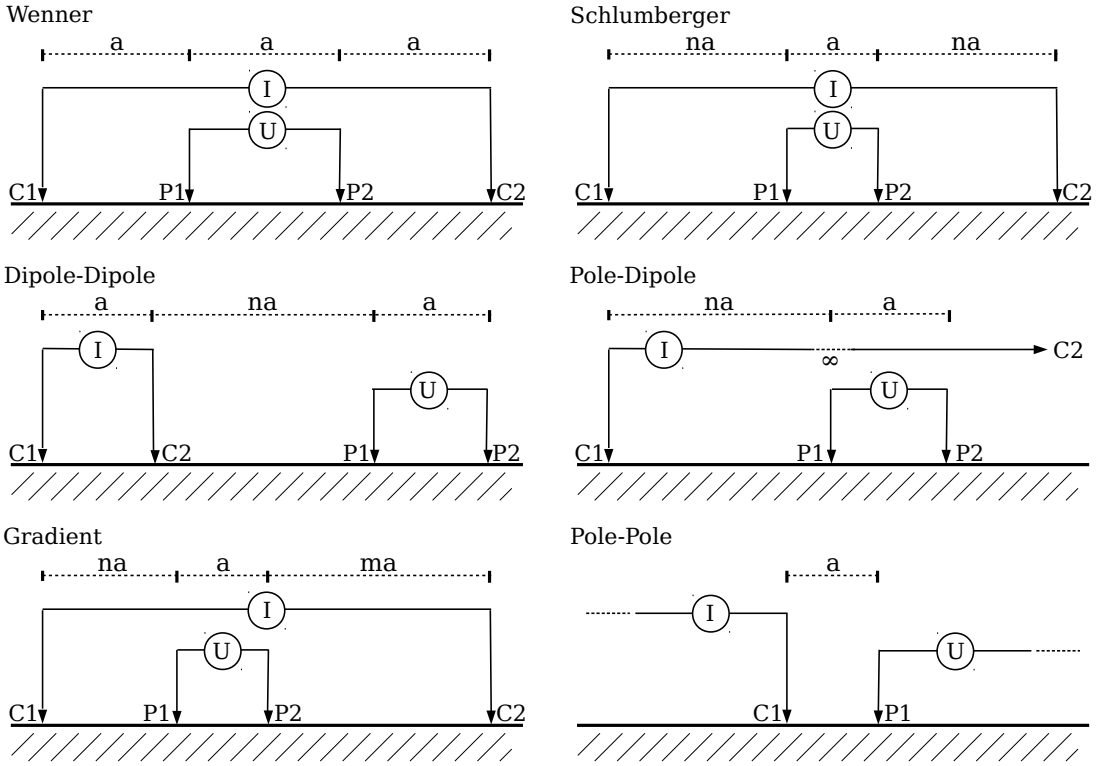

Figure 2.6.: *Conventional DC arrays: A direct current I is injected through electrodes C_1 and C_2, a potential difference $\Delta\Phi = U$ is measured between electrodes P_1 and P_2. Distances between electrodes are given in terms of the smallest electrode distance a and integer factors n and m.*

Table 2.1.: *Geometry factors and depth of investigation DOI_t according to Barker (1989) for conventional DC arrays.*

Array Type	Geometry Factor	DOI_t
Wenner	$2\pi a$	$0.17 \cdot \overline{C_1C_2}$
Schlumberger	$\pi an(n+1)$	$0.19 \cdot \overline{C_1C_2}$
Dipole-Dipole	$\pi an(n+1)(n+2)$	$0.25 \cdot \overline{C_1P_2}$
Pole-Dipole	$2\pi an(n+1)$	$0.33 \cdot \overline{C_1P_2}$
Gradient	$2\pi a\frac{n(n+1)m(m+1)}{(m-n)(m-n+1)}$	$0.19 \cdot \overline{C_1C_2}$
Pole-Pole	$2\pi a$	$0.35 \cdot \overline{C_1P_1}$

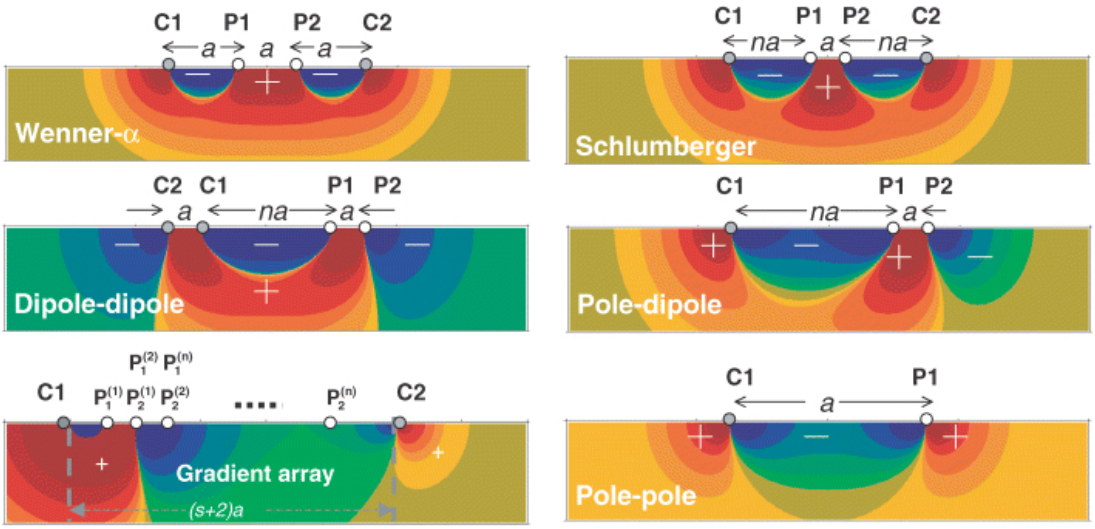

Figure 2.7.: *Sensitivity patterns of different array types (Dahlin and Zhou, 2004).*

Field Application

Dependent on the geophysical question and on the geological setting, different procedures of combining single 4-electrode measurements exist:

- *Mapping* is used to investigate near-surface resistivity variations in lateral direction. Therefore, a fixed 4-point electrode setting is moved along a profile. The most suitable electrode configuration is the Wenner array.
- *Sounding* is applied to investigate vertical resistivity variations such as horizontal layers with different resistivity. By increasing the electrode spacing, information of deeper layers contributes to the obtained apparent resistivity. A suitable electrode configuration is the Schlumberger array.
- *Multi-electrode* measurements combine the procedures of mapping and sounding. A larger number of electrodes is distributed over a profile and are connected to the device by a multi-core cable. Many electrode combinations are measured automatically. The combinations are defined in a protocol that states which combinations of electrode distance a and n-spacing n are to be realized. The result is a two-dimensional cross-section of the subsurface (in lateral and vertical direction), which is combined into a resistivity pseudo-section (see Figure 2.8). In the pseudo-section, the measured data is visualized for each applied electrode combination. The x-axis refers to the center of the electrode setup or the center of the receiving dipole. The y-axis either refers to the pseudo-depth in m or the n-level.

Since the obtained apparent resistivity is not equal to the real subsurface values, a model of the subsurface resistivity distribution is desired that explains the measured data. This is determined by the concept of inversion which is introduced in Chapter 4.

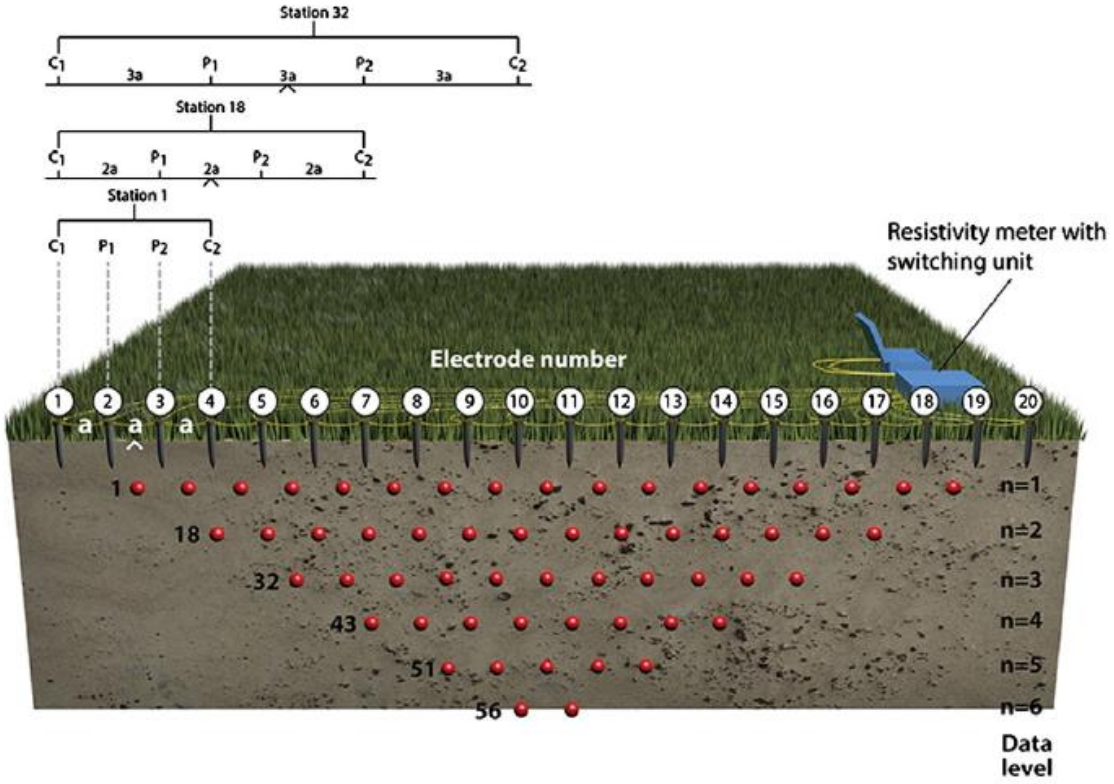

Figure 2.8.: *Sketch of a multi-electrode setup and the positions of acquired data in the 2D pseudosection according to the involved 4-point electrode configuration (British Geological Survey (c) NERC 2013).*

2.3. Induced Polarization Method

The IP method is closely related to the DC resistivity method. It makes use of polarization effects in the subsurface. Due to these effects, the voltage does not drop to zero instantly when the injected current is turned off. IP data is commonly acquired with the same electrode setup and devices as the DC data. The measurement and data processing is done either in the time-domain or in the frequency-domain.

The two basic electrochemical phenomena that provoke the polarization effects are depicted in Figure 2.9:

Membrane Polarization (or *electrolytic polarization*) occurs in porous rocks without metallic content. In saturated pores, negative surface charges cause an accumulation of positively charged ions in the pore fluid, especially at pore throats or when clay particles are present (cf. Figure 2.9-a). If an external electric field is excited, the movement of anions is disturbed because the accumulation of cations blocks the pore space. Thus, zones of ion concentration and zones of ion deficiency are produced (cf. Figure 2.9-b).

Electrode Polarization (or *overvoltage*) is driven by (metallic) minerals with electronic conductance that block the pores in a saturated rock. When the pore space is free, the ions can move freely when an external electrical field is applied (cf. Figure 2.9-c). If a mineral blocks the pore space, there is a transition between electrolytic conduction of the pore fluid and electronic conduction of the metallic mineral. When an electrical field is applied, ions accumulate at both interfaces between mineral and electrolyte to build a double layer (cf. Figure 2.9-d).

When the external field is turned off, the ions move back to the normal state within a finite time interval which applies for both polarization phenomena. The electrode polarization effect is stronger than the membrane polarization. The membrane polarization is often referred to as background polarization.

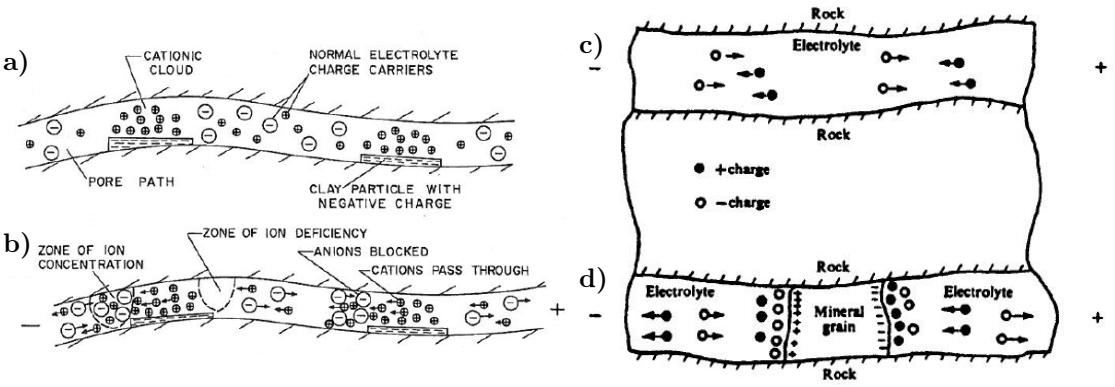

Figure 2.9.: *Schematic of the two main phenomena causing induced polarization effects.* ***Left:*** *Membrane polarization in a porous sandstone with clay content;* ***(a)*** *No DC voltage is applied, ions normally distributed in pore fluid, accumulation of positively charged ions near clay particles;* ***(b)*** *DC voltage is applied, membrane polarization occurs. After Ward and Fraser (1967); Sumner (1976).* ***Right:*** *electrode polarization in a porous rock with mineral content; DC voltage is applied.* ***c)*** *Electrolytic conductance is predominant and* ***d)*** *Electrode polarization occurs, caused by mineral grain blocking the pore; (Telford et al., 1990).*

Without polarization effects, the measured voltage after turn-off of the DC current (t_0) would theoretically drop to zero instantly. However, the diffusion of ions back to the normal state causes the voltage $U(t)$ to decay within a finite decay time (or relaxation time) after an instant drop from DC-voltage U_p to a secondary voltage U_s. An exemplary voltage decay curve is displayed in Figure 2.10.

2.3.1. Time-Domain IP measurements

The time-domain IP datum is the chargeability

$$M = \frac{U_s}{U_p} \tag{2.30}$$

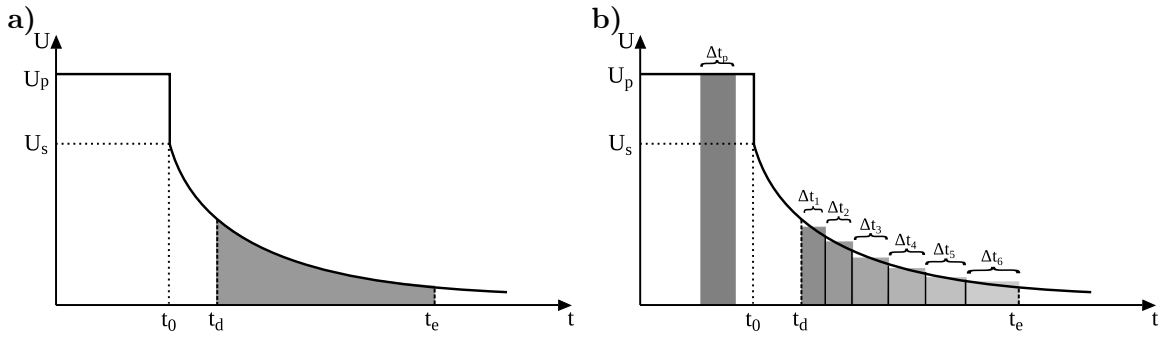

Figure 2.10.: *Voltage decay curve $U(t)$. The current is switched off at $t = t_0$. The primary voltage U_p is measured at $t < t_0$. At t_0 the voltage drops to the secondary voltage U_s.* ***a)*** *The area under the voltage decay curve is integrated from delay time t_d to last time point t_e.* ***b)*** *The voltage decay is averaged within several time intervals Δt_i (with $i = 1, 2, 3, \dots$) to approximate the area under the curve. The primary voltage is averaged within a time interval Δt_p.*

which is the secondary voltage U_s normalized to the primary voltage U_p and is given in V/V with values $\in [0, 1]$ or in mV/V with values $\in [0, 1000]$. It is a measure for the energy that is stored during the polarization processes. Technically, the measurement of U_s is very challenging. Therefore, another formulation of the chargeability is used in practice:

$$m = \frac{1}{U_p} \int_{t_d}^{t_e} U(t)\,\mathrm{d}t \ . \tag{2.31}$$

This is equivalent to the area under the voltage decay curve within a time interval $[t_d\ t_e]$, normalized to the primary voltage. Most receiver systems measure the voltage decay curve $U(\Delta t)$ in several time intervals Δt_i (with $i = 1, 2, 3, \dots$), with integration time $\sum_i \Delta t_i = t_e - t_d$ (see Figure 2.10). The area under the decay curve A is then approximated by the sum of all time intervals $A = \sum_i U(\Delta t_i)\Delta t_i$. The unity of the integrated chargeability m is ms.

However, this formulation of chargeability is strongly dependent on the time interval between delay time t_d and last measured time point t_e. Therefore, the chargeability is usually calibrated to the Newmont Standard M_{331}, which is the chargeability for a standard square wave with integration time = 1 s and transmitter on-time = 3 s and off-time = 3 s (Swift Jr, 1973). The numerical value of the calibrated chargeability m in ms is then approximately the same as for the chargeability M in mV/V (Sumner, 1976)[2].

The transmitter signal $I(t)$ is usually an alternating direct current with 50% duty cycle. The current is switched on for a certain on-time T_{on} and switched off for an off-time $T_{\text{off}} = T_{\text{on}}$. Then the current is switched on again with opposite sign for a

[2]In Chapter 3 and the following chapters, the variable m is used to represent both definitions of chargeability. In mathematical formulations, the chargeability usually refers to the ideal definition (2.30) in V/V. However, in formulations regarding the practical application, the chargeability refers to the definition in (2.31).

time T_{on} and so on. The switching frequency $\omega = 2\pi/T$ has to be chosen carefully. If the frequency is too large, T_{on} and T_{off} may be insufficient for the polarization effects to build up and relax fully. Thus, the polarization effects of consecutive cycles overlap and would influence the time-domain measurements.

Frequency-domain IP (or Spectral IP) makes use of the effects of using different frequencies, such as different amplitude of measured voltage and a phase shift between transmitter current and received voltage signal. However, the frequency used in time-domain IP should be small to ensure that frequency effects are small. Also, there needs to be a certain delay time t_d between current switch-off t_0 and the first data point because EM effects might occur directly after t_0 that superimpose the measured IP-voltage decay. The time t_e of the last data point is a time point before the measured voltage reaches the noise level.

As an overview, chargeability values for several materials are listed in Table A.3 and Table A.4 in the Appendix. Note, the values are rather qualitatively since they are not given in Newmont Standard. However, it is apparent that the polarization effect caused by electrode polarization in a material containing portions of sulfide ores is strong. With regard to the interpretation of field data described in Chapter 7, strong chargeability anomalies are expected due to the presence of a copper ore deposit with sulfide content in the survey area.

Note that the interpretation of chargeability is a powerful tool for detecting disseminated sulfide ore bodies. Inference about texture and concentration of polarizable material is only derived from spectral interpretation. Methods of retrieving spectral information from TDIP data and modeling were presented by Hönig (2002), Hördt et al. (2006), Hönig and Tezkan (2007) and Fiandaca et al. (2012).

2.3.2. Frequency-Domain Measurements

Frequency-domain measurements make use of the frequency dependence of the apparent resistivity. Measurements are conducted using at least two different frequencies in the range 0.1 Hz-10 Hz. Thereby, the relation

$$\text{FE} = \frac{\rho_{a,0} - \rho_{a,1}}{\rho_{a,1}} \tag{2.32}$$

is referred to as frequency effect. Here, $\rho_{a,0}$ is the apparent resistivity determined at low frequency whereas $\rho_{a,1} < \rho_{a,0}$ corresponds to the apparent resistivity determined at a higher frequency. The percentage frequency effect is $\text{PFE} = 100 \times \text{FE}$. The metal factor

$$\text{MF} = 2\pi \times 10^5 \frac{\rho_{a,0} - \rho_{a,1}}{\rho_{a,0}\rho_{a,1}} \tag{2.33}$$

was introduced by Marshall and Madden (1959). It is a normalization of the PFE to reduce the variation of the IP effect with the effective resistivity of the host rock (Keary et al., 2002).

In theory, the FD frequency effect is equivalent to the TD chargeability, assuming that the chargeability is

$$M = \left(\lim_{t\to\infty} U(t) - \lim_{t\to 0} U(t)\right) / \lim_{t\to\infty} U(t) \ . \tag{2.34}$$

Then, the resistivity $\rho_{a,1}$ is replaced by resistivity $\rho_{a,\infty}$ which corresponds to a very high frequency. This yields (Telford et al., 1990)

$$M = \frac{\rho_{a,0} - \rho_{a,\infty}}{\rho_{a,0}} = 1 - \frac{\rho_{a,1}}{\rho_{a,0}} \tag{2.35}$$

$$= 1 - \frac{1}{1+\mathrm{FE}} = \frac{\mathrm{FE}}{1+\mathrm{FE}} \approx \mathrm{FE} \tag{2.36}$$

when FE$\ll 1$. However, in practice, this is not entirely valid since the exact theoretical analysis of the IP effect is unknown and the utilized systems cannot realize the DC and infinite frequencies (Telford et al., 1990).

Spectral IP

In spectral induced polarization (SIP), a variety of frequencies is utilized. In field measurements, the frequency range is between 1 mHz and 100 Hz and in laboratory measurements between 1 μHz and 50 kHz (Revil et al., 2012). The amplitude of the voltage and a phase lag φ between transmitted and measured signal is acquired. The real valued resistivity σ is derived from the voltage using a geometry factor as in (2.29). These quantities are combined to the complex conductivity σ^*, which is defined as (e.g. Revil et al., 2012)

$$\sigma^* = |\sigma| e^{i\varphi} = \sigma_r + i\sigma_i \tag{2.37}$$

with real and imaginary parts σ_r and σ_i, magnitude $|\sigma| = \sqrt{\sigma_r^2 + \sigma_i^2}$ and $\varphi = \arctan(\sigma_i/\sigma_r)$.

An exemplary spectral IP response is shown in Figure 2.11. The dispersion between low and high frequencies is also referred to as 'relaxation' (Reynolds, 1997). The shape of the resistivity (or impedance) dispersion is described by the Cole-Cole model (Cole and Cole, 1941; Pelton, 1977)

$$\rho^*(\omega) = \rho_0 \left[1 - m\left(1 - \frac{1}{1+(i\omega\tau)^c}\right)\right] \tag{2.38}$$

where ρ_0 is the real valued DC resistivity, m is the chargeability, τ is the time constant (also referred to as relaxation time) and c is the exponent of the angular frequency ω. The parameters τ and c are diagnostic for the texture of the probed material, such as grain size and grain size distribution of polarizable particles (Reynolds, 1997).

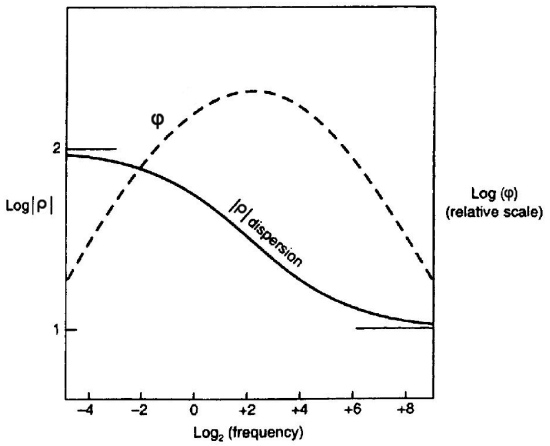

Figure 2.11.: *IP response in terms of resistivity $|\rho|$ and phase φ dependent on the frequency modified after (Pelton et al., 1983; Reynolds, 1997).*

Further relaxation models, such as the Debye-model (Pelton, 1977) or the Dias model (Dias, 1968) are summarized by Dias (2000).

2.3.3. Mathematical Formulation after Seigel

The mathematical formulation according to Seigel (1959) explains the TD polarization effects by the presence of a volume density of dipolar sources. The primary potential in the absence of polarization effects is

$$\Phi = \frac{I}{\sigma} F \tag{2.39}$$

and the current density is $\vec{j} = \sigma \vec{E}$. The factor F refers to electrode geometry and distance r similar to the factor G in Equation (2.29). When polarization effects occur, a volume distribution of current dipoles anti-parallel to the electric field appear. The volume current moment strength is $\vec{M} = -m\vec{j}$. It is shown that, in this case, the total current density becomes $\vec{j}' = \vec{j} + \vec{M} = \vec{j}(1-m)$. The primary potential is altered to

$$\Phi' = \frac{I}{\sigma(1-m)} F = \frac{\Phi}{(1-m)} \ . \tag{2.40}$$

That means that the primary potential and therefore also a measured apparent resistivity is increased. Figure 2.12 displays a typical potential curve for a current switch-on at $t = t_{0,\mathrm{on}}$ and a switch-off at $t = t_{0,\mathrm{off}}$. When the current is switched on, the potential instantly jumps to Φ. The presence of polarization effects leads to a transient potential increase up to a level $\Phi' = \Phi_p$. When switching the current off, the potential instantly drops by $\Phi = (1-m)\Phi'$ to the secondary potential

$$\Phi_s = \Phi' - \Phi = \left(\frac{IF}{\sigma}\right)\left(\frac{m}{1-m}\right) = m\Phi' \ . \tag{2.41}$$

After that drop, the potential decays slowly to zero due to the relaxation of polarization effects. The shape of the potential increase and decay curve is not subject of this

approach. Regarding the discussed potentials, the chargeability can be expressed as secondary potential normalized by the primary potential in the form

$$m = \frac{\Phi_s}{\Phi_p} = \frac{\Phi' - \Phi}{\Phi'} \ . \tag{2.42}$$

This is consistent with the definition of chargeability in Equation (2.30).

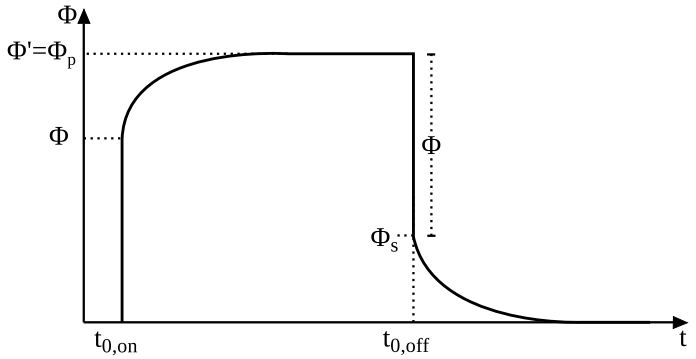

Figure 2.12.: *Sketch of potential $\Phi(t)$ for a transmitter switch-on at $t_{0,\mathrm{on}}$ and transmitter switch-off at $t_{0,\mathrm{off}}$. When the transmitter is switched on, the potential increases instantly to Φ, then the potential increases slowly to a constant level Φ'. When the transmitter is switched off, the potential decreases instantly to Φ_s, then it decays to zero with time.*

3. Forward Modeling of DC and TDIP Data

This chapter gives an introduction into the 2D DC and TDIP forward calculation as it is implemented in the algorithm `ResIPIn2D`. The algorithm is based on the finite element approach using an unstructured triangular mesh. Synthetic IP data are obtained according to the model after Seigel (1959). To prove the accuracy of the newly developed algorithm, several forward modeling results are assessed by comparison with analytical solutions and results obtained by established algorithms, and by evaluating the reciprocity. The descriptions in this chapter follow mainly Rücker et al. (2006) and Kemna (2000).

3.1. Basic Equations

Current injecting electrodes are simulated by introducing a source term $\nabla \cdot \vec{j}_q$ with current density $\vec{j}_q$ into Poisson's equation (2.13), leading to

$$\nabla \cdot (\sigma \nabla \Phi) = -\nabla \cdot \vec{j}_q \ . \tag{3.1}$$

All sources are considered to be point current sources at positions $\vec{r}_q = (x_q, y_q, z_q)$ that follow

$$\nabla \cdot \vec{j}_q = I\delta(\vec{r} - \vec{r}_q) \ . \tag{3.2}$$

Here, I is the injected current and δ is Dirac's Delta function.

The goal is to calculate synthetic DC data (ρ_a) and TDIP data (m_a) for a given 2D subsurface model with resistivity distribution $\rho(x, z)$ and chargeability distribution $m(x, z)$. The x- and y-axes are horizontal, whereas the z-axis is positive downwards with $z = 0$ at the surface. In the 2D case, the x-axis is parallel to the profile direction and perpendicular to the strike direction of the model, whereas the y-axis coincides with the strike direction. That means that the 2D model is constant in the y-direction. Therefore, we consider only the 2D (x, z)-plane of the model by omitting the y-components and allowing source positions only at $y_q = 0$. Equation (3.1) is solved for certain boundary conditions that are explained in Chapter 3.1.3. The result is a potential distribution $\Phi(x, y, z)$ produced by current injection at a single source electrode. To obtain apparent resistivity values for a given electrode setup, the potential distribution needs to be calculated for all current electrodes. Subsequently, the potentials are superposed according to Equation (2.28). The calculation of apparent chargeability values is explained in Chapter 3.4.

3.1.1. Fourier Cosine Transformation

Although the examined model is two-dimensional (x, z), the potential of a point current source extends in three dimensions (x, y, z). Therefore, this setting is referred to as 2.5 dimensional. To replace the dependence on the y-direction, a Fourier Cosine transformation (FCT) from (x, y, z)-space to wavenumber domain (x, k, z) is applied:

$$\tilde{\Phi}(x, k, z) = \int_0^\infty \Phi(x, y, z) \cos(ky)\, \mathrm{d}y \tag{3.3}$$

where k is referred to as wavenumber and $\tilde{\Phi}$ is the transformed potential in the (x, k, z)-space. The transformation back into (x, y, z)-space is performed by Inverse Fourier Cosine transformation (IFCT):

$$\Phi(x, y, z) = \frac{2}{\pi} \int_0^\infty \tilde{\Phi}(x, k, z) \cos(ky)\, \mathrm{d}k \ . \tag{3.4}$$

Since we allow electrodes only in the (x, z)-plane, meaning $y_q = 0$, Equation (3.4) reduces to

$$\Phi(x, 0, z) = \int_0^\infty \tilde{\Phi}(x, k, z)\, \mathrm{d}k \tag{3.5}$$

This equation can be expressed as sum in the form (e.g. Xu et al. (2000))

$$\Phi(r) \approx \sum_{j=1}^{n} \tilde{\Phi}(r, k_j) g_{k,j} \tag{3.6}$$

with radial distance to the source $r = \sqrt{(x - x_q)^2 + (z - z_q)^2}$. The coefficients k_j are discretized values of k and $g_{k,j}$ are the corresponding weighting coefficients. The potential decreases inversely with growing r, thus the asymptotic behavior of the transformed potential is similar to that of the function $K_0(rk)$ (Queralt et al., 1991). K_0 is the modified Bessel function of order zero and second kind. Considering this behavior we get (Xu et al., 2000)

$$\frac{1}{r} = \frac{2}{\pi} \int_0^\infty K_0(kr)\, \mathrm{d}k \approx \sum_{j=1}^{n} K_0(k_j r) g_{k,j} \ . \tag{3.7}$$

That means that the potential of a homogeneous half-space is proportional to K_0, $(|\tilde{\Phi}| \propto K_0(kr))$. The values of k_j and $g_{k,j}$ need to be chosen carefully in order to reproduce r sufficiently. There are different approaches of determining the coefficients such as Gaussian quadrature or Laguerre integration (LaBrecque et al., 1996). The coefficients implemented in `ResIPIn2D` were obtained from Erdoğan et al. (2008) and were calculated with the optimization approach after Xu et al. (2000). They are listed in Appendix B.1. Applying the FCT (Eq. 3.3) on Poisson's equation (3.1) yields

$$\frac{\partial}{\partial x}\left(\sigma \frac{\partial}{\partial x}\tilde{\Phi}\right) + \frac{\partial}{\partial z}\left(\sigma \frac{\partial}{\partial z}\tilde{\Phi}\right) - \sigma k^2 \tilde{\Phi} = -I\delta(x - x_q)\delta(z - z_q) \ . \tag{3.8}$$

This is the 2D (or 2.5D) Helmholtz equation.

3.1.2. Singularity Removal

Due to Dirac's delta function in the source term, a singularity exists in the vicinity of the source. This leads to an erroneous calculation of potentials. To overcome this problem, the total potential $\tilde{\Phi}$ is separated into a primary potential $\tilde{\Phi}_p$ and a secondary potential $\tilde{\Phi}_s$ (Coggon, 1971):

$$\tilde{\Phi} = \tilde{\Phi}_p + \tilde{\Phi}_s \ . \tag{3.9}$$

The primary potential is a part of the total potential that can be calculated analytically and is also referred to as background potential. It is calculated for a background model $\sigma_0(x, z)$ which may either be a homogeneous half-space or a horizontally layered half-space. The Helmholtz equation for the primary potential is

$$\frac{\partial}{\partial x}\left(\sigma_0 \frac{\partial}{\partial x}\tilde{\Phi}_p\right) + \frac{\partial}{\partial z}\left(\sigma_0 \frac{\partial}{\partial z}\tilde{\Phi}_p\right) - \sigma_0 k^2 \tilde{\Phi}_p = -I\delta(x - x_q)\delta(z - z_q) \ . \tag{3.10}$$

The solution of Equation (3.10) for a homogeneous half-space with a constant conductivity σ_0 is a combination of Equation (2.18) and Equation (3.7):

$$\tilde{\Phi}_p = \frac{I}{2\pi\sigma_0} K_0(kr) \ . \tag{3.11}$$

The secondary potential is the part that contains all deviations of the total field from the primary field due to deviations $\Delta\sigma = \sigma - \sigma_0$ of the conductivity distribution from the background model. Inserting Equations (3.10) and (3.9) in Equation (3.8) yields the Helmholtz equation with respect to the secondary potential in the form

$$\begin{aligned} &\frac{\partial}{\partial x}\left(\sigma \frac{\partial}{\partial x}\tilde{\Phi}_s\right) + \frac{\partial}{\partial z}\left(\sigma \frac{\partial}{\partial z}\tilde{\Phi}_s\right) - \sigma k^2 \tilde{\Phi}_s + \frac{\partial}{\partial x}\left(\Delta\sigma \frac{\partial}{\partial x}\tilde{\Phi}_p\right) \\ &= -\left[\frac{\partial}{\partial z}\left(\Delta\sigma \frac{\partial}{\partial z}\tilde{\Phi}_p\right) - \Delta\sigma k^2 \tilde{\Phi}_p\right] \ . \end{aligned} \tag{3.12}$$

The singularity due to Dirac's delta function has been removed. In order to obtain the total potential, Equation (3.12) has to be solved with respect to the secondary potential and afterwards the known primary potential is added.

Lowry et al. (1989) suggested using a mean conductivity as background model σ_0. However, in this case, the singularity is not completely removed. According to Zhao and Yedlin (1996), it is more suitable to use the conductivity in direct vicinity to the source electrode as σ_0 instead. To save computational time it is convenient to calculate the primary potential with $\sigma_0 = 1$ and multiply it later with the actual conductivity at the source (Rücker et al., 2006).

3.1.3. Boundary Conditions

When examining the potential distribution within a limited computational area, the problem to solve is a boundary value problem. In the 2D case, the computational area (Ω) is a half-space within the (x, z)-plane with boundary $\Gamma = \Gamma_s + \Gamma_h$. Γ

is split into the boundary at the earth surface (Γ_s) and further boundaries of the half-space (Γ_h) in depth and to the sides. Equation (3.12) needs to be solved in Ω under consideration of certain boundary conditions. Commonly, Neumann boundary conditions are defined for the surface boundary Γ_s:

$$\sigma \frac{\partial \Phi}{\partial n} = 0 \quad \text{on } \Gamma_s \ . \tag{3.13}$$

Here, n describes the outward normal direction. That means that no current flow is allowed through the earth surface. For the half-space boundaries, either Neumann or Dirichlet boundary conditions are suitable. The Dirichlet condition demands that the potential has decreased to zero:

$$\Phi = 0 \quad on\ \Gamma_h \ . \tag{3.14}$$

To meet this condition, the extent of the computational area needs to be sufficiently large. These boundary conditions are adequate in many cases, but according to Coggon (1971), the Dirichlet condition might suppress the potential at Γ_h, whereas the Neumann condition might amplify the potential at Γ_h. To overcome this problem, Dey and Morrison (1979) recommend the use of mixed boundary conditions considering an asymptotic behavior of Φ and $\partial\Phi/\partial n$ at the half-space boundaries Γ_h. The mixed boundary conditions (Dey and Morrison, 1979) are

$$\frac{\partial}{\partial n}\Phi + \alpha \frac{\Phi}{r} = 0 \tag{3.15}$$

with $\alpha = 0$ for Γ_s, $\alpha = \cos\theta$ for Γ_h and θ being the angle between r and n. Following Queralt et al. (1991), the boundary conditions for the transformed potential $\tilde{\Phi}(x, k, z)$ are

$$\sigma \frac{\partial}{\partial n}\tilde{\Phi} + \beta \tilde{\Phi} = 0 \tag{3.16}$$

with

$$\beta = 0 \qquad \text{on } \Gamma_s \tag{3.17}$$

$$\beta = \sigma \cos\theta \frac{K_1(rk)}{K_0(rk)} k \qquad \text{on } \Gamma_h \tag{3.18}$$

and K_1 being the modified Bessel function of order one and second kind. The boundary value problem is solved with the Finite Element approach explained in Chapter 3.2.

3.2. Finite Element Method

The Finite Element (FE) approach follows Hamilton's principle of the minimization of energy. It was firstly applied on geophysical field data by Coggon (1971). He applied the FE method on electromagnetic and induced polarization effects in two dimensions. Solving a boundary value problem with FE commonly makes use of a

variational principle. The energy or power is expressed as an integral over volume V. In the general DC case, the field power and the power of the current source are

$$P_f = \int_V \sigma(\nabla\Phi)^2 \,\mathrm{d}V \quad \text{field power} \tag{3.19}$$

$$P_q = \int_V 2\Phi\nabla\cdot\vec{j}_q \,\mathrm{d}V \quad \text{current source power} \tag{3.20}$$

with total power $P_t = P_f + P_q$. Minimization is accomplished by the requirement that the variation ΔP_t needs to be zero:

$$\Delta\left(P_f + P_q\right) = \Delta \int_V \left\{\sigma(\nabla\Phi)^2 + 2\Phi\nabla\cdot\vec{j}_q\right\} \mathrm{d}V = 0 \ . \tag{3.21}$$

The boundary value problem consists of Equations (3.12) and (3.16). After including the FCT into the 2.5-dimensional (x, k, z)-space, the point current source term, the singularity removal and the boundary conditions, the variational equation becomes (Kemna, 2000)

$$\begin{aligned}\Delta \iint_\Omega \Bigg\{ &\frac{1}{2}\sigma\left[\left(\frac{\partial\tilde{\Phi}_s}{\partial x}\right)^2 + \left(\frac{\partial\tilde{\Phi}_s}{\partial z}\right)^2\right] + \frac{1}{2}\sigma k^2\tilde{\Phi}_s^2 \\ &- \left[\frac{\partial}{\partial x}\left(\Delta\sigma\frac{\partial\tilde{\Phi}_p}{\partial x}\right) + \frac{\partial}{\partial z}\left(\Delta\sigma\frac{\partial\tilde{\Phi}_p}{\partial z}\right) - \Delta\sigma k^2\tilde{\Phi}_p\right]\tilde{\Phi}_s\Bigg\} \,\mathrm{d}x\,\mathrm{d}z + \oint_\Gamma \frac{1}{2}\beta\tilde{\Phi}_s^2 \,\mathrm{d}\Gamma = 0\end{aligned} \tag{3.22}$$

Here, the integration of the left term is done over the area Ω and the integration of the right term over the boundary Γ with step length $d\Gamma$.

In order to explain the procedure of splitting the computational area into finite elements, we first consider the solution of the following variational equation for the sake of simplicity:

$$\Delta F = 0 \tag{3.23}$$

$$\text{with } F = \int_\Omega f(\Phi) \,\mathrm{d}\Omega \ , \tag{3.24}$$

with unknown (field) quantity Φ and known function $f(\Phi)$. Dividing the computational area Ω into M finite elements, reduces the integral over Ω into a sum of the integrals over the areas Ω_i of each element i:

$$F = \sum_{i=1}^{M}\left[\int_{\Omega_i} f(\Phi)\,\mathrm{d}\Omega\right] \ . \tag{3.25}$$

The continuous, unknown field quantity Φ is now discretized into a vector $\vec{\Phi} = (\Phi_1, \Phi_2, \ldots, \Phi_N)$ at N discrete nodes located at the edges of the elements (see Figure 3.1-a). The discrete values of $\vec{\Phi}$ are connected by shape functions s_i

$$F \approx \sum_{i=1}^{M} s_i(\Phi_{i1}, \ldots, \Phi_{i\tau}) \tag{3.26}$$

with τ being the number of nodes at element i. This problem can be expressed as matrix formulation since it can be reduced to the search for a minimum of a function depending on a set of independent variables by setting the partial derivatives equal to zero (Coggon, 1971).

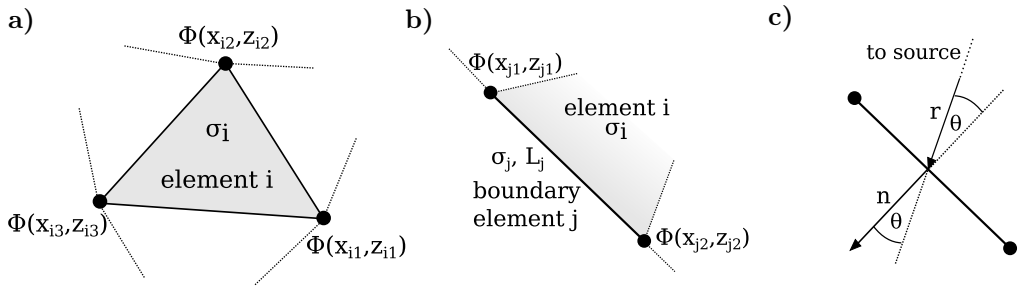

Figure 3.1.: a) *Schematic of a triangular element i with constant conductivity σ_i and Potentials $\Phi_{i\tau}$ at the three edge nodes with coordinates $(x_{i\tau}, z_{i\tau})$ and $\tau = (1, 2, 3)$.* ***b)*** *Boundary element j with constant length L_j, conductivity $\sigma_j = \sigma_i$ and potentials Φ_{jl} at the two nodes with coordinates (x_{jl}, z_{jl}) with $l = (1, 2)$.* ***c)*** *Directions $\vec{r}$ from the source to the center of the boundary element and the normal direction $\vec{n}$ form the angle θ used in calculation of the boundary factor β_j.*

In our case, the computational area is divided into a set of M_e triangular elements and N nodes. Each triangular element i is described by three edge nodes and has a constant conductivity σ_i (cf. Figure 3.1-a). The discretized transformed potentials $\vec{\tilde{\Phi}} = \vec{\tilde{\Phi}}_p + \vec{\tilde{\Phi}}_s$ at the nodes are connected by linear shape functions. That means, within element i, the continuous potential is approximated in the form

$$\tilde{\Phi}(x, z) = a_i + b_i x + c_i z \ . \tag{3.27}$$

with real valued variables a_i, b_i and c_i. Applying the boundary element method (e.g. Okabe, 1981; Queralt et al., 1991), a set of M_b one-dimensional elements is introduced at the boundaries in order to include the boundary conditions. Each boundary element j is described by two nodes, has a length L_j and the same conductivity $\sigma_j = \sigma_i$ as the adjacent triangular element i (see Figure 3.1-b). The unknown field quantity is $\tilde{\Phi}_s$. Following the FE approach, Equation (3.22) is reduced to a system of linear equations (SLE) in matrix syntax (Kemna, 2000):

$$\mathbf{S}\vec{\tilde{\Phi}}_s = \vec{b} \tag{3.28}$$

with system matrix

$$\mathbf{S} = \sum_{i=1}^{M_e} \sigma_i \left(\mathbf{S}_{1,i} + k^2 \mathbf{S}_{2,i}\right) + \sum_{j=1}^{M_b} \beta_j \mathbf{S}_{3,j} \tag{3.29}$$

and right-hand side vector

$$\vec{b} = -\left[\sum_{i=1}^{M_e} \Delta\sigma_i \left(\mathbf{S}_{1,i} + k^2\mathbf{S}_{2,i}\right) + \sum_{j=1}^{M_b} \Delta\beta_j \mathbf{S}_{3,j}\right] \vec{\tilde{\Phi}}_p = -\mathbf{S}_b \vec{\tilde{\Phi}}_p \ . \tag{3.30}$$

The system matrix $\mathbf{S}$ and the matrix $\mathbf{S}_b$, consisting of the term in squared brackets in (3.30), are of similar form: The left term refers to contributions of the triangular elements, whereas the right term refers to contributions of the boundary elements, realized by a sum over all M_e triangular elements and M_b boundary elements, respectively. The element matrices $\mathbf{S}_{1,i}$, $\mathbf{S}_{2,i}$ and $\mathbf{S}_{3,j}$ include the information of geometry and shape functions of the individual elements. Their exact form is given in Appendix B.2. Matrices $\mathbf{S}$ and $\mathbf{S}_b$ differ in the contribution of conductivity σ_i and $\Delta\sigma_i$. The boundary factors β_j are calculated after Equation (3.18) using conductivity σ_j and angle θ as displayed in Figure 3.1-c. The unknown field quantity $\vec{\tilde{\Phi}}_s$ is obtained by solving Equation (3.28). In order to calculate synthetic data for a given multi-electrode setup, the SLE (3.28) needs to be solved for every source electrode.

3.2.1. Solving the System of Linear Equations

The system matrix $\mathbf{S}$ is sparse and symmetric with most entries on the main and few secondary diagonals. Therefore, it is handy to store $\mathbf{S}$ in the compressed sparse row (csr) storage format. This format is memory efficient because it stores only the nonzero entries. For example, a mesh consisting of 2506 triangular elements and $N = 1372$ nodes, has a system matrix with in total 1372*1372=1.882.384 entries, whereas there are only $nnz = 9126$ nonzero entries. Using the csr format, the matrix is replaced by three arrays. Real array A consists of all nonzero entries of $\mathbf{S}$ and has a length of nnz. The entries of the integer array JA are the column indices of the nonzero entries regarding $\mathbf{S}$. The length of the array is nnz. The entries of the integer array IA are pointers to the index of an entry of A that belongs to a new row regarding S. The number of entries in IA is $N + 1$.
Generally, an SLE can be solved using direct methods, such as Cholesky or LU decomposition, or iterative methods, such as conjugate gradient (CG) methods. Due to the size of the problem and the sparsity of the system matrix, the application of an iterative CG solver is sufficient (Rücker et al., 2006). The convergence is improved by applying preconditioning (Li and Spitzer, 2002). The SLE implemented in `ResIPIn2D` is solved using `QMRPACK` (Freund and Nachtigal, 1996). This package includes iterative quasi-minimal residual (QMR) algorithms that are related to biconjugate gradient algorithms (Freund and Nachtigal, 1994). The SSOR preconditioner is chosen since it is suitable for large meshes (Spitzer, 1995).

3.2.2. Calculation of Synthetic Data for Multi-electrode setups

The work-flow of the forward calculation implemented in `ResIPIn2D` is sketched as flowchart in Figure 3.2. Input is the mesh including the model, i.e. the distribution

of resistivity on the triangular elements and distribution of chargeability, if also IP forward calculation is required. Furthermore, the number and location of electrodes and a sample data file is required including the specification of the array type and a protocol specifying for which electrode setups the synthetic data is to be calculated. For every wavenumber k (cf. wavenumber-loop) and every source location q (cf. source-loop) the LSE (3.28) is set up and solved. Result of each LSE is the transformed potential $\tilde{\vec{\Phi}}_{s,q}(x,k,z)$. The total transformed potential $\tilde{\vec{\Phi}}_{q}(x,k,z)$ is directly obtained after Equation (3.9) by adding the primary transformed potential $\tilde{\vec{\Phi}}_{p,q}(x,k,z)$. Then, an inverse FCT (Eq. 3.4) is applied to obtain the distribution of the total potential $\vec{\Phi}_q(x,0,z)$ at the node locations due to every source electrode q (cf. source-loop2). The synthetic apparent resistivity values ρ_a are calculated after Equation (2.29). For every data point, the involved source and potential electrodes are stated in the sample data file. According to the indices of these electrodes, the required potential difference $\Delta\Phi$ is obtained by superposition of potentials after Equation (2.25). The calculation of synthetic IP data is explained in the Chapter 3.4.

In order to save computational effort, the following simplifications are made when setting up the SLE:

a) Element matrices $\mathbf{S}_1$, $\mathbf{S}_2$, $\mathbf{S}_3$ are independent from source location and wavenumber, thus they are calculated only once.

b) The boundary element coefficients β_j are only calculated once for a center source position because the distance between boundary element and source is so large that the exact position of the source does not change the angle θ significantly.

c) The term $\cos\theta$ in Equation (3.18) is derived from $\partial r/\partial n$ and is implemented in the form $\vec{n} \cdot \frac{\vec{r}}{|\vec{r}|}$.

d) Due to a) and b), the coefficient matrix $\mathbf{S}$ and the right-hand side matrix $\mathbf{S}_b$ is independent of source location. Thus, they are arranged outside of the source-loop. However, since they are dependent on the wavenumber, they need to be arranged for every wavenumber.

3.3. Mesh

As already mentioned in the preceding section, the computational domain is discretized into a mesh consisting of a finite number of elements and nodes located at the edges of the elements. There are different types of meshes used in geophysical computations referring to element shape and structure (cf. Figure 3.3). In 2D, the element shape commonly is triangular, rectangular or tetragonal. The structure might be structured, unstructured or a mixture of both. A structured mesh usually follows a certain regularity, and when expressing the mesh geometry in matrix form, neighboring mesh elements are also neighboring matrix elements. This facilitates the arrangement of the linear system of equations. An unstructured mesh does not follow any regularity. Advantages of unstructured meshes compared to structured

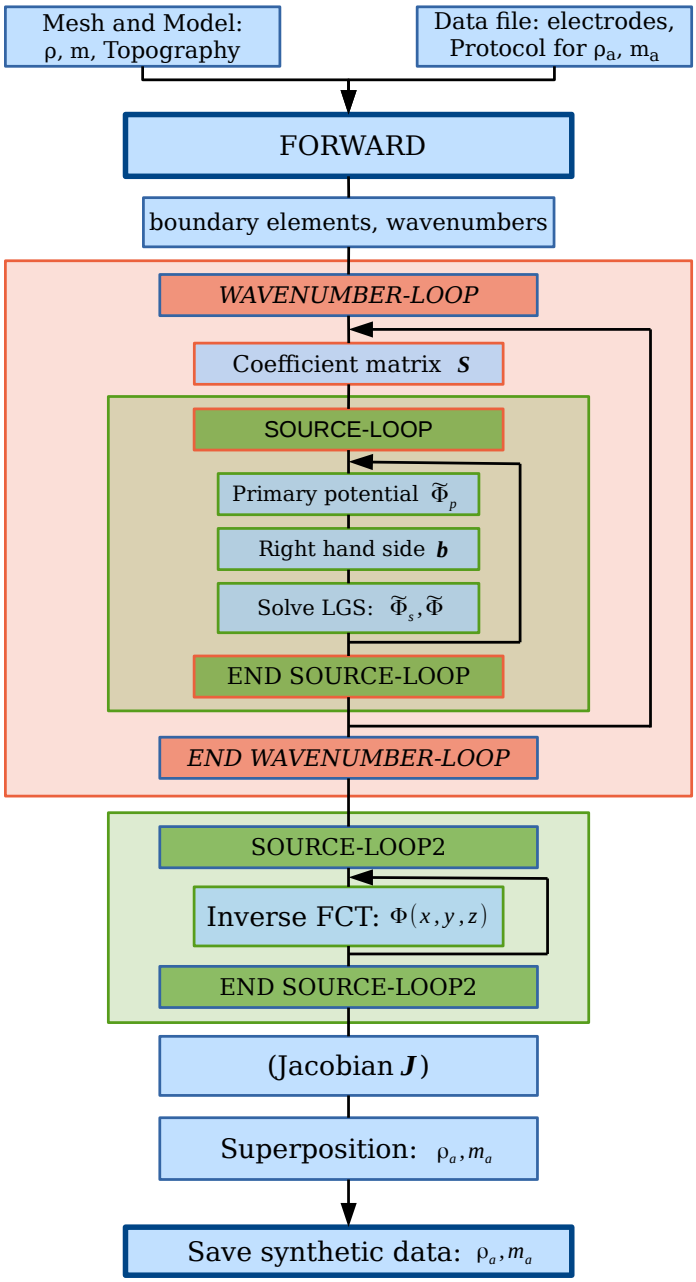

Figure 3.2.: *Flowchart of the forward calculation within the inversion algorithm* `ResIPIn2D`.

meshes are the ability to implement non-blocky surface topography and arbitrarily shaped model features and fewer degrees of freedom (DOF), i.e. fewer nodes and fewer elements. A further key advantage is the possibility of local mesh refinement (Rücker et al., 2006).

The choice of mesh type and element shape depends on the requirements of the geophysical problem and the computational approach, such as the Finite Difference (FD) or Finite Element approach. In FD, typically structured rectangular meshes

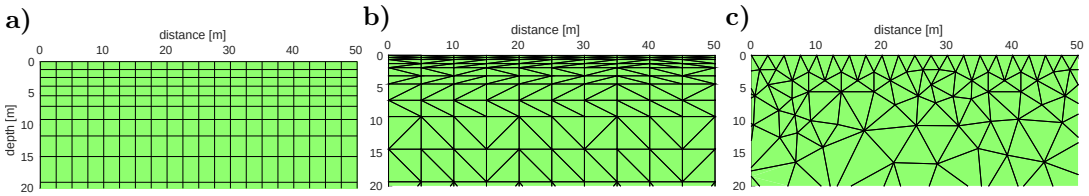

Figure 3.3.: *Different mesh types.* ***a)*** *structured rectangular,* ***b)*** *structured triangular,* ***c)*** *unstructured triangular.*

are used. In FE, the element shape is commonly triangular, and the mesh is either structured or unstructured. `ResIPIn2D` uses unstructured triangular meshes. The meshes are constructed with the mesh generator `triangle` written in `C` by Shewchuk (1996) which is an algorithm for 2D constrained Delaunay triangulation and Ruppert's Delaunay refinement for quality mesh generation. As an input, the node coordinates at the surface (defined by electrode positions and required nodes between the electrodes) and the node coordinates of the four outer corners are given. One important triangulation constraint is the smallest permitted angle α. This constraint forces the triangulation to produce no triangular elements whose angles are smaller than α or larger than $180 - \alpha$. In a perfect triangle, α is 60°. However, for most meshes, the constraint $\alpha = 60°$ leads to a large amount of very small triangles in different parts of the modeling domain, such as in 90°-corners. A constraint of $\alpha = 33.4°$ is suitable (personal communication with Thomas Günther). The output mesh of the Delaunay triangulation is fine close to the surface where sensitivity is large and accuracy is required and coarse in depth and to the sides where sensitivity is low. Consequently, the number of DOF is kept low, where high accuracy is unnecessary.

Following Rücker et al. (2006), a set of three meshes is employed in `ResIPIn2D` to meet different requirements but without introducing an unnecessarily large amount of DOF. The inversion procedure itself (cf. Chapter 4), such as calculation of the Jacobian and the model update is discretized on a *parameter mesh*: The outer boundaries in lateral direction are located in a few times the smallest electrode distance; the lower boundary is located in a depth, where no significant sensitivity is assumed. The element size in shallow depth is regulated by electrode position and number of nodes in between (see Figure 3.4-b). The calculation of the secondary potential is done on the *secondary mesh*: This mesh coincides with the parameter mesh but is extended at the sides and at depth to meet the boundary conditions (cf. Figure 3.4-a). The *primary mesh* is a refinement of the secondary mesh: For the singularity removal, it is crucial to calculate the primary potential very accurately. This is achieved by introduction of additional nodes (cf. Figure 3.4-c) beneath each electrode in a depth of 1/10 of the electrode distance (Rücker et al., 2006). Due to the angle-constraint, local mesh refinement is achieved.

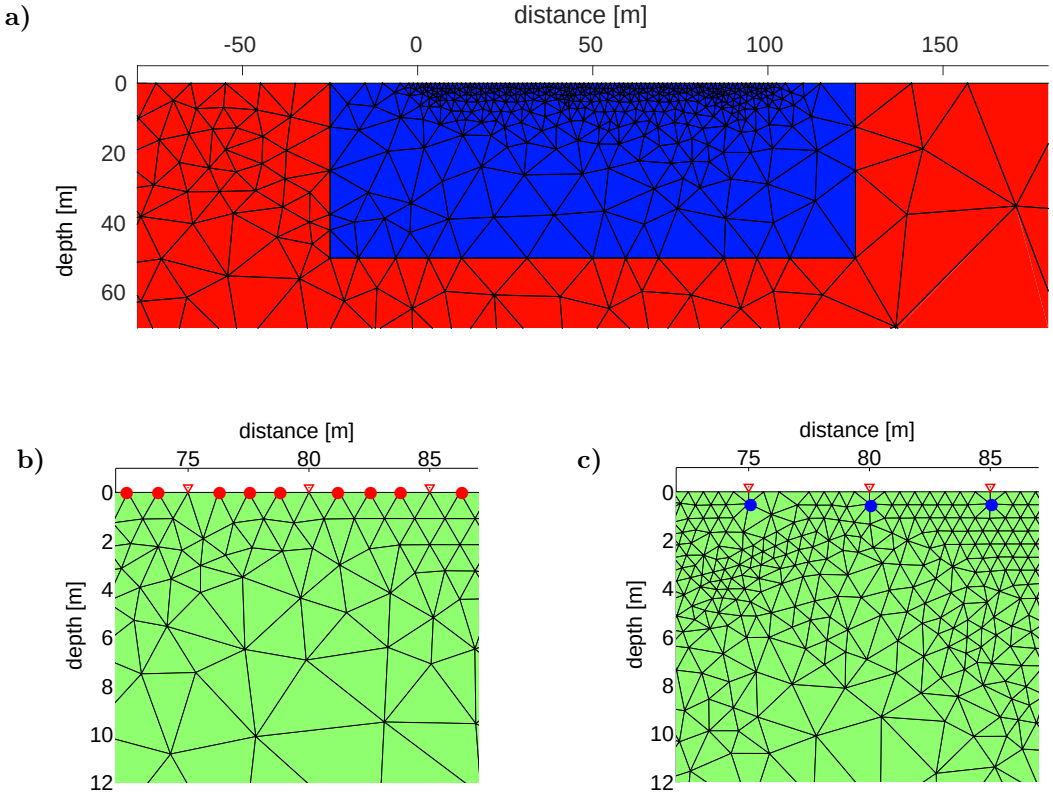

Figure 3.4.: *Excerpts of the three meshes that are used for modeling of an exemplary array. The electrode distance is* $a = 5\,\mathrm{m}$ *and the profile length is* $100\,\mathrm{m}$. ***a)*** *The parameter mesh is indicated by blue elements. In this area, the parameter mesh and the secondary mesh coincide. Outside of the parameter mesh, the secondary mesh is indicated by red elements. It expands further in lateral and vertical directions than the presented excerpt.* ***b)*** *Detailed view of the secondary mesh. Constraints for the triangulation are nodes at the electrode positions (red triangles), three nodes in between (red dots) and* $\alpha = 33.4°$. ***c)*** *Detailed view of the primary mesh. Based on the nodes of the secondary mesh, the refined primary mesh is obtained by a further triangulation after introducing additional nodes (blue dots) in a depth of* $1/10a$ *below each electrode.*

3.4. Incorporation of IP in the DC Forward Modeling Algorithm

For the incorporation of TDIP into the forward algorithm, we assume that induction effects are negligible. That means that $\partial\vec{B}/\partial t = 0$. In practice, this is ensured by using small frequencies or by removing inductive coupling effects (Kemna, 2000).

Following the approach of Seigel (1959), an intrinsic chargeability m acts as small perturbation of the (intrinsic) background resistivity ρ. According to Equation (2.40), the effective resistivity ρ' is increased to

$$\rho' = \frac{\rho}{(1-m)} \ . \tag{3.31}$$

Following this simple linear relation and Equation (2.42), the synthetic apparent chargeability m_a can be calculated by double DC forward calculation $f_{dc}(\rho)$ and $f_{dc}(\rho')$:

$$m_a = \frac{f_{dc}(\rho') - f_{dc}(\rho)}{f_{dc}(\rho')} \ . \tag{3.32}$$

The apparent chargeability values can be visualized as pseudo-section like it is done for apparent resistivity values. Please note that the chargeability m needs to be inserted in terms of V/V in both equations. However, in modeling examples, the chargeability is given in mV/V. This approach requires an additional forward calculation, but since the same mesh geometry is used, the element matrices are the same, and thus the extra computational effort is rather small.

3.5. Modeling Examples: Verification of `ResIPIn2D`

In the following, the DC and TDIP forward algorithm within `ResIPIn2D` is verified. Where existent, the results of numerical modeling are compared to the analytical solution. However, for most 2D models, no analytical solution exists. Besides the comparison with other established algorithms, the reciprocity measure r can be used to determine the quality of the numerical results (Rücker et al., 2006):

$$r = 2\frac{\rho_{a,\text{forward}} - \rho_{a,\text{reverse}}}{\rho_{a,\text{forward}} + \rho_{a,\text{reverse}}} \ . \tag{3.33}$$

Here, $\rho_{a,\text{forward}}$ is the result of a usual electrode setup and $\rho_{a,\text{reverse}}$ is the result of the same electrode setup but with interchanged current and potential electrodes. The idea goes back to Coggon (1971) and was established by Günther (2004). It follows the concept of reciprocity: In theory, the results should be the same, if current and potential electrodes are interchanged. Deviations are based on numerical errors (Rücker et al., 2006).

In the following examples, forward modeling is representatively shown for one or two array types per model and for n-levels with near-surface, intermediate and largest pseudo-depths. The applied electrode protocols including the pseudo-depth are listed in Appendix B.3.

3.5.1. Homogeneous Half-Space

We begin with the forward response of a homogeneous half-space with $\rho_0 = 100\,\Omega\text{m}$. The expected signature is $\rho_a = \rho_0 = 100\,\Omega\text{m}$.

The corresponding calculated apparent resistivity is shown for the forward and reverse electrode configuration and fixed n-levels in Figure 3.5. The left column represents the forward response determined by applying the singularity removal whereas

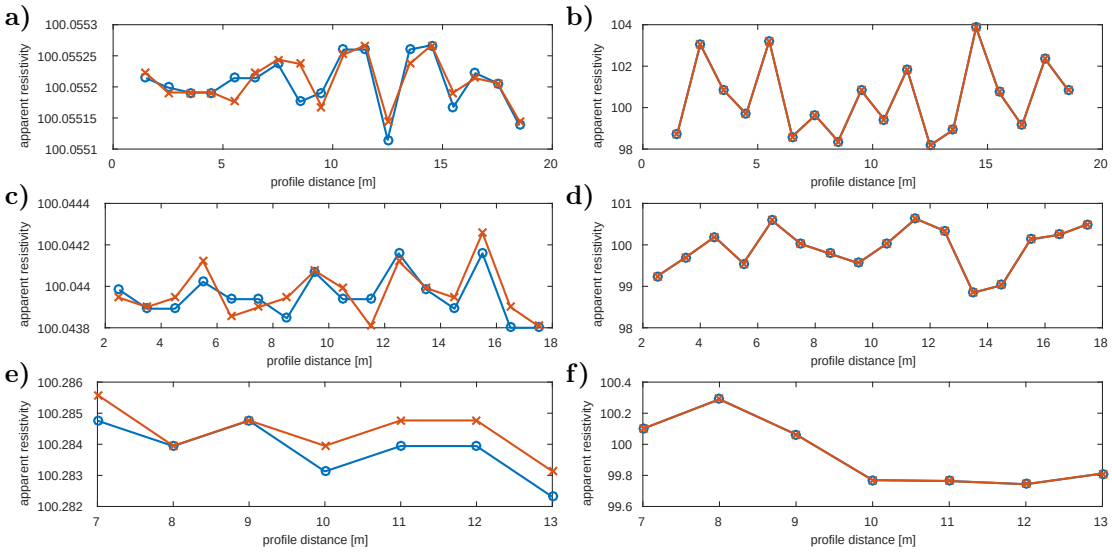

Figure 3.5.: *Dipole-dipole forward calculation (ρ_a in Ωm) of a homogeneous half-space with $\rho_0 = 100\,\Omega$m; Left column is with singularity removal, right column is without singularity removal:* ***a,b)*** *n-level=1,* ***c,d)*** *n-level=3,* ***e,f)*** *n-level=12, blue represents $\rho_{a,\text{forward}}$ and red $\rho_{a,\text{reverse}}$, respectively. The utilized protocol is listed in Table B.2 in the Appendix. Note that the y-axes in the left and right column are different.*

the data shown in the right column was calculated without singularity removal. For both datasets, with and without singularity removal, the reciprocity measure is between 10^{-5} and 10^{-3}. However, the accuracy of the data calculated with singularity removal is higher which is expressed by different scales of the y-axes between the left and right column. While the deviation from the expected $100\,\Omega$m is overall below 0.3% with singularity removal, the deviation is up to 4% in the first n-level of the data without singularity removal (see Figure 3.5-b). With increasing n-level, the relative difference decreases. In the 3rd n-level, the deviation is maximum 1% (cf. Figure 3.5-d) and for the 12th n-level it is maximum 0.3%. From this comparison, it is seen that the singularity removal technique helps to increase accuracy, especially in the first n-levels.

3.5.2. Two Horizontal Layers

The next example is a 1D model with two horizontal layers (cf Figure 3.6). The resistivities of the first and second layer are $\rho_1 = 100\,\Omega$m and $\rho_2 = 10\,\Omega$m. The thickness of the first layer is $d_1 = 1$ m and the smallest electrode distance is $a = 1$ m. Figure 3.7 shows a comparison between the analytical solution and the numerical results for a Dipole-Dipole array in the left column and for a Schlumberger array in the right column. For each array type, the apparent resistivity sounding curves are shown for the forward and reverse electrode configurations. Both numerical Dipole-Dipole signatures are in good correspondence with the analytical solution. The relative difference of $\rho_{a,\text{forward}}$ with respect to the analytical solution is below

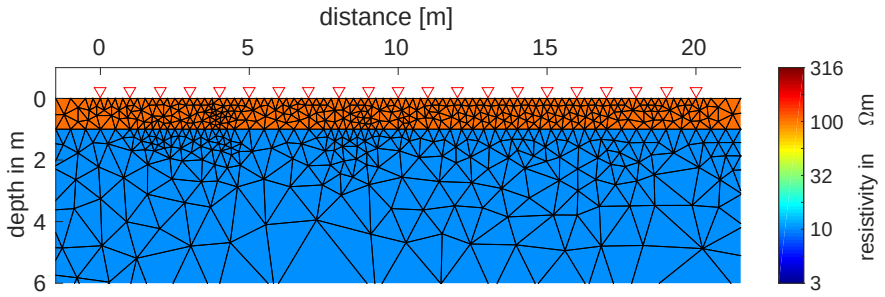

Figure 3.6.: *Two horizontal layers with resistivities* $\rho_1 = 100\,\Omega\mathrm{m}$ *and* $\rho_2 = 10\,\Omega\mathrm{m}$ *and thickness of the surface layer* $d_1 = 1\,\mathrm{m}$. *Electrode positions are indicated by red triangles, smallest electrode distance is* $a = 1\,\mathrm{m}$.

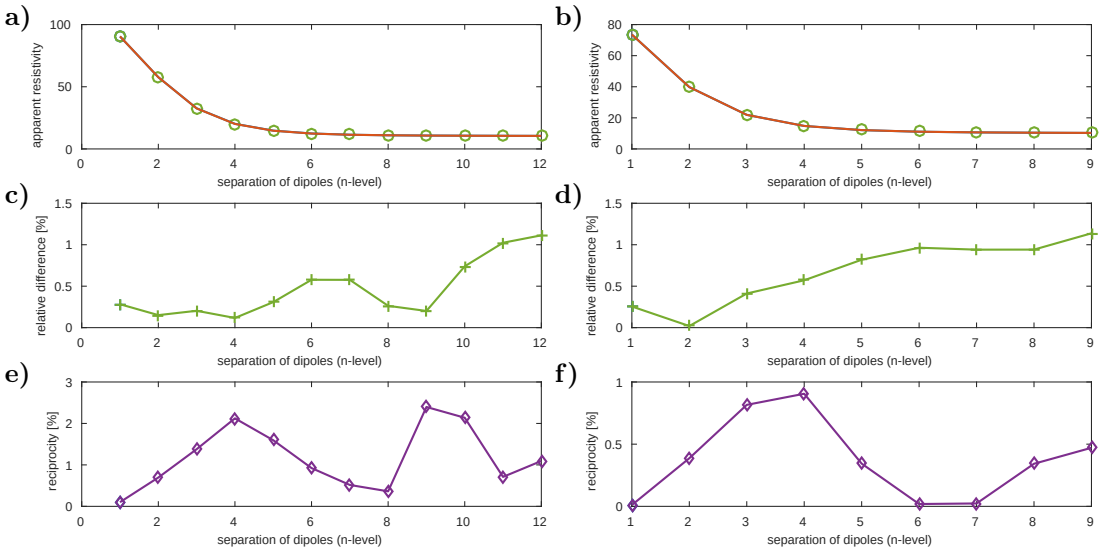

Figure 3.7.: *Forward calculation for the 2-layer model in Figure 3.6. Left: Dipole-dipole; Right: Schlumberger.* ***a,b)*** *Comparison of the sounding curve of apparent resistivity (in* $\Omega\mathrm{m}$*) between the analytical solution (green circles),* $\rho_{a,\mathrm{forward}}$ *(blue line) and* $\rho_{a,\mathrm{reverse}}$ *(red line). Note: the blue line is masked by the red line.* ***c,d)*** *Relative difference between* $\rho_{a,\mathrm{forward}}$ *and the analytical solution.* ***e,f)*** *Reciprocity in % for* $\rho_{a,\mathrm{forward}}$ *and* $\rho_{a,\mathrm{reverse}}$ *numerical data. The applied electrode protocols are listed in Table B.2 and Table B.5 in the Appendix.*

1% and the reciprocity is mostly below 2%. In this case, the reciprocity has more or less the same magnitude as the relative difference, but there is no clear connection between small relative difference and small reciprocity. The agreement between the numerical Schlumberger sounding curves and the analytical solution is of similar quality. The relative difference and the reciprocity are mostly below 1%.

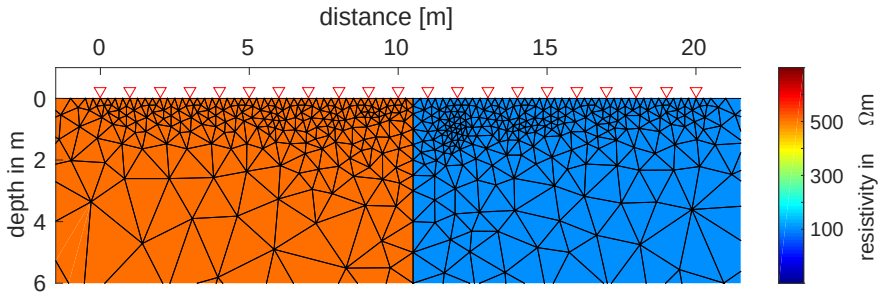

Figure 3.8.: *Vertical contact at* $x = 10.5\,\mathrm{m}$ *between* $\rho_1 = 100\,\Omega\mathrm{m}$ *on the left and* $\rho_2 = 500\,\Omega\mathrm{m}$ *on the right. Electrode locations are indicated by red triangles and the smallest electrode distance is* $a = 1\,\mathrm{m}$.

3.5.3. Vertical Contact

The Wenner forward response of a vertical contact between two different resistivities (cf. Figure 3.8) is shown in Figure 3.9. The left column refers to n-level 1 and the right column to n-level 3. The calculated apparent resistivity values for the forward and reverse electrode configuration are in good agreement with the analytical solution (see Figure 3.9-a,b). Consequently, the relative difference between $\rho_{a,\mathrm{forward}}$ and the analytical solution is mostly below 1% (cf. Figure 3.9-c,d). This is also true for the reciprocity between $\rho_{a,\mathrm{forward}}$ and $\rho_{a,\mathrm{reverse}}$ (cf. Figure 3.9-e,f). In regions, where the resistivity gradient is high, the relative difference and the reciprocity increase.

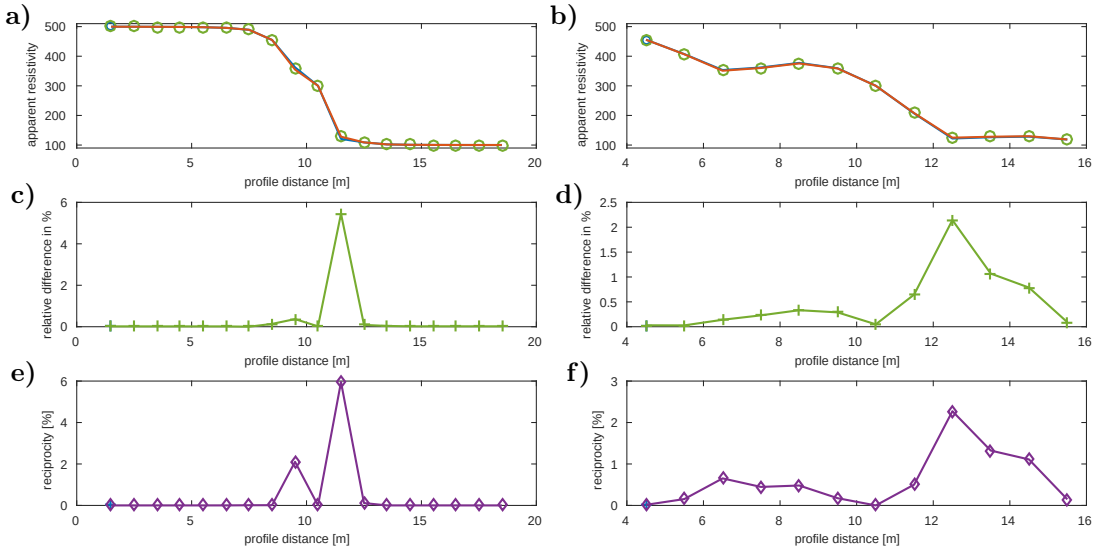

Figure 3.9.: *Wenner forward calculation of the vertical contact shown in Figure 3.8. Left: n-level=1; Right: n-level=3.* ***a,b)*** *Comparison of apparent resistivity (in* $\Omega\mathrm{m}$*) between the analytical solution (green circles),* $\rho_{a,\mathrm{forward}}$ *(blue line) and* $\rho_{a,\mathrm{reverse}}$ *(red line). Note: the blue line is masked by the red line.* ***c,d)*** *Relative difference between* $\rho_{a,\mathrm{forward}}$ *and the analytical solution.* ***e,f)*** *Reciprocity in % for* $\rho_{a,forward}$ *and* $\rho_{a,\mathrm{reverse}}$ *numerical data. The Wenner protocol including the pseudo-depths is listed in Table B.7.*

The Dipole-Dipole forward calculation of the model in Figure 3.8 is shown for the forward and reverse electrode configuration in Figure 3.10. For all presented n-levels, the signatures of both electrode configurations are in good agreement. Therefore, the reciprocity measure is mostly smaller than 1% except for the location of steepest resistivity gradient and in the left part of the largest n-level.

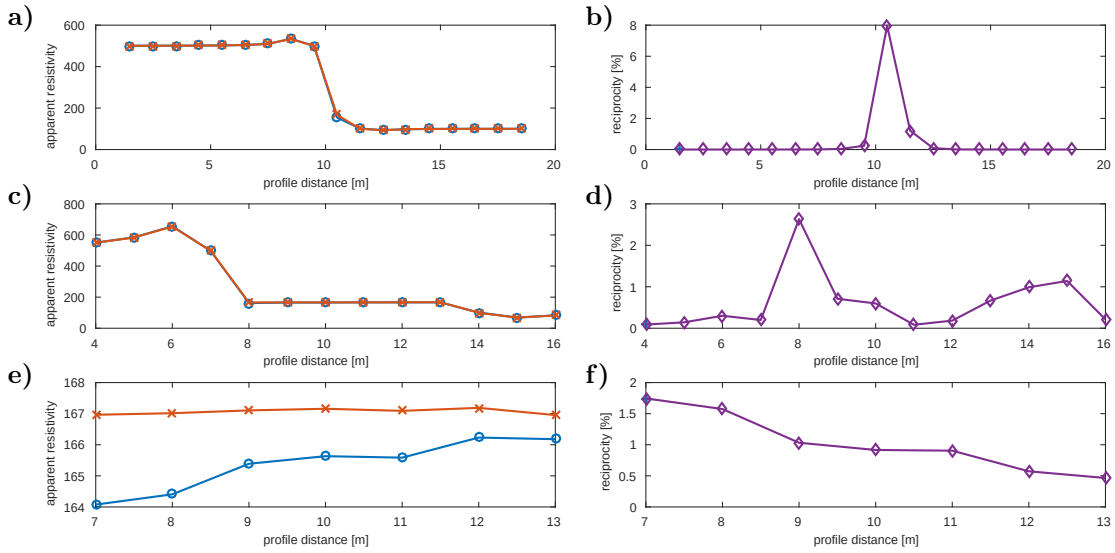

Figure 3.10.: *Dipole-Dipole forward calculation for the fault model in Figure 3.8. Left column: Apparent resistivity (in* Ωm*) for* **a)** *n-level=1,* **c)** *n-level=6 and* **e)** *n-level=12, shown as* $\rho_{a,\text{forward}}$ *(blue) and* $\rho_{a,\text{reverse}}$ *(red). Right column: Reciprocity in % for the corresponding data on the left. The applied electrode protocol is listed in Table B.2 in the Appendix.*

In Figure 3.11, the forward response of a similar fault model obtained by `ResIPIn2D` is compared to the results of the FD algorithm `DC2DInvRes` and to te FD and FE responses of `Res2DInv`. In this example, the vertical contact is located at $x = 102.5\,\text{m}$, the smallest electrode distance is $a = 5\,\text{m}$ and the profile is 200 m long. The `ResIPIn2D` data generally agrees with the `DC2DInvRes` data. The RMS error between both data-sets is 0.58% for the 1st n-level and 0.46% for the 5th n-level. Both `Res2DMod` data-sets of the 1st n-level show clear deviations in the left part of the profile where it underestimates the expected 500 Ωm half-space signature. This results in RMS errors of 1.92% for the FD result and 2.42% for the FE result with respect to the `ResIPIn2D` data. However, these deviations only occur in the first n-level. Accordingly, the RMS errors of the 5-th n-level are below 1%.

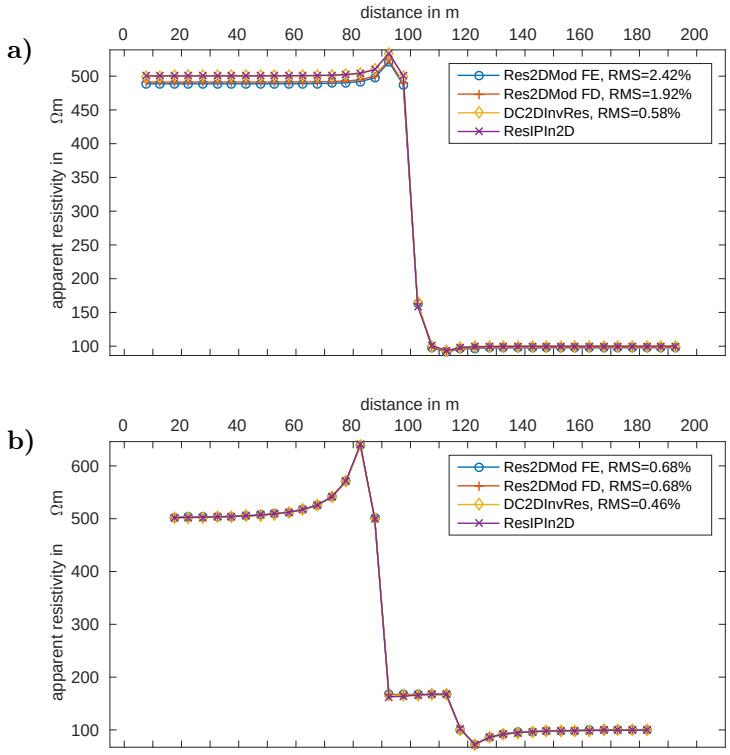

Figure 3.11.: *Comparison of Dipole-Dipole forward calculations of a vertical contact at profile distance $x = 102.5\,\mathrm{m}$ between $500\,\Omega\mathrm{m}$ on the left and $100\,\Omega\mathrm{m}$ on the right. The electrode distance is $5\,\mathrm{m}$ and the profile length is $200\,\mathrm{m}$: Calculated apparent resistivity for* **a)** *the 1st n-level and* **b)** *the 5th n-level. RMS errors refer to the difference between synthetic data calculated by* `ResIPIn2D` *and the other corresponding algorithm.*

3.5.4. Buried Block

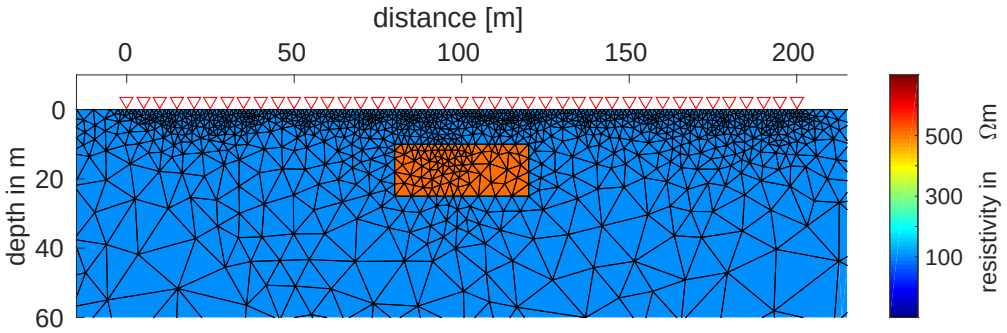

Figure 3.12.: *Buried block with lateral extension of $80\,\mathrm{m}$ to $120\,\mathrm{m}$ and vertical extension of $10\,\mathrm{m}$ to $25\,\mathrm{m}$. The resistivity of the block is $\rho_{\mathrm{block}} = 500\,\Omega\mathrm{m}$ and that of the surrounding half-space is $\rho_{hs} = 100\,\Omega\mathrm{m}$. Electrode locations are indicated by red triangles and the smallest electrode spacing is $a = 5\,\mathrm{m}$.*

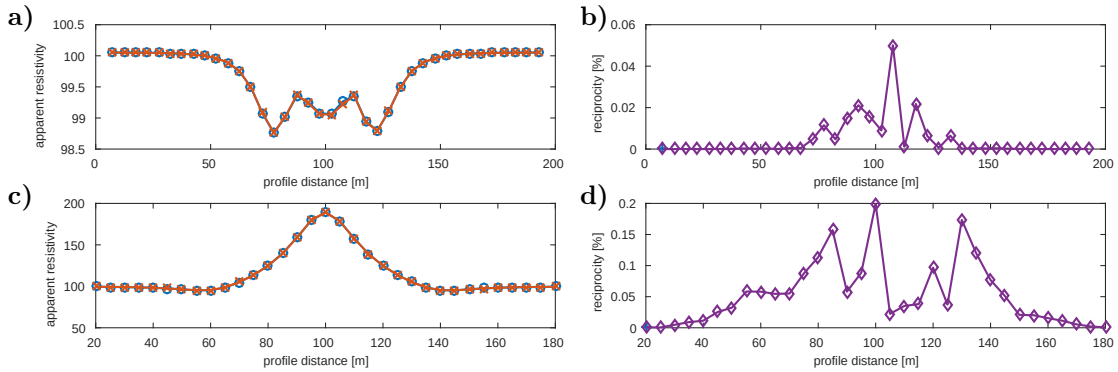

Figure 3.13.: *Dipole-Dipole forward calculation for the model including a buried block shown in Figure 3.12. Left column: Apparent resistivity (in* Ωm*) for* **a)** *n-level=1 and* **b)** *n-level=6, shown as* $\rho_{a,\text{forward}}$ *(blue) and* $\rho_{a,\text{reverse}}$ *(red). Right column: reciprocity in % for the corresponding data on the left. The applied electrode protocol is listed in Table B.2 in the Appendix.*

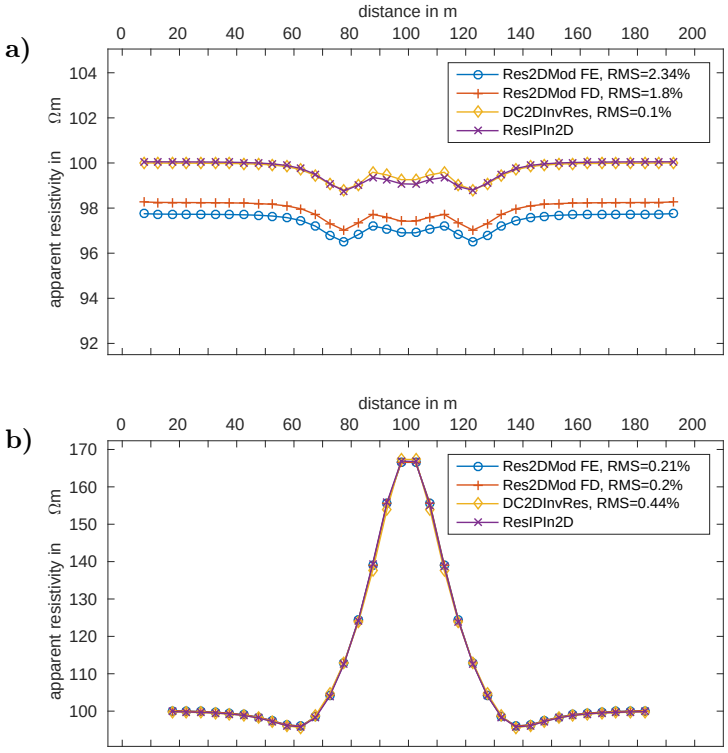

Figure 3.14.: *Comparison of Dipole-Dipole forward calculations of the 2D model in Figure 3.12: Calculated apparent resistivity for* **a)** *n-level= 1 and* **b)** *n-level=5. RMS errors refer to the difference between synthetic data calculated by* `ResIPIn2D` *and the according other algorithm.*

The forward calculation of the model displayed in Figure 3.12 including a resistive body with $\rho_{\text{body}} = 500\,\Omega\text{m}$ within a $100\,\Omega\text{m}$ half-space is shown in Figure 3.13. For both presented n-levels, the synthetic apparent resistivity values of the forward and

the reverse electrode configuration are in good agreement. This is supported by an overall low reciprocity measure which is lower than 1%. The reciprocity is lowest for small electrode distances. For the 1st n-level it is maximum 0.05%. It increases with growing electrode distance to a maximum of 0.2% for the 6th n-level. Again, the reciprocity is close to zero where the response is close to a homogeneous half-space signature and it is increased where the gradient of apparent resistivity is high.

Figure 3.14 presents a comparison of the forward response corresponding to the 2D model in Figure 3.12 with results of DC2DInvRes and Res2DInv. Again, the agreement between ResIPIn2D and DC2DInvRes is very good for the 1st n-level, which is supported by an RMS error of 0.1%. Both Res2DMod data sets again underestimate the expected signature of the 1st n-level. Moreover, the agreement of the 5th n-level is very good for all data sets which is underlined by RMS errors of less than 0.5%.

3.5.5. IP Example

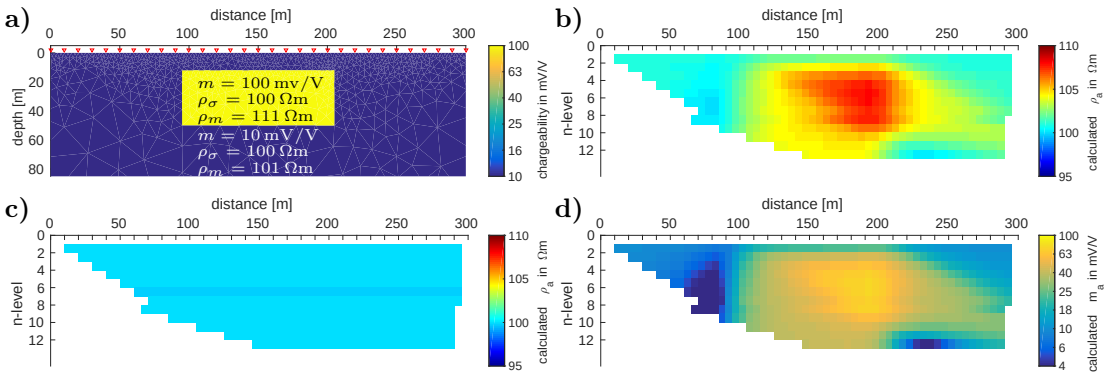

Figure 3.15.: ***a)*** *DC-resistivity and IP-chargeability model including a buried block with intrinsic resistivity* $\rho_{\text{block}} = 100\,\Omega$m *and chargeability* $m_{\text{block}} = 100\,\text{mV/V}$ *within a half-space with* $\rho_{hs} = 100\,\Omega$m *and* $m_{hs} = 10\,\text{mV/V}$. *Electrodes are indicated by red triangles. The applied Pole-Dipole configuration is listed in Table B.6 in the Appendix.* ***b)*** *Synthetic apparent resistivity* $\rho'_a = f_{dc}(\rho')$, ***c)*** *synthetic apparent resistivity* $\rho_a = f_{dc}(\rho)$ *and* ***d)*** *synthetic apparent chargeability* m_a *calculated by Equation* (3.32).

An example of a Pole-Dipole IP forward calculation is shown in Figure 3.15. The IP model (cf. Figure 3.15-a) consists of a highly chargeable block with chargeability $m_{\text{block}} = 100\,\text{mV/V}$ buried within a half-space with $m_{hs} = 10\,\text{mV/V}$. The corresponding intrinsic resistivity model is a homogeneous half-space with $\rho_{hs} = 100\,\Omega$m. After Equation (3.31), the effective IP-resistivity of the chargeable body is $\rho'_m = 111.11\,\Omega$m and that of the surrounding half-space is $\rho'_{hs} = 101.01\,\Omega$m. The results of the DC-forward calculation of ρ (cf. Figure 3.15-c) and of ρ' (cf. Figure 3.15-b) are combined using Equation (3.32) to obtain the apparent chargeability data shown in Figure 3.15-d. This example shows that the determination of IP data relies on deviations in DC signatures that are about 10% for the relatively strong IP anomaly

of 100 mV/V, but only around 1% for smaller IP effects of 10 mV/V. Hence, the DC forward algorithm requires a high accuracy to determine reliable IP results.

As a comparison, the synthetic apparent chargeability calculated with `Res2DMod` is shown as pseudo-section in Figure 3.16-a. Both apparent chargeability pseudo-sections are in good agreement. In Figure 3.16-b,c, the IP forward responses of `ResIPIn2D` and `Res2DMod` are presented together for a near surface n-level and a large n-level, respectively. Additionally, the sounding curve for profile distance 190 m is shown for both algorithms in Figure 3.16-d. The deviation between the responses obtained by both algorithms is below 1%.

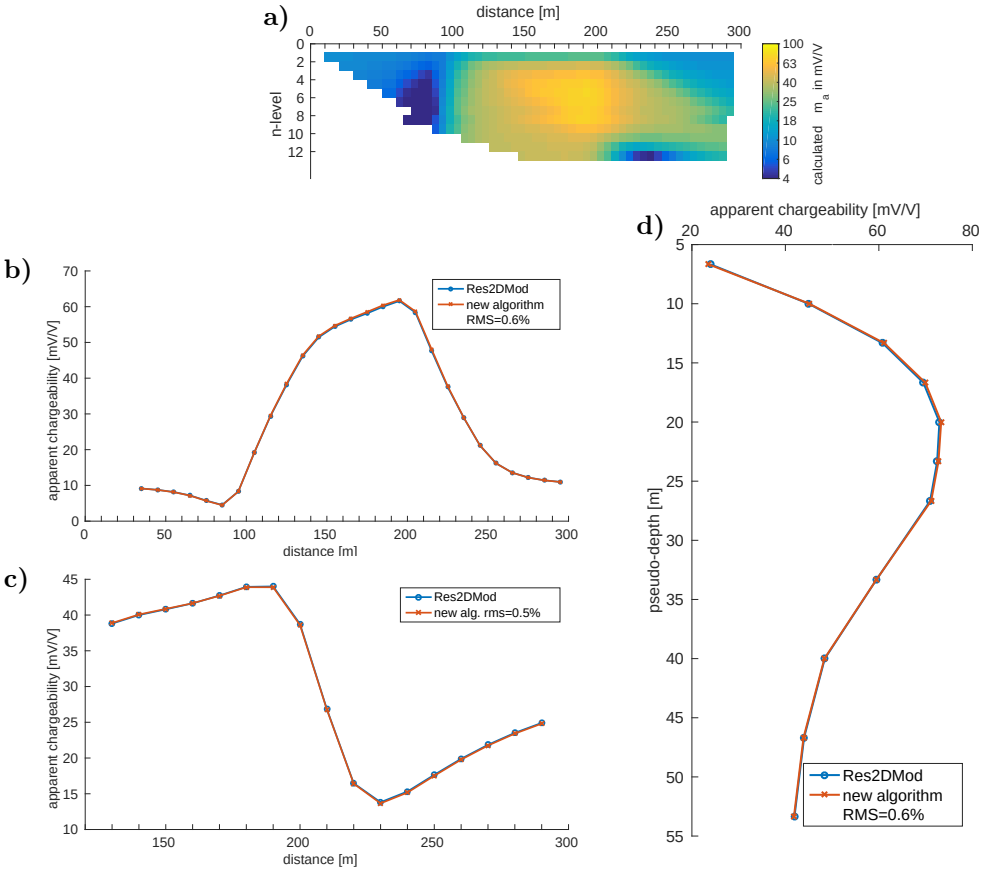

Figure 3.16.: *Comparison with Res2DMod.* ***a)*** *Apparent chargeability pseudo-section calculated with* `Res2DMod` *for the model in Figure 3.15-a. Left: Comparison of apparent chargeability for fixed n-levels 3 (**b**) and 11 (**c**).* ***d)*** *Comparison of apparent chargeability sounding curve at $x = 190$ m. The label new algorithm refers to* `ResIPIn2D`*. The RMS errors refer to the difference between data calculated by* `ResIPIn2D` *and* `Res2DMod`*.*

3.5.6. Conclusions

The presented examples prove that the newly developed algorithm produces reliable DC and IP chargeability forward calculations. The obtained forward responses are in good agreement with analytical solutions and with established algorithms. According to the reciprocity measure, the signatures of forward and reverse electrode configurations are very similar. Only when the resistivity gradient is high, the reciprocity measure is increased. Therefore, numerical inaccuracies may arise according to abrupt parameter jumps.

Furthermore, it was shown that the singularity removal technique is especially important for the accuracy of the first n-level. However, when no singularity removal is applied, the accuracy increases with increasing n-spacing and is adequate from the 3rd n-level downwards. Nevertheless, the accuracy is overall increased when applying the separation of potential technique. Therefore, it is recommended to be used when possible.

4. Smoothness Constrained Regularization Inversion of DC and TDIP Data

In this chapter, the basics of geophysical inverse theory are introduced. In particular, the smoothness constrained regularization approach is described and further features implemented in `ResIPIn2D`. The applicability and accuracy of the newly developed algorithm are assessed by inversion of synthetic data in Chapter 5.

In the preceding chapter, the concept of DC and IP forward modeling, i.e. the prediction of synthetic data based on a simplified subsurface model following certain physical and numerical conditions, was introduced. The concept of inversion serves to address the reverse problem: estimate a subsurface model based on acquired data. The earth's subsurface is represented by a simplified model with individual model parameters that are discretized at predefined mesh elements. In the following, these model parameters are represented by a parameter vector

$$\vec{p} = [p_1, p_2, \ldots, d_M]^T \tag{4.1}$$

with length M corresponding to a set of M mesh elements. In case of the 2D DC/TDIP inversion implemented in `ResIPIn2D` these parameter entries either refer to a resistivity model (ρ_i) or a chargeability model (m_i). A set of D data points, is represented by a vector in the form

$$\vec{d} = [d_1, d_2, \ldots, d_D]^T \quad . \tag{4.2}$$

Measured data are denoted by a superscript $\vec{d}^{\text{meas}}$. The model response $\vec{d} = f(\vec{p})$, which is the forward calculation f of model $\vec{p}$, is represented by a vector[1] in similar form. Now, we seek a model whose response fits the measured data, i.e. $f(\vec{p}) \approx \vec{d}^{\text{meas}}$. In case of a linear problem, the model response can be expressed as

$$f(\vec{p}) = \mathbf{F}\vec{p} \tag{4.3}$$

by representing the forward operator as matrix $\mathbf{F}$. In the simplest case, the solution of the latter equation can be obtained by simply forming the inverse of the matrix $\mathbf{F}$. However, most geophysical problems are non-linear and under-determined, in particular, if they are based on Maxwell's equations. That means, it is not possible to directly calculate a subsurface model from measured data. The forward operator is dependent on the model itself. Consequently, an iterative model update scheme is

[1] The forward operator is actually a vector function. The identification as vector is omitted for the sake of simplicity.

applied. Synthetic data is calculated from an initial model by forward calculation. These synthetic data are compared to the measured data. Then, the initial model is altered iteratively until the model response fits the measured data adequately. This concept is referred to as non-linear Inversion. Günther (2004) gives an elaborate overview of different inversion strategies. Thus, the descriptions in the following subchapters mainly follow this thesis. Refer to Günther (2004) or Zhdanov (2002) for further reading.

4.1. Non-linear Inversion Strategies

During the inversion process, an initial model $\vec{p}^0$ is altered iteratively. In every iteration k, a model update $\Delta\vec{p}^k$ is determined and the model of the current iteration $\vec{p}^k$ is updated to gain

$$\vec{p}^{k+1} = \vec{p}^k + \Delta\vec{p}^k \ . \tag{4.4}$$

The problem is linearized by Taylor-approximation of first order of the updated model:

$$f(\vec{p}^k + \Delta\vec{p}^k) = f(\vec{p}^k) + \frac{\partial f(\vec{p}^k)}{\partial \vec{p}^k}\Delta\vec{p}^k + \cdots \approx f(\vec{p}^k) + \mathbf{J}\Delta\vec{p}^k \ . \tag{4.5}$$

Here, $\mathbf{J}$ is a $D \times M$-Matrix with entries $\partial f_i(\vec{p}^k)/\partial p_j^k = \partial d_i^k/\partial p_j^k$. This is the Sensitivity or Jacobian matrix. Each entry represents the sensitivity of a data point d_i with respect to changes of a model parameter p_j. Superscripts denote the iteration number, so e.g. $\vec{d}^k = f(\vec{p}^k)$ is the synthetic data calculated from model $\vec{p}^k$ in iteration k. Equation (4.5) can be expressed as

$$\mathbf{J}\Delta\vec{p}^k = \vec{d}^{k+1} - f(\vec{p}^k) \tag{4.6}$$

with data vector $\vec{d}^{k+1} = f(\vec{p}^k + \Delta\vec{p}^k)$ which is the model response of the updated model. Now, we seek a solution of Equation (4.6) that minimizes the residual vector

$$\Delta\vec{d}^{k+1} = \vec{d}^{\,\mathrm{meas}} - \vec{d}^{k+1} \ . \tag{4.7}$$

4.1.1. Error Weighting

For measured data, we usually assign a certain data error ϵ_i. Then, the data misfit has to be treated according to this error. Therefore, a data functional Ψ_d, which is to be minimized, is defined by weighting the residual vector by the data error:

$$\Psi_d(\vec{p}) = \sum_{i=1}^{D} \left| \frac{d_i^{\mathrm{meas}} - f_i(\vec{p})}{\epsilon_i} \right|^p = \| \ \mathbf{W}_d(\vec{d}^{\,\mathrm{meas}} - f(\vec{p})) \ \|_p^p \ . \tag{4.8}$$

Here, $\mathbf{W}_d$ is the diagonal error weighting matrix with diagonal entries $w_{d,ii} = 1/\epsilon_i$ and $\| \cdots \|_p^p$ refers to an L_p-norm. Assuming Gaussian noise requires the use of the L_2-norm. Then, the data functional can be rewritten to

$$\begin{aligned} \Psi_d &= \left[\mathbf{W}_d \left(\vec{d}^{\,\mathrm{meas}} - f(\vec{p})\right)\right]^T \left[\mathbf{W}_d \left(\vec{d}^{\,\mathrm{meas}} - f(\vec{p})\right)\right] \\ &= \left(\vec{d}^{\,\mathrm{meas}} - f(\vec{p})\right)^T \mathbf{W}_d^T \mathbf{W}_d \left(\vec{d}^{\,\mathrm{meas}} - f(\vec{p})\right) \ . \end{aligned} \tag{4.9}$$

Taking the data errors into account, the quality of the data-fit is evaluated by

$$\begin{aligned} \chi = & \sqrt{\frac{1}{D}\left(\mathbf{W}_d \cdot \Delta\vec{d}\right)^T \left(\mathbf{W}_d \cdot \Delta\vec{d}\right)} \\ = & \sqrt{\Psi_d / D} \ . \end{aligned} \tag{4.10}$$

A data-fit of $\chi = 1$ is desired since it refers to a fit within the error bounds. A fit of $\chi < 1$ refers to an over-fit because the deviation between measured and calculated data is smaller than the data error, whereas a fit of $\chi > 1$ refers to an under-fit. Then, the deviation is larger than the data errors.
The data-fit without consideration of the errors is determined by the root mean square (RMS) error according to

$$RMS = \sqrt{\frac{1}{D}\sum_{i=1}^{D} \frac{(d_i^{\text{meas}} - d_i)^2}{(d_i^{\text{meas}})^2}} \times 100 \ . \tag{4.11}$$

A perfect fit in terms of RMS error refers to $RMS = 0\%$.

4.1.2. Newton-Type Methods

For an updated model, the second order Taylor series of the functional $\Psi = \Psi_d(\vec{p} + \Delta\vec{p})$ is

$$\Psi(\vec{p} + \Delta\vec{p}) \approx \Psi(\vec{p}) + (\nabla_p \Psi(\vec{p}))^T \Delta\vec{p} + \frac{1}{2}\Delta\vec{p}^T (\nabla_p^2 \Psi(\vec{p}))^T \Delta\vec{p} + \ldots \tag{4.12}$$

with Hessian matrix $\mathbf{H}_p$ with entries

$$(\mathbf{H}_p)_{ij} = \left(\nabla_p \nabla_p^T \Psi\right)_{ij} = \frac{\partial^2 \Psi}{\partial p_i \partial p_j} \ . \tag{4.13}$$

We obtain the minimum of Equation (4.12) by demanding that the partial derivative with respect to Δp is equal to zero:

$$\nabla_p \Psi(\vec{p}) + \nabla_p^2 \Psi(\vec{p}) \Delta\vec{p} = 0 \tag{4.14}$$

$$\Rightarrow (\nabla_p^2 \Psi) \Delta\vec{p} = -\nabla_p \Psi \ . \tag{4.15}$$

In every iteration, the linear subproblem (4.15) has to be solved to get the sought model update $\Delta\vec{p}$. For the functional Ψ_d defined in Equation (4.9), the Hessian matrix has the form

$$\mathbf{H}_d^k = \nabla_p \nabla_p^T \Psi_d \tag{4.16}$$

$$= \nabla_p \left(\mathbf{J}^T \mathbf{W}_d^T \mathbf{W}_d \mathbf{J} (f(\vec{p}^k) - \vec{d})\right) \tag{4.17}$$

$$= \mathbf{J}^T \mathbf{W}_d^T \mathbf{W}_d \mathbf{J} + \left\{ (\nabla_p^T \mathbf{J}^T) \mathbf{W}_d^T \mathbf{W}_d (f(\vec{p}^k - \vec{d})) \right\} \ . \tag{4.18}$$

The term in curly brackets in Equation (4.18) is difficult to compute. When the term $\nabla_p^T \mathbf{J}^T$ is small, i.e. the problem is not strongly non-linear, this term can be neglected. Then, the Hessian approximation is

$$\mathbf{H}_d^k = \mathbf{J}^T \mathbf{W}_d^T \mathbf{W}_d \mathbf{J} \ . \tag{4.19}$$

This method is referred to as Gauss-Newton method. From that, the linear sub-problem can be rewritten as

$$\left((\mathbf{W}_d\mathbf{J})^T(\mathbf{W}_d\mathbf{J})\right)\Delta\vec{p}^k = (\mathbf{W}_d\mathbf{J})^T\mathbf{W}_d\Delta\vec{d}^k \tag{4.20}$$

which is the least squares solution of the basic equation

$$\mathbf{W}_d\mathbf{J}\Delta\vec{p}^k = \mathbf{W}_d\Delta\vec{d}^k \ . \tag{4.21}$$

4.1.3. Regularization Methods

In many geophysical problems, the number of DOF is larger than the amount of data points. The problems are under-determined. Consequently, poorly resolved model domains exist. That leads to a whole set of models that fit the data in the same quality. This is also referred to as ambiguity or equivalence. Several regularization techniques exist that serve to remove these ambiguities. This is accomplished by avoiding the singularity that may arise in the left-hand side term in Equation (4.20). The regularization may either be implicit or explicit. The term explicit refers to a regularization that is applied directly on the model, e.g. by introducing a model functional Ψ_p, which is a function of the model update or of the model itself. Also, it is distinguished between local and global regularization. A local regularization constrains the model update in every iteration. It has the form of an L_2-norm: $\Psi_p = \| \vec{c}(\Delta\vec{p}) \|^2$. The simplest form is setting $\vec{c} = \Delta\vec{p}$ as used in the Marquardt-Levenberg method (Marquardt, 1963). In this method, oscillations of the model are prevented which is often referred to as damping. Global regularizations, on the other hand, constrain the model itself: $\Psi_p = \| \vec{c}(\vec{p}) \|^2$. This concept is e.g. useful to keep the model close to the initial model or a background model (e.g. derived from a priori information), both denoted as $\vec{p}^0$. Other global concepts influence the model complexity where rather simple models are favored over heavily structured ones. This approach is often referred to as Occam's inversion or smooth model inversion (Constable et al., 1987; Beard et al., 1996).

Explicit Smoothness Constrained Regularization

To combine the data functional Ψ_d with the model regularization, the functional Ψ is redefined and a regularization parameter λ is introduced (Tikhonov and Arsenin, 1977):

$$\Psi = \Psi_d + \lambda\Psi_p \ . \tag{4.22}$$

The regularization parameter λ handles the trade-off between data-fit and model constraints. Often, the choice of λ is crucial for the resulting model and data-fit. This aspect is outlined in Chapter 4.4. Another common but very similar formulation introduces a Lagrange parameter μ:

$$\Psi' = \Psi_p + \mu\,|\Psi_d - \Psi_d^*| \ . \tag{4.23}$$

Here, Ψ_d^* is the data-functional that corresponds to the estimated data variances. Convergence is achieved by minimizing Ψ' corresponding to $\Psi_d = \Psi_d^*$. The Lagrange

parameter $\mu = 1/\lambda$ is simply the inverse of the regularization parameter λ. That means, both formulations are equivalent. In the following, the formulation referring to equation (4.22) is enhanced.

Application of Newton's method on the complete functional yields:

$$\left(\nabla_p^2\Psi_d + \lambda\nabla_p^2\Psi_p\right)\Delta\vec{p} = -\nabla\Psi_d - \lambda\nabla_p\Psi_p \ . \tag{4.24}$$

As for the data functional, the formulation of the model functional Ψ_p uses an l_2-norm over a matrix-vector product:

$$\Psi_p = \| \ \mathbf{C}(\vec{p} - \vec{p}^{\,0}) \ \|_2^2 = (\vec{p} - \vec{p}^{\,0})^T\mathbf{C}^T\mathbf{C}(\vec{p} - \vec{p}^{\,0}) \ . \tag{4.25}$$

Matrix $\mathbf{C}$ is the smoothness constraint matrix. The model functional contains the gradient $\nabla_p\Psi_p = \mathbf{C}^T\mathbf{C}(\vec{p} - \vec{p}^{\,0})$ and the Hessian matrix $\nabla_p^2\Psi_p = \mathbf{C}^T\mathbf{C}$. Introducing the contribution of Ψ_p into the Gauss-Newton approach (Eq. 4.20) results in (Park and Van, 1991):

$$\left(\mathbf{J}^T\mathbf{W}_d^T\mathbf{W}_d\mathbf{J} + \lambda\mathbf{C}^T\mathbf{C}\right)\Delta\vec{p} = \mathbf{J}^T\mathbf{W}_d^T\mathbf{W}_d\Delta\vec{d}\left\{-\lambda\mathbf{C}^T\mathbf{C}\delta\vec{p}\right\} \ . \tag{4.26}$$

This is the smoothness constrained regularization approach including global regularization. The choice of constraint matrix $\mathbf{C}$ implemented in `ResIPIn2D` is specified in Chapter 4.7. Equation (4.26) can be simplified to a set of linear equations in matrix form like

$$\mathbf{M}\vec{x} = \vec{b} + \left\{\vec{b'}\right\} \tag{4.27}$$

that has to be solved in every iteration step k with respect to the model update

$$\vec{x} = \Delta\vec{p}^{\,k} = \vec{p}^{\,k+1} - \vec{p}^{\,k} \ . \tag{4.28}$$

Referring to Equation (4.26), the matrix $\mathbf{M}$ represents the term in brackets on the left-hand side. The right-hand side vectors $\vec{b}$ and $\vec{b'}$ represent the terms on the right outside and within the curly brackets, respectively. The vector

$$\delta\vec{p} = \vec{p}^{\,k} - \vec{p}^{\,0} \tag{4.29}$$

refers to the deviation between the model of the current iteration and the initial (or background) model $\vec{p}^{\,0}$. The choice of $\vec{p}^{\,0}$ regulates the consequence of global regularization. If a background model in combination with a diagonal constraint matrix $\mathbf{C}$ is chosen, the resulting model is kept close to $\vec{p}^{\,0}$. Choosing a homogeneous half-space as initial model leaves the influence on the resulting model for the constraint matrix itself.

For local regularization the complete functional reads

$$\Psi = \| \ \mathbf{W}_d(\mathbf{J}\Delta\vec{p}^{\,k} - \Delta\vec{d}^{\,k}) \ \|_2^2 + \lambda \ \| \ \mathbf{C}\Delta\vec{p}^{\,k} \ \|_2^2 \ . \tag{4.30}$$

This functional is to be minimized with respect to $\Delta\vec{p}^{\,k}$ which leads to

$$\left(\mathbf{J}^T\mathbf{W}_d^T\mathbf{W}_d\mathbf{J} + \lambda\mathbf{C}^T\mathbf{C}\right)\Delta\vec{p} = \mathbf{J}^T\mathbf{W}_d^T\mathbf{W}_d\Delta\vec{d} \ . \tag{4.31}$$

This is the smoothness constraint regularization approach with local regularization. In comparison to the approach including global regularization (Eq. 4.26), only the second term on the right hand side, represented by $\vec{b'}$ in Equation (4.27), is missing.

The inversion procedure is terminated when one of the following criteria is met:

- the predefined maximum number of iterations is achieved
- the problem converged ($\chi \approx 1$)
- the data-fit cannot be reduced further ($\chi^k \approx \chi^{k-1}$) and the minimum predefined regularization parameter is achieved
- the problem diverged ($\chi^k > \chi^{k-1}$)

All `ResIPIn2D` inversion results shown in the following chapters are obtained applying a local smoothness constrained regulazitation according to Equation (4.31). The LSE is solved by the preconditioned conjugate gradient solver by Freund and Nachtigal (1996).

4.2. Sensitivity (Jacobian Matrix)

The most intuitive way to determine the sensitivity (or Jacobian) matrix **J** is to apply a perturbation method. In this case, the partial derivatives $\partial f_i(\vec{p})/\partial p_j$ are approximated by a variation Δp of the single model parameters

$$J_{ij} \approx \frac{f_i(\vec{p} + \Delta p \vec{\delta}_j) - f_i(\vec{p})}{\Delta p} \ . \tag{4.32}$$

Here, $\vec{\delta}_j$ is Dirac's function with 1 at position j and zero else. That means that the forward calculations of the variation of one parameter p_j refer to the determination of one column of **J**. To determine the complete Jacobian for a model domain with M elements, M extra forward calculations need to be conducted. This is apparently very time consuming; even if the complete Jacobian is only calculated in the very first iteration and updated in the following iterations as proposed by Broyden (1972).

4.2.1. Derivation of Sensitivity by the Reciprocity Principle

Taking advantage of the reciprocity of the electrical potential leads to the opportunity to obtain the complete Jacobian with little extra effort (Tripp et al., 1984). The approach follows Kemna (2000) and goes back to an idea by Sasaki (1989). Thus, the subsequent descriptions follow the latter two references. The term reciprocity refers to the equality of obtained potential when interchanging the location of current injection and potential determination. This is not only true for the obvious case of interchanging locations of current and potential electrodes at the surface. It is also true for the location of an electrode at the surface and a node location in the subsurface. Now, we seek the potential gradients within each parameter element due to current injection at each electrode. During the DC forward calculation, the transformed potential at the location of the grid nodes is calculated individually for every electrode. Since the discretized transformed potentials are connected by discrete shape functions, also the gradient information is part of the forward problem. Consequently, the finite element equations are used as basis for the derivation of sensitivities (Kemna, 2000; Rodi, 1976). Building the derivatives of Equation

(3.28) with respect to the elements conductivities that result from the substitution of Equations (3.29) and (3.30) yields the relation

$$\mathbf{S}\frac{\partial\tilde{\Phi}}{\partial\sigma_j} = -\left(\mathbf{S}_{1j} + k^2\mathbf{S}_{2,j}\right)\tilde{\Phi} \tag{4.33}$$

for the j-th parameter element. The boundary elements do not contribute to this formulation because they are not part of the model domain itself (Kemna, 2000). Apparently, there is a resemblance between Equation (4.33) and the FE Equation (3.28). According to Sasaki (1989) the right-hand side of Equation (4.33) can be regarded as kind of source term, since the matrix-vector multiplication results in a column vector $\vec{s} = -\left(\mathbf{S}_{1j} + k^2\mathbf{S}_{2,j}\right)\tilde{\Phi}$. In other words, the entries of the right hand side can be referred as a set of line sources located at the nodes that are involved in the corresponding parameter element. Then, the partial derivative $\partial\tilde{\Phi}/\partial\sigma_j$ at a certain point in the element is equivalent to the field that originates from the line sources at the nodes. Due to the concept of reciprocity, the partial derivative is equal to the superposition of fields at the nodes (involved in the element) originating from a fictitious source at the point in the element. In terms of Equation (4.33) the partial derivative of the transformed potential $\tilde{\Phi}_{i,l}$ at node i produced by current injection at node l with respect to the conductivity σ_j of the j-th element is

$$\frac{\partial\tilde{\Phi}_{i,l}}{\partial\sigma_j} = 2\sigma_j^2\sum_{m=1}^{3}\sum_{n=1}^{3}a_{j,mn}\tilde{\Phi}_{m,i}\tilde{\Phi}_{n,l}\ . \tag{4.34}$$

Here, $\tilde{\Phi}_{m,i} = \tilde{\Phi}_{i,m}$ is the transformed potential at node i produced by fictitious current injection at node m (node m belongs to element j). The double sum is over all nodes m and n belonging to the j-th element. The term a_{mn} refers to the mn-th element of matrix $A_j = (\mathbf{S}_{1,j} + k^2\mathbf{S}_{2,j})$ which is used in the forward calculation (cf. (Eq. 3.29)). Therefore, only additional memory is required and little extra computational effort in order to determine the Jacobian entries.
To obtain the partial derivatives of the untransformed potential Φ_i, an inverse FCT is applied:

$$\frac{\partial\Phi_{i,l}}{\partial\sigma_j} = \sum_m\sum_n k_{k,n}\frac{\partial\tilde{\Phi}_{i,m}}{\partial\sigma_j}(k_n)\ . \tag{4.35}$$

Finally, the sought partial derivatives of the synthetic data d_i with respect to the element's conductivity σ_j are obtained by superposition of the partial derivatives of the potentials of all (current or potential) electrodes that are involved in the according array. Like for the calculation of the actual data point, the superimposed potential is then also multiplied with the corresponding geometry factor G. So, the Jacobian entry J_{ij} is obtained by

$$J_{ij} = \frac{\partial d_i}{\partial\sigma_j} = G\left\{\left(\frac{\partial\Phi_{P1,C1}}{\partial\sigma_j} - \frac{\partial\Phi_{P1,C2}}{\partial\sigma_j}\right) - \left(\frac{\partial\Phi_{P2,C1}}{\partial\sigma_j} - \frac{\partial\Phi_{P2,C2}}{\partial\sigma_j}\right)\right\}\ . \tag{4.36}$$

The term in curly brackets is denoted as J_{ij}^{dc} and will be used in the determination of the IP chargeability Jacobian.

4.3. TDIP Two-step Inversion Approach

Oldenburg and Li (1994) proposed three inversion methods for TDIP data (cf. Chapter 1). The third method is implemented in `ResIPIn2D`, which is not limited to small chargeability effects. The first step of this two-step procedure is a pure DC inversion using the apparent resistivity data. The recovered resistivity model represents the effective resistivity of Seigel's model. The second inversion step is a non-linear IP inversion resulting in a chargeability model. The descriptions in this section follow mainly Oldenburg and Li (1994).

4.3.1. Non-linear Chargeability Inversion

Referring to Figure 2.12, it is assumed that the resistivity inversion in the first step uses the (intrinsic) potential Φ to recover the intrinsic or background conductivity σ. In concurrence with Seigel's model, synthetic chargeability data is calculated by

$$m_a = \frac{f_{dc}\left(\sigma(1-m)\right) - f_{dc}\left(\sigma\right)}{f_{dc}\left(\sigma(1-m)\right)} \ . \tag{4.37}$$

The data equations are linearized about the chargeability model m. The Jacobian matrix required in the chargeability inversion contains the entries

$$J_{ij} = \frac{\partial d_i}{\partial m_j} \tag{4.38}$$

with m_j being the chargeability of element j and $d_i = m_{a,i}$ being the i-th data point. We assume that the potentials Φ and Φ' are the result of forward calculation of the background conductivity σ and of $\sigma' = \sigma(1-m)$, respectively. Then, Equation (4.37) is rewritten to

$$d_i = \frac{\Phi'_i - \Phi_i}{\Phi'_i} \ . \tag{4.39}$$

After differentiating Equation (4.39) with respect to m_j, we get

$$\frac{\partial d_i}{\partial m_j} = \frac{\Phi_i}{(\Phi'_i)^2}\frac{\partial \Phi'_i}{\partial m_j} \ . \tag{4.40}$$

Considering that σ'_j produces Φ'_i, the partial derivative on the right-hand side yields

$$\frac{\partial \Phi'_i}{\partial m_j} = -\sigma_j \frac{\partial \Phi'_i}{\partial \sigma'_j} = -\sigma_j J^{dc}_{ij} \tag{4.41}$$

where $J^{dc}_{ij} = \partial\Phi'_i/\partial\sigma'_j$ is just the term in curly brackets of the resistivity sensitivity in (4.36). According to this, the IP-Jacobian $\mathbf{J}^{ip}$ can be obtained by scaling of the DC sensitivity:

$$J^{ip}_{ij} = \frac{\partial d_i}{\partial m_j} = -\sigma_j \frac{\Phi_i}{(\Phi'_i)^2} J^{dc}_{ij} \tag{4.42}$$

The chargeability inversion is conducted by solving a similar inverse problem as in the resistivity inversion step. Only the data and model parameters refer to chargeability instead of resistivity, and the IP-Jacobian is used.

4.3.2. Practical Considerations

Oldenburg and Li (1994) propose some practical considerations about the applicability of the two-step inversion procedure on field data. The authors point out that the secondary potential Φ is not measured directly in field surveys. Instead, the primary potential Φ' is recorded and used to determine the DC resistivity data (compare Figure 2.10). Therefore, they recommend the following procedure:
The first step is a DC resistivity inversion of the apparent resistivity data obtained from acquired potential Φ'. The result is a conductivity model σ' that corresponds to the effective conductivity. The subsequent chargeability inversion uses the associated partial derivatives $\partial\Phi'_i/\partial\sigma'_j$ to recover a chargeability model. In each chargeability inversion, the intrinsic (or background) conductivity model is updated by $\sigma = \sigma'/(1-m)$. The procedure is repeated until the apparent chargeability data calculated according to Equation (4.37) fits the measured data adequately.

4.3.3. Implementation in `ResIPIn2D`

The two-step TDIP inversion implemented in `ResIPIn2D` considers the preceding practical considerations. The inversion procedure is summarized in Figure 4.1. It is obligatory that the measured apparent chargeability data $\vec{m}_a^{\,\text{meas}}$ is given in Newmont Standard. The measured DC data refers to apparent resistivity $\vec{\rho}_a^{\,\text{meas}}$ or voltage $\vec{U}^{\,\text{meas}} = \Delta\vec{\Phi}^{\,\text{meas}}$ derived from measurement of potential Φ'. The following descriptions confine to formulations using ρ_a, but also hold for measured voltages. In contrast to the descriptions following Oldenburg and Li (1994), DC model parameters are given by resistivity values rather than conductivities.

The first step is a pure DC resistivity inversion that searches for a resistivity model whose model response fits the measured apparent resistivity data within the error-bounds. In particular, referring to the formulations in Chapter 4.1 the following variables are used in the first inversion step:

- The measured data vector contains the measured apparent resistivity data: $\vec{d}^{\,\text{meas}} = \vec{\rho}_a^{\,\text{meas}}$.
- The initial model is a resistivity model: $\vec{p}^{\,0} = \vec{\rho}^{\,0}$.
- The iteration index is denoted by k.
- The residual vector $\Delta\vec{d}^{\,k}$ refers to the deviation between measured resistivity data and forward response $f(\vec{\rho}^{\,k})$ of the resistivity model of the k-th iteration: $\Delta\vec{d}^{\,k} = \vec{\rho}_a^{\,\text{meas}} - f(\vec{\rho}^{\,k})$.
- In every iteration k, Equation (4.31) is solved with respect to the resistivity model update $\Delta\vec{p}^{\,k} = \Delta\vec{\rho}^{\,k}$ and an updated resistivity model $\vec{\rho}^{\,k+1}$ is obtained.
- Convergence is achieved, when the data-fit reaches $\chi_{dc} \approx 1$, determined by $\chi_{dc} = \sqrt{\frac{1}{D}\left(\mathbf{W}_d \cdot \Delta\vec{d}^{\,k}\right)^T\left(\mathbf{W}_d \cdot \Delta\vec{d}^{\,k}\right)}$.

The result of the resistivity inversion after the k-th iteration is model $\vec{\rho}^{\,k}$ that in terms of the formulation of the IP-perturbation approach refers to the effective

resistivity, i.e. $\vec{\rho}^k \widehat{=} \vec{\rho}'$.

The final resistivity model is kept fixed during the subsequent chargeability inversion. This second inversion step contains the following variables and sub-steps:

- The measured data vector contains the apparent chargeability data: $\vec{d}^{\text{meas}} = \vec{m}_a^{\text{meas}}$
- The iteration index is denoted by h.
- The initial model is a chargeability model: $\vec{p}^0 = \vec{m}^{\,0}$.
- Based on the initial chargeability model $\vec{m}^{\,0}$ and the final effective resistivity model $\vec{\rho}' = \vec{\rho}^k$ an initial "intrinsic" resistivity model $\vec{\rho}^0$ is calculated according to Equation (3.31): $\vec{\rho}^0 = \vec{\rho}'(1 - \vec{m}^0)$.
- In every iteration h, the forward response of the chargeability model $\vec{m}^h$ is calculated according to Equation (3.32) by double DC forward calculation: $f(\vec{p}^h) = \vec{m}_a^h = \frac{f_{dc}(\vec{\rho}') - f_{dc}(\vec{\rho}^h)}{f_{dc}(\vec{\rho}')}$.
- The residual vector $\Delta\vec{d}^h$ refers to the difference between measured chargeability data and forward response $\vec{m}_a^h$: $\Delta\vec{d}^h = \vec{m}_a^{\text{meas}} - \vec{m}_a^h$.
- In every iteration h, Equation (4.31) is solved with respect to the chargeability model update $\Delta\vec{p}^h = \Delta\vec{m}^h$ and an updated chargeability model $\vec{m}^{h+1}$ is obtained
- In every iteration, also the "intrinsic" resistivity model is altered due to the updated chargeability model, i.e. $\vec{\rho}^h = \vec{\rho}'(1 - \vec{m}^h)$, while the effective resistivity model $\vec{\rho}'$ is kept fixed.
- Convergence is achieved, when the data-fit reaches $\chi_{ip} \approx 1$, determined by $\chi_{ip} = \sqrt{\frac{1}{D}\left(\mathbf{W}_d \cdot \Delta\vec{d}^h\right)^T \left(\mathbf{W}_d \cdot \Delta\vec{d}^h\right)}$.

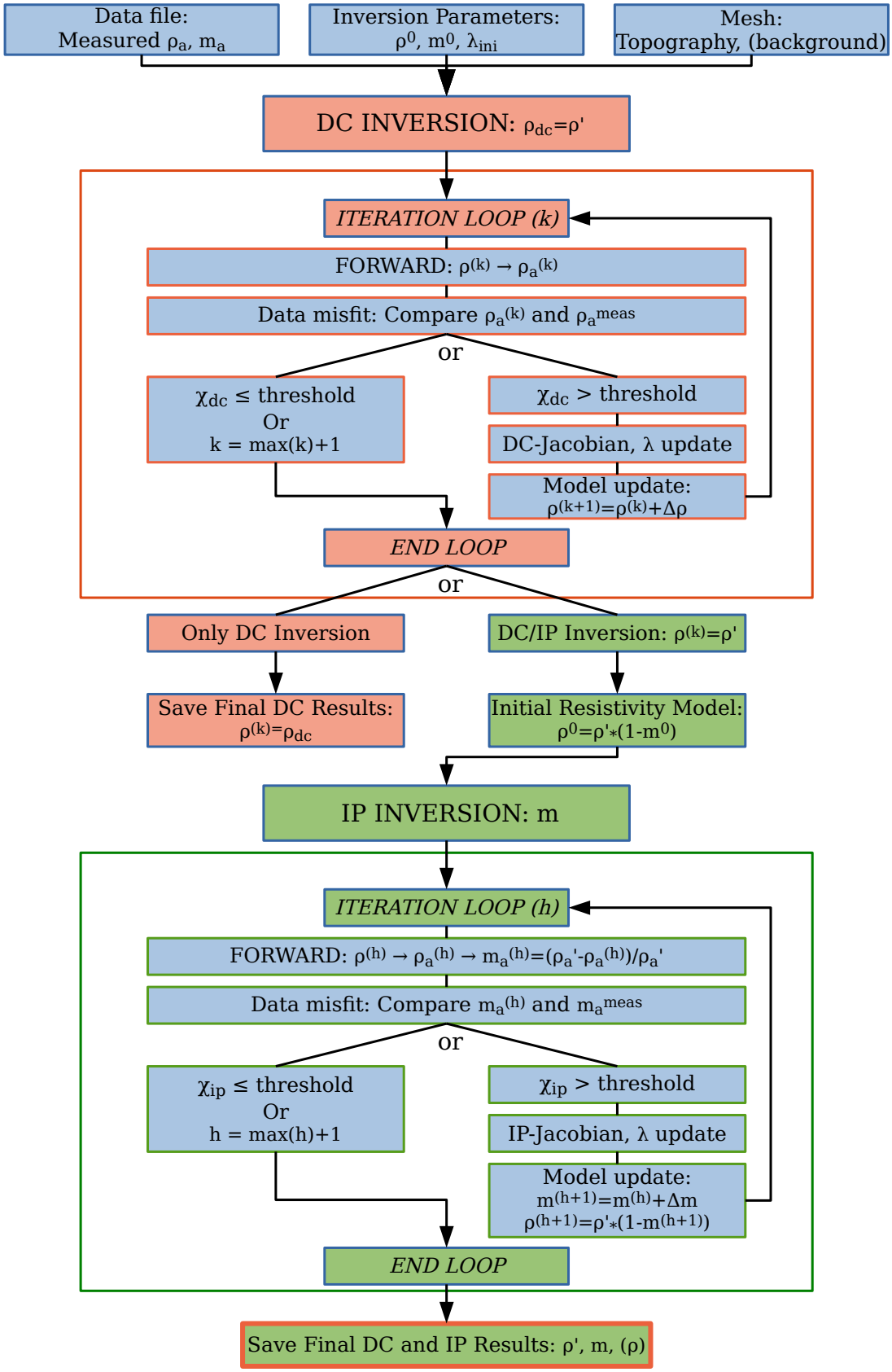

Figure 4.1.: *Flowchart of the inversion algorithm* `ResIPIn2D`.

4.4. Regularization Parameter and Step-length of Model Update

The regularization parameter λ regulates the trade-off between model smoothness and data-fit. As mentioned in Subsection 4.1.3, the choice of λ may influence the model characteristics and the quality of data-fit of the final inversion model. Generally, a small λ leads to a good data-fit disregarding the model smoothness. A large λ, on the other hand, increases the influence of the smoothness constraints and therefore leads to a smooth model but with disregard of data-fit.

A common approach of finding an adequate value of λ is the L-curve technique (Hansen and O'Leary, 1993). In this approach, the data and model functionals $\Psi_{d,i}$ and $\Psi_{p,i}$ are determined for a broad range of λ_i (e.g. $\lambda_i = 0.1 - 1000$). The resulting curve usually has a typical L-shaped form if the range of regularization parameters has been chosen appropriately. The favored trade-off between both functionals is found in the corner of this L-curve, i.e. where the curvature is at its maximum. Choosing the λ corresponding to this corner leads to the most balanced compromise between model smoothness and data-fit. When applying global constraints, the choice of regularization should be made before the inversion and kept constant during. When applying local constraints, there is an independent subproblem to be solved in every iteration. Thus, the L-curve technique might be applied in every iteration (Günther, 2004).

Another approach referred to as discrepancy principle, pleads for minimization of the functional Ψ_p under the condition that $\Psi_d = \Psi_d^*$ is achieved. For a set of D measured data points, the target limit is $\Psi_d^* = D$ which corresponds to an optimum convergence of $\chi = 1$ for known data errors. The optimum λ with regard to the discrepancy principle is, therefore, the λ for which the minimization achieves $\Psi_d = \Psi_d^*$ or for which Ψ_d is closest to Ψ_d^*. However, in non-linear inversion, the target misfit is usually not achieved in the very first iteration. Thus only intermediate steps between $\Psi_d(\vec{p}^0)$ and Ψ_d^* are met.

A further procedure is to start the first iteration with a rather large initial λ_{ini} to create a smooth model and to prevent overshooting. Then, the regularization parameter is reduced in further iterations until a predefined minimum λ_{min} is reached. This is done to refine the model characteristics and simultaneously improving the data-fit (Günther, 2004). This concept is applied by Kemna (2000), Candansayar (2008) and Marquardt (1963) who use local regularization schemes and by Farquharson and Oldenburg (2004) who use a global regularization scheme. The procedure is sometimes referred to as cooling approach.

Another important aspect is the right choice of step length of the model update. Due to the non-linearity of the regularization problem, the model update $\Delta\vec{p}$ found by the solution of Equations (4.26) or (4.31) might overshoot and prevent convergence. To control this, the step length (or line search parameter) $\tau \in [0, 1]$ is introduced that decreases the model update:

$$\vec{p}^{k+1} = \vec{p}^k + \tau\Delta\vec{p}^k \ . \tag{4.43}$$

In every iteration k, we seek the step-length τ that minimizes $\chi^2(\vec{p}^{\,k} + \tau\Delta\vec{p}^{\,k})$ in a so-called line-search. Here, the χ^2 misfit is used which is the square of the definition of χ in Equation (4.10). There are several line-search procedures. Three procedures are explained in the following (Günther, 2004):

- Exact line-search: Forward responses of updated models $\vec{p}^{k+1}$ are calculated for a set of τ_n covering the range between 0 and 1. The optimum τ corresponds to the minimum of $\chi^2(\tau_n)$. The advantage of this procedure is that it is precise. The disadvantage is that it is time-consuming because many extra forward calculations are required in every iteration.
- Two-point parabola: Two extra model responses are calculated for updated models corresponding to half a step-length ($\tau_1 = 0.5$) and full step-length ($\tau_2 = 1.0$). The response of the model of the current iteration corresponds to step-length $\tau_0 = 0.0$. The three known misfit values $\chi^2(\tau_0)$, $\chi^2(\tau_1)$ and $\chi^2(\tau_2)$ define a parabola, when they are not arranged in a straight line. The minimum of the parabola corresponds to the optimum step-length τ. When the minimum lies outside the interval $\tau \in [0, 1]$, the optimum step-length is set to either 0 or 1. This method is not as precise as the exact line search, but it saves computational time since a maximum of two extra forward calculations is required in every iteration.
- Linear interpolation: Forward responses of updated models corresponding to a set of τ_n are approximated by linear interpolation between $f(\tau_0 = 0.0)$ and $f(\tau_1 = 1.0)$. In particular, the linear interpolation is done according to $f(\tau_n) \approx f(\tau_0) + \tau(f(\tau_1) - f(\tau_0))$. For all τ_n the misfit $\chi^2(\tau_n)$ is determined. The optimum τ refers to the minimum of $\chi^2(\tau_n)$. The advantage is that only one extra forward calculation ($\tau_1 = 1.0$) is needed.

A comparison of the three approaches obtained by `ResIPIn2D` applying local regularization is shown in Figure 4.2 for the first iteration of a resistivity and a chargeability inversion. The benefit of the line-search is revealed by clear differences between the minimum misfit and the misfit corresponding to the full step-length. Proceeding the inversion with an optimum step-length prevents overshooting, and convergence is achieved after fewer iterations. In comparison to the linear interpolation, the parabola technique has a better analogy with the exact line search. Since the computational effort for the parabola line-search is less than that of the exact line search, I recommend the two-point parabola technique when using `ResIPIn2D`.

Finding the optimum combination of λ and τ

A simultaneous search for an optimum λ and τ is impractical (Günther, 2004). Hence, to combine the advantages of both optimizations, I suggest following the recommendation of Günther (2004). The author suggests beginning the inversion process with a rather large λ_{ini} which is kept fixed in the first iterations. In every iteration, a line-search for the optimum step-length τ is conducted. Only when the data-fit does not improve further, and the required misfit is not achieved, λ is reduced. In the following, this approach is denoted as stepwise cooling. The

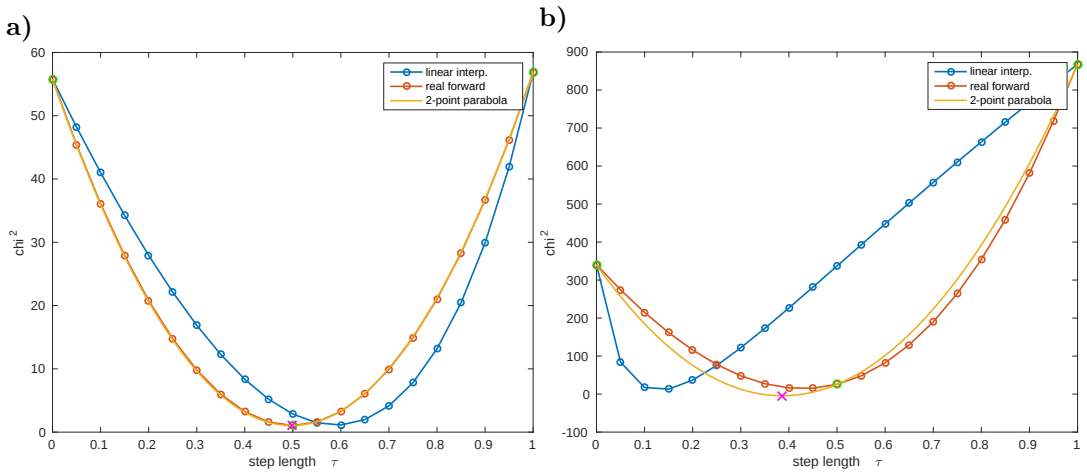

Figure 4.2.: *Line-search for the model update of the first iteration of* ***a)*** *a resistivity inversion and* ***b)*** *a chargeability inversion. Comparison between exact line-search (red), the two-point parabola (yellow line) and linear interpolation (blue). The sampling points of the two-point parabola are indicated by green circles and the minimum of the parabola by a pink cross.*

applicability of this method is tested on inversion of synthetic data in Chapter 5.2.

Implementation in `ResIPIn2D`

In `ResIPIn2D`, three options for the determination of λ and τ are implemented. Referring to the regularization parameter λ the user can choose between a fixed λ, a cooling type reduction of λ in every iteration or stepwise cooling. The initial regularization parameter λ_{ini} and minimum λ_{min} is requested in the input-file. For the cooling methods, also the reduction factor r is specified in the input-file. When a reduction of λ^k is required in the k-th iteration, the reduced parameter is determined by $\lambda^{k+1} = \frac{\lambda^k}{r}$. When the parameter passes λ_{min} the inversion process is terminated, even if the required convergence is not achieved.
The step-length τ is either fixed to $\tau_{fix} = 0.5$ or it is determined by a line-search. As line-search procedure linear interpolation or the two-point parabola can be selected. In concurrence with Figure 4.2 and the investigations in Chapter 5.2, my recommendation is the stepwise cooling of λ and a two-point parabola line search for the optimum step-length.

4.5. Inversion Mesh

Similar to the FE forward calculation, also the inversion itself is carried out on an unstructured triangular mesh. This does not coincide with other inversion algorithms that also apply an FE forward calculation on a triangular mesh, but use a parameterization with rectangular elements for the inversion process, (e.g Loke

and Barker, 1996b). Beside other reasons, this was certainly due to save computational time because fewer parameter elements are required, and in contrast to the forward problem, the system matrix of the system of linear equations to be solved is not necessarily sparse. Thus, more nonzero entries are present. I make use of the triple-mesh scheme that was introduced by Rücker et al. (2006) and Günther et al. (2006) who apply triple meshes for the 2D and 3D inversion of DC data. The inversion procedures, such as the calculation of the Jacobian matrix, the application of smoothness constraints and the determination of the model update by solving Equation (4.27) is done on the so-called parameter mesh. As it was already described in Chapter 3.3, the parameter mesh is an excerpt of the secondary mesh which is used in the forward calculation (cf. Figure 3.4). That means the outer boundaries of the secondary and primary mesh are far away from the electrodes to meet the boundary conditions whereas the outer boundaries of the parameter mesh are closer to the electrode positions to save DOF and with that computational effort during the inversion procedure. This is reasonable because of the insignificant sensitivity in large depths and far from the electrodes in the lateral direction. However, the model is only updated where the parameter mesh coincides with the forward meshes. Therefore, the parameter mesh should neither be too small to prevent effects of the outer secondary mesh on synthetic data. The parameter-elements within the model domain overlapping the secondary mesh may either coincide completely, or the parameter mesh is coarser so that one parameter-element contains several secondary elements. This might be useful to save computational time as fewer DOF are required where sensitivity is low.

Because of the non-regular element shapes and sizes, it is advantageous to define special smoothness constraints that regard these characteristics of the mesh. A description follows in Chapter 4.7.

4.6. Parameterization

Due to the large dynamic range of model parameters and data, a parameterization is done to prevent numerical errors and to ensure positivity. Several parametrization functions are commonly used, such as $\log_{10} = \lg$ or $\log_e = \ln$. In `ResIPIn2D` the forward calculation uses linear parameters, but for inversion procedures a lg-parameterization is chosen. Applying a parameterization apparently pleads for consideration of several adjustments:

The data residual vector is obtained using the log-values of measured and calculated data. For the i-th data point it reads

$$\Delta d_i = \lg(d_i^{\text{meas}}) - \lg(d_i^{\text{calc}}) \ . \tag{4.44}$$

Furthermore, the diagonal entries of the error weighting matrix $\mathbf{W}_d$ are modified to (following Friedel (2003)):

$$w_{d,i} = \frac{1}{\lg(1+\epsilon_i)} \tag{4.45}$$

for data point i with relative data error ϵ ($\epsilon = 0.05$ if the relative error is 5%). Please note: Using these adjustments, a misfit of $\chi = 1$ still refers to a data-fit within the

error bounds, but other values ($\chi \neq 1$) slightly differ from the corresponding linear misfit. That means that the qualitative evaluation of a misfit should always consider if linear values or parameterized values are involved. Also, only those results are quantitatively comparable to each other, if the same parameter function has been used.

The entries of the Jacobian matrix in logarithmic case J_{ij}^{lg} are altered to

$$J_{ij}^{lg} = \frac{\partial \lg(d_i)}{\partial \lg(p_j)} = \underbrace{\frac{\partial d_i}{\partial p_j}}_{J_{ij}^{lin}} \frac{\frac{\partial \lg(d_i)}{\partial d_i}}{\frac{\partial \lg(p_j)}{\partial p_j}} \tag{4.46}$$

where J_{ij}^{lin} are the corresponding linear entries. Considering $\frac{d}{dx}(\lg(x)) = \frac{1}{\ln(10)x}$ leads to the simple form

$$J_{ij}^{lg} = J_{ij}^{lin} \frac{p_j}{d_i} \ . \tag{4.47}$$

The logarithmic Jacobian entries are simply obtained by scaling the linear Jacobian entries with the corresponding parameter p_j and data point d_i. It is easily shown that the same holds for a parameterization using the natural logarithm ln. The application of logarithmic parameterization directly leads to positivity of the parameters since the logarithm is not defined for negative values.

4.7. Smoothness Constraint Matrix

The constraint matrix $\mathbf{C}$ is the matrix form of the constraint function $\vec{c}$. The easiest form is to set the matrix $\mathbf{C}$ equal to the identity matrix. In combination with a damping factor, this is applied in the Marquardt inversion scheme (Marquardt, 1963). To privilege well-resolved model domains over poorly resolved model domains, weights may be introduced on the diagonal entries. However, this requires an a priori estimation of resolution.

When smoothness constraints are to be applied, the matrix $\mathbf{C}$ controls the smoothness of the model by regulating parameter transitions between neighboring elements. That means, it prevents abrupt jumps between neighboring parameters. Generally, it represents a discrete approximation of partial differential operators (Günther et al., 2006). For example in Occam's inversion, it represents the first order or second order derivatives: In this case, the model functional is represented by roughness R_1 or R_2, where the first one refers to the first order derivatives and the second to the second order derivatives, respectively (Constable et al., 1987):

$$\begin{aligned} R_1 &= \| \mathbf{C}_1 \vec{p} \|^2 \quad \text{and} \quad R_2 = \| \mathbf{C}_2 \vec{p} \|^2 \\ &= \int \left(\tfrac{dp}{dz}\right)^2 \mathrm{d}z \qquad\qquad = \int \left(\tfrac{d^2p}{dz^2}\right)^2 \mathrm{d}z \ . \end{aligned} \tag{4.48}$$

For a one-dimensional model with L horizontal layers, parameters p_i and parameter changes in z-direction, the discretized form is

$$R_1 = \sum_{i=1}^{L} (p_i - p_{i-1})^2 \quad \text{and} \quad R_2 = \sum_{i=1}^{L-1} (p_{i+1} - 2p_i + p_{i-1})^2 \ . \tag{4.49}$$

This represents the discrete form of the contribution of a model parameter p_i and its neighboring parameters p_{i-1} and p_{i+1} to roughness R_1 or R_2. According to Equation (4.49), each line i in matrix $\mathbf{C}$ refers to the contribution of parameter p_i to the roughness R. The real prefactors of the model parameters are inserted in the columns referring to the index of the parameter itself and the index of the neighbors. The remaining entries are zero. For R_1 the entries of the i-th line in $\mathbf{C}_1$ are $c_{i,i-1} = -1$, $c_{i,i} = 1$ and 0 else. For R_2 the corresponding entries in the i-th line in $\mathbf{C}_2$ are $c_{i,i+1} = 1$, $c_{i,i} = -2$, $c_{i,i-1} = 1$ and 0 else. Please note that the constraint matrix $\mathbf{C}_2$ can be determined from matrix $\mathbf{C}_1$ by $\mathbf{C}_2 = \mathbf{C}_1^T\mathbf{C}_1$.

This particular example only applies for one-dimensional models where neighboring model parameters have consecutive indices. However, we can simplify the roughness as norm of the vector

$$\vec{r} = \mathbf{C}\vec{p} \tag{4.50}$$

with $R = \| \vec{r} \|^2$. Regarding R_1, the entry of the i-th element with neighbor n_1 is

$$r_i = \underbrace{-1}_{C_{i,n_1}} p_{n_1} + \underbrace{1}_{C_{i,i}} p_i \ . \tag{4.51}$$

Then the formulation also holds for neighboring model parameters where the indices are not necessarily consecutive.

Now, for a two-dimensional model consisting of rectangular elements with element boundaries parallel to the x- and z-direction, the derivatives are determined in both (x and z) directions. A constraint matrix can be determined for every direction ($\mathbf{C}_x$, $\mathbf{C}_z$) in the same manner as explained above. These matrices can be combined to a complete constraint matrix (Li and Oldenburg, 2000):

$$\mathbf{C}^T\mathbf{C} = \alpha_x\mathbf{C}_x^T\mathbf{C}_x + \alpha_z\mathbf{C}_z^T\mathbf{C}_z \ . \tag{4.52}$$

The real factors α_i can be used to favor a stronger smoothness in one or the other direction. In this form, the constraints can be directly included in the minimization of the functional (Eq. 4.26).

Please note, that for explicit local regularizations (cf. Equation (4.30)), the matrix-vector multiplication in Equation (4.50) is actually between the constraint matrix and the model update vector:

$$\vec{r} = \mathbf{C}\Delta\vec{p} \ . \tag{4.53}$$

For global regularization with a reference model $\vec{p}^0$ (cf. Equation (4.25)) the constraint matrix is multiplied with the deviation between model and reference model ($\delta\vec{p} = \vec{p} - \vec{p}^0$):

$$\vec{r} = \mathbf{C}\delta\vec{p} \ . \tag{4.54}$$

The characteristics of the applied unstructured triangular mesh, however, requires special regularization. This is because the orientation of the triangles' sides is arbitrary, the size of triangles varies strongly, and the three side lengths of each element are not equal. We consider a triangular element i with three neighboring elements $n1$, $n2$ and $n3$ (cf. Figure 4.3). The easiest form is to consider each neighboring element equally. Following the 1D approach, we derive partial derivatives for the

parameter changes of element i across each of the element's sides by considering the corresponding neighboring element. The entries of the roughness regarding the first order derivatives with local regularization have the form

$$r_i = 1\Delta p_i - 1\Delta p_{n1} + 1\Delta p_i - 1\Delta p_{n2} + 1\Delta p_i - 1\Delta p_{n3} \quad (4.55)$$

$$= \underbrace{3}_{C_{i,i}}\Delta p_i \underbrace{-1}_{C_{i,n_1}}\Delta p_{n_1} \underbrace{-1}_{C_{i,n_2}}\Delta p_{n_2} \underbrace{-1}_{C_{i,n_3}}\Delta p_{n3} \; . \quad (4.56)$$

In the modeling examples in Chapter 5, this type of constraint matrix is denoted as $\mathbf{C}_a$. In order to consider the differences in triangle sizes and side lengths, we directly introduce the elements lengths $L(n_1)$, $L(n_2)$, $L(n_3)$ (cf. Figure 4.3) into the smoothness constraint matrix, yielding

$$r_i = \underbrace{L_1}_{C_{i,n_1}}\Delta p_{n_1} + \underbrace{L_2}_{C_{i,n_2}}\Delta p_{n_1} + \underbrace{L_3}_{C_{i,n_3}}\Delta p_{n_1} + \underbrace{-L_{all}}_{C_{i,i}}\Delta p_i \quad (4.57)$$

with perimeter of the element L_{all}. This type of constraint matrix is denoted as $\mathbf{C}_b$ in the following. It is sometimes handy to scale the entries of Matrix $\mathbf{C}$ with the Diagonal entries ($\frac{1}{C_{i,i}}$) which can be referred as a matrix multiplication $\mathbf{C}'\mathbf{C}$ with a diagonal matrix $\mathbf{C}' = diag(1/C_{i,i})$. This smoothness type is denoted as $\mathbf{C}_c$ in the following. In case of matrix $\mathbf{C}_b$ entries of bigger elements (in terms of perimeter L_{all}) have larger values, so different element sizes are considered. Scaling all entries with the diagonal entries ($C_{i,i} = L_{all,ii}$) in $\mathbf{C}_c$ has the effect that different element sizes are not respected but the varying side lengths within each element is still considered.

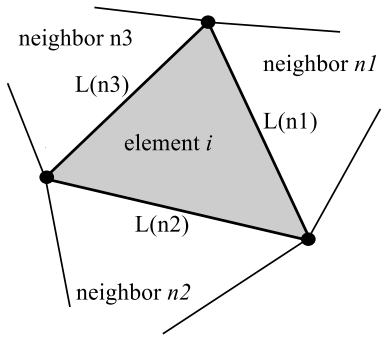

Figure 4.3.: *Sketch of the triangular element i with neighboring elements n_1, n_2, n_3 and lengths of the element's sides $L(n_1)$, $L(n_2)$, $L(n_3)$ shared with the corresponding neighbors.*

All constraint matrices described above are sparse with nonzero entries only on the main diagonal and on few sub-diagonals. Different types of constraint matrices can also be combined by either addition or multiplication. Multiplication with a diagonal matrix usually applies for weighting as done in matrix $\mathbf{C}_c$.
For elements located at the boundaries of the model domain, special constraints apply. In case of the constraint matrices defined in (4.56) and (4.57) that is simply realized by setting the constraints only for these element sides to nonzero that have neighbors within the parameter domain.

In `ResIPIn2D` smoothness constraint matrices $\mathbf{C}_a$, $\mathbf{C}_b$ and $\mathbf{C}_c$ are implemented. The effect of the choice of smoothness matrix and a recommendation is derived from inversion of synthetic data in Chapter 5.2. Under consideration of the concept of simplicity that prefers smooth models, the goal of the inversion is to minimize the roughness R (representing the model functional Ψ_p) under the requirement to achieve a data misfit of $\chi = 1$ (confining to $\Psi_d = \Psi_d^*$).

4.8. Depth of Investigation

Many studies about the depth of investigation have been conducted. Some simple rules that are based on type and spread of an applied electrode array are given by Roy and Apparao (1971) and Barker (1989). Further investigations are based on a resolution matrix (e.g Friedel, 2003), a cumulative sensitivity (e.g Kemna, 2000) and choice of initial models (Oldenburg and Li, 1999).

Here, the term depth of investigation (DOI) is used in a general sense as a depth limit that defines a transition between model domains that are regarded as reliable and those that are rather vague. In the following, three different concepts are taken into account: The rule of thumb according to (Barker, 1989), the derivation from the coverage matrix which is a cumulated sensitivity (see Chapter 4.8.2) and the DOI index according to Oldenburg and Li (1999) that is derived from the results obtained by different initial models.

4.8.1. Rule of Thumb

The DOI rules according to Roy and Apparao (1971) and Barker (1989) are functions of the largest electrode distance that is used in the applied multi-electrode array. This distance is multiplied with a real factor that is dependent on the array type (see Table 2.1). The DOI obtained by the rule of thumb after Barker (1989) is denoted as DOI_t in the following. As for all presented methods, this determination is only an approximation. It is best suited for homogeneous parameter domains. Anyway, it provides an idea about the depth range that can be investigated by a certain electrode setup in 2D environments.

4.8.2. Coverage

The coverage (cov) represents a cumulative sensitivity. For model parameter j it is defined in the general form as (Günther, 2004)

$$\mathrm{cov}_j = \sum_{i=1}^{D} |J_{ij}| \tag{4.58}$$

which is the sum of the Jacobian entries of the j-th column. When data weighting is applied by the error weighting matrix $\mathbf{W}_d$, the coverage is obtained from the

summation over the column entries of $\mathbf{W}_d\mathbf{J}$ to confine to the effect of error weighting (e.g. Park and Van, 1991; Martin, 2009):

$$\mathrm{cov}_j = \frac{1}{\mathrm{cov}_{max}} \sum_{i=1}^{D} |W_{d,ii} J_{ij}| \ . \tag{4.59}$$

To make sure that the coverage of different data-sets is comparable, the entries are scaled with the overall maximum amplitude cov_{max}. Then, the new maximum amplitude is equal to 1. In the case of an unstructured mesh, the elements sizes vary significantly. Since the sensitivity depends on the parameterization, larger sensitivity values are obtained for larger elements. Thus, the coverage is normalized by the area of each element A_j to be better comparable:

$$\mathrm{cov}_j = \frac{1}{\mathrm{cov}_{max}} \left(\frac{1}{A_j} \sum_{i=1}^{D} |W_{d,ii} J_{ij}| \right) \ . \tag{4.60}$$

Then cov_{max} is the maximum coverage after normalization to the element areas.

Like the physical parameter values (resistivity and chargeability), the coverage can be visualized as a color-coded map since every parameter element is attributed with a coverage value. An example is shown in Figure 4.4-a for a Pole-Dipole array obtained from the sensitivity of a homogeneous half-space model. It visualizes the coverage of the sensitivities of all electrode setups included in the multi-electrode protocol. The coverage is highest close to the electrode locations and decreases with growing distance. Accordingly, the model parameter elements close to the surface have a higher contribution to calculated data than elements in distance to the electrodes which correspond to lower coverage values. Expressed in accordance with the definition of sensitivity, changing the parameter values of elements with low coverage has little influence on the calculated data whereas a parameter perturbation for elements with high coverage has a strong influence on the data. Since the sensitivity depends on the parameter model, also the coverage does. Deviations from a homogeneous model disturb the sensitivity pattern and with that also the coverage distribution. An example is shown in Figure 4.4-b for a 2D resistivity model with a high resistive model block in the center of the profile. Both figures reveal which model domains have higher sensitivities than other domains. To derive a depth of investigation, a coverage threshold needs to be defined.

Martin (2009), used the coverage to derive the depth of investigation for transient electromagnetic data. He suggests a threshold of $1 \leq \mathrm{cov}_j \leq 10^{-2}$ to refer to well resolved and $10^{-2} \leq \mathrm{cov}_j \leq 10^{-4}$ to refer to poorly resolved model domains. Here, we derive a coverage threshold based on the homogeneous model and the DOI_t. This idea is inspired by a similar approach by Yogeshwar (2014) who applied it on 2D EM inversion results.

Since the DOI_t is most accurate for homogeneous models, it is handy to compare it with the coverage of a homogeneous half-space model (usually the initial model). We determine the coverage value cov_t that coincides with the maximum DOI_t (red cross), which is found in the center of the multi-electrode setup. This value cov_t is then used as the threshold for the coverage corresponding to the 2D models of the

subsequent iterations. The coinciding depth is assumed as the approximate DOI and is denoted as DOI_{app}. The isoline according cov_t is indicated by a black line in the coverage plots for the homogeneous model as well as for the inhomogeneous model. It is clearly seen that the approximate DOI is shifted towards the subsurface in the center of the profile which is due to a model block with higher resistivity than the surrounding half-space.

Surely, the DOI_{app} can only be interpreted as an approximate indication of the transition between well-resolved model domains and less resolved domains. It does not give a strict limit between resolution and no resolution.

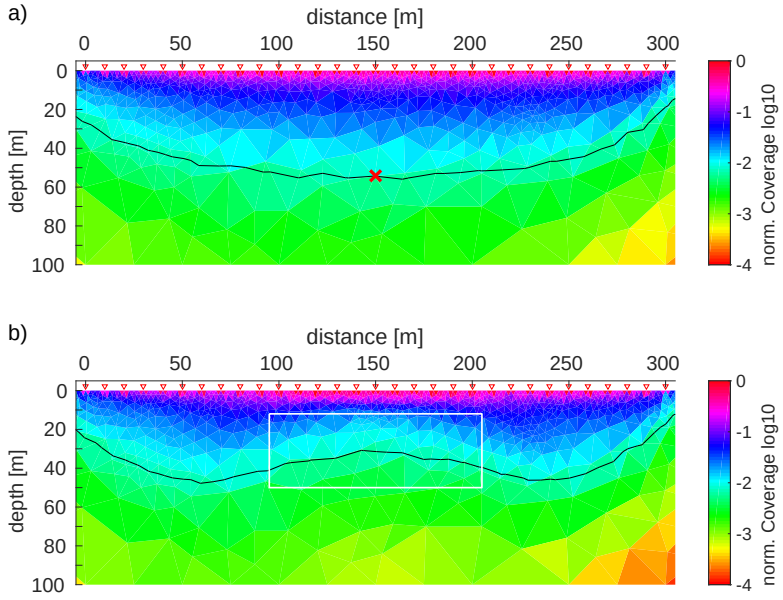

Figure 4.4.: a) *Normalized coverage of a Pole-Dipole array for a homogeneous half-space with resistivity $\rho_{hs} = 10\,\Omega\mathrm{m}$. The red cross indicates the DOI_t. The coverage threshold cov_t=-2.15 is the coverage value coinciding with DOI_t. The approximate DOI_{app} (black line) is defined by the coverage isoline corresponding to cov_t.* ***b)*** *Normalized coverage according to an inhomogeneous model including a buried block with $\rho_{\mathrm{block}} = 100\,\Omega\mathrm{m}$ within a half-space with $\rho_{hs} = 10\,\Omega\mathrm{m}$. The white line indicates the outline of the body. The black cov_t isoline denotes the approximate DOI_{app}. Electrode loactions are indicated by red triangles.*

4.8.3. DOI index

Another method that approximates the depth of investigation of an inversion result is the DOI-index, that was introduced by Oldenburg and Li (1999). The main idea is to determine which parts of the model domain are important to fit the data. This is achieved by comparison of the inversion results obtained using different starting models. In particular, this means that it is investigated where the inversion results are similar to each other and where the results differ. Especially when global

regularization is applied, the parameter values of elements with low sensitivity are forced to stay close to the initial model.

The procedure is as follows: The mean value of the measured data d_{mean} is determined. The main inversion is carried out using d_{mean} as parameter for the homogeneous initial model $\vec{p}^0$. After that, two additional inversions are carried out using an initial model with increased parameter value (in our case resistivity or chargeability) of $\vec{p}_1^0 = 10\vec{p}^0$ and one with decreased initial parameter model $\vec{p}_2^0 = 1/10\vec{p}^0$. The corresponding inversion results are then denoted as $\vec{p}_1$ and $\vec{p}_2$, respectively. From these two inversion models, the DOI-index $\vec{R}$ is derived after

$$R_j = \frac{p_{1,j} - p_{2,j}}{p_{1,j}^0 - p_{2,j}^0} \tag{4.61}$$

where R_j is the entry corresponding to the j-th parameter element. Referring to the main inversion, the amplitude of R_j indicates if the parameter value of element j depends more on the initial model or on the measured data. If $R_j \approx 0$, then the inversion results $p_{1,j}$ and $p_{2,j}$ are equal, which means that parameter j is independent from the choice of the initial model. Thus, it is only influenced by the measured data. In case of $R_j \approx 1$, the difference between the inversion results $p_{1,j}$ and $p_{2,j}$ are equal to the difference between the initial models. That means, parameter j is only affected by the initial model and is not influenced by the measured data.

The DOI-index can be plotted as a color-coded 2D map, since a value is obtained for each parameter element. This visualizes the dependency on the inversion result of the choice of initial model. Similar to the coverage method described in the preceding subsection, a maximum depth of investigation DOI_r is estimated by defining a contour-line as a threshold. Oldenburg and Li (1999) suggest a threshold of 0.1 or 0.2 that limits reliable model domains from less reliable domains.

Examples for the determination of DOI_r for the inversion with `ResIPIn2D` are shown in Chapter 5.3 and 7.1.6.

4.8.4. Features of `BERT` and `Res2DInv`

In Chapters 5.4.3 and 7.1.7, inversion results obtained by `ResIPIn2D` are compared to 2D results of the established algorithms `BERT` and `Res2DInv`. The main features of these algorithms are listed in the following:

`BERT`

- Inversion of DC data
- global smoothness constrained regularization scheme:

$$\left(\mathbf{J}^T\mathbf{W}_d^T\mathbf{W}_d\mathbf{J} + \lambda\mathbf{C}^T\mathbf{C}\right)\Delta\vec{p} = \mathbf{J}^T\mathbf{W}_d^T\mathbf{W}_d\Delta\vec{d} - \lambda\mathbf{C}^T\mathbf{C}\delta\vec{p}$$

- error weighting

- Finite Element approach
- triple-grid with unstructured triangular meshes, including topography
- determination of the Jacobian by reciprocity principle
- inexact linesearch for optimum steplength by linear interpolation

`Res2DInv`

- Inversion of DC and TDIP data using the two-step approach
- global smoothness constrained regularization:

$$\left(\mathbf{J}^T\mathbf{J} + \lambda\mathbf{C}^T\mathbf{C}\right)\Delta\vec{p} = \mathbf{J}^T\Delta\vec{d} - \lambda\mathbf{C}^T\mathbf{C}\delta\vec{p}$$

- no error weighting
- Finite Element or Finite Difference approach
- inversion on block model, distorted according to topography
- determination of Jacobian by perturbation approach or Broyden update
- cooling of the regularization parameter λ

5. Inversion of Synthetic Data

This chapter serves to prove the accuracy of the newly developed inversion algorithm and to assess the functionality of the implemented approaches by inversion of synthetic data. The main focus lies on the assessment of the following questions:

a) Is the resolution of a highly chargeable anomaly dependent on the corresponding resistivity anomaly?

b) What is the effect of different smoothness constraints and different regularization parameters on the resulting inversion models?

c) Is it reasonable to derive an approximate depth of investigation from normalized sensitivity coverage?

Aside from these key questions, it is evaluated whether the newly developed algorithm produces results that are reasonable in comparison to established algorithms. The investigations of this chapter are the basis for the inversion of field data that is presented in Chapter 7.

5.1. Resolution of Chargeability Dependent on Resistivity Model?

The first question is about the precision and ability of the algorithm to resolve chargeability structures independent from the resistivity model. As shown in Chapter 3.4, the presence of a rather high chargeability anomaly of 100 mV/V corresponds to an increase of effective resistivity by 11%. In turn, this results in a peak increase of effective apparent resistivity of 8%. Therefore, a high accuracy is crucial.

The basis of this investigation is the original model shown in Figure 5.1. It contains four buried model blocks. The resistivity and chargeability values are listed in Table 5.1. Each of the blocks has a chargeability of $m_{\text{block}} = 100\,\text{mV/V}$. The surrounding half-space has a chargeability of $m_{hs} = 10\,\text{mV/V}$ and intrinsic resistivity $\rho_{hs} = 100\,\Omega\text{m}$ which yields an effective resistivity of $\rho'_{hs} = 101\,\Omega\text{m}$. The resistivity of blocks A and D clearly differs from the surrounding half-space by minus and plus $50\,\Omega\text{m}$, respectively. The resistivity of B is $91\,\Omega\text{m}$ which results in an effective resistivity that is nearly equivalent to the effective resistivity of the surrounding half-space. Thus, no resistivity anomaly will be recognized in synthetic data. Block C has the same intrinsic resistivity as the surrounding half-space, but due to a higher chargeability value, the effective resistivity is increased. Figure 5.1-c,d shows the calculated synthetic apparent resistivity ρ'_a and chargeability pseudo-sections for a Dipole-Dipole setup . As expected, the resistivity anomalies due to blocks A and D

are most prominent. The apparent resistivity anomaly due to block C is weak but recognizable whereas there is no signature due to block B. However, there are clear apparent chargeability anomalies corresponding to all 4 model blocks. The apparent chargeability anomaly due to block D seems to be slightly weaker than the other signatures. Before inversion, 3% noise was added to the resistivity and chargeability data (see Figure 5.1-e,f).

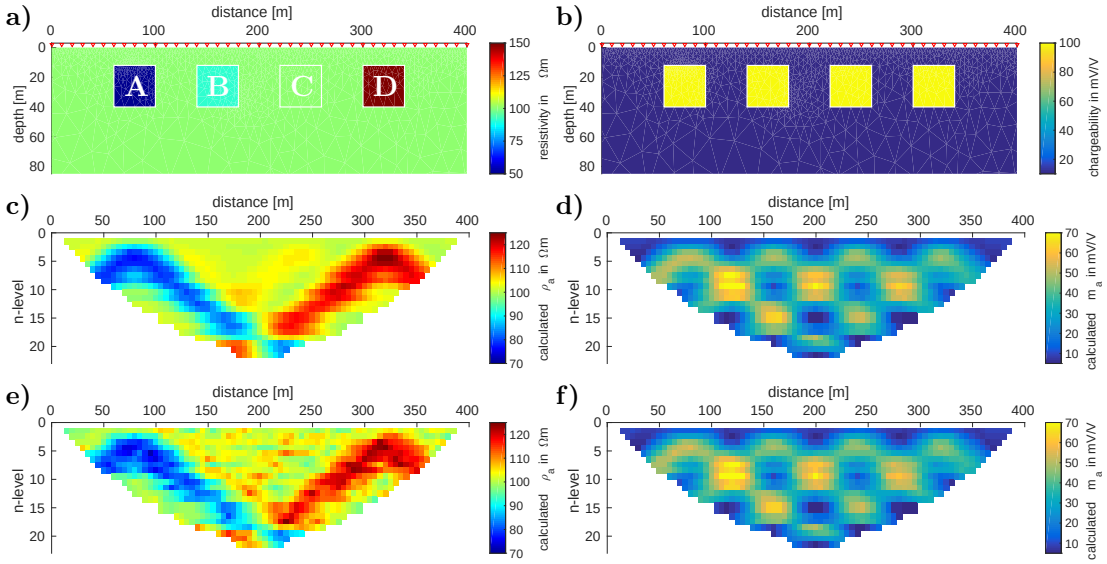

Figure 5.1.: ***a)*** *Original resistivity model $\rho(x, z)$,* ***b)*** *original chargeability model $m(x, z)$. The resistivity and chargeability values of the buried model blocks are listed in Table 5.1. The surrounding half space has a resistivity of $\rho = 100\,\Omega$m and a chargeabilty of $m = 10\,$mV/V. Electrode locations are indicated by red triangles.* ***c)*** *Synthetic effective apparent resistivity pseudo-section (ρ'_a),* ***d)*** *synthetic apparent chargeability pseudo-section of the model in a and b calculated for the Dipole-Dipole protocol listed in Table B.3.* ***e,f)*** *Synthetic data including 3% noise.*

Table 5.1.: *Chargeability and resistivity values of the buried model blocks and the surrounding half-space (hs) in Figure 5.1.*

Body	m in mV/V	ρ in Ωm	ρ' in Ωm
A	100	50	56
B	100	91	101
C	100	100	111
D	100	150	167
hs	10	100	101

Exemplary inversion results of the Dipole-Dipole data in Figure 5.1-e,f are shown in Figure 5.2. The following inversion settings were used: Smoothness constraint

matrix $\mathbf{C}_b$, a constant regularization parameter $\lambda = 79$ and a 2-point parabola line-search was done to determine the optimum step-length in every iteration. The initial model was a homogeneous half-space with $\rho^0 = 80\,\Omega\text{m}$ and $m^0 = 8\,\text{mV/V}$. The mesh used for the inversion is unbiased in the sense that it does not include the exact boundaries of the original model blocks.

The resistivity model ρ' obtained by the 1st step of the applied two-step IP inversion approach, which is the pure resistivity inversion, is displayed in Figure 5.2-a. The resistivity model ρ shown in Figure 5.2-b and the chargeability model shown in Figure 5.2-c are the result of the subsequent chargeability inversion. The corresponding model responses are presented in Figure 5.2-d,f and the relative difference to the original synthetic data in Figure 5.2-f,g, respectively.

According to $\chi_{dc} = 0.96$, the fit of the resistivity data is within the error bounds while the chargeability data-fit is $\chi_{ip} = 1.62$. Consequently, deviations of more than 10% appear in the relative difference in Figure 5.2-f. Overall, the original resistivity and shape of the four model blocks were reproduced. Only the size of block D is underestimated. As expected, blocks B and C are nearly invisible due to small resistivity contrast to the surrounding half-space. However, all chargeability blocks are reproduced adequately. Again, the size of block D is underestimated. This is partly because the original apparent resistivity anomaly has a smaller amplitude compared to the other blocks. The other reason is that the triangular elements within the area of block D are larger than those in the areas of the other model blocks. Thus, due to the applied smoothness constraints, the transition from large to small model parameters is approximated by larger steps than in the case of a finer mesh. To check on the latter aspect, the study was repeated using the same mesh for inversion of synthetic data calculated from model blocks in the opposite order. That means that block A is on the right and block D is on the left-hand side. In the resulting chargeability model, the size of block D is in better agreement with the original size. All in all, the shape and amplitude of chargeability anomalies can be reproduced by inversion with `ResIPIn2D` independent from the corresponding resistivity anomaly.

5.2. Comparison of Smoothness Constraints and Regularization Parameters

This chapter deals with the comparison of inversion results obtained using different smoothness constraints and regularization parameters. The focus lies on smoothness matrices $\mathbf{C}_a$ and $\mathbf{C}_b$. They differ in the sense that in $\mathbf{C}_a$ all triangular elements are considered equally whereas in $\mathbf{C}_b$ the element's size and shape are considered (cf. Chapter 4.7). Furthermore, the optimum range of regularization parameter λ for each smoothness matrix is investigated. This is of special interest when applying the stepwise cooling approach described in Chapter 4.4. The initial λ_{ini} should be large enough to prevent scattered models in the first iterations. Since convergence is also dependent on the right choice of the model update step-length τ, this parameter is subject to this investigation as well. Basis of all examples presented in this chapter

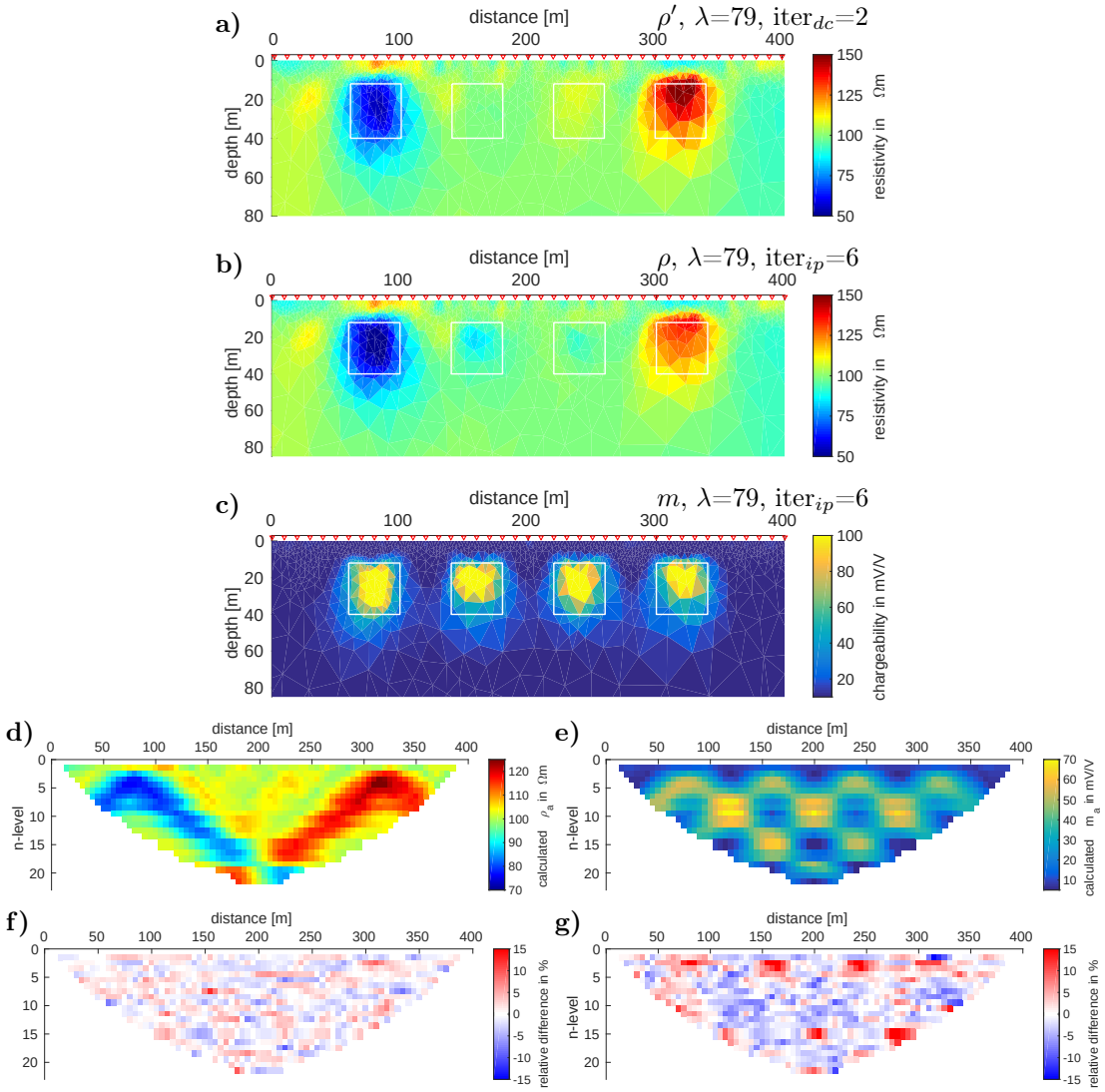

Figure 5.2.: *Inversion results of the original synthetic data in Figure 5.1-e,f using* $\mathbf{C}_b$*, a fixed* $\lambda = 79$ *and a 2-point parabola line-search for* τ*.* ***a)*** *Resistivity model* ρ' *resulting from the DC inversion. The data-fit is* $\chi_{dc} = 0.96$*.* ***b)*** *Intrinsic resistivity model* ρ *and* ***c)*** *chargeability model* m *resulting from the 6th iteration of the IP inversion. The data-fit is* $\chi_{ip} = 1.62$*.* ***d)*** *Model response* ρ'_a *and* ***e)*** *model response* m_a*.* ***f,g)*** *Relative difference between the calculated data above and the original data.*

is the synthetic data corresponding to the 4-block model displayed in Figure 5.1.

Figure 5.3 presents an overview over the data-fit χ^2 during the first three iterations of the resistivity inversion for different λ-τ-combinations. The overview according to the first three chargeability iterations is shown in Figure 5.4. Here, χ^2 instead of χ is chosen for the visualization because it is easier to distinguish a minimum. The subfigure-columns refer to the smoothness constraint matrices $\mathbf{C}_a$ (a,d,g), $\mathbf{C}_b$ (b,e,h) and $\mathbf{C}_c$ (c,f,i) and the rows represent the progress during iterations 1 (a,b,c), 2 (d,e,f) and 3 (g,h,i). In each subfigure, the step-length covers the range $0 \leq \tau \leq 1$.

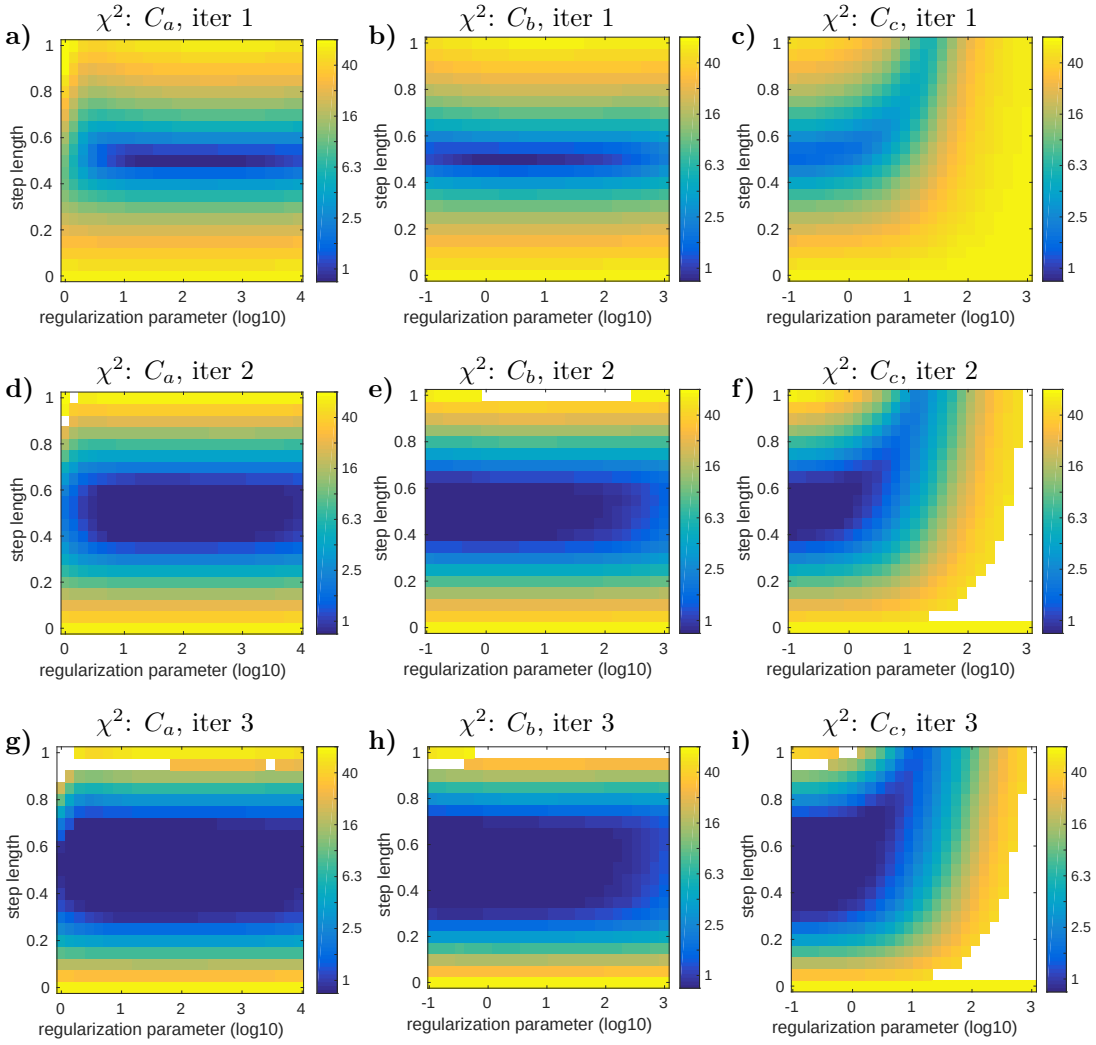

Figure 5.3.: *Resistivity inversion: Data misfit χ^2_{dc} for different combinations of regularization parameter λ and step length τ. Each column refers to inversion using a different smoothness constraint matrix, such as $\mathbf{C}_a$ **(a,d,g)**, $\mathbf{C}_b$ **(b,e,h)** and $\mathbf{C}_c$ **(c,f,i)**. Each row refers to the according iteration number: **a,b,c)** iteration 1, **d,e,f)** iteration 2 and **g,h,i)** iteration 3. White cells represent that there is no entry.*

Due to different amplitudes of the entries in the smoothness matrices, the range of the regularization parameter is $10^0 \leq \lambda \leq 10^4$ for C_a and $10^{-1} \leq \lambda \leq 10^3$ for $\mathbf{C}_b$ and $\mathbf{C}_c$. Please note that the λ-ranges, shown for the chargeability inversion, are only excerpts of these ranges and the color scale in Figure 5.4 covers a wider χ^2-interval. Each cell represents one inversion procedure in which λ and τ are kept fixed. White cells represent that the inversion terminated, either because the stopping criterion is already met or the problem diverged.

Referring to the resistivity inversion (cf. Figure 5.3), the best improvement of χ^2_{dc} is generally reached around the step-length of $\tau = 0.5$. During the first three iterations, the desired misfit of $\chi^2 \approx 1$ is achieved for step-length of $0.3 \leq \tau \leq 0.7$. As expected, the improvement of χ^2 is also dependent on the regularization parameter λ with an

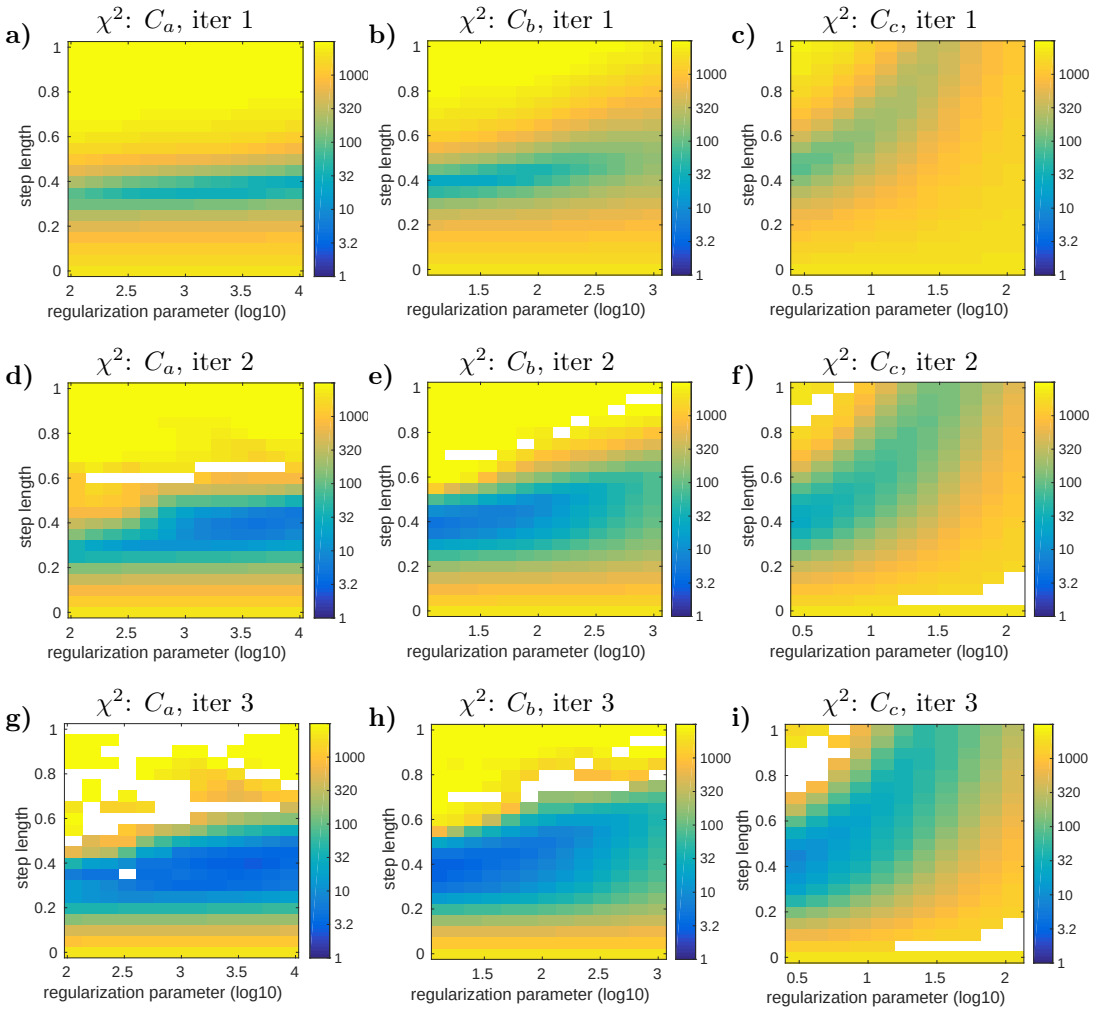

Figure 5.4.: *Chargeability inversion: Data misfit χ^2_{ip} for different combinations of regularization parameter λ and step length τ. Each column refers to inversion using a different smoothness constraint matrix, such as $\mathbf{C}_a$ **(a,d,g)**, $\mathbf{C}_b$ **(b,e,h)** and $\mathbf{C}_c$ **(c,f,i)**. Each row refers to the according iteration number: **a,b,c)** iteration 1, **d,e,f)** iteration 2 and **g,h,i)** iteration 3. White cells represent that there is no entry.*

upper and lower limit. Referring to the displayed ranges, the best improvement is reached using $10^1 \leq \lambda \leq 10^4$ for $\mathbf{C}_a$, $10^{-1} \leq \lambda \leq 10^2$ for $\mathbf{C}_b$ and $10^{-1} \leq \lambda \leq 10^1$ for $\mathbf{C}_c$.

In case of the chargeability inversion (cf. Figure 5.4), the smallest χ^2_{ip}-values are shifted to smaller step-length. For $\mathbf{C}_a$, the preferred λ-range is shifted towards the highest values that were recommended for the resistivity inversion whereas in case of $\mathbf{C}_b$ the preferred range is shifted towards the smallest values, respectively.

For more detailed information, Figure 5.5 shows the final χ_{ip} for different regularization parameters, that were kept fixed during the iterations. The left-hand side refers to $\mathbf{C}_a$, the right-hand side refers to C_b. The optimum step-length was determined by the 2-point parabola technique in every iteration. Overall, we see that the smaller

the regularization parameter λ, the smaller the data-fit χ_{ip}. The only exception is the data-fit corresponding to the smallest λ used with $\mathbf{C}_a$.

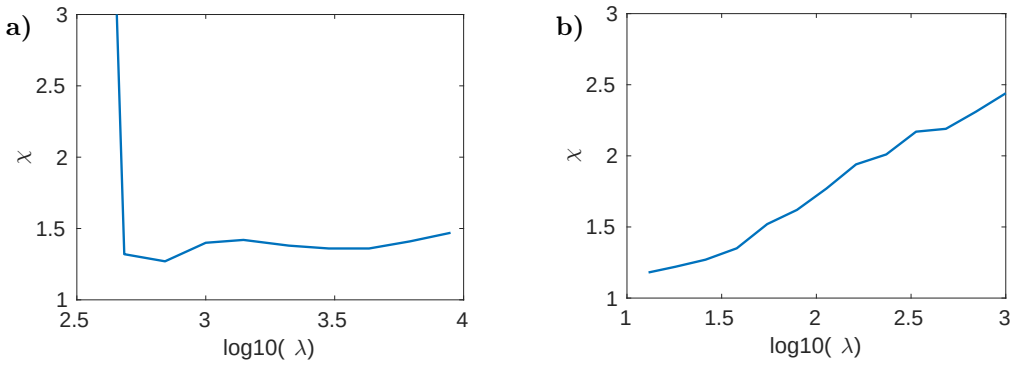

Figure 5.5.: *Final chargeability data-fit χ_{ip} for different fixed regularization parameters. The optimum step-length τ was determined by the 2-point parabola technique.* ***a)*** *Using smoothness matrix $\mathbf{C}_a$ and* ***b)*** *using smoothness matrix $\mathbf{C}_b$.*

From these results (Figure 5.3 and Figure 5.4), I suggest choosing an initial $\lambda_{ini} \geq 10^4$ when using $\mathbf{C}_a$ and an initial $\lambda_{ini} \geq 10^2$ in case of $\mathbf{C}_b$. Like this, a rather smooth model is preferred in the first iterations. Only when the data misfit cannot be reduced further, the regularization parameter is reduced. The chargeability inversion is then started with the same initial value for λ, and the same cooling procedure is applied, when the misfit cannot be reduced further. In the following, the focus will lie only on smoothness matrices C_a and C_b, since the models resulting the inversion using C_c are rather scattered and unfavorable in comparison to the models produced by the other matrices. An example inversion result is shown in Figure B.1 in the Appendix. Furthermore, it is shown that a line-search for an optimum step-length is advantageous especially for the chargeability inversion.

To emphasize the efficiency of the stepwise cooling (when desired), more inversion results of the original synthetic data corresponding to the 4-body model (cf. Figure 5.1) are presented. In practice, the stepwise cooling is applied in both, the resistivity and the chargeability inversion. When dealing with inversion of synthetic data, the resistivity inversion tends to converge within the first few iterations so that the reduction of the regularization parameter is not necessary. Therefore, the examples, shown here, concentrate on the chargeability inversion. In particular, it is investigated whether the chargeability data-fit can be improved without triggering a scattered model.

The chargeability inversion result shown in Figure 5.2 was obtained using $\mathbf{C}_b$ and a fixed $\lambda = 79$ after the 6th IP iteration. Figure 5.6 shows the final result after applying the step-wise cooling of λ. After the 6th iteration, λ was reduced by factor 2 and was kept fixed until the data-fit did not reduce further. This procedure is generally either continued until the convergence criterion of $\chi_{ip} = 1$ is achieved or a predefined minimum λ_{min} is reached.

The course of χ_{ip}, λ and τ during iterations is displayed in Figure 5.6-e. The final

regularization parameter is $\lambda = 2.5$ resulting in data-misfit of $\chi_{ip} = 1.1$. The reproduction of the shape of the model blocks is slightly improved, especially in the chargeability model displayed in Figure 5.6-a. However, the chargeability appears to be increased in the lower left corner of the model, which is interpreted as an inversion artifact because the sensitivity is low in this part of the model domain. The intrinsic resistivity model ρ (cf. Figure 5.6-b) is similar to the corresponding model after the 6th iteration. But, the relative deviation between the original data and the final model response (cf. Figure 5.6-4) proves that the IP chargeability data-fit is overall enhanced.

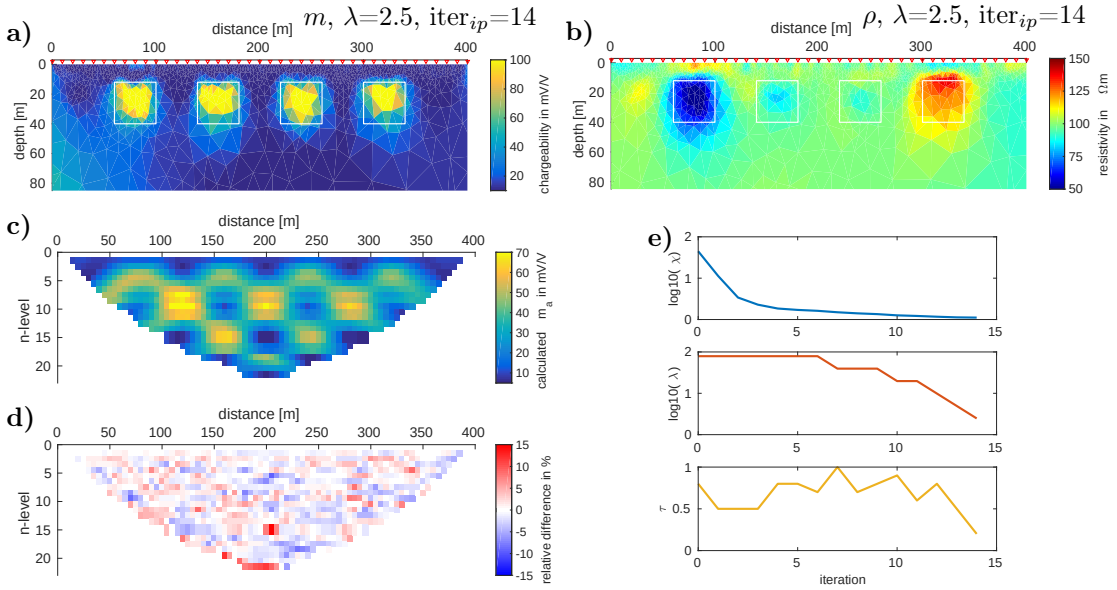

Figure 5.6.: *Results of the 14th iteration of the chargeability inversion, additional to the results displayed in Figure 5.2 (using $\mathbf{C}_b$). After stepwise cooling, the final values are $\lambda = 2.5$ and $\chi_{ip} = 1.11$.* ***a)*** *Chargeability model m,* ***b)*** *intrinsic resistivity model ρ,* ***c)*** *calculated apparent chargeability m_a and* ***d)*** *relative difference between the data in (c) and the original data.* ***e)*** *Data misfit χ_{ip}, regularization parameter λ and step-length τ during iterations of chargeability inversion.*

As a comparison, the inversion results using C_b and a fixed $\lambda = 2.5$ during all iterations is shown in Figure 5.7. The final data-fit is $\chi_{ip} = 1.12$. However, especially the resistivity models appear to be noisier than the models obtained after stepwise cooling, even though the noise is not prominent in the chargeability model. The reproduction of the blocks and the surrounding half-space is not as precise as it is when applying the stepwise cooling.

The final inversion results using smoothness matrix $\mathbf{C}_a$ and an initial regularization parameter of $\lambda_{ini} = 8900$ are shown in Figure 5.8. The resistivity model ρ' resulting from the second iteration of the resistivity inversion (cf. Figure 5.8-a) has a data-fit of $\chi_{dc} = 0.96$. Overall, the shape and the resistivity of the model blocks is reproduced, but the resistivity of the surrounding half-space is slightly overestimated and more scattered compared to the results obtained using $\mathbf{C}_b$. The chargeability model resulting from the 5th chargeability iteration using $\lambda = 8900$ is shown in

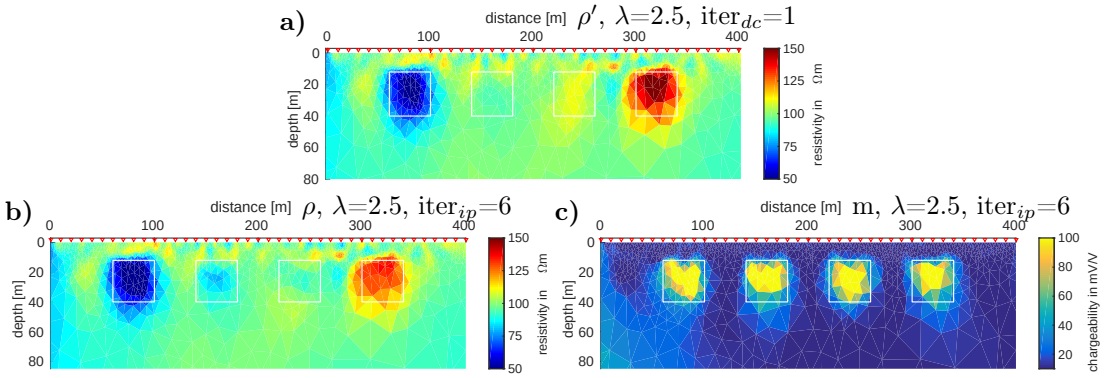

Figure 5.7.: *Inversion results of the synthetic data in Figure 5.2-e,f using C_b, a fixed $\lambda = 2.5$ and a 2-point parabola line-search for τ.* ***a)*** *Resistivity model ρ' resulting from DC inversion.* ***b)*** *Intrinsic resistivity model ρ and* ***c)*** *chargeability model m resulting from the 6th iteration of the chargeability inversion. The final data misfit is $\chi_{ip} = 1.12$.*

Figure 5.8-b. The corresponding data-fit is $\chi_{ip} = 1.47$. The model is comparable to the chargeability models obtained using $\mathbf{C}_b$. The chargeability and shape of the original model blocks are reproduced satisfactorily. After the 15th chargeability iteration, the data-fit is further reduced to $\chi_{ip} = 1.21$ and the final regularization parameter is $\lambda = 35$ (see Figure 5.8-e). The resulting intrinsic resistivity model ρ and chargeability model m are shown in Figure 5.8-c-d, respectively. The resistivity and shape of the model blocks are again reproduced well. Only the background resistivity is slightly overestimated, similar to the ρ'-model. As expected when using a smaller regularization parameter, the transitions of the chargeability model are slightly sharper than in subfigure b. The lower boundary of block B apparently smears out towards greater depths.

According to the results shown in this chapter, I recommend using smoothness matrix $\mathbf{C}_b$ when dealing with unstructured grids including a large variety of triangle size and triangle shape. It was shown that the application of a stepwise cooling serves to improve the data-fit without producing unnecessary scattered or blocky models that appear when applying a rather small initial λ. Furthermore, it is seen that the parabola line-search for the optimum step-length of the model update is advisable in contrast to a fixed step length because the optimum step-length varies from iteration to iteration in the shown examples. Generally, the choice of the initial and minimum regularization parameter is to be handled with care. The optimum choice is also dependent on the data quality and mesh geometry. Therefore, it is advantageous to check not only the model resulting from the last iteration (and final λ) but also the models resulting from the intermediate iterations.

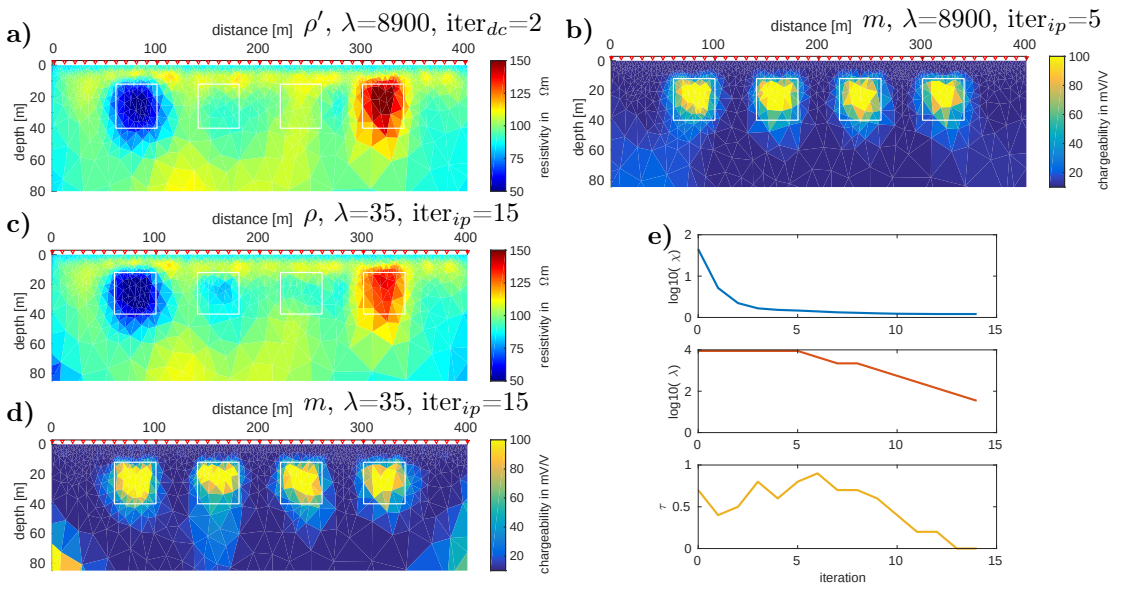

Figure 5.8.: *Inversion results of the synthetic data in Figure 5.2-e,f using* $\mathbf{C}_a$, $\lambda_{ini} = 8900$ *and a 2-point parabola line-search for* τ. ***a)*** *Resistivity model* ρ' *resulting from the DC inversion. The data misfit is* $\chi_{dc} = 0.95$. ***b)*** *Chargeability model* m *resulting from the 5th iteration of IP inversion. The data-fit is* $\chi_{ip} = 1.47$. ***c)*** *Intrinsic resistivity model* ρ *and* ***d)*** *chargeability model* m *resulting from the 15th iteration. Final values are* $\lambda = 35$, $\chi_{ip} = 1.21$. ***e)*** *Data misfit* χ_{ip}, *regularization parameter* λ *and step-length* τ *during iterations of chargeability inversion.*

5.3. Influence of Initial Model

`ResIPIn2D` allows the use of various initial models. In most cases, a homogeneous half-space is suitable. However, when apriori information is available, or the model is to be triggered into the right direction, a predefined 2D resistivity/chargeability model can be used as the initial model. Including a priori information is apparently not fair when testing an algorithm as preparation for the use on real field data. Therefore, for the examples presented in the preceding chapter and for all following inversion studies, the initial model is a homogeneous half-space. When not stated otherwise, the mesh discretization is unbiased meaning that no additional model block boundaries are included in the mesh as it is the case when calculating synthetic data from an original model.

The influence of the choice of the initial (homogeneous) resistivity on the final inversion model is investigated in the following. All inversion examples shown above and in the following are obtained applying a local smoothness regularization scheme. In this case, the dependence of the final inversion model on the initial model is expected to be weaker than it is when applying a global regularization scheme. However, the applicability of the DOI index (cf. Equation (4.61)) as approximation of the depth of investigation is assessed.

Again, we inspect inversion results of the synthetic data corresponding the 4-block

model displayed in Figure 5.1. The main inversion is conducted using the mean values of the data $\rho^0 = 100\,\Omega\text{m}$ and $m^0 = 30\,\text{mV/V}$ as initial values. The final resistivity model ρ' and chargeability model m are displayed in Figure 5.9-a,b. The DOI index $\vec{R}$ is derived from two further inversions using an initial value p_2^0 that is decreased by a factor of 10 and an initial value p_1^0 that is increased by a factor of 10. This is done for both, the resistivity and the chargeability inversion (cf. Figure 5.9-c,d). Oldenburg and Li (1999) suggest a threshold of 0.1-0.2 as the limit of reliable model domains. According to Figure 5.9-c,d, the inversion results are not influenced by choice of initial resistivity or chargeability until a depth of at least 150 m. This is 1.5 times the DOI according to the rule of thumb ($DOI_t = 100\,\text{m}$). Only the DOI index referring to the chargeability inversion shows values $R > 0.2$ in the lateral direction outside of the electrode array. Consequently, it is not suitable to derive the depth of investigation from the DOI index when applying a local smoothness regularization in `ResIPIn2D`.

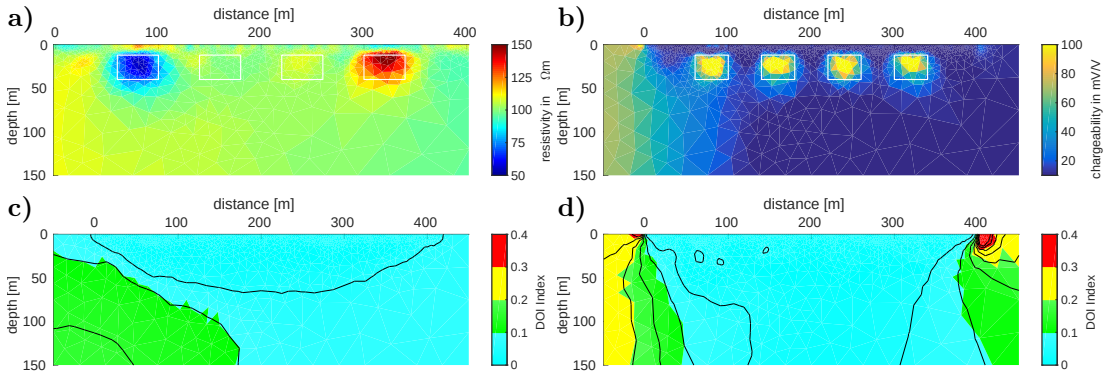

Figure 5.9.: ***a)*** *Resistivity model ρ' resulting from DC inversion with initial resistivity of $\rho^0 = 100\,\Omega\text{m}$.* ***b)*** *Chargeability model m resulting from IP inversion with initial chargeability $m^0 = 30\,\text{mV/V}$.* ***c)*** *DOI index R after Oldenburg and Li (1999) for the resistivity model above determined from inversion using initial resistivity $\rho_1^0 = 1000\,\Omega\text{m}$ and $\rho_2^0 = 10\,\Omega\text{m}$ and* ***d)*** *DOI index R for the chargeability model above determined from inversion using initial chargeability $m_1^0 = 300\,\text{mV/V}$ and $m_2^0 = 3\,\text{mV/V}$. Isolines of R are indicated by black lines in steps of 0.05.*

5.4. Resolution of the lower boundary of a model block

The investigations in this chapter are based on a question that was derived from the analysis of field data discussed in Chapter 7. The question is whether the lower boundary of a highly chargeable model block can be detected with a given field setup and be resolved by inversion? And more important, to what extent? These investigations include the assessment of the depth of investigation.
In the preceding chapter, it was shown that the DOI index tends to overestimate the

depth of investigation when applying a local regularization scheme. In the following, the depth of investigation according to the rule of thumb DOI_t is correlated with the coverage (Eq. 4.60) and used as an approximate DOI_{app} as described in Chapter 4.8.2. The applicability of this approximation is assessed by inversion of synthetic data calculated from models with parameter boundaries in varying depth. A further aspect of this investigation is the question whether the depth of investigation is larger for chargeability than for resistivity because the chargeability is determined by a division of two resistivity values.

All following examples were calculated for the same electrode setup that was used during the field survey in Elbistan, Turkey (cf. Chapter 7). The profile length is 300 m, the smallest electrode spacing is $a = 10$ m and the array type is a Pole-Dipole setup with 14 n-levels according to the protocol listed in Table B.6. The depth of investigation according to the rule of thumb is $\mathrm{DOI}_t = 53$ m. First, we confine to the resolution of the lower boundary of a resistivity model as shown in Figure 5.10. Subsequently, a similar investigation is done regarding a chargeability model as shown in Figure 5.16.
For all presented examples, inversion was conducted using smoothness matrix $\mathbf{C}_b$, a stepwise cooling of the regularization parameter with initial $\lambda_{ini} = 79$ and a parabola line-search to determine the optimum step-length in every iteration. Please note that the mesh used for the inversion procedure is unbiased, that means that the exact borders of the model blocks are not included in the mesh. For the forward calculation of the original synthetic data, the borders were included. Before inversion, 3% noise is added to each original synthetic dataset.

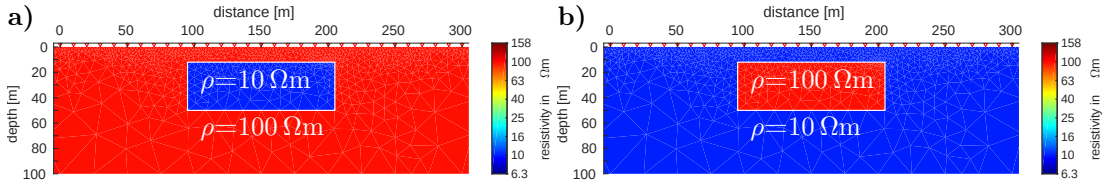

Figure 5.10.: *Original resistivity models including a block with lateral extension* $x = 95 - 205$ m *and vertical extension* $z = 12 - 50$ m. *The resistivity of the block* ρ_{block} *and the half-space* ρ_{hs} *are* ***a)*** ρ_{block}=10 Ωm, ρ_{hs}=100 Ωm *and* ***b)*** ρ_{block}=100 Ωm, ρ_{hs}=10 Ωm.

5.4.1. Lower Boundary of Resistivity Anomaly

The original resistivity models are shown in Figure 5.10. The model on the left-hand side consists of a low resistive model block with ρ_{block}=10 Ωm within a homogeneous half-space with resistivity of ρ_{hs}=100 Ωm. The resistivity of the model on the right-hand side is opposite with a high resistive model block with ρ_{block}=100 Ωm within a half-space with ρ_{hs}=10 Ωm. The lateral extent of the blocks is $x = 95 - 205$ m. The upper boundary is constant at $z = 12$ m. The lower boundary is varied in 10 m-steps from $z = 20$ m to $z = 100$ m. To check the detectability of the lower boundary, synthetic Pole-Dipole sounding curves $\rho_a(z)$ are calculated for all models

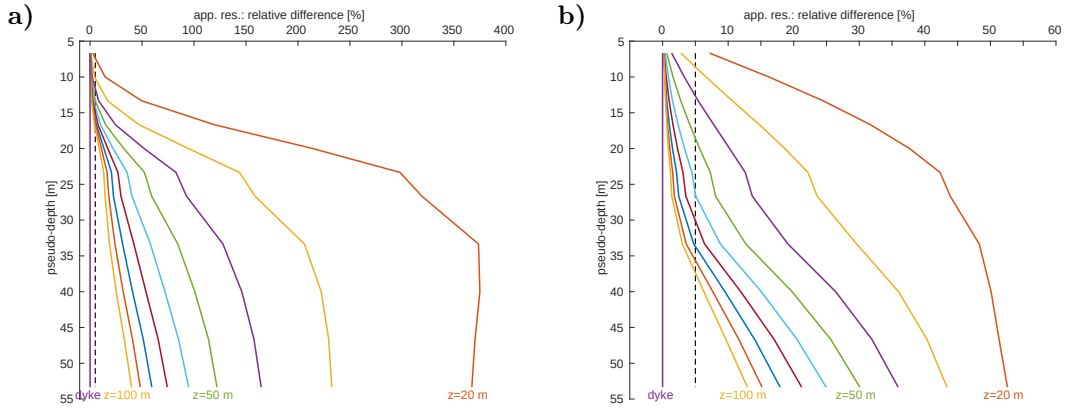

Figure 5.11.: *Apparent resistivity sounding curves at* $x = 190\,\mathrm{m}$ ***a)*** *calculated for the model in Figure 5.10-a and* ***b)*** *for the model in Figure 5.10-b, each with lower boundaries of the anomaly between* 20 m *and* 100 m *depth. The signatures are shown as relative difference to the signature of a dyke in %. The 5% limit is indicated by a dashed black line.*

and compared to the signature of a dyke $\rho_{a,\mathrm{dyke}}$ with lower boundary in infinite depth. This is approximated by a model block with lower boundary in $z = 1000\,\mathrm{m}$. In Figure 5.11 synthetic sounding curves at profile distance $x = 190\,\mathrm{m}$ are shown as relative difference to the dyke signal in percent. As an orientation, the 5% limit is indicated by a dashed line. The relative difference is more prominent in case of the low resistive model block (cf. Figure 5.11-a) than that of the high resistive model block (cf. Figure 5.11-b). Also, the pseudo-depth in which the relative difference exceeds the 5% limit is larger in the case of the high resistive model block. So, according to the curves shown in Figure 5.11 the lower boundary of the model block is detected at least until a depth of 100 m in both cases (high and low resistive model block). Furthermore, the curves according to 100 m depth differ significantly from the curve according to 50 m depth which is roughly the depth DOI_t. According to this, it is expected that generally the model blocks with low resistivity are better reproduced by inversion than the high resistive model blocks because the sounding curves show a larger variety. Anyway, in both cases, it is expected that the lower boundary is detected even in depth larger than the DOI_t at least to some extend.

The inversion results of the original synthetic data corresponding to the model including the low resistive block, shown in Figure 5.10-a, are presented for lower boundaries in 30, 50, 70 and 90 m depth in Figure 5.12-a-d and the result for the dyke model in Figure 5.12-e. The corresponding normalized coverage is shown in Figure 5.13. The approximate DOI_{app} is indicated by a dashed white line in the inversion results and by a black line in the coverage plots. In both figures, the original outline of the model blocks is indicated by a white line.
Referring to the resistivity models, the original outline of the model blocks is recognizable, even if the lower boundary of the model block lies below the $\mathrm{DOI}_t = 53\,\mathrm{m}$. The resistivity within the block boundaries reaches values of around the original $10\,\Omega\mathrm{m}$. Although some artifacts are noticeable in the surrounding half-space, the original resistivity of $100\,\Omega\mathrm{m}$ is reproduced adequately. However, since this investiga-

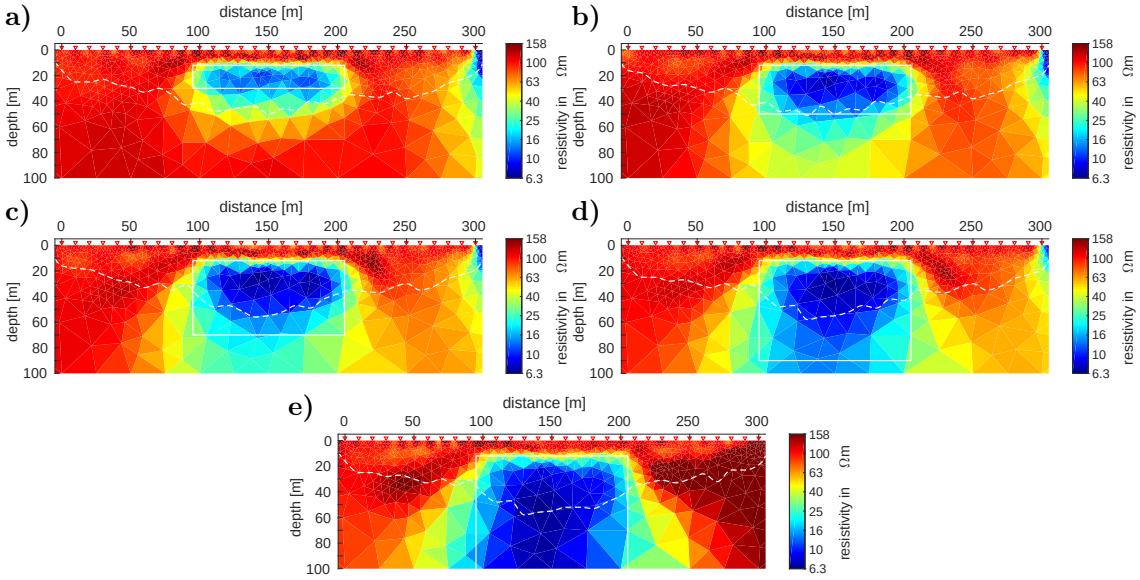

Figure 5.12.: *Resistivity models resulting from inversion of the original synthetic data based on the model in Figure 5.10-a with lower boundaries of the model block in different depth:* ***a)*** 30 m, ***b)*** 50 m, ***c)*** 70 m *and* ***d)*** 90 m; *and* ***e)*** *dyke model. The outline of the original block is indicated by a white line. The dashed white line represents the* DOI_{app}. *Electrode locations are indicated by red triangles. The initial model is a homogeneous half-space with resistivity* $\rho^0 = 80\,\Omega$m.

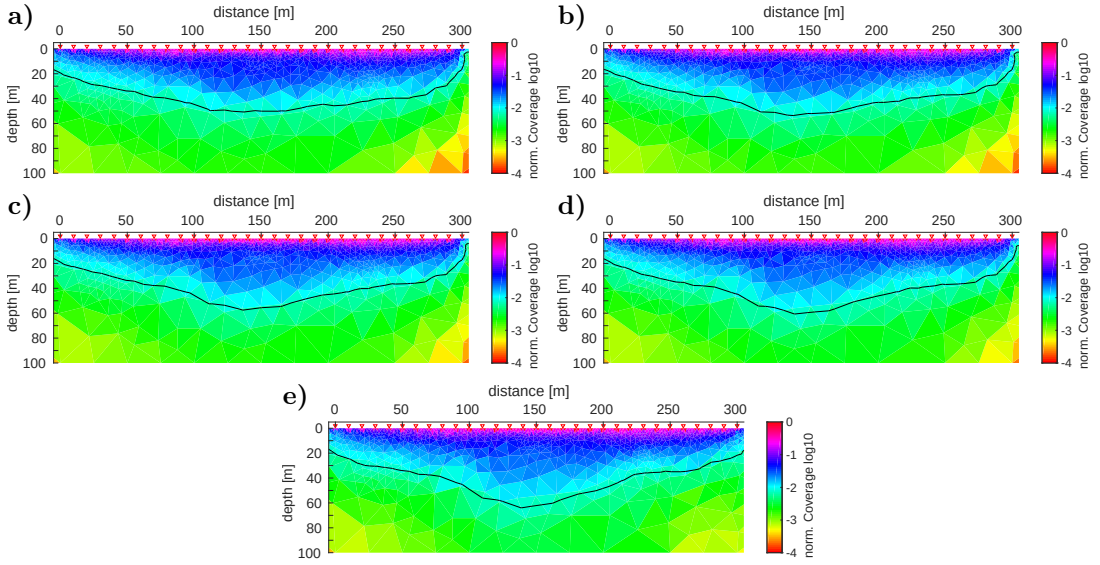

Figure 5.13.: *Normalized coverage corresponding to the resistivity models resulting from inversion of synthetic data based on the model in Figure 5.10-a with lower boundaries of the anomaly in different depth:* ***a)*** 30 m, ***b)*** 50 m, ***c)*** 70 m *and* ***d)*** 90 m; *and* ***e)*** *dyke model. For all models, a* $\chi \leq 1$ *is achieved. The black isoline refers to the* DOI_{app}. *Electrode locations are indicated by red triangles.*

tion deals with the reproduction of the model block itself, these effects are negligible. In all cases, the low resistivity of the block smears out towards larger depth which is due to several reasons. The size of the triangular mesh elements increases with growing depth, and since the smoothness constraints force the parameter change into a smooth transition from element to element, the resistivity change from 10 Ωm to 100 Ωm is stretched over several elements. Furthermore, the sensitivity is weaker at larger depth which is supported by the trend of the normalized coverage (cf. Figure 5.13).
Referring to the resistivity model corresponding to the block boundary in 70 m depth (Figure 5.12-c), a clear increase in resistivity appears below the model block. But, the resistivity increase already begins at a depth of about $50 - 60$ m. This means that the lower boundary is resolved by the inversion, at least to some extent.
The resistivity model corresponding to the block boundary in 90 m depth (Figure 5.12-d) clearly differs from the dyke model displayed in Figure 5.12-e indicating that the lower boundary has some influence on the inversion result. The lateral extension of the reproduced low resistive anomaly narrows below ca. $50 - 60$ m depth. This indicates that the DOI_{app} limits domains that are well resolved from less resolved model domains. There is, however, still some sensitivity below this line, since the block boundaries in 70 and 90 m depth influence the inversion results. It is also apparent that the isolines of the normalized coverage are slightly bent towards larger depth within the low resistive block. According to this, the sensitivity is larger in low resistive model domains than in high resistive parts.

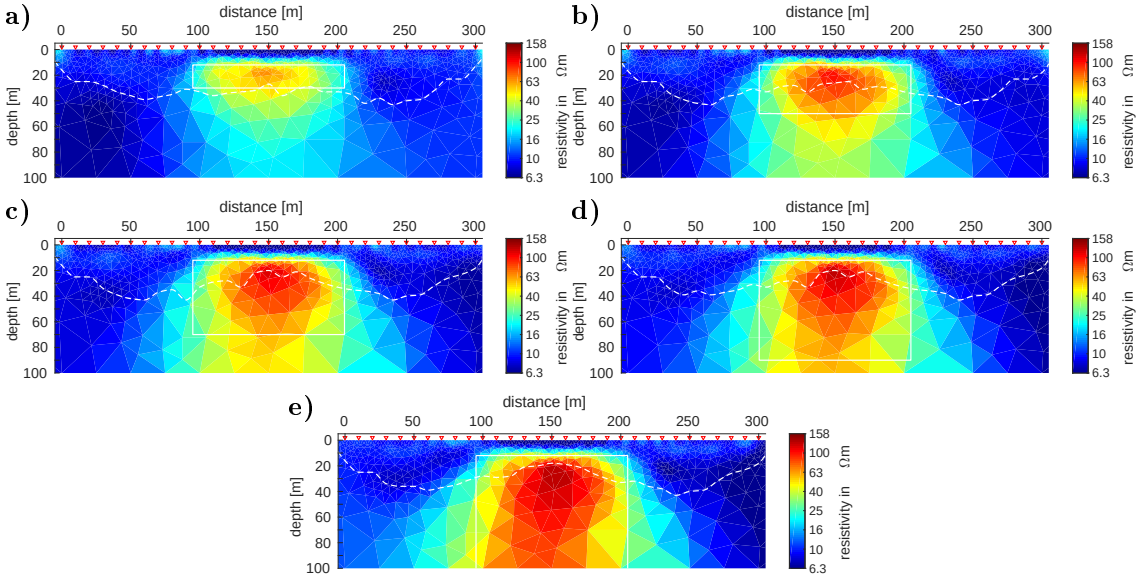

Figure 5.14.: *Resistivity models resulting from inversion of the original synthetic data based on the model in Figure 5.10-b with lower boundaries of the anomaly in different depth:* ***a)*** 30 m, ***b)*** 50 m, ***c)*** 70 m *and* ***d)*** 90 m*; and* ***e)*** *dyke model. For all models, a* $\chi \leq 1$ *is achieved. The outline of the original block is indicated by a white line. The dashed white line represents the* DOI_{app}*. Electrode locations are indicated by red triangles. The initial model is a homogeneous half-space with resistivity* $\rho^0 = 8\,\Omega\mathrm{m}$*.*

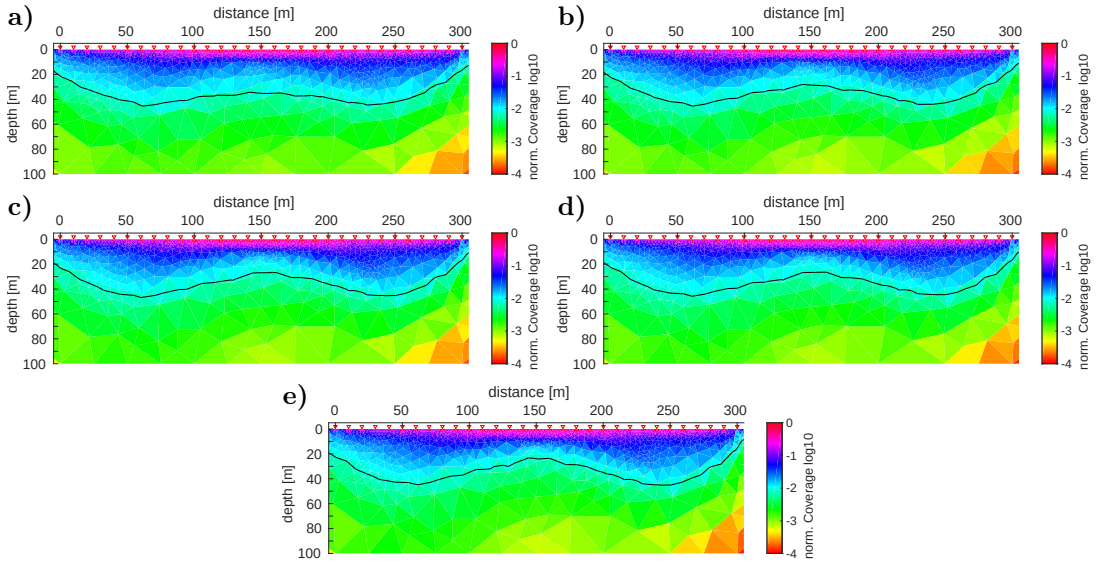

Figure 5.15.: *Normalized coverage corresponding to the resistivity models resulting from inversion of synthetic data based on the model in Figure 5.10-b with lower boundaries of the anomaly in different depth:* ***a)*** 30 m, ***b)*** 50 m, ***c)*** 70 m *and* ***d)*** 90 m*; and* ***e)*** *dyke model. The black isoline refers to the* DOI_{app}*. Electrode locations are indicated by red triangles.*

Inversion results of the original synthetic data calculated from the models with high resistive model blocks (cf. Figure 5.10-b) are shown in Figure 5.14 and the corresponding normalized coverage is shown in Figure 5.15. The lateral extent of the model block is not as well reproduced as it is the case for the low resistive block. Similar to the preceding example, the resistivity of the model block smears out towards larger depth and to the lower sides. A transition from high to lower resistivity appears below both, the block boundary in 70 and 90 m depth (cf. Figure 5.14-c,d). Both inversion models differ from the dyke model (Figure 5.14-e), but the transition from high to low resistivity below the block is not as obvious as it is for the model with block boundary in 50 m depth (Figure 5.14-b). Furthermore, the lateral extent of the anomaly decreases below a certain depth. In contrast to the example discussed before, the isolines of the normalized coverage are bent towards the surface within the outlines of the model blocks which is apparently due to the higher resistivity in contrast to the surrounding half-space. This indicates that the sensitivity is lower in high resistive model domains. In this case, the DOI_{app} underestimates the depth of investigation, but it gives a good impression in which parts of the model the sensitivity is higher or lower in relation to each other. Anyway, similar to the preceding example, it can be interpreted as a limit between different stages of resolution. The lower limit of the model block has an influence on the inversion result even if it lies below the DOI_t and the DOI_{app}-isoline.

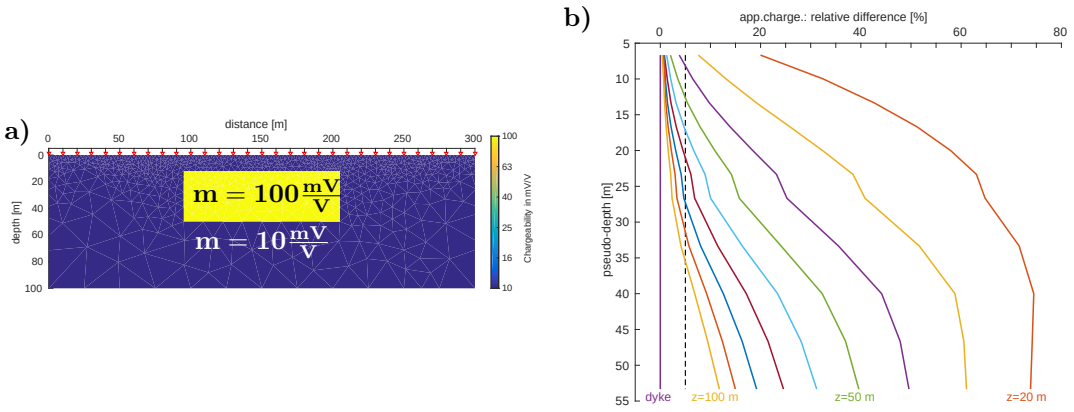

Figure 5.16.: ***a)*** *Original chargeability model m. The corresponding resistivity model ρ is a 100 Ωm homogeneous half-space.* ***b)*** *Apparent chargeability sounding curves at $x = 190\,\mathrm{m}$ calculated for the model in a) with lower boundaries of the anomaly between 20 m and 100 m depth. The signatures are shown as relative difference to the signature of a dyke in %. The 5% limit is indicated by a dashed black line.*

5.4.2. Lower Boundary of Highly Chargeable Model Block

The original chargeability model is shown in Figure 5.16-a. The chargeability of the block is $m_{\mathrm{block}} = 100\,\mathrm{mV/V}$ and that of the surrounding half-space is $m_{\mathrm{hs}} = 10\,\mathrm{mV/V}$. The corresponding intrinsic resistivity model is a homogeneous half-space with $\rho = 100\,\Omega\mathrm{m}$. The lower boundary of the block is varied between $z = 20\,\mathrm{m}$ and $z = 100\,\mathrm{m}$. Synthetic apparent resistivity and apparent chargeability data is calculated using the Pole-Dipole protocol listed in Table B.6 and compared to synthetic data calculated for a dyke model (approximated by a model block with lower boundary in 1000 m depth). As an example, synthetic apparent chargeability sounding curves are extracted from the 2D pseudo-section at profile distance $x = 190\,\mathrm{m}$ and displayed in terms of relative difference regarding the dyke signal in Figure 5.16-b. All curves exceed the 5% limit which means that the lower boundary of the body is detectable by the applied Pole-Dipole protocol at least until a depth of $z = 100\,\mathrm{m}$.

Figure 5.17 shows the chargeability inversion results of the original synthetic data corresponding to models with lower block boundary in 30, 50, 70, and 90 m depth. The original outline of the model blocks is indicated by white lines. The corresponding normalized coverage is shown in Figure 5.18. Similar to the resistivity inversion results discussed above, the high chargeability anomaly smears out below the original outline of the model block. But, the lower boundary of the block is resolved as a clear transition from high to low chargeability. Only the case where the boundary is located in 90 m depth, it is not clearly resolved. However, the width of the increased chargeability narrows below the DOI_{app}, which is contrary to the inversion model according to the dyke (cf. Figure 5.17-e). Note that, except for the dyke model, the shape of the high resistive structure adapts to the DOI_{app} isoline. Below this line, the chargeability either decreases (cf. Figure 5.17-c) or the width narrows (cf.

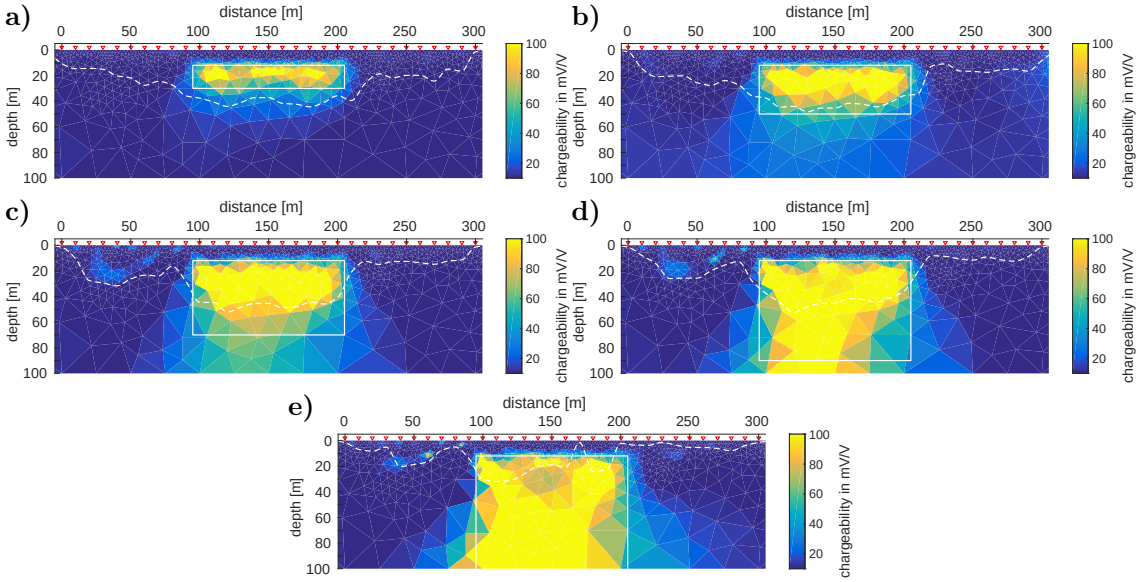

Figure 5.17.: *Chargeability models resulting from chargeability inversion of the original synthetic data based on the model in Figure 5.16 with lower boundaries of the anomaly in different depth:* ***a)*** $30\,\mathrm{m}$, $\chi = 0.97$, ***b)*** $50\,\mathrm{m}$, $\chi = 0.97$,***c)*** $70\,\mathrm{m}$, $\chi = 1.05$ *and* ***d)*** $90\,\mathrm{m}$, $\chi = 1.6$*; and* ***e)*** *dyke model,* $\chi = 1.5$. *The outline of the original block is indicated by a white line. The dashed white line represents the* DOI_{app}. *Electrode locations are indicated by red triangles. The initial model is a homogeneous half-space with resistivity* $\rho^0 = 80\,\Omega\mathrm{m}$ *and chargeability* $m^0 = 8\,\mathrm{mV/V}$.

Figure 5.17).

From Figure 5.18 we see that the normalized chargeability coverage seems to be stronger influenced by chargeability changes than the resistivity coverage. Especially at the beginning and end of the profile, where the chargeability is low, the isoline referring to the DOI_{app} is significantly shallower than in the highly chargeable domain in the center. In the case of the dyke model (cf. Figure 5.18-e), the approximate DOI is not applicable, since the corresponding isoline clearly underestimates the depth of investigation.

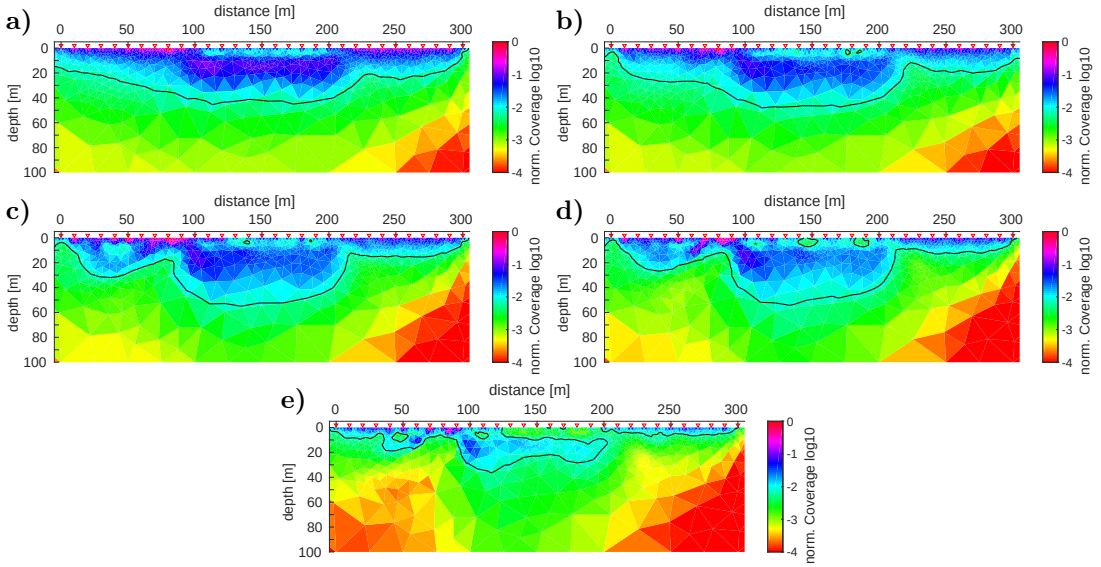

Figure 5.18.: *Normalized Coverage for the corresponding chargeability models resulting from chargeability inversion of the original synthetic data based on the model in Figure 5.16 with lower boundaries of the anomaly in different depth:* ***a)*** 30 m, ***b)*** 50 m, ***c)*** 70 m *and* ***d)*** 90 m*; and* ***e)*** *dyke model. The black line refers to the* DOI_{app}*. Electrode locations are indicated by red triangles.*

5.4.3. Comparison of Inversion Results with other Algorithms

In the following, the `ResIPIn2D` inversion is compared to results obtained by other algorithms. This comparison does not serve to decide which algorithm provides the best results. The idea is to check whether the newly developed algorithm is capable of reproducing the original model in a similar manner as the well-established algorithms. Usually, inversion results are never perfect if the initial model is not very close to the original model and if the exact boundaries of model features are not part of the used mesh. Furthermore, smoothness constraints lead to smooth parameter transitions instead of abrupt changes. Surely, every algorithm has its advantages and disadvantages, and the results may vary if different inversion parameters are chosen.

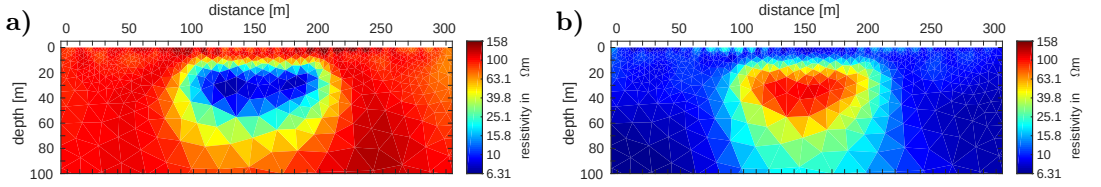

Figure 5.19.: *Resistivity models obtained by* `BERT`*: Inversion (using* $\lambda = 30$*) of synthetic data calculated from the models with lower boundary of the model block in* 50 m *depth and with* ***a)*** *a high resistive anomaly (*$\chi_{dc} = 0.93$*) and* ***b)*** *a low resistive anomaly (*$\chi_{dc} = 0.95$*) as shown in Figure 5.10-a,b.*

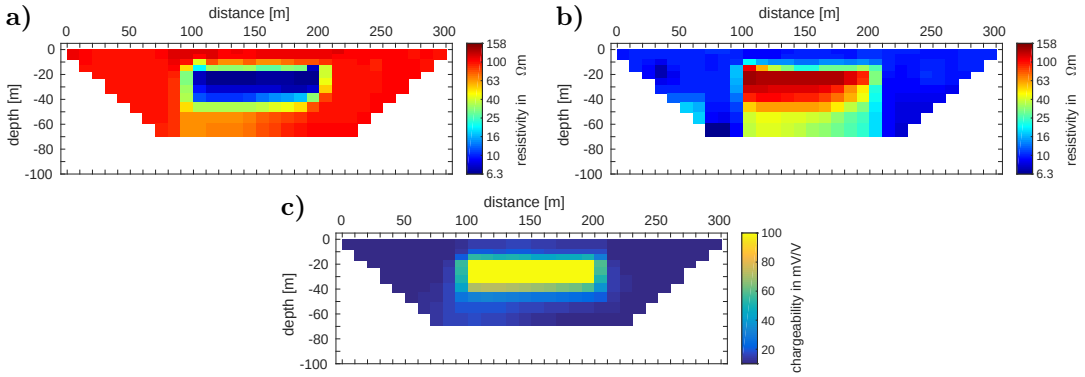

Figure 5.20.: *Resistivity models obtained by* `Res2DInv`*: Inversion of synthetic data calculated from the models with lower boundary of the model block in* 50 m *depth and with* ***a)*** *a high resistive anomaly* ($RMS_{dc} = 2.2\%$) *and* ***b)*** *a low resistive anomaly* ($RMS_{dc} = 2.1\%$) *as shown in Figure 5.10-a,b.* ***c)*** *Chargeability model* ($RMS_{ip} = 0.92\%$) *of the synthetic data calculated from the model shown in Figure 5.16-a.*

In this comparison, we confine to the model with lower block boundary located in 50 m depth as shown in Figure 5.10 and Figure 5.16-a. First, we refer to the resistivity inversion models obtained by `BERT` displayed in Figure 5.19. Similar to `ResIPIn2D`, `BERT` applies the finite element approach on an unstructured triangular meshes. In the results of both algorithms, the resistivity of the model block smears out towards deeper depths. For the high resistive model block, this effect is slightly stronger in the `ResIPIn2D` model (cf. Figure 5.14-b). Furthermore, the width of the high resistive model block is better reproduced by the `BERT` model than by the `ResIPIn2D` model. Both algorithms produce artifacts that are most prominent in the model with the low resistive anomaly.
The `Res2DInv` resistivity and chargeability inversion results are displayed in Figure 5.20. The inversion is conducted using rectangular model blocks with the width of one electrode distance whereas the forward calculation is conducted on a refine mesh. For the results shown here, the forward response was calculated by the finite difference method. Due to the rectangular model elements, the rectangular shape of the anomaly can be reproduced better than by an unstructured triangular mesh. Similar to the `ResIPIn2D` resistivity model according to the low resistive anomaly (Figure 5.12-b), an elongated high resistive artifact appears above the block. The resistivity of the high resistive model anomaly smears out towards deeper depths in a similar manner as in the corresponding `ResIPIn2D` result (Figure 5.14-b). The original highly chargeable model block is reproduced well. Only the lower boundary is slightly underestimated as it is the case in the `ResIPIn2D` result (Figure 5.17-b). According to these comparisons, the inversion results obtained by the newly developed algorithm can thoroughly be compared to the results of well-established algorithms.

5.5. Conclusions

The presented synthetic data examples prove that the DC and the two-step IP inversion with `ResIPIn2D` produce reliable results. Original models are reproduced adequately within the error bounds of the original synthetic data including noise. The inversion models are comparable to the DC results of `BERT` and the DC/TDIP results of `Res2DInv`. The discussed examples include blocky structures. Therefore, the advantage of using an unstructured triangular mesh over the employment of a structured rectangular mesh is not fully exploited. By inversion of synthetic data, several research question were investigated assessing computational and practical aspects.

It was shown that highly chargeable structures could be recovered by the inversion algorithm whether the structure is significant in the resistivity model or not. Furthermore, the derivation of an approximate DOI_{app} from the normalized sensitivity coverage is a useful tool to distinguish well-resolved model domains from poorly resolved model domains. However, according to the presented inversion examples, it is surely not a strict limit for the depth of investigation.

The influence of different smoothness constraint matrices on inversion results was compared. Moreover, the effect of the choice of regularization parameter and the step-length of model updates on the convergence of the inversion problem was investigated. From these studies, the following recommendations for the use of `ResIPIn2D` are derived:

- The employment of smoothness matrix $\mathbf{C}_b$ is advantageous for the utilized unstructured mesh. This matrix considers the irregular shape of the mesh elements.
- The application of a stepwise cooling helps to enhance the data-fit without triggering a scattered model. According to the presented convergence studies, a value of $\lambda_{ini} \geq 80$ is adequate as initial regularization parameter. It is reduced when the minimum data-fit corresponding to the current regularization parameter is achieved, but the desired misfit of $\chi = 1$ is not met.
- Convergence is enhanced by using an inexact parabola line-search for the optimum step-length in every iteration.

6. Consideration of Topography Effects

The presence of distinctive surface topography has a strong influence on measured DC data. That means that apparent resistivity values obtained over a homogeneous resistivity distribution beneath surface topography differ significantly from a homogeneous half-space signature. Without consideration of topography effects that might lead to misinterpretation. According to Fox et al. (1980), the topography effect is significant for slope angles greater than 10° and for slopes that are longer than one dipole length. The influence of topography on measured apparent resistivity is mainly based on two reasons: The first reason is that the topography affects the shape of the electrical potential and therefore also the direction of the electrical current lines. This effect is shown in Figure 6.1 for a distant source electrode. Underneath a hill, the equipotential surfaces diverge, and thus the measured potential difference between two points is lower than that of a flat surface. Underneath a valley, the effect is opposite. In this case, the equipotential surfaces converge, and therefore the measured potential difference is higher than that of a flat topography. The other reason is the use of flat-surface geometry factors (Eq. 2.28) that are only accurate, when topography is absent. Therefore, the influence of topography on measured apparent resistivity is a superposition of a potential distortion and a geometry effect.

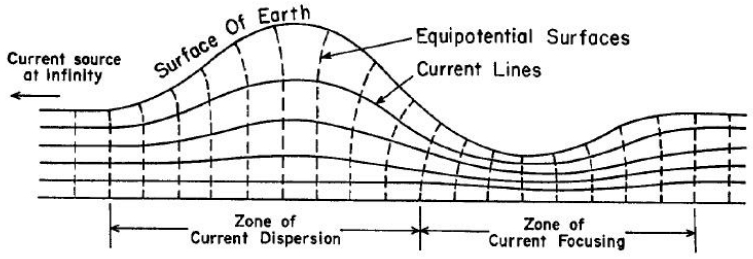

Figure 6.1.: *Effect of topography on the equipotential surfaces and current lines of a distant source electrode (Fox et al., 1980).*

Investigations of topography effects on DC data and on inversion using the FE method were e.g. conducted by Coggon (1971), Tong and Yang (1990) and Fox et al. (1980). However, the surface topography structures investigated in these studies were composed of blocky model cells. Erdoğan et al. (2008) conducted 2D DC modeling studies using FD and FE solutions on structured rectangular and triangular grids.
Unstructured meshes are suited well to compose complex surface topography due

to the flexibility of the individual mesh elements and the possibility of local mesh refinement. Rücker et al. (2006) and Günther et al. (2006) apply unstructured tetrahedral meshes for 3D modeling and inversion of DC data. The corresponding algorithm `BERT` also includes a 2D DC inversion applying unstructured triangular meshes similar to `ResIPIn2D`.

Within this Chapter, the reliability of 2D DC/TDIP forward modeling and inversion with `ResIPIn2D` including topography effects is investigated. First, forward calculations of models with surface topography structures are compared to the conclusions of Fox et al. (1980) and examples of Erdoğan et al. (2008). These examples are restricted to rather simple structures in order to emphasize the influence of topography. Then, two methods of handling topography effects in data interpretation are introduced. The first method is a correction for topography effects whereas the second method includes topography into the inversion mesh. By inversion of synthetic data including topography effects, it is investigated to what extent the original model is reproduced when applying both methods. As a comparison, inversion results of established algorithms are presented. Furthermore, recommendations for the interpretation of field data are given.

6.1. Topography Effects of Hill and Valley Examples

In this section, the visualization of topography effects as pseudo-section results from the forward calculation of a model with surface topography and constant subsurface resistivity $\rho_0 = 100\,\Omega\text{m}$. Consequently, the value of obtained synthetic apparent resistivity $\rho_{a,\text{topo}}$ corresponds directly to the relation between data influenced by topography and the flat earth signature ($\rho_{a,\text{flat}} = 100\,\Omega\text{m}$) in percent. That means, e.g. when the calculated synthetic data influenced by topography is $\rho_{a,\text{topo}} = 150\,\Omega\text{m}$, then the effect of topography is an increase by 50% to a value that is 150% of the data without topography influence.
Note, that the data including topography effects are determined using the flat-earth geometry factors G_{flat} according to

$$G_{\text{flat}} = 2\pi \left[\left(\frac{1}{r_1} - \frac{1}{r_2} \right) - \left(\frac{1}{r_3} - \frac{1}{r_4} \right) \right]^{-1} \tag{6.1}$$

with electrode distances r_i as introduced in Equation (2.27). These geometry factors are usually applied for the determination of field data.

The effect of different slope angles is displayed in terms of the topography factor t according to Rücker et al. (2006) which is based on an idea by Fox et al. (1980):

$$t = \frac{\Delta\Phi_{\text{topo}}}{\Delta\Phi_{\text{flat}}} = \frac{\Delta\Phi_{\text{topo}} G_{\text{flat}}}{\Delta\Phi_{\text{flat}} G_{\text{flat}}} = \frac{\rho_{a,\text{topo}}}{\rho_{a,\text{flat}}} \; . \tag{6.2}$$

Here, $\Delta\Phi_{\text{topo}}$ is the potential difference that is obtained from the model including surface topography and $\Delta\Phi_{\text{flat}}$ is the potential difference corresponding to a model with the same resistivity distribution underneath a flat surface. For a four-electrode

setup, the potential differences $\Delta\Phi$ are defined in concurrence with Equation (2.25) by

$$\Delta\Phi = (\Phi_{11} - \Phi_{21}) - (\Phi_{12} - \Phi_{22}) \tag{6.3}$$

where the subscripts refer to the indices of the involved current and potential electrodes. Referring to the topography factor, a value of $t > 1$ indicates that the presence of topography increases the apparent resistivity by the factor t. A value $t < 1$ means that the apparent resistivity is decreased. A topography factor of $t = 1$ refers to the absence of topography influence.

For all examples discussed in the following, the Dipole-Dipole and the Wenner-Schlumberger configurations were chosen representatively for all configurations because they are symmetric but produce opposite topography effects due to a different sequence of current and potential electrodes.
Note that the range of the color scale according to Wenner or Schlumberger arrays is smaller than that referring to Dipole-Dipole arrays because the topography effect is more prominent for the Dipole-Dipole array and the applied color-scales coincide with the examples by Erdoğan et al. (2008). The topography factors for different slope angles are displayed for fixed n-levels which are extracted from the corresponding pseudo-sections.

Hill Example

First, the influence of a simple hill structure on synthetic apparent resistivity is examined (cf. Figure 6.2). The electrode distance is 1 m and the profile length is 40 m. The applied electrode protocols are listed in Table B.3 and Table B.4. The pseudo-depth of the last Wenner n-level is ca. 6 m and of the last Dipole-Dipole level it is ca. 10 m. The Dipole-Dipole pseudo-section (Figure 6.2-c) shows the signature that was expected according to Fox et al. (1980): Where the base is flat, and none of the four electrodes ascends a flank of the hill ($x < 10$ m and $x > 30$ m) the apparent resistivity is equal to that of a flat homogeneous half-space. If all four electrodes are on the same flank of the hill, the apparent resistivity is decreased. When the dipoles straddle the summit, the apparent resistivity is increased. Where the "corner" at the base of the flank is straddled, it is decreased. The effect on the Wenner configuration (Figure 6.2-b) is different due to the different electrode sequence. In the Dipole-Dipole configuration, both current electrodes are on the same side of the hill, and the potential electrodes are on the opposite side, whereas in the Wenner configuration, both current electrodes are on opposite sides of the hill and the potential electrodes are in a central position also on opposite sides of the hill. That leads to a decrease of apparent resistivity below the summit of the hill and an increase of apparent resistivity below the corners.

The topography factors for different slope angles and a fixed n-level emphasizes this opposite influence of Dipole-Dipole and Wenner. Figure 6.2-d,e shows the topography for the 4-th Wenner n-level and the 6-th Dipole-Dipole n-level. Both levels have a pseudo-depth of ca. 2 m. Also, it is apparent that the topography influence within a fixed n-level is largest directly below the summit, and it overall increases with growing slope angle. The highest peak is reached in the n-level where all four

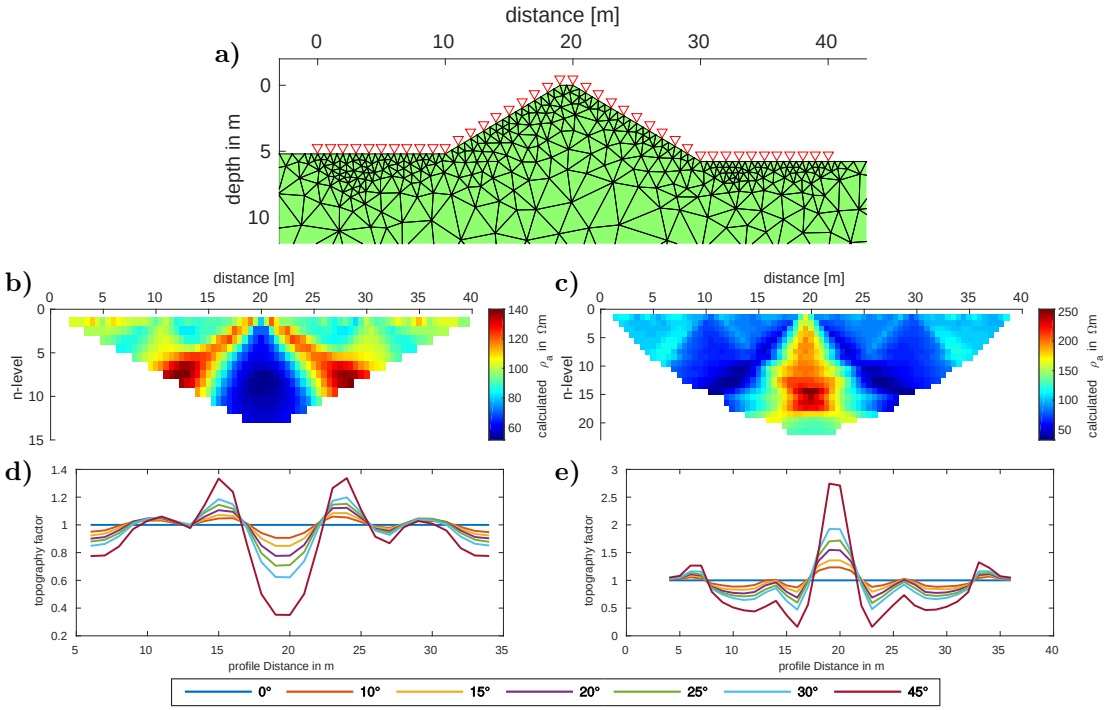

Figure 6.2.: a) *Hill model with 30° slope angle. Constant subsurface resistivity is* $\rho_0 = 100\,\Omega$m. *Electrode locations are indicated by red triangles. Calculated apparent resistivity pseudo-section for a Wenner (**b**) and Dipole-Dipole configuration (**c**). Topography factor t for different slope angles referring to the 4-th n-level of the Wenner configuration (**d**) and the 6-th level of the Dipole-Dipole configuration (**e**). The applied electrode protocols are listed in Table B.3 and Table B.4.*

electrodes of the central data point are in different parts of the hill structure. Even for a slope angle of only 10° the apparent resistivity directly under the summit is significantly increased by a factor of max. 1.4 in the 14-th Dipole-Dipole n-level and decreased by a factor of min. 0.67 in the 5-th Wenner n-level.

Comparison of Hill Example to Other Study

Erdoğan et al. (2008) compared 2D DC forward calculations using different FD and FE grids. Unstructured grids were, however, not part of this study. Their result is that the application of a distorted FE mesh is most accurate amongst the investigated meshes when dealing with topography. In this case, the whole mesh is distorted according to the surface topography as it is shown in Figure 6.3-a. This avoids the implementation of air cells and an increase of additional DOF. Furthermore, it is more accurate than the use of rectangular elements as done in FD meshes. However, the mesh they applied still underlies a certain regularity since it is based on rectangles and parallelograms that are divided into triangles (see Figure 6.3-a). This restricts the implementation of topography to rather simple and regular shapes.

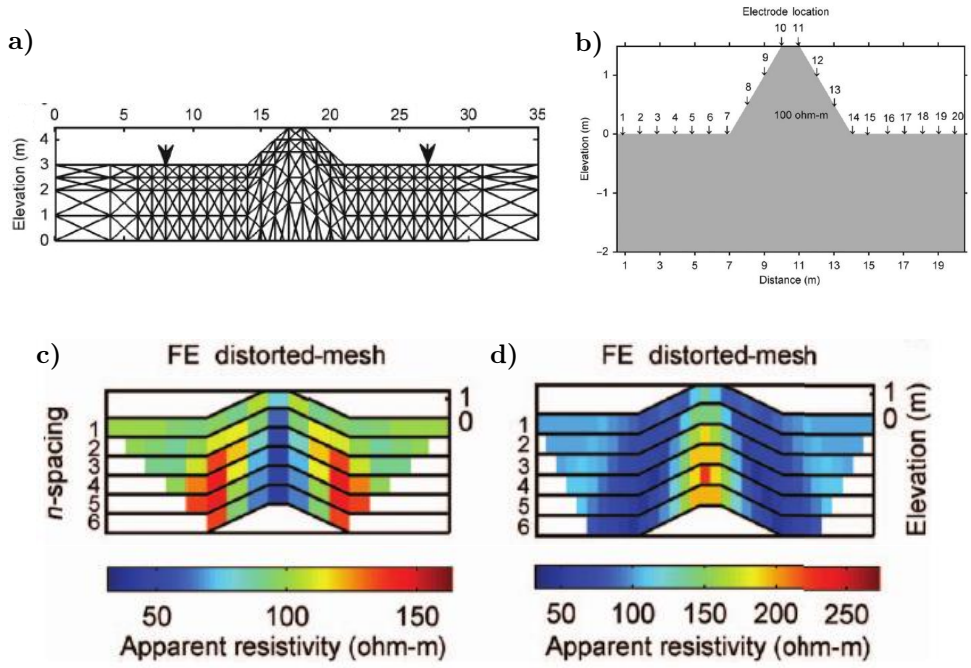

Figure 6.3.: ***a)*** *FE distorted mesh example as it is used by Erdoğan et al. (2008).* ***b)*** *Hill model with 30° slope angle. Surface resistivity is* $\rho_0 = 100\,\Omega\text{m}$*. Electrode locations are indicated by arrows. Synthetic apparent resistivity for a Schlumberger (**c**) and Dipole-Dipole configuration (**d**). All subfigures are extracted from Erdoğan et al. (2008).*

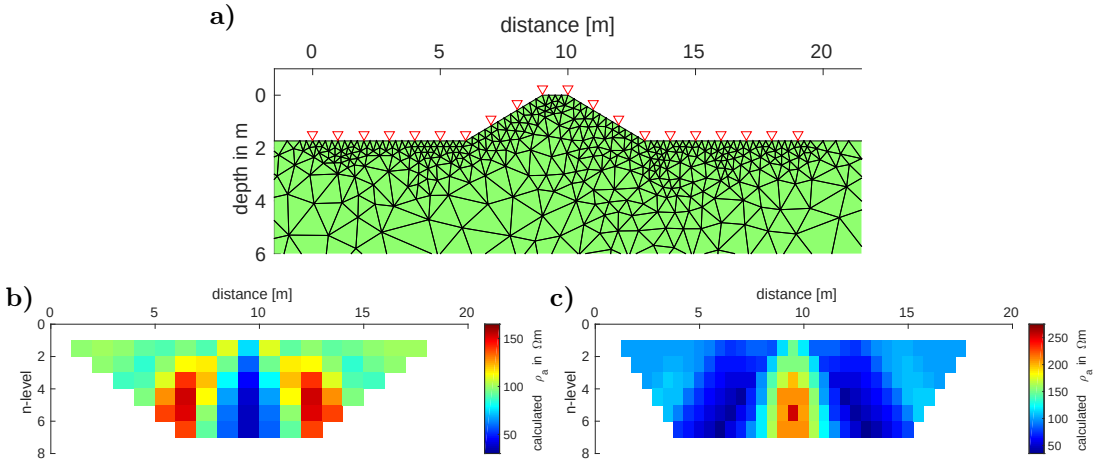

Figure 6.4.: ***a)*** *Hill model with 30° slope angle. Constant subsurface resistivity is* $\rho_0 = 100\,\Omega\text{m}$*. Electrode locations are indicated by red triangles. Synthetic apparent resistivity for a Schlumberger (**b**) and Dipole-Dipole configuration (**c**) obtained by* `ResIPIn2D`*.*

The introduction of additional nodes on the surface to reproduce the transitions between different slope angles more accurate would require the continuation of the vertical line of element boundaries until the end of the mesh.

The unstructured mesh used in `ResIPIn2D` is capable of local refinement to rebuild arbitrarily shaped surface topography without increasing the number of elements in depth. However, for the simple 30° hill model with constant subsurface resistivity of $\rho_0 = 100\,\Omega$m indicated in Figure 6.3-b, the results of forward calculation using the unstructured triangular mesh in Figure 6.4-a should be comparable to the results of Erdoğan et al. (2008) using the FE distorted mesh as in Figure 6.3.

The forward responses obtained by `ResIPIn2D` displayed in Figure 6.4-b,c were calculated for the same electrode setup and protocols as the responses by Erdoğan et al. (2008) that are shown in Figure 6.3-b,c. Also, the color-scale was chosen accordingly. For each of the presented electrode configurations (Schlumberger and Dipole-Dipole), the topography signatures between both algorithms are quite similar in shape and amplitude.

Valley Example

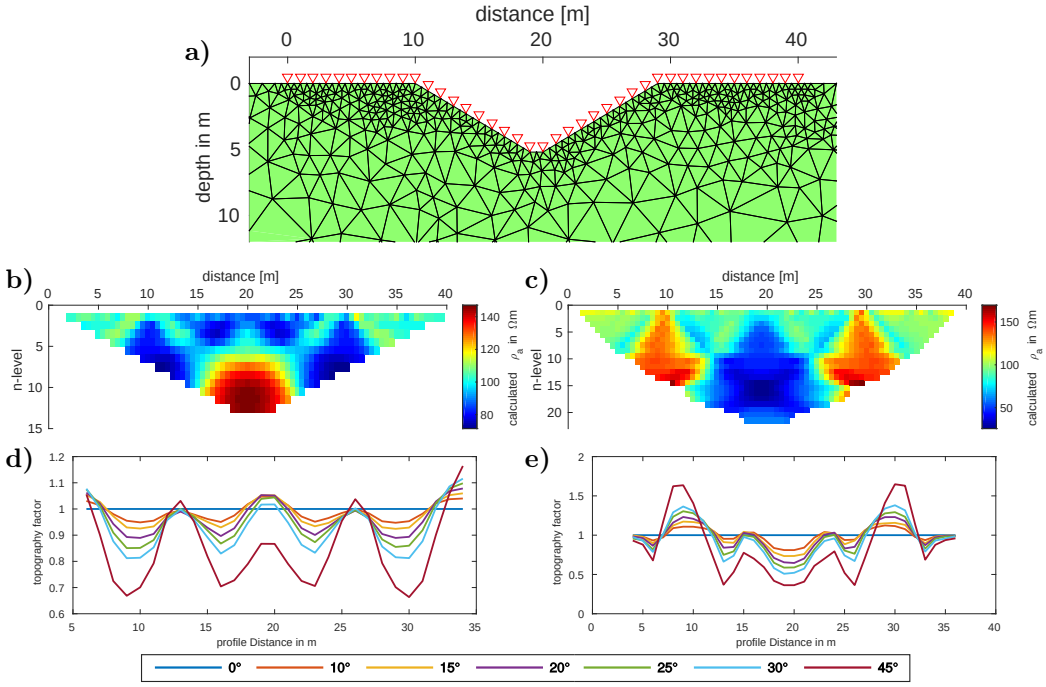

Figure 6.5.: a) *Valley model with 30° slope angle. Constant subsurface resistivity is $\rho_0 = 100\,\Omega$m. Electrode locations are indicated by red triangles. Calculated apparent resistivity pseudo-section for a Wenner (**b**) and Dipole-Dipole configuration (**c**). Topography factor t for different slope angles referring to the 4-th n-level of the Wenner configuration (**d**) and the 6-th n-level of the Dipole-Dipole configuration (**e**). The applied electrode protocols are listed in Table B.3 and Table B.4.*

The forward modeling results corresponding to the valley model shown in Figure 6.5-a with constant subsurface resistivity of $\rho_0 = 100\,\Omega$m and 30° slope angle are displayed in Figure 6.5-b,c. The topography factor t for different slope angles and fixed

n-level is shown in Figure 6.5-d,e. As expected, the presence of the valley has the opposite effect as the hill structure. That means, below the trough of the valley, an apparent resistivity minimum appears for Dipole-Dipole and a maximum for the Wenner configuration. Below the corners, there is an apparent resistivity high for Dipole-Dipole and a low for the Wenner configuration. Referring to the topography factors, the deviations from the homogeneous half-space signature is already significant for a slope angle of 10°, and it is highest if all four electrodes are on different parts of the valley structure.

2D Example with Hill-and-Valley Structure

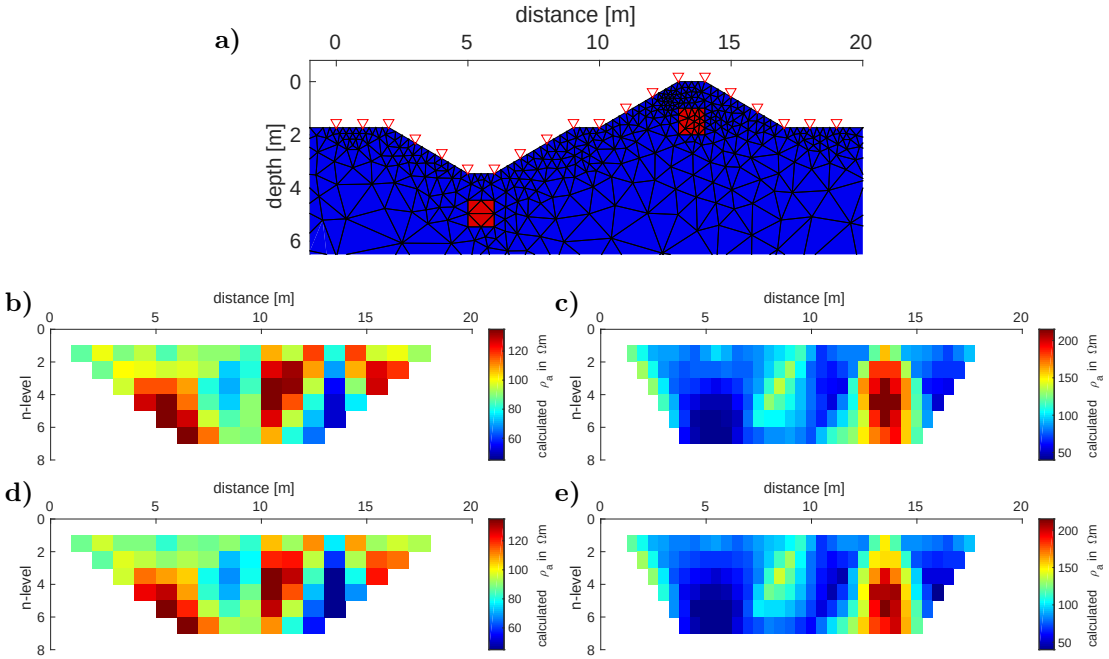

Figure 6.6.: a) *Hill-and-valley model with two high resistive anomalies with* 500 Ωm *(red) buried in* 1 m *depth below the trough and the summit. The surrounding resistivity is* 100 Ωm*. Electrode locations are indicated by red triangles.* ***Left column:*** *Schlumberger,* ***right column:*** *Dipole-Dipole.* ***b,c)*** *Synthetic apparent resistivity for the 2D model in (a) and* ***d,e)*** *for the topography model in (a) with homogeneous resistivity* $\rho_0 = 100\,\Omega$m*.*

A more complex example consisting of a hill-and-valley topography structure including two buried high resistive bodies is shown in Figure 6.6-a. The corresponding synthetic Schlumberger and Dipole-Dipole data calculated with `ResIPIn2D` are displayed in Figure 6.6-b,c. The pseudo-sections are in good agreement with the results of Erdoğan et al. (2008) (cf. Figure 6.7) that were obtained applying an FE distorted mesh.

As a comparison, synthetic data calculated for a model with the same topography but a constant subsurface resistivity of $\rho_0 = 100\,\Omega$m is shown in Figure 6.6-d,e. These synthetic datasets, differ only slightly from the datasets including the high re-

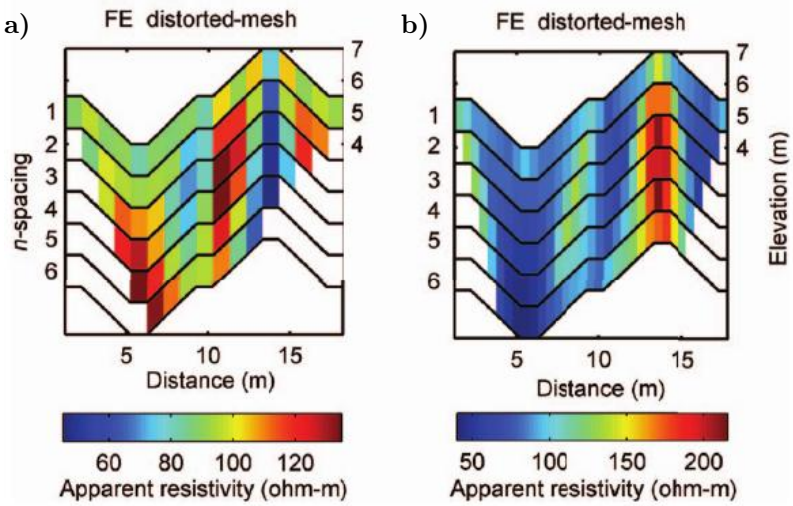

Figure 6.7.: *Forward modeling results using the FE distorted mesh for the hill-and-valley model with resistivity distribution as in Figure 6.6-a extracted from Erdoğan et al. (2008):* ***a)*** *Schlumberger,* ***b)*** *Dipole-Dipole.*

sistive anomalies. Consequently, the signatures of the buried bodies are disguised by the topography influence. In the Schlumberger pseudo-section, this is most prominent at profile distance $x = 14\,\mathrm{m}$ where a resistivity minimum ($\rho_a < 100\,\Omega\mathrm{m}$) occurs. This is apparently caused by the hill structure and not by the high resistive body. For the Dipole-Dipole pseudo-section, this is the case for the anomaly buried beneath the valley (at profile distance $x = 6\,\mathrm{m}$). There is a resistivity low due to the valley effect instead of a resistivity high which is expected for a resistive buried anomaly. This example emphasizes the importance of the incorporation of topography in forward and inverse calculations.

IP Example

IP measurements are based on normalized data. Therefore, the topography effect is mostly removed during the normalization, and thus the effect on the apparent chargeability is subtle. This is visualized by the hill-and-valley example in Figure 6.8: The apparent chargeability pseudo-sections shown in Figure 6.8-b,c were calculated for a constant chargeability of $m_0 = 10\,\mathrm{mV/V}$ underneath the surface topography as in Figure 6.6-a. Without any correction, the synthetic data is very close to the flat-surface signature $m_a = 10\,\mathrm{mV/V}$ corresponding to a homogeneous half-space. Note, that the range of the color-scale is very short.
Introducing highly chargeable bodies ($100\,\mathrm{mV/V}$) buried in 1 m depth beneath the valley and the hill leads to increased chargeability signatures in the pseudo-sections (cf. Figure 6.8-d,e). However, for both electrode configurations, the amplitude of the anomaly below the valley is weaker than that of the anomaly beneath the hill. As a comparison, Figure 6.9-b,c shows the synthetic apparent chargeability data corresponding to the flat-surface model in Figure 6.9-a. In this model, the chargeable bodies are also buried in 1 m depth below the surface. In contrast to

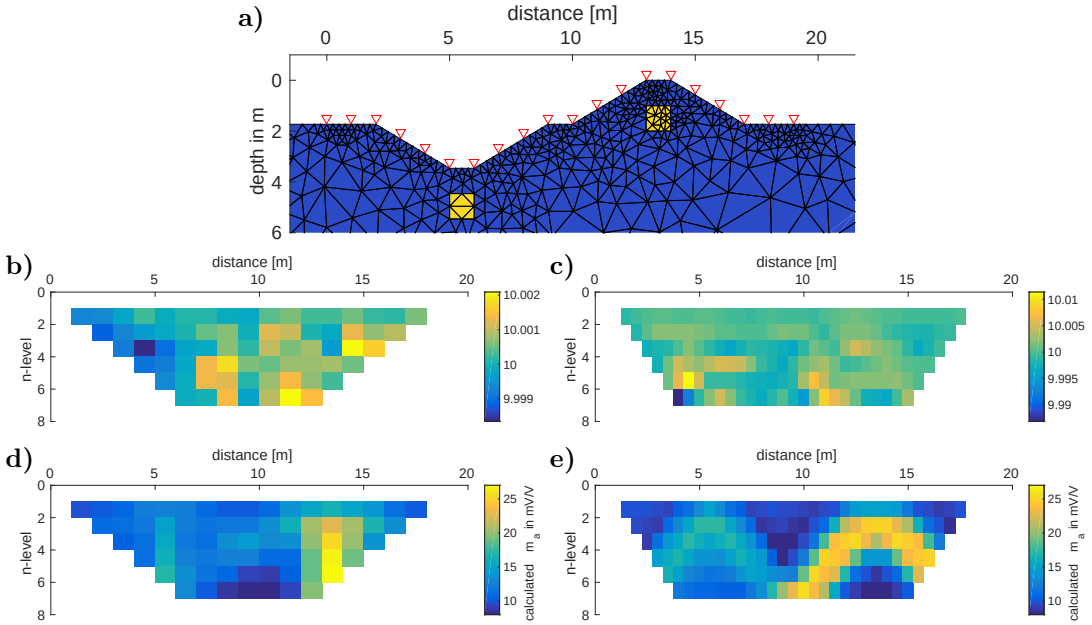

Figure 6.8.: ***a)*** *Hill-and-valley model with two chargeable bodies with* $m_{\text{body}} = 100\,\text{mV/V}$ *(yellow) buried in* $1\,\text{m}$ *depth below the valley and the summit. The surrounding chargeability is* $m_{hs} = 10\,\text{mV/V}$*. The intrinsic resistivity is constant* $\rho_0 = 100\,\Omega\text{m}$*. Electrode locations are indicated by red triangles.* ***b,c)*** *Synthetic apparent chargeability data (in* mV/V*) for a constant chargeability* $m^0 = 10\,\text{mV/V}$ *below the surface topography shown in a). Note the limited color scale.* ***d,e)*** *Synthetic apparent chargeability calculated for the model in a).* ***Left:*** *Schlumberger,* ***right:*** *Dipole-Dipole.*

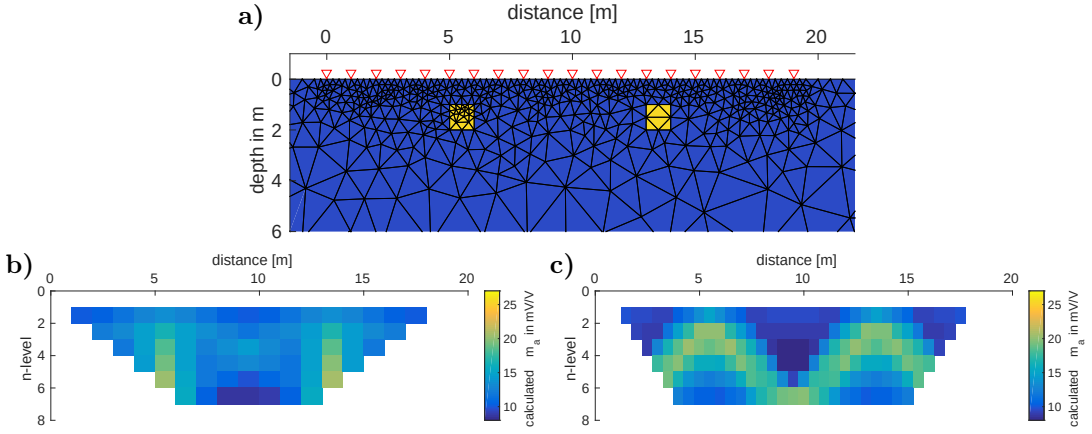

Figure 6.9.: ***a)*** *Flat surface model with two highly chargeable bodies with* $100\,\text{mV/V}$ *buried in* $1\,\text{m}$ *depth. The surrounding chargeability is* $10\,\text{mV/V}$ *and the corresponding intrinsic resistivity is constant* $\rho_0 = 100\,\Omega\text{m}$*. Electrode locations are indicated by red triangles. Synthetic apparent chargeability data calculated for the model in a):* ***b)*** *Schlumberger,* ***c)*** *Dipole-Dipole.*

the topography example, the anomalies induced by both buried bodies have the same amplitude. Therefore, it can be assumed that the normalization removes the topography influence but the location and amplitude of anomalies are distorted. This is because, due to the topography, bodies buried beneath a hill are closer to surface electrodes than bodies buried under a valley.

6.2. Handling Topography Effects in Interpretation

The forward modeling examples presented in Chapter 6.1 confirmed the assumptions made by Fox et al. (1980) and are in agreement with modeling results of Erdoğan et al. (2008): The presence of distinctive surface topography has a strong influence on DC data. The effect is significant for slope angles $> 10°$ and is most prominent when all electrodes of a configuration are located on different parts of a topography structure. Therefore, the consideration of topography effects is crucial in forward and inverse modeling. The examples also suggest that the influence on Dipole-Dipole-type configurations is stronger than the effect on Wenner-Schlumberger arrays. In this chapter, two approaches of handling topography effects are presented, and recommendations for the interpretation of field data are given.

6.2.1. Topography Correction

The correction method according to Fox et al. (1980) aims to determine the unknown topography geometry factors G_{topo}. The corrected data $\rho^c_{a,\text{topo}} = \Delta\Phi_{\text{topo}} G_{\text{topo}}$ are then theoretically completely liberated from topography effects and can be interpreted by inversion using a flat surface mesh. Demanding the equality $\rho^c_{a,\text{topo}} = \rho_{a,\text{flat}}$ leads directly to

$$\Delta\Phi_{\text{topo}} G_{\text{topo}} = \Delta\Phi_{\text{flat}} G_{\text{flat}} \ . \tag{6.4}$$

After inserting the topography factor (Eq. 6.2) in form $t = \Delta\Phi_{\text{topo}}/\Delta\Phi_{\text{flat}}$, the topography geometry factor can be determined by

$$G_{\text{topo}} = \frac{G_{\text{flat}}}{t} \ . \tag{6.5}$$

The geometry factor according to Equation (6.5) is only applicable in forward modeling because the subsurface resistivity distribution needs to be known for the determination of $\Delta\Phi_{\text{flat}}$. In field surveys, the subsurface resistivity is the desired unknown. Therefore, the topography factor for field data is determined from the division of forward calculation of a constant subsurface resistivity of e.g., $\rho^{100} = 100\,\Omega\text{m}$, including the known topography ($\rho^{100}_{a,\text{topo}}$) by the forward response for a flat surface $\rho^{100}_{a,\text{flat}}$:

$$t = \frac{\rho^{100}_{a,\text{topo}}}{\rho^{100}_{a,\text{flat}}} = \rho^{1}_{a,\text{topo}} \ . \tag{6.6}$$

This corresponds to $\rho^1_{a,\text{topo}}$ being the forward response of constant resistivity $\rho^1 = 1\,\Omega\text{m}$ including topography. Consequently, the topography corrected data $\rho^c_{a,\text{topo}}$ can

be directly derived from the measured data $\rho_{a,\text{topo}}$ by

$$\rho^c_{a,\text{topo}} = \frac{\rho_{a,\text{topo}}}{\rho^1_{a,\text{topo}}} \ . \tag{6.7}$$

This method helps to reveal those anomalies that are caused by subsurface resistivity structures but are disguised by topography effects. There are, however, some drawbacks as pointed out by Tong and Yang (1990) such as the alteration of near surface anomalies. This effect is investigated in the next example presented in Figure 6.10.

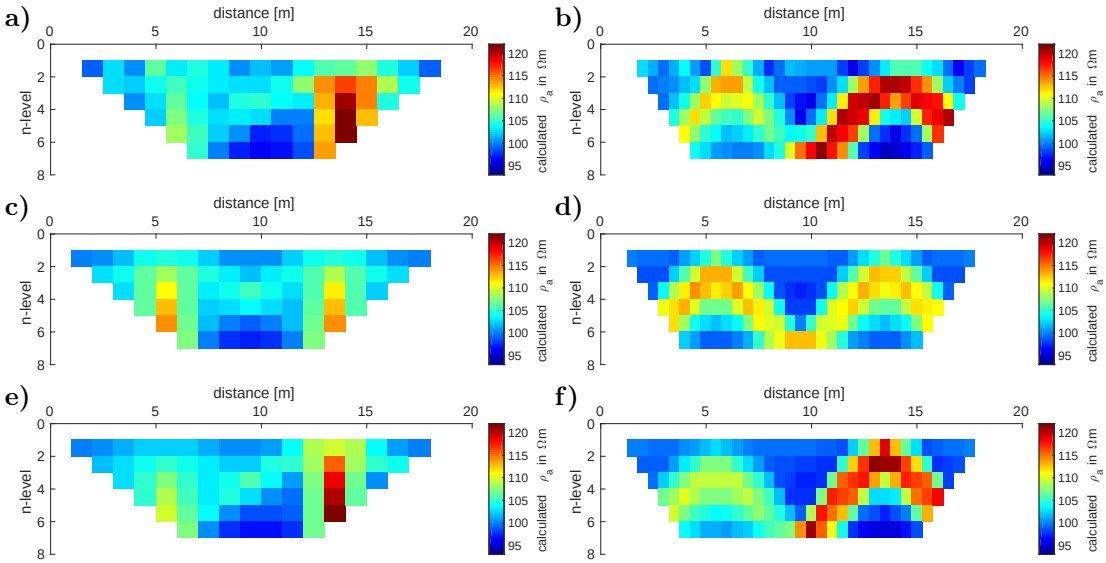

Figure 6.10.: ***a,b)*** *Topography corrected synthetic data* $\rho^c_{a,\text{topo}}$ *corresponding to the model in Figure 6.6-a;* ***c,d)*** *Forward responses of the model in Figure 6.11-a;* ***e,f)*** *Forward responses of the model in Figure 6.11-b;* ***left:*** *Schlumberger,* ***right:*** *Dipole-Dipole.*

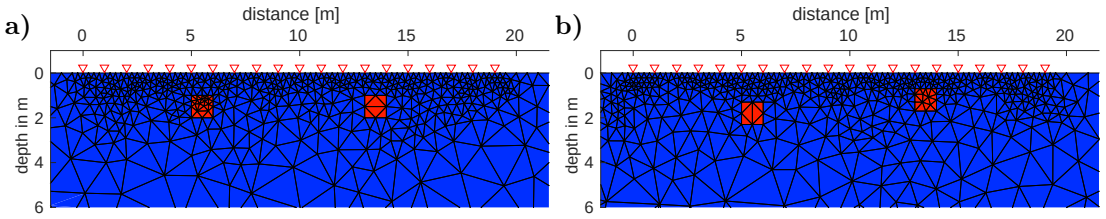

Figure 6.11.: *Flat surface model with 2 buried bodies with resistivity* ρ_{body}=500 Ωm *within a half-space with* ρ_{hs}=100 Ωm. ***a)*** *Upper boundaries of both bodies lies in* 1 m *depth.* ***b)*** *The upper boundary of the left body is in* 1.2 m *depth and that of the right body in* 0.8 m *depth. Electrode locations are indicated by red triangles.*

The pseudo-sections in Figure 6.10-a,b represent the data shown in Figure 6.6-b,c after topography correction according to (6.7). Similar to the IP example shown in Figure 6.8, the amplitude of the right anomaly, which corresponds to the body

buried beneath the hill, is stronger than the anomaly corresponding to the body buried below the valley. This is not in good agreement with the forward responses of the flat earth model with bodies buried in 1 m depth (Figure 6.11-a) that are shown in Figure 6.10c,d. As expected, the high resistive anomalies in the flat-earth responses (corresponding to the left and right block) are of the same amplitude. As a comparison, Figure 6.10-e,f present the forward responses according to the flat earth model shown in Figure 6.11-b. In this model, the left body is buried in an increased depth of 1.2 m and the right body in a decreased depth of 0.8 m. These responses are in better agreement with the topography corrected data in Figure 6.10-a,b. This shows that the alteration of near surface anomalies is connected to differences in distances between buried body and surface electrodes. For a hill structure, the electrodes enclose the body, and therefore, it appears to be closer to the surface. In the case of a valley structure, the electrodes bend away from the body, and thus, it seems to be at greater depths.

6.2.2. Incorporation of Topography into Inversion Mesh

The incorporation of surface topography directly into the inversion mesh was first introduced by Tong and Yang (1990) who developed a 2D DC inversion algorithm using the finite element method. Like this, no further topography corrections are needed prior to the inversion of field data. Furthermore, original resistivity anomalies are not altered as it is the case for the correction method explained in the preceding section. This approach is especially suitable for the use of an unstructured mesh since it provides flexibility and local refinement. There is, however, a disadvantage compared to the topography correction method: Since the analytical solution of a homogeneous half-space in the (x,k,z)-space is not valid below surface topography, the singularity removal technique is not applicable (Rücker et al., 2006). Therefore, inaccuracies in the first n-level of forward responses might occur.

6.2.3. Comments and Recommendations

From the investigations of the preceding sections, several recommendations are derived for the interpretation of field data that are subject to topography effects:

For field surveys in areas with distinctive topography, it is crucial to either measure the topography and location of electrodes as precisely as possible or to include topography data of the area to be able to reconstruct the surface topography in the mesh accurately.

It is preferable to interpret measured potential differences $\Delta\Phi$ instead of apparent resistivity values ρ_a. Like this, it is given that the same geometry factors G_{flat} are used for calculation of measured apparent resistivity data (from measured $\Delta\Phi$) and for the calculation of forward responses. This is important because, in the inversion procedure, the initial model is altered until the model response fits the measured data. The corresponding best-fit model is only reliable if the measured and calculated apparent resistivity data are determined by the same geometry factor. This aspect is illustrated by the following example.

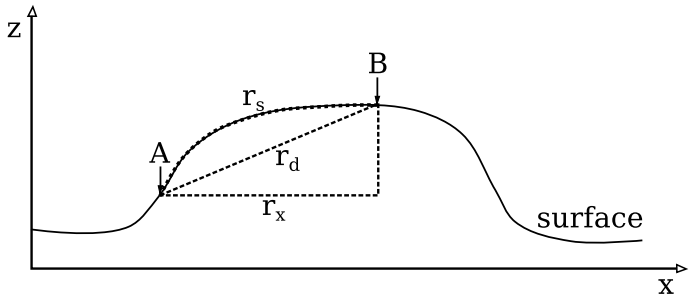

Figure 6.12.: *Sketch of two electrodes A and B at the surface of a topography structure: r_s refers to the electrode distance along the surface, r_d is the shortest distance between A and B and r_x is the x-component of the electrode distance.*

The geometry factors according to (6.1) rely on distances r between electrodes. As depicted in Figure 6.12, the electrode distances can be either determined along the surface (r_s), as direct distance r_d or by the x-component of the distance r_x. Since these distances differ from each other, also the corresponding geometry factors differ. Note that all synthetic datasets presented in Chapter 6.1 were calculated using distances referring to r_x.
The potential differences $\Delta\Phi_{\text{topo}}$ according to the first 8 n-levels of the Dipole-Dipole pseudo-section calculated for the hill model with constant subsurface resistivity of $\rho_0 = 100\,\Omega$m in Figure 6.2 are displayed in Figure 6.13. The apparent resistivity pseudo-sections shown below were determined by geometry factors based on electrode distances r_x (Figure 6.13-b), r_s (Figure 6.13-c) and r_d (Figure 6.13-d), respectively. Most prominent is the high resistive anomaly in the center of the profile which has a different amplitude dependent on the choice of electrode distance. For instance, the anomaly based on r_x has a maximum amplitude of ca. $250\,\Omega$m while the maximum amplitude based on r_s is only ca. $200\,\Omega$m. If, e.g., field data is determined based on r_d and the inversion algorithm uses distances r_x, high resistive structures might occur beneath a hill structure in the inversion result that are only due to topography effects and not produced by the subsurface resistivity distribution.

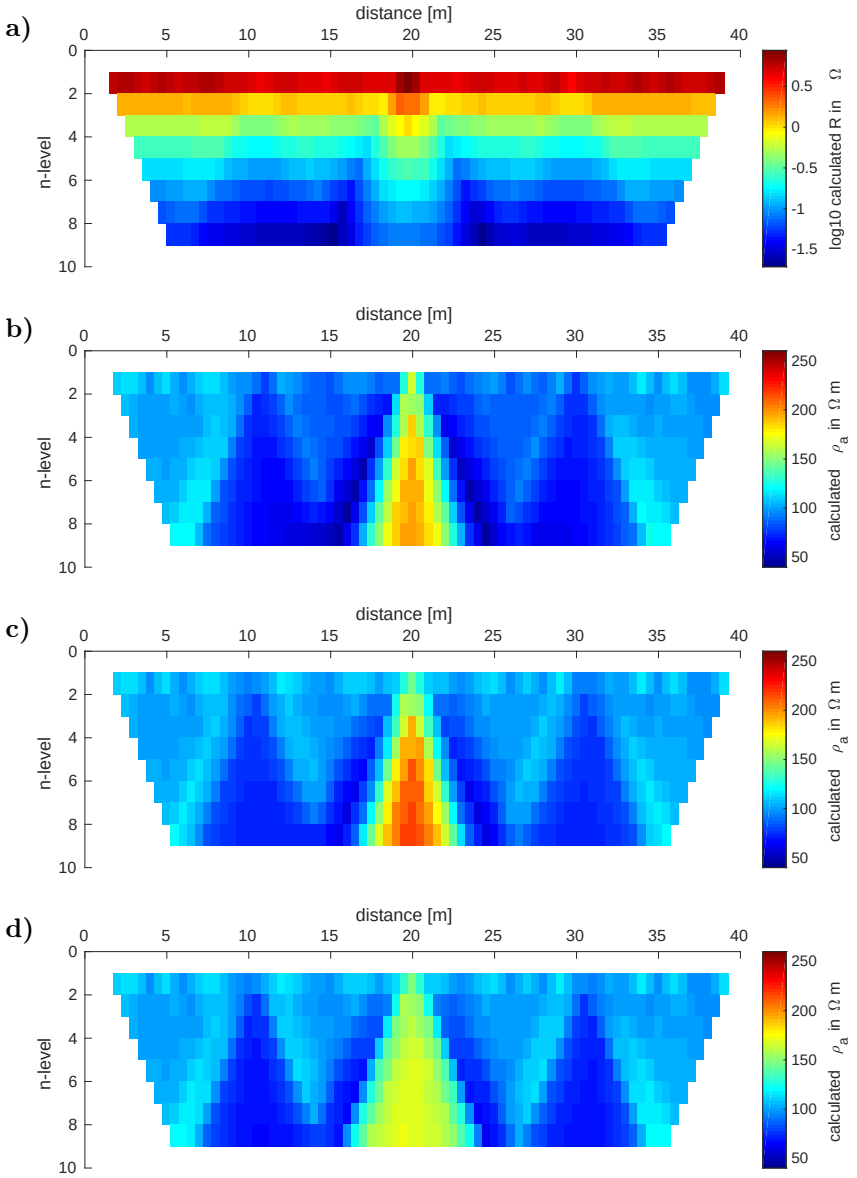

Figure 6.13.: *Dipole-Dipole forward calculation of the 30° hill model (cf. Figure 6.2-a) with constant subsurface resistivity of* $\rho_0 = 100\,\Omega\mathrm{m}$ *using different geometry factors. Pseudo-sections shown as* ***a)*** *potential difference* $\Delta\Phi$, ***b)*** *apparent resistivity using electrode distances* r_x, ***c)*** *using surface distances* r_s *and* ***d)*** *using linear distances* r_d.

6.3. Inversion of Synthetic Data Under Consideration of Topography Effects

In Chapter 6.2, different strategies of handling topography in forward calculation and inversion were introduced. In this chapter, the capability of reproducing original 2D resistivity structures buried beneath surface topography is tested by inversion of synthetic data using `ResIPIn2D`. The favored procedure is the inclusion of surface topography in the inversion mesh following Tong and Yang (1990). The results are compared to the inversion of data that is corrected for topography effects according to Fox et al. (1980). Furthermore, results of inversions using flat-surface meshes are presented for data with and without topography influence.

As a preparation of field data analysis, all datasets shown in the following examples are calculated using the same electrode setup and protocol that was applied during the field survey discussed in Chapter 7. The profile length is 300 m, the smallest electrode distance is $a = 10$ m and the Pole-Dipole setup listed in Table B.6 is used. When topography is present, electrode distances are derived from the surface distance r_s. Note that the lateral location of each data point is displayed in the center of the receiving dipole in the Pole-Dipole pseudo-sections. Therefore, the pseudo-sections are asymmetric, and the resistivity anomalies appear tilted. In literature, two conventions of Pole-Dipole pseudo-sections are found: One that locates the data-point in the center between the near current electrode and the second receiver electrode and one that places the data-point in the center of the receiver dipole. Here, the latter convention was chosen due to sensitivity that is also asymmetric. All inversions are carried out using smoothness matrix C_b, a stepwise cooling of the initial regularization parameter $\lambda_{ini} = 80$, and a two-point parabola line-search for the optimum step-length τ is done in every iteration.

6.3.1. Circular Body Buried Beneath a Hill Structure

Table 6.1.: *Details of the buried body with circular cross-section.*

ρ_{body}	ρ_{hs}	Diameter	Depth
10 Ωm	100 Ωm	40 m	20 m

In the first example, a circular shaped body as specified in Table 6.1 is buried below a hill structure with 20° slope angle. The depth is specified as the distance between the upper boundary of the body and the surface. The depth of investigation according to the rule of thumb for the given electrode setup is $DOI_t = 53$ m. However, the simple rule does not take into account that the electrode distances and the distances to anomalies are altered due to the topography. Therefore, it is not as straightforward to correlate the DOI_t with an isoline of the normalized coverage as it has been for the examples with flat surface topography shown in the preceding chapter. Anyway, all isolines used as approximate DOI_{app} corresponded to a value of ca. -2.15. Therefore, the isoline corresponding to a normalized coverage of $\text{cov}_t = -2.15$ is used in the

following examples to derive the DOI_{app}. This is surely only a rough estimation, but it serves as an indication for sensitivity differences between certain model domains.

Low Resistive Anomaly

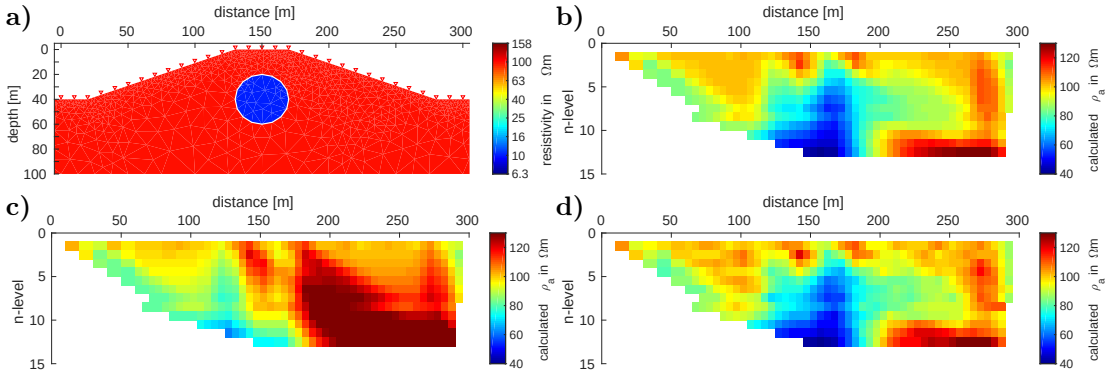

Figure 6.14.: a) *Original resistivity model including a body with circular cross section (cf. Table 6.1) buried beneath a surface topography structure with* 20° *slope angle. Electrode locations are indicated by red triangles.* ***b)*** *Synthetic Pole-Dipole data calculated from the model in a).* ***c)*** *Synthetic Pole-Dipole data calculated for a constant resistivity of* $\rho_0 = 100\,\Omega$m *below the surface topography shown in a).* ***d)*** *Synthetic data shown in b) including 3% noise.*

In the first example, the buried circular body has lower resistivity compared to the surrounding. Details of the body are listed in Table 6.1. The original model is shown in Figure 6.14-a and the synthetic data resulting from forward calculation is shown as apparent resistivity pseudo-section in Figure 6.14-b. The same data including 3% noise is displayed in Figure 6.14-d. A low resistive anomaly is visible in the center of the pseudo-section which is induced by the presence of the low resistive body. To estimate the topography effect that superposes the pure resistivity anomaly, the synthetic data for the same topography structure but with a constant resistivity of 100 Ωm is shown in Figure 6.14-c. There is a clear alteration due to topography effects which leads to an increase of apparent resistivity of up to 20% in the right part of the pseudo-section and a decrease of up to 40% in the left part.

First, the results of inversion including the surface topography in the inversion mesh are discussed. The result of the original synthetic data without noise (cf. Figure 6.14-b) are shown in Figure 6.15-a. In this example, the mesh used for the inversion procedure is the same that was used for the forward calculation of the original synthetic data. That means that not only the surface topography is the same. Also, the arrangement of the triangular mesh elements is the same, including the exact outline of the circular body which is highlighted by a white line. As it was the case for the flat surface inversion examples shown in Chapter 5, the resistivity of the anomaly smears out towards deeper depths, and some high resistive artifacts occur above the buried body and in the lower corners of the shown excerpt of the inversion mesh. But certainly, the sensitivity is low in the corners. The

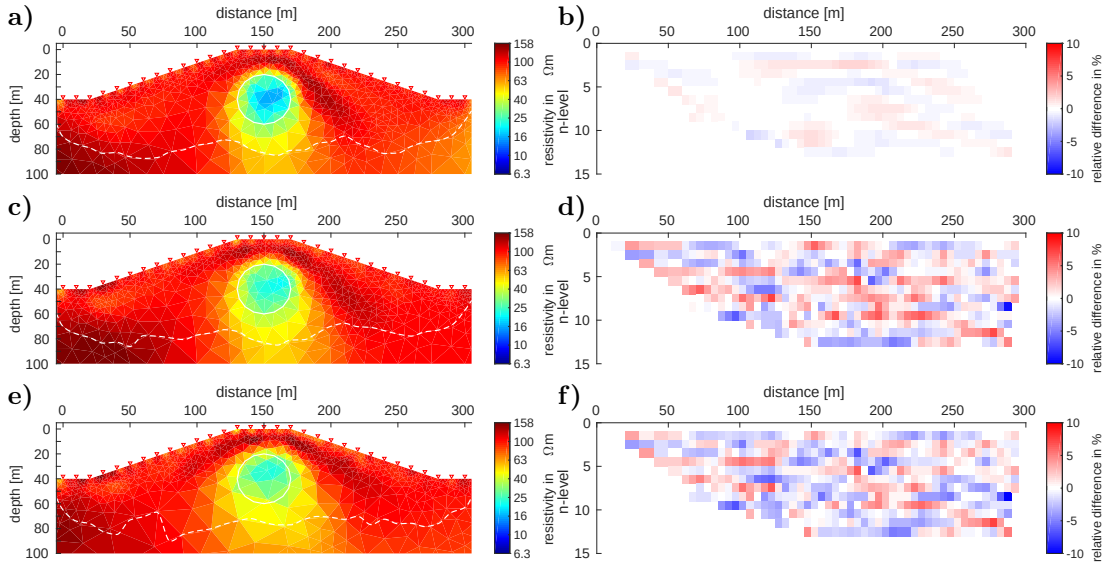

Figure 6.15.: *Final inversion models using a mesh including surface topography in the inversion:* ***a)*** *for the original data without noise (cf. Figure 6.14-b), the applied mesh includes the original boundaries of the buried body, χ=0.18, RMS=0.12%;* ***c)*** *for the original data including 3% noise (cf. Figure 6.14-d) using the same mesh as in a), χ=0.93 ;* ***e)*** *for the original data including 3% noise using an unbiased unstructured mesh, χ=0.93. Electrode locations are indicated by red triangles and the DOI_{app} by a dashed white line, respectively.* ***b,d,f)*** *Relative difference between the model response of the corresponding model on the left and the original data. The initial resistivity is* 80 Ωm.

resistivity of the body is slightly overestimated, but generally, the circular body is reproduced adequately. The data-fit between the original data and the model response is very accurate which is supported by the corresponding relative difference plot in Figure 6.15-b. However, this example represents a perfect case when the data is noise-free, and the exact outline of the original resistivity model is part of the inversion mesh.
As a comparison, inversion results of the original data including 3% noise (cf. Figure 6.14-d) are shown in Figure 6.15-c for the same mesh and in Figure 6.15-e for an unbiased mesh. The corresponding relative difference between the model response and the original data is shown in Figure 6.15-d,f, respectively. According to the relative difference plots, the data-fit is similar for both meshes. As expected, the overall relative difference is higher in the latter cases than that of the noise-free data because the data error is 3% and the convergence criterion of $\chi \approx 1$ is achieved. In contrast to the resistivity model in Figure 6.15-a, both models overestimate the resistivity of the body. The shape of the body in Figure 6.15-c is reproduced similarly to the result in Figure 6.15-a. Due to larger triangular elements, the shape is not as well reproduced in Figure 6.15-e, but the location and size of the body is reckoned.

Now, we compare these findings with inversion results using an unbiased flat surface inversion mesh. Figure 6.16-a shows the resistivity model resulting from inversion of the original data including topography effects and 3% noise (cf. Figure 6.14-d).

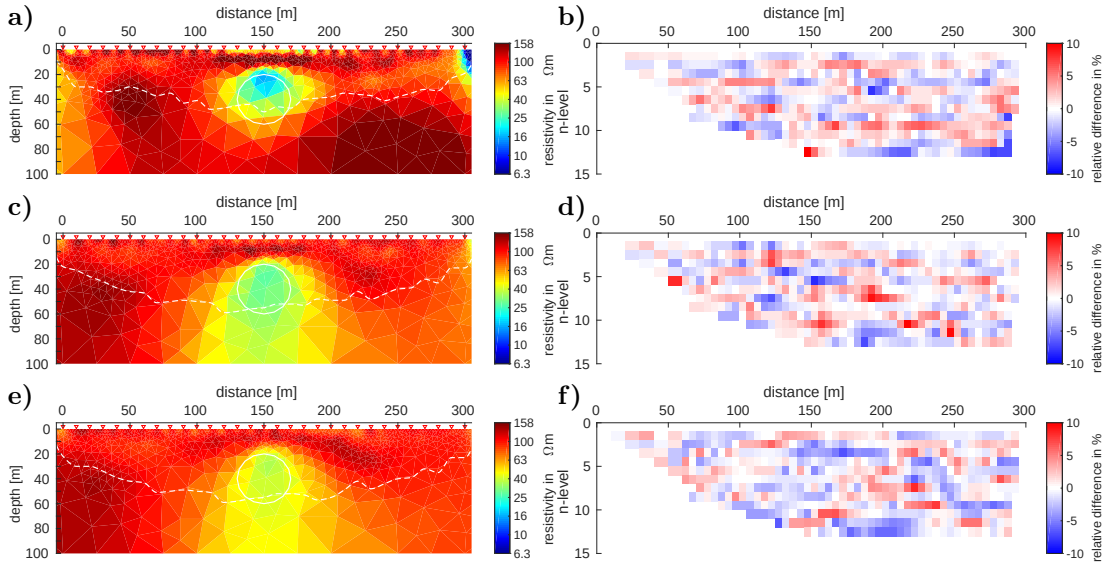

Figure 6.16.: *Final inversion models using a mesh with flat surface in the inversion:* ***a)*** *for the original data including 3% noise (cf. Figure 6.14-d), χ=0.97;* ***c)*** *for the topography corrected data (cf. Figure 6.17-b) including 3% noise, χ=0.98;* ***e)*** *for the original data calculated for the model without surface topography (cf. Figure 6.17-a) including 3% noise, χ=0.97. Electrode locations are indicated by red triangles and the DOI_{app} by a dashed white line, respectively.* ***b,d,f)*** *Relative difference between the model response of the corresponding model on the left and the original data. The initial resistivity is $\rho^0 = 80\,\Omega$m.*

Generally, the location and resistivity trend of the buried body is reproduced, but the shape seems stretched in the lateral direction and slightly shifted towards the surface. Furthermore, several high resistive areas occur in the surrounding of the body. These are not only artifacts as seen in the results discussed before. Apparently, they are partly induced by topography effects such as the area to the bottom right of the body which can be correlated to the high resistive anomaly in Figure 6.14-c.

Removing this effect according to the method after Fox et al. (1980) leads to the pseudo-section in Figure 6.17-b. The signature looks similar to the apparent resistivity calculated for the same body buried beneath a flat surface topography which is shown in Figure 6.17-a. Anyway, both pseudo-sections differ in amplitude and width of the anomaly which is seen in the relative difference plot in Figure 6.17-c. Therefore, also the inversion results are expected to differ from each other.

The resistivity model in Figure 6.16-c is the result of inversion of the data corrected for topography effects according to Fox et al. (1980) as shown in Figure 6.17-b including 3% noise. The shape of the circular body smears out more towards greater depths than in Figure 6.16-a. But in comparison to this result, the high resistive structures to the left and lower right of the body that are due to topography effects have disappeared. However, similar artifacts occur above the body and at the beginning of the profile as it was the case in Figure 6.15. The inversion result of the original data calculated without surface topography (cf. Figure 6.17-a) including

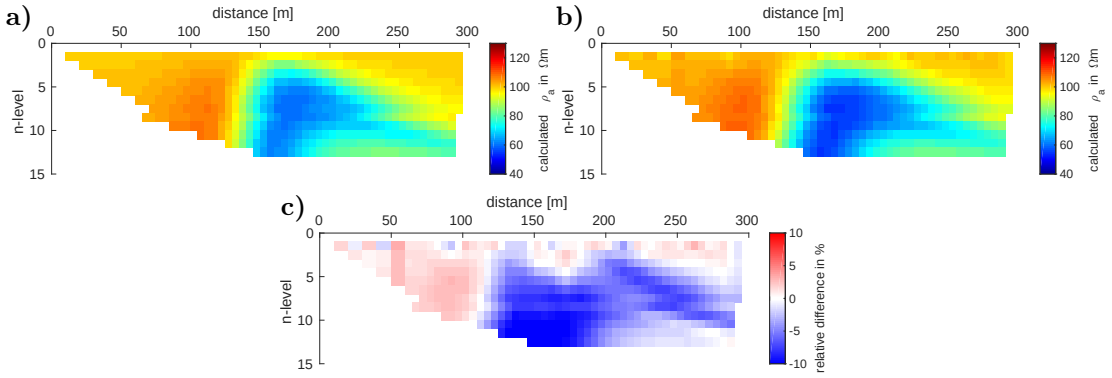

Figure 6.17.: ***a)*** *Synthetic Pole-Dipole data calculated for the body specified in Table 6.1 buried beneath a flat surface.* ***b)*** *Synthetic data shown in Figure 6.14-b corrected for the topography effect by division with the signature of a homogeneous resistivity distribution (cf. Figure 6.14-c) according to Fox et al. (1980).* ***c)*** *Relative difference between the data shown in a) and b).*

3% noise is displayed in Figure 6.16-e. As expected from the relative difference of the original data (Figure 6.17-c) the resistivity model differs from the model in Figure 6.16-c. The low resistivity of the circular body is more confined to the original outline. However, the original resistivity of the body is a little less precise. The fact that the body buried below the flat surface is not as well reproduced as the body buried below topography might be because it is closer to the surface electrodes due to the hill structure and thus the sensitivity is larger.
According to the relative difference plots shown in Figure 6.15 and Figure 6.16 the data-fit is similar for all inversions except the inversion of the noise-free data. Consequently, the differences between resistivity models are only influenced by original data and sensitivity and not by a varying data-fit.

High Resistive Anomaly

In the next example, the resistivity of the circular body is $\rho_{\text{body}} = 100\,\Omega\text{m}$ and that of the surrounding is $\rho_{hs} = 10\,\Omega\text{m}$ as shown in Figure 6.18-a. The corresponding calculated synthetic Pole-Dipole data is shown in Figure 6.18-b. The synthetic data calculated for the same body buried beneath a flat surface is displayed in Figure 6.18-c. Apparently, the anomaly that is induced by the buried body is weaker than the topography effect, which is supported by the relative difference plot in Figure 6.18-d.

The resistivity inversion result of the original data including topography effects and 3% noise using an inversion mesh including topography is displayed in Figure 6.19-a and the corresponding relative difference between original data and model response in Figure 6.19-b. The shape of the body is noticeable, but the resistivity is clearly underestimated. According to χ and the relative difference plot, the data-fit is comparable to the results corresponding to the example with the low resistive buried body. That the resistivity is not reproduced as well as in the preceding example is due to lower sensitivity regarding high resistivity together with smoothness regular-

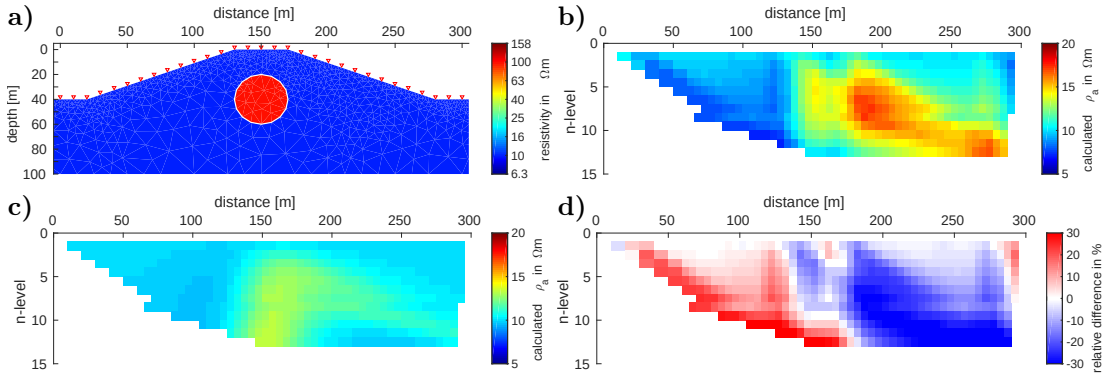

Figure 6.18.: ***a)*** *Original resistivity model buried beneath a surface topography structure with 20° slope angle. Electrode locations are indicated by red triangles.* ***b)*** *Synthetic Pole-Dipole apparent resistivity data calculated for the model in a).* ***c)*** *Synthetic Pole-Dipole data calculated for the same body buried beneath a flat surface.* ***d)*** *Relative difference between the data shown in b) and c).*

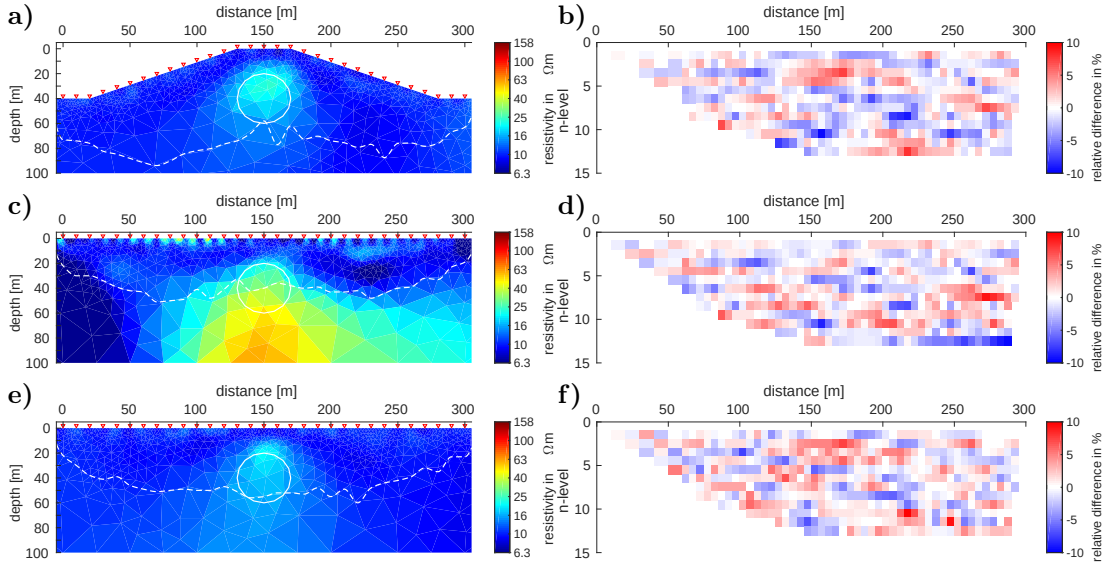

Figure 6.19.: *Final resistivity inversion models:* ***a)*** *for the original data calculated with surface topography (cf. Figure 6.18-b) with 3% noise, the inversion mesh includes topography, χ=0.99;* ***c)*** *for the same data as in a), using a flat-surface inversion mesh, χ=0.99;* ***e)*** *for the original data calculated for the model without surface topography (cf. Figure 6.18-c) with 3% noise, χ=0.99.* ***b,d,e)*** *Relative difference between the model response of the corresponding model on the left and the original data. Red triangles indicate electrode locations, the dashed white line the DOI_{app}, respectively. The initial resistivity model is $\rho^0 = 8\,\Omega$m.*

ization in combination with an unbiased mesh with rather large elements.

However, this inversion result is more reasonable than the resistivity model resulting from inversion of the same data applying a flat surface inversion mesh (cf. Figure 6.19-c). Here, the shape of the circular body is not recognizable because it is

superposed by another high resistive structure located in the lower center of the profile below the DOI_{app}. This is most certainly produced by the topography effect which causes a high resistive anomaly visible in Figure 6.18-b. Again, the relative difference between original data and model response is of similar amplitude as that corresponding to the inversion with a topography mesh.

As a comparison, the inversion result of the flat-surface data (cf. Figure 6.18-c) including 3% noise using a flat-surface inversion mesh is shown in Figure 6.19-e and the corresponding relative difference plot in Figure 6.19-f. Here, the original resistivity of the buried body is reproduced less than in the topography example (cf. Figure 6.19-a), but the high resistive artifact that appears in Figure 6.19-b is absent.

Highly Chargeable Anomaly

Table 6.2.: *Details of the buried body with circular cross-section with IP effect.*

m_{body}	m_{hs}	ρ_{body}	ρ_{hs}	Diameter	Depth
100 mV/V	10 mV/V	100 Ωm	100 Ωm	40 m	20 m

The IP hill example consists of the circular buried body described in Table 6.2. The original model including topography is shown in Figure 6.20-a. As discussed in Chapter 6.1, the synthetic apparent chargeability data (cf. Figure 6.20-b) resulting from forward calculation of the model including topography is not superposed by topography effects as it is the case for resistivity. The amplitude and shape of near surface anomalies are, however, altered in comparison to flat-surface data: In comparison to the synthetic data calculated for the same body buried beneath a flat surface (displayed in Figure 6.20-c) the highly chargeable anomaly has a similar shape but is wider with a higher amplitude. These differences are visualized by the relative difference plot in Figure 6.20-d.

The chargeability inversion results are presented in Figure 6.21. The chargeability model in Figure 6.21-a is the result corresponding to topography data (cf. Figure 6.20-b) including noise obtained using a topography inversion mesh. The inversion result of the same data obtained by inversion using a flat-surface mesh is shown in Figure 6.21-c. According to the corresponding χ-values and the relative difference plots in Figure 6.21-b,d, the data-fit of both results is similar. In both inversion models, the shape and chargeability of the original body are generally reproduced but smaller. However, in case of the flat inversion mesh, the high chargeability of the body smears out more towards deeper depth.
As comparison, Figure 6.21-e shows the inversion result of the flat-surface data (cf. Figure 6.20-c) using a flat inversion mesh. The chargeability of the reproduced body is smaller than that resulting from the topography data. This is in agreement with the amplitude of chargeability anomalies in the original data, which is smaller for the flat-surface data than in the topography data.

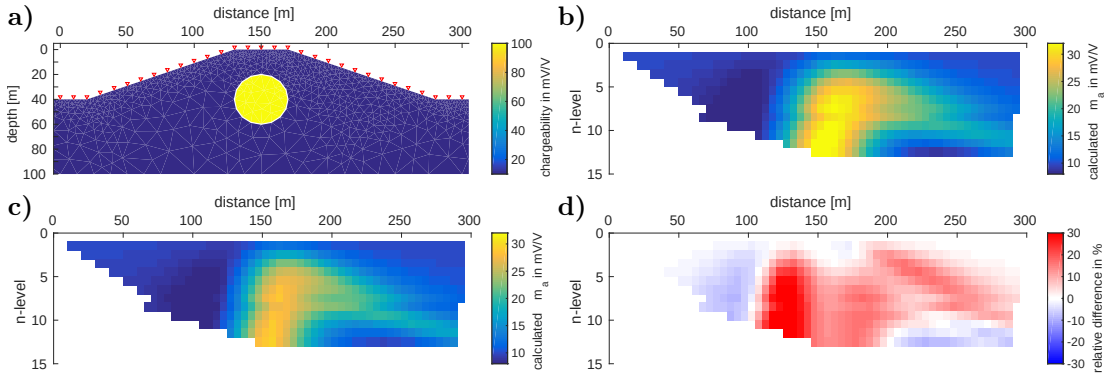

Figure 6.20.: ***a)*** *Original chargeability model including a body with circular cross section (cf. Table 6.2) buried beneath a surface topography structure with* $20°$ *slope angle. Electrode locations are indicated by red triangles.* ***b)*** *Synthetic Pole-Dipole apparent chargeability data calculated from the model in a).* ***c)*** *Synthetic Pole-Dipole apparent chargeability data calculated for the body specified in Table 6.2 buried beneath a flat surface.* ***d)*** *Relative difference between the data shown in b) and c).*

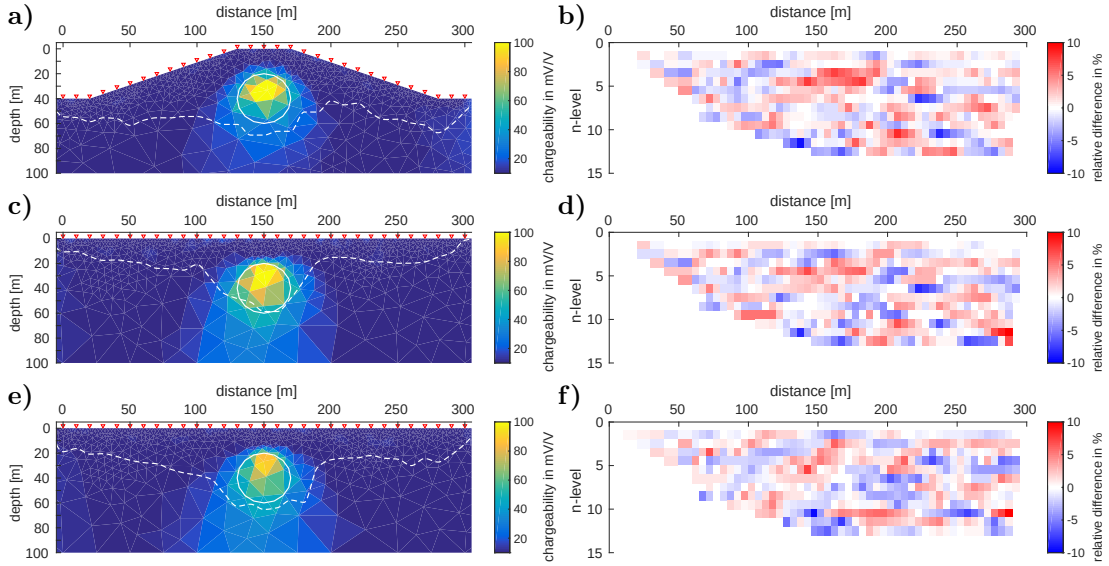

Figure 6.21.: *Final chargeability inversion models:* ***a)*** *for the original data calculated with surface topography (cf. Figure 6.20-b) with 3% noise, the inversion mesh includes topography,* χ*=0.99;* ***c)*** *for the same data as in a) using a flat-surface inversion mesh,* χ*=0.99;* ***e)*** *for the original data calculated without topography (cf. Figure 6.20-c) with 3% noise using a flat-surface inversion mesh,* χ*=0.97.* ***b,d,f)*** *Relative difference between the model response of the corresponding model on the left and the original data. Red triangles indicate electrode locations, the dashed white line the* DOI_{app}*, respectively. The initial chargeability is* $\rho^0 = 8\,\mathrm{mV/V}$.

6.3.2. Rectangular Block Buried Beneath a Valley Topography

Table 6.3.: *Details of the buried block with rectangular cross-section.*

ρ_{block}	ρ_{hs}	Lateral Extension	Vertical Extension	Distance to Surface
10 Ωm	100 Ωm	80 − 280 m	40 − 80 m	11 m

The next example model is shown in Figure 6.22-a. It consists of a wide rectangular model block which is buried beneath a valley structure. The flanks of the valley have a slope of 20°, and the trough in the center is 100 m wide. The block details are listed in Table 6.3. The lateral extension of the model block is chosen to be wider than the trough of the valley.

Low Resistive Anomaly

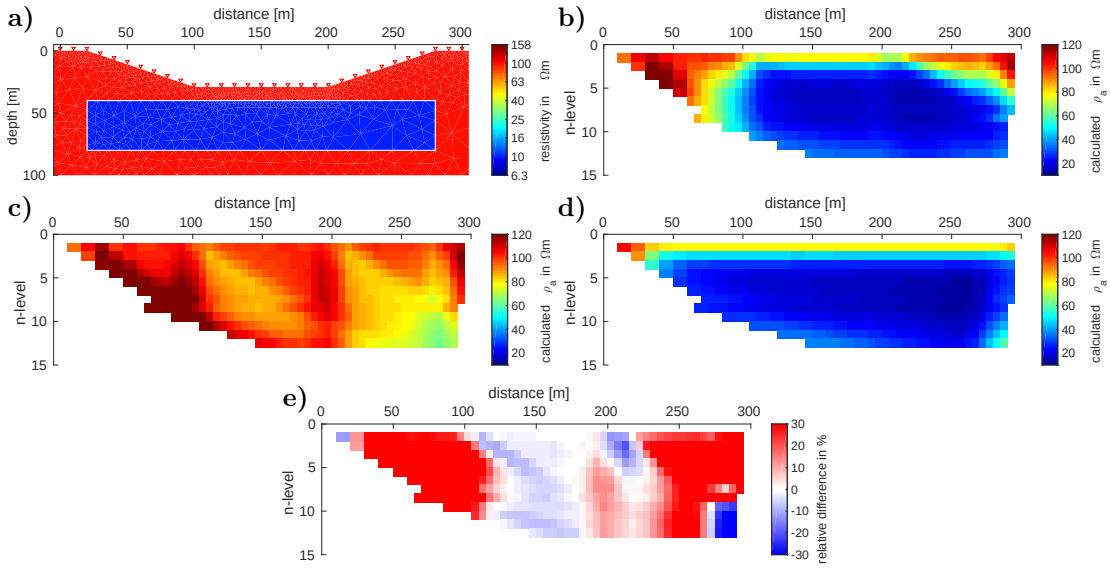

Figure 6.22.: ***a)*** *Original resistivity model buried beneath a surface topography structure with 20° slope angle. Electrode locations are indicated by red triangles.* ***b)*** *Synthetic Pole-Dipole apparent resistivity data calculated for the model in a).* ***c)*** *Synthetic Pole-Dipole data calculated for a homogeneous resistivity of 100 Ωm below the valley topography.* ***d)*** *Synthetic Pole-Dipole data calculated for the same body buried beneath a flat surface.* ***e)*** *Relative difference between the data shown in b) and d).*

We begin with the example of a low resistive model block as shown in Figure 6.22-a. The corresponding synthetic data is displayed in Figure 6.22-b. From comparison to the forward response of a model with constant subsurface resistivity of 100 Ωm under

the same valley topography, which is presented in Figure 6.22-c, it is seen that the presence of topography leads to a low resistive anomaly but the resistivity anomaly due to the model block is stronger than the topography effect. As a comparison, the synthetic data calculated for the model block buried in 11 m depth below a flat surface is shown in Figure 6.22-d and the relative difference to the topography data is presented in Figure 6.22-e. From the relative difference, we see that the amplitude of the low resistive anomaly is very similar in the center of the profile. But both data-sets differ in the beginning and end of the profile. The flat-surface is similar to the signature of a layered half-space whereas the data corresponding to the valley structure shows changes of apparent resistivity in the lateral direction. This is because of the growing distance between electrodes and model block in the topography case.

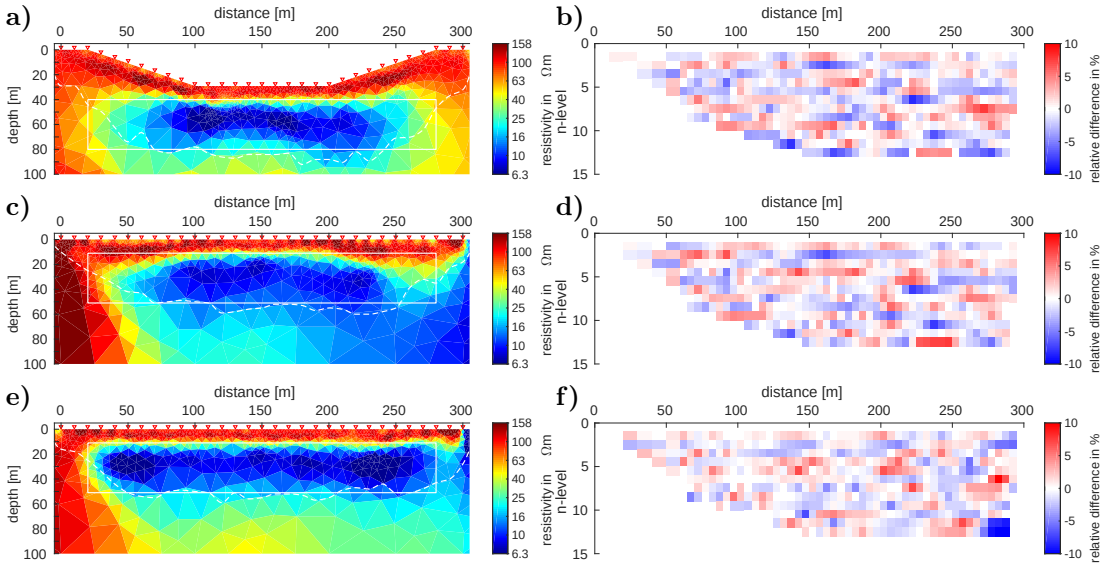

Figure 6.23.: *Final resistivity inversion models:* ***a)*** *for the original data calculated with surface topography (cf. Figure 6.22-b) with 3% noise, the inversion mesh includes topography, χ=0.99;* ***c)*** *for the same data as in a), using a flat-surface inversion mesh, χ=0.96;* ***e)*** *for the original data calculated without surface topography (cf. Figure 6.22-d) with 3% noise, χ=0.95.* ***b,d,f)*** *Relative difference between the model response of the corresponding model on the left and the original data. Red triangles indicate electrode locations, the dashed white line the DOI_{app}, respectively. The initial resistivity is $\rho^0 = 80\,\Omega$m.*

Figure 6.23-a displays the inversion result of the topography data (cf. Figure 6.22-b) including noise using an inversion mesh with surface topography. The inversion result of the same data obtained by inversion with a flat-surface mesh is shown in Figure 6.23-c. The corresponding relative difference plots between original data and model responses are presented in Figure 6.23-b and Figure 6.23-d, respectively. Both models reproduce the original resistivity and depth of the model block well. However, as expected, the beginning and end of the block are poorly reproduced since the sensitivity is low. This is because of growing distance between the model block and surface electrodes. Furthermore, the center of the model block in Figure 6.23-

c appears to be bent upwards. Also, the low resistivity of the block smears out strongly towards the lower right. This is certainly due to topography effects (cf. Figure 6.22-c) that are not removed or considered in this inversion. Again, the relative difference plots are similar, but the χ-value of the inversion with flat surface mesh is smaller.
As further comparison, the inversion result of the flat surface data (cf. Figure 6.22-d) including noise is presented in Figure 6.23-e. The shape and resistivity of the original model block are reproduced well even though the low resistivity also smears out towards deeper depths but not as strong as in the model above. In contrast to the data corresponding to the topography model, the left and right boundary of the block is reproduced. The amplitude of the relative difference (cf. Figure 6.23-f) is slightly smaller than that of the topography data, except in the lower right corner. Even though the approximate DOI_{app} lies at the lower boundary of the buried block, the presence of the boundary results in a resistivity increase below the block. The sensitivity beyond the corresponding coverage isoline is, however, poor.

High Resistive Anomaly

The next example is similar to the model discussed before; only the resistivity values are interchanged. Now, the resistivity of the model block is $\rho_{\text{block}} = 100\,\Omega\text{m}$, and the surrounding has a resistivity of $\rho_{hs} = 10\,\Omega\text{m}$. The original model including surface topography is shown in Figure 6.24-a and the corresponding original synthetic apparent resistivity is displayed in Figure 6.24-b. As for the example discussed before, the width of the apparent resistivity anomaly is smaller in the topography data than in the synthetic data, shown in Figure 6.24-c, which are calculated for the same block buried beneath a flat surface. This is also supported by the relative difference between the two datasets displayed in Figure 6.24-d. According to this, the amplitude of the anomaly is similar in the center, but there are large differences in the beginning and end of the profile.

The inversion results of the topography data including 3% noise using an inversion mesh with surface topography are shown in Figure 6.25-a. Similar to the example with the low resistive model block, the left and right boundaries of the block are not resolved. The vertical extension is, however, reproduced well even though the resistivity is underestimated. Besides, the lateral extension of the model block appears to be even smaller than that of the example with the low resistive block. This coincides with the studies regarding inversion of synthetic data presented in Chapter 5 where the same effect was observed when dealing with high resistive blocks.
However, the result of the same data obtained using a flat surface inversion mesh (cf. Figure 6.25-b), looks similar but also slightly bent. But the effect is not as strong as for the low resistive model block.
As a comparison, the inversion result of the flat surface data (shown in Figure 6.24-c) is presented in Figure 6.25-e. The upper and left boundaries of the model block are reproduced well. The resistivity is partly overestimated and smears out towards larger depths. For the sake of completeness, the relative difference between original data and response of the corresponding model on the right is shown in Figure 6.25-

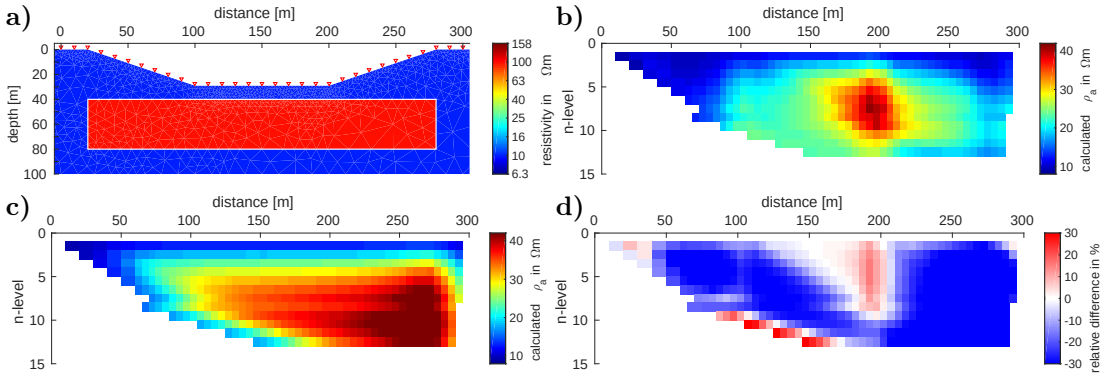

Figure 6.24.: ***a)*** *Original resistivity model buried beneath a surface topography structure with 20° slope angle. Electrode locations are indicated by red triangles.* ***b)*** *Synthetic Pole-Dipole apparent resistivity data calculated for the model in a).* ***c)*** *Synthetic Pole-Dipole data calculated for the same body buried beneath a flat surface.* ***d)*** *Relative difference between the data shown in b) and c).*

b,d,f. It is seen that the data-fit is overall similar for the different inversions. In all three inversion models, the approximate DOI_{app} lies within the high resistive block. However, the lower boundary is resolved to some extent in the models corresponding to the topography data. Only for the flat-surface data, the lower boundary of the block is not resolved.

Highly Chargeable Anomaly

The last example includes a chargeability anomaly as shown in Figure 6.26-a. Here, the model block has a chargeability of $m_{\text{block}} = 100\,\text{mV/V}$ and the surrounding a chargeability of $m_{hs} = 10\,\text{mV/V}$. The intrinsic resistivity is constant with $\rho_0 = 100\,\Omega\text{m}$. Figure 6.26-b shows the corresponding calculated synthetic apparent chargeability pseudo-section. The forward response of the same block buried beneath a flat surface is displayed in Figure 6.26-c. The width of the highly chargeable anomaly is wider in the flat surface data. According to the relative difference between both datasets, presented in Figure 6.26-d, the anomaly is of similar amplitude in the center and varies strongly in the beginning and end of the profile.

The final chargeability inversion results are shown in Figure 6.27 including the corresponding relative difference between calculated and original synthetic data. The chargeability model in Figure 6.27-a is the result of the topography data including noise using an inversion mesh with surface topography and the model in Figure 6.27-c is the result of the same data-set applying a flat-surface inversion mesh. In both models, the chargeability of the original block is reproduced well. The high chargeability of the block smears out towards the end of the profile in both models. Therefore, the right boundary is not resolved. The upper left and lower boundaries of the block are resolved, even though the lower boundary coincides with the approximate DOI_{app}. However, in the model including topography (Figure 6.27-a) the lower boundary of the block is slightly shifted upwards in the center. This effect

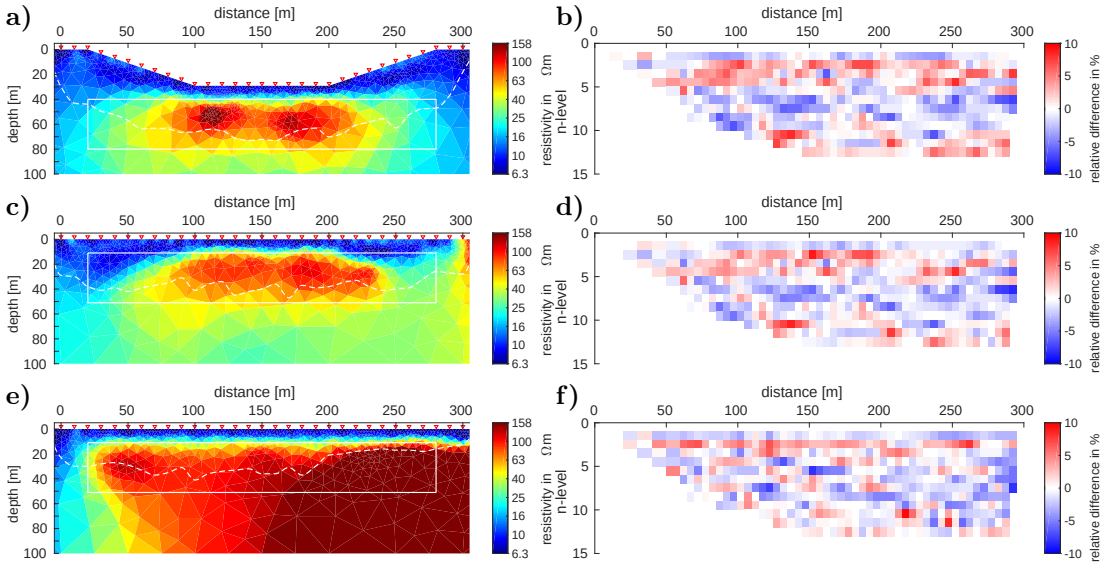

Figure 6.25.: *Final resistivity inversion models:* ***a)*** *for the original data calculated with surface topography (cf. Figure 6.24-b) with 3% noise, the inversion mesh includes topography, χ=0.97;* ***c)*** *for the same data as in a), using a flat-surface inversion mesh, χ=0.97;* ***e)*** *for the original data calculated for the model without surface topography (cf. Figure 6.24-c) with 3% noise, χ=1.00.* ***b,d,e)*** *Relative difference between the model response of the corresponding model on the left and the original data. Red triangles indicate electrode locations, the dashed white line the DOI_{app}, respectively. The initial resistivity is $\rho^0 = 8\,\Omega$m.*

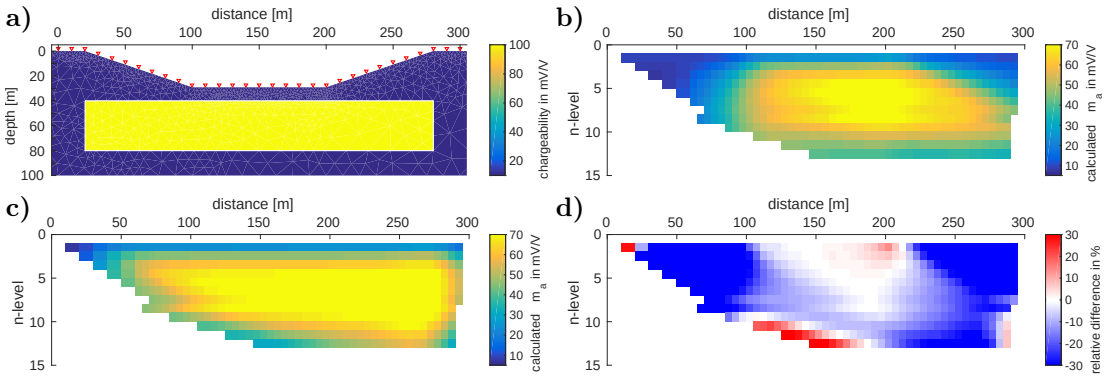

Figure 6.26.: ***a)*** *Original chargeability model buried beneath a surface topography structure with 20° slope angle. Electrode locations are indicated by red triangles.* ***b)*** *Synthetic Pole-Dipole apparent chargeability data calculated for the model in a).* ***c)*** *Synthetic Pole-Dipole data calculated for the same body buried beneath a flat surface.* ***d)*** *Relative difference between the data shown in b) and c).*

is stronger in the result of the flat-surface mesh (Figure 6.27-c), where the block is bent upwards in the center and downwards in the left and right. Furthermore, the lateral extension is shorter than the original. This deformation is indeed caused by

the growing distance between surface electrodes and buried block beneath the flanks of the valley structure in the original model.

As comparison, Figure 6.27-e presents the chargeability inversion results of the flat-surface data (cf. Figure 6.26-c) including noise using a flat-surface inversion mesh. The chargeability of the block and the upper left and lower boundary is reproduced well. At the right boundary, the high chargeability smears out towards the end of the profile as in the latter examples. In contrast to the inversion of topography data using the flat-surface mesh, the block is not deformed. The relative difference plots overall have the same amplitude except for the end of the profile. According to this, the differences are not influenced by a lack of data-fit but by topography effects and sensitivity.

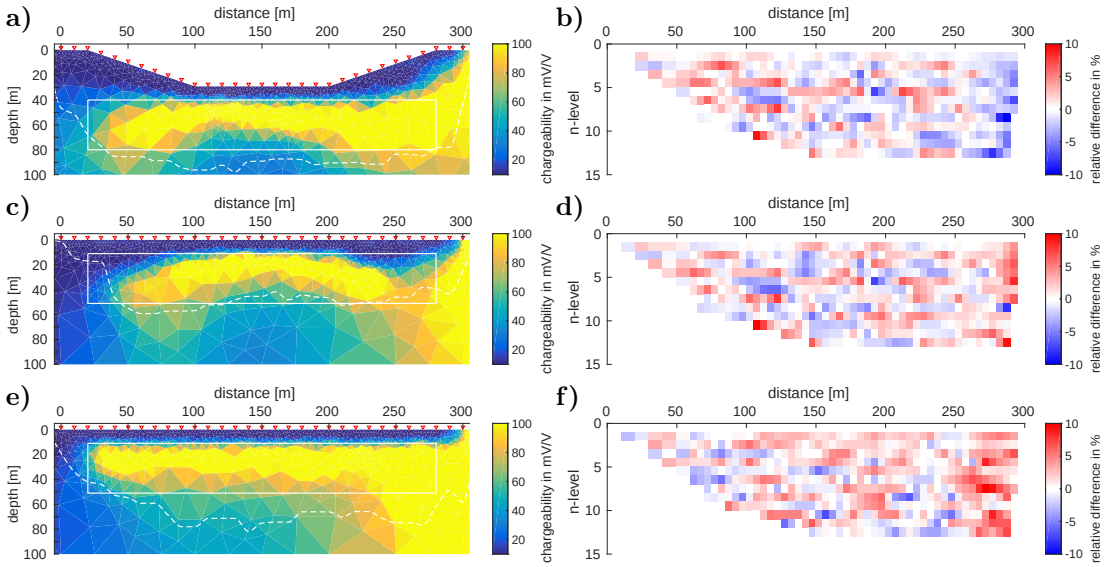

Figure 6.27.: *Final chargeability inversion models:* ***a)*** *for the original data calculated with surface topography (cf. Figure 6.26-b) with 3% noise, the inversion mesh includes topography, χ=0.97;* ***c)*** *for the same data as in a), using a flat-surface inversion mesh, χ=1.00;* ***e)*** *for the original data calculated without surface topography (cf. Figure 6.26-c) with 3% noise, χ=1.03.* ***b,d,f)*** *Relative difference between the model response of the corresponding model on the left and the original data. Red triangles indicate electrode locations, the dashed white line the DOI_{app}, respectively. The initial chargeability is $m^0 = 8\,\mathrm{mV/V}$.*

6.3.3. Comparison with other algorithms

Like in Chapter 5.4.3, the `ResIPIn2D` inversion results are compared to the models obtained by well-established algorithms. The purpose is to check whether the results are reasonable and to identify similarities and differences.

Figure 6.28 shows inversion results obtained by `BERT` for the hill and valley model, each with high and low resistive model block. Generally, the circular body is repro-

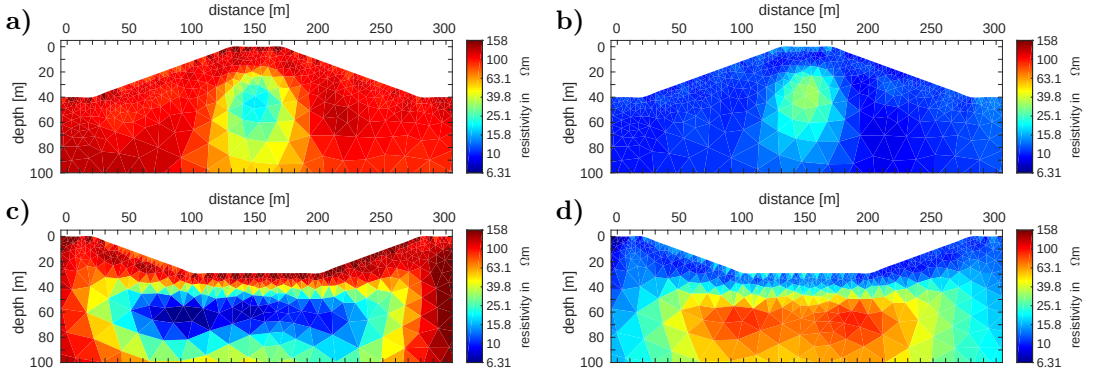

Figure 6.28.: *Resistivity models obtained by* `BERT` *(using $\lambda = 30$): Inversion of synthetic data calculated from* ***a)*** *the hill model with low resistive anomaly in Figure 6.14-a ($\chi_{dc} = 0.98$),* ***b)*** *the hill model with high resistive anomaly in Figure 6.18-a ($\chi_{dc} = 0.98$),* ***c)*** *the valley model with low resistive anomaly in Figure 6.22-a ($\chi_{dc} = 5.2$) and* ***d)*** *the valley model with high resistive anomaly in Figure 6.24-a ($\chi_{dc} = 5.4$).*

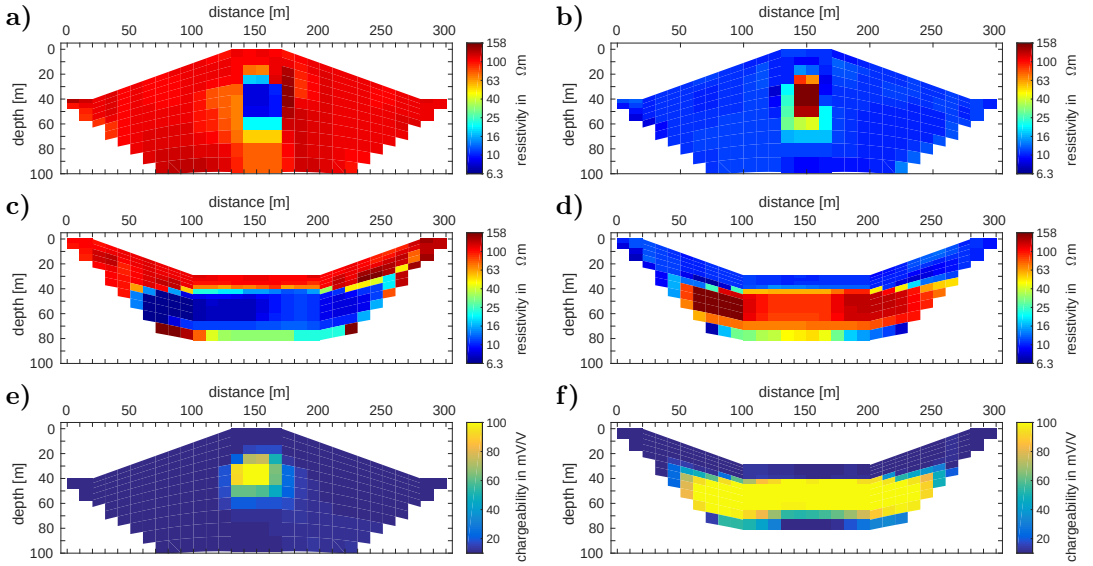

Figure 6.29.: *Resistivity and chargeability models obtained by* `Res2DInv`*: Inversion of original synthetic data calculated from* ***a)*** *the hill model with low resistive anomaly in Figure 6.14-a ($RMS_{dc} = 2.2\%$),* ***b)*** *the hill model with high resistive anomaly in Figure 6.18-a ($RMS_{dc} = 2.1\%$),* ***c)*** *the valley model with low resistive anomaly in Figure 6.22-a ($RMS_{dc} = 3.7\%$),* ***d)*** *the valley model with high resistive anomaly in Figure 6.24-a ($RMS_{dc} = 2.3\%$),* ***e)*** *the hill model with highly chargeable anomaly in Figure 6.20-a ($RMS_{ip} = 1.2\%$) and* ***f)*** *the valley model with highly chargeable anomaly in Figure 6.26-a ($RMS_{ip} = 0.37\%$).*

duced in a similar manner as it is in the `ResIPIn2D` models (cf. Figure 6.15-e and Figure 6.19-a). Especially, the hill model with low resistive anomaly appears to be scattered in the surrounding of the body, which is certainly due to the noise that

was added to the original data. The valley models are also similar to the results of the new algorithm. In the results of both algorithms, the left and right boundaries of the anomaly influence the inversion models, even though the width is underestimated in both. The high resistive anomaly in Figure 6.28-d appears slightly shifted towards the bottom left.

The resistivity and chargeability inversion results obtained by `Res2DInv` are shown in Figure 6.29. The shape of the circular body is not reproduced as well as by the other two algorithms, which is certainly due to the rectangular model cells. However, the resistivity and chargeability change between neighboring model cells is more abrupt so that the resistivity of the anomalies is closer to the original models. The influence of the noise floor of the original data is again most prominent in the hill model with the low resistive anomaly. Referring to the valley models, the resistivity and upper boundary of the rectangular block is well met. However, the lower boundary is shifted upwards and no left or right boundary is resolved, which might be caused by the limited size of the inversion model mesh. Furthermore, the anomaly seems to be bent which is caused by the model cells that are deformed corresponding to the surface topography.

According to these examples, the newly developed algorithm yields reasonable inversion results that are comparable to the results obtained by well-established algorithms when topography is present. These examples also revealed advantages of using an unstructured triangular mesh to reproduce surface topography and non-rectangular structures.

6.3.4. Conclusions

In this chapter, it was shown that the newly developed algorithm `ResIPIn2D` is capable of reproducing an original model that includes surface topography reasonably with the help of inversion examples of synthetic data. As a preparation for the interpretation of field data discussed in Chapter 7, the same profile length, and electrode setup was used. The valley example is derived from the field survey since the survey area includes a valley structure. It was shown that the favored method of including the surface topography directly in the inversion mesh produces the most reasonable results. However, with regard to real field data, it is not to forget to use the same electrode distances in the inversion that are used during the production of the data. Otherwise artifacts might occur due to wrong geometry factors (see also Chapter 6.2). According to Figure 6.16-c reasonable results can also be obtained applying the topography correction after Fox et al. (1980). However, this approach requires an additional, manual forward calculation and correction of the data before the inversion procedure. And as mentioned by Tong and Yang (1990), this approach might lead to inaccuracy regarding resistivity structures close to the surface. An advantage is, though that the singularity removal technique is applicable when using a flat surface mesh.

Furthermore, it was shown that the use of a flat surface inversion mesh together with data including topography effects might lead to errors. The shape of original structures is stretched or bent. But more important, additional structures that are

induced only by topography effects might occur, or original structures might be disguised due to superposition of topography effects.

Referring to apparent chargeability data, it was shown that the topography does not affect the data as it is the case for apparent resistivity data. However, a structure might appear deformed when using a flat surface mesh for the inversion. In the case of the valley example, the lower boundary of the highly chargeable block is better resolved than the lower boundary of a resistivity anomaly in the same depth. Furthermore, the valley example showed that structures that extend towards the flanks of the valley could occur shorter than the original outline because of the growing distance to the electrodes and with that less sensitivity.

When topography was included in the inversion mesh, the coverage threshold for the approximate DOI_{app} was derived from a flat surface mesh example. The considered buried anomalies were mostly located above the DOI_{app}. However, for the high resistive block buried beneath the valley (cf. Figure 6.25), the DOI_{app} lies within the block. In this case, the outlines of the block are not reproduced as well as for the other examples. This implies that the sensitivity beyond the DOI_{app} is reduced.

7. Inversion of Field Data

In this Chapter, the newly developed inversion algorithm is applied on DC/TDIP field data that was acquired on a copper ore deposit in southeastern Turkey. Before the inversion and interpretation of field data, a few aspects need to be considered, such as the estimation of data errors, EM coupling or topography effects.

Data error estimation

As a first estimation, the errors of the apparent resistivity data can be assumed to be composed of a geometry, a voltage and a current error. The current error is, however, presumably small, so that it can be neglected. So, we assume the maximum relative error of apparent resistivity to obey (Günther, 2004)

$$\left|\frac{\delta\rho_a}{\rho_a}\right| \leq \left|\frac{\delta G}{G}\right| + \left|\frac{\delta U}{U}\right| \tag{7.1}$$

where δ refers to a variation of the corresponding property. The geometry error $\left|\frac{\delta G}{G}\right|$ refers to the error of the geometry factor G that is caused by electrode misplacement δx. Building the partial derivatives of the geometry factor with respect to the electrode positions leads to the general formula for the maximum relative geometric error

$$\left|\frac{\delta G}{G}\right|_{max} = \left|\frac{\delta x}{G}\right| \left(\left|\frac{\partial G}{\partial x_{C_1}}\right| + \left|\frac{\partial G}{\partial x_{C_2}}\right| + \left|\frac{\partial G}{\partial x_{P_1}}\right| + \left|\frac{\partial G}{\partial x_{P_2}}\right|\right) \tag{7.2}$$

with terms

$$\left|\frac{\partial G}{\partial x_{C_1}}\right| = \frac{G^2}{2\pi}\left(-\frac{\alpha_{C_1P_1}}{\overline{C_1P_1}^2} + \frac{\alpha_{C_1P_2}}{\overline{C_1P_2}^2}\right) \tag{7.3}$$

$$\left|\frac{\partial G}{\partial x_{C_2}}\right| = \frac{G^2}{2\pi}\left(\frac{\alpha_{C_2P_1}}{\overline{C_2P_1}^2} - \frac{\alpha_{C_2P_2}}{\overline{C_2P_2}^2}\right) \tag{7.4}$$

$$\left|\frac{\partial G}{\partial x_{P_1}}\right| = \frac{G^2}{2\pi}\left(\frac{\alpha_{C_1P_1}}{\overline{C_1P_1}^2} - \frac{\alpha_{C_2P_1}}{\overline{C_2P_1}^2}\right) \tag{7.5}$$

$$\left|\frac{\partial G}{\partial x_{P_2}}\right| = \frac{G^2}{2\pi}\left(-\frac{\alpha_{C_1P_2}}{\overline{C_1P_2}^2} + \frac{\alpha_{C_2P_2}}{\overline{C_2P_2}^2}\right) \tag{7.6}$$

and real factors

$$\alpha_{ij} = \begin{cases} 1 & , x_j > x_i \\ -1 & , x_j < x_i \\ 0 & , \text{one of the electrodes is not used} \end{cases} \tag{7.7}$$

In this form, the geometry error can be estimated for every 3- or 4-electrode array type. From Equation (7.2), it is easily shown that the relative geometry error is highest for small n-spacings and decreases with increasing n-spacings (assuming the same positioning error δx for all setups). Furthermore, in comparison to all common array types, the Dipole-Dipole and Pole-Dipole together with Schlumberger arrays have larger geometry errors than the Wenner and Pole-Pole arrays.
The relative voltage error is determined by estimating the variation or accuracy of measured voltages:

$$\left|\frac{\delta U}{U}\right| = \frac{\delta U|G|}{\rho_a I} \ . \tag{7.8}$$

Here, δU refers to the minimum voltage limit that can be distinguished by the applied device. When a variation of measured voltages is estimated by stacking, also this should be considered. From this formula, it is easily shown that the voltage error generally increases with increasing n-spacings. However, the relative voltage error is usually smaller than the relative geometry error. Due to large geometry factors, the voltage errors are highest for the Dipole-Dipole and Pole-Dipole arrays. Pole-Pole and Wenner arrays have the smallest voltage errors in comparison with the other array types.
It is often advantageous to add an error floor e when estimating the data errors of real data:

$$\frac{\delta \rho_a}{\rho_a} = e + \left|\frac{\delta G}{G}\right|_{max} + \left|\frac{\delta U}{U}\right| \ . \tag{7.9}$$

The error floor is a summary of errors that cannot be estimated by the geometry or voltage error, such as geological noise. Adding an error floor of e.g. 1-5% can help to improve the data-fit and prevent artifacts in the inversion model due to over-fitting noisy data. The chargeability data is appointed with the same relative error as the resistivity data.

EM coupling

There are certain EM effects that may disturb TDIP measurements, usually referred to as EM coupling:

a) EM coupling between the cables and the surface of the earth or between the cables of different channels within a multi-core cable

b) EM effect caused by the process of turning the current on and turning the current off

The EM coupling regarding a) refers to the inductive or capacitive coupling of the cables. It depends on the frequency and the cable length (or dipole length) (Pelton et al., 1978). There are several recommendations of how to remove these coupling effects and which cable arrangements are less influenced by the coupling. However, it was shown by several authors, e.g. Schmutz et al. (2014), that the effects are negligible for transmitter frequencies $< 10\,\mathrm{Hz}$. Since the frequency used for the acquisition of the field data dealt with in this chapter was $< 1\,\mathrm{Hz}$, the issue is not further assessed in the framework of this thesis.

The EM effect in terms of b) is due to the induction of a secondary magnetic field caused by a time-dependent variation of the primary magnetic field caused by switching the transmitter current on or off. This induces a voltage that may superpose the actual IP decay curve of interest. These EM effects are subject to transient electromagnetic or controlled source EM methods but are "unwanted" signals in IP data. To avoid these effects, it is recommended to apply a certain delay time, i.e. time after turn-off until the first data point is measured, when acquiring the "wanted" voltage decay curve. That means the first data point should be measured when the EM effects have vanished. Kang and Oldenburg (2016) investigated the superposition of EM induction and IP response with time after transmitter turn-off. From that, a minimum delay time can be estimated, that is enough to avoid a disturbance. However, the authors also present a procedure to remove the "unwanted" effects from the IP data.

Chargeability approximation

For the IP perturbation approach after Seigel (1959) and the two-step inversion approach after Oldenburg and Li (1994), the secondary voltage is required (cf. Figure 2.10 and Figure 2.12) to obtain the apparent chargeability. But instead, the voltage decay curve is measured and the integrated apparent chargeability is derived. Therefore, the amplitude of the measured IP data is always dependent on the used delay time and integration time. Thus, also the inversion result should be interpreted with care. Either one accepts that the inversion model actually needs to be scaled. Then the obtained chargeability values are at least comparable to each other and to other measurements with the same time settings. Or the measured data is preprocessed before to the inversion in order to approximate the apparent chargeability that corresponds to the measurement of secondary voltage. This is often done by converting the measured integrated apparent chargeability data to the Newmont Standard (cf. Chapter 2.3). Then the inversion results are in either case comparable to measurements in which different time settings are applied.

Topography

In Chapter 6, it was shown that topography significantly influences the measured data, at least for slope angles $> 10°$. In this case, the topography needs to be considered during inversion to prevent misinterpretation. Thus it is recommended to already decide during the field work if a significant topography is present. If yes, as much effort as possible should be used to determine the exact electrode locations, i.e., in horizontal as well as in vertical direction. Whenever very large electrode separation is applied, it may be helpful to measure the elevation also at points between electrode locations. Then, the topography can be included as accurate as possible into the parameter mesh. Visualizing the topography effect for the topography-mesh as presented in Chapter 6.1, e.g., in Figure 6.2, gives a valuation about the importance of considering topography for the according profile.

7.1. Survey on a Copper Ore Deposit in Elbistan, Turkey

In August 2013, a geophysical survey was conducted on a copper ore deposit near Elbistan in Turkey. The survey area and the geophysical results are presented and discussed in the following.

Figure 7.1.: *Location of the survey area (green symbol), 20 km west of the city Elbistan in Turkey. The location of the Berit Mountain and the Isbendere Ophiolite are indicated by blue symbols; Google Earth (2016).*

7.1.1. Geological Background

The survey area lies approximately 20 km west of the city Elbistan in the province of Kahramanmaraş in southeastern Turkey (see Figure 7.1). It is located on Miocene-Pliocene material (Karaoğlan et al., 2013) in the East Anatolian Fault Zone (see Figure 7.2-a). This fault zone includes the Tauride thrust belt where several ophiolitic structures occur (Karaoğlan et al., 2013). Ophiolites are composed of oceanic crust and are often connected to the occurrence of ore deposits (Press and Siever, 2003).

In the Cretaceous, the Neotethys Ocean including a volcanic arc existed between Arabia and the Tauride platform at the southeastern edge of Anatolia (see Figure 7.2-b). The Arabian platform moved towards Anatolia. By the Late Cretaceous (see Figure 7.2-c), the oceanic arc was subsided beneath and partly thrust onto the Tauride platform building a supra-subduction zone (SSZ) (Karaoğlan et al., 2013).

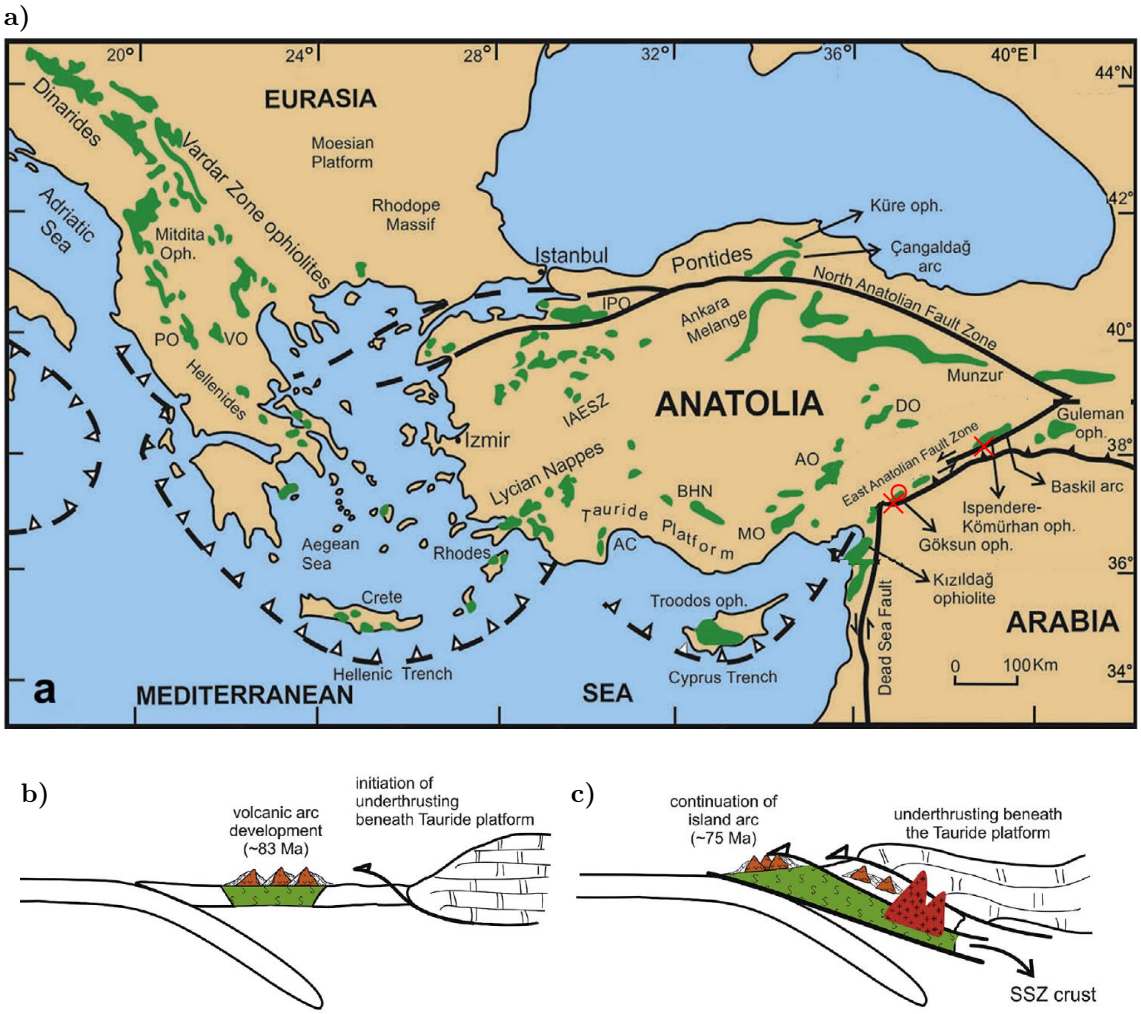

Figure 7.2.: a) *Major tectonic features and distribution of the Neotethyan ophiolites (green) in the eastern Mediterranean region; modified after (Dilek and Flower, 2003; Karaoğlan et al., 2013)). The Survey area is indicated by a red circle, the Göksun and the Isbendere Ophiolite by a red cross, respectively.* ***b,c)*** *Sketch of the development of SSZ-type ophiolites, granitoid intrusions and volcanic sediments, related to the arc, that were subducted or accreted during the late Cretaceous in the northern part of the southern Neotethys (Karaoğlan et al., 2013).*

The accreted material forms the South-East Anatolian Ophiolites which are cropping out along the thrust belt (Kozlu et al., 2014).

The Göksun Ophiolite (see Figure 7.2-a) includes the Berit Mountain (2.028 masl) which lies 17 km south of our survey area (Figure 7.3). Robertson et al. (2006) describes the constitution of the northern part of the Berit Ophiolite as follows: The ophiolite is mainly non-metamorph and contains ultramafic-mafic cumulates, isotropic gabbro, a sheeted dyke complex, plagiogranite and volcanic units. Extrusive mafic rocks are exposed e.g. in the Nurhak-Elbistan area. They are comprised of basalt, basaltic andesite, andesite, dacite and rhyolite. Furthermore, volcanic sediments and intercalcations of limestone and mudstone occur.

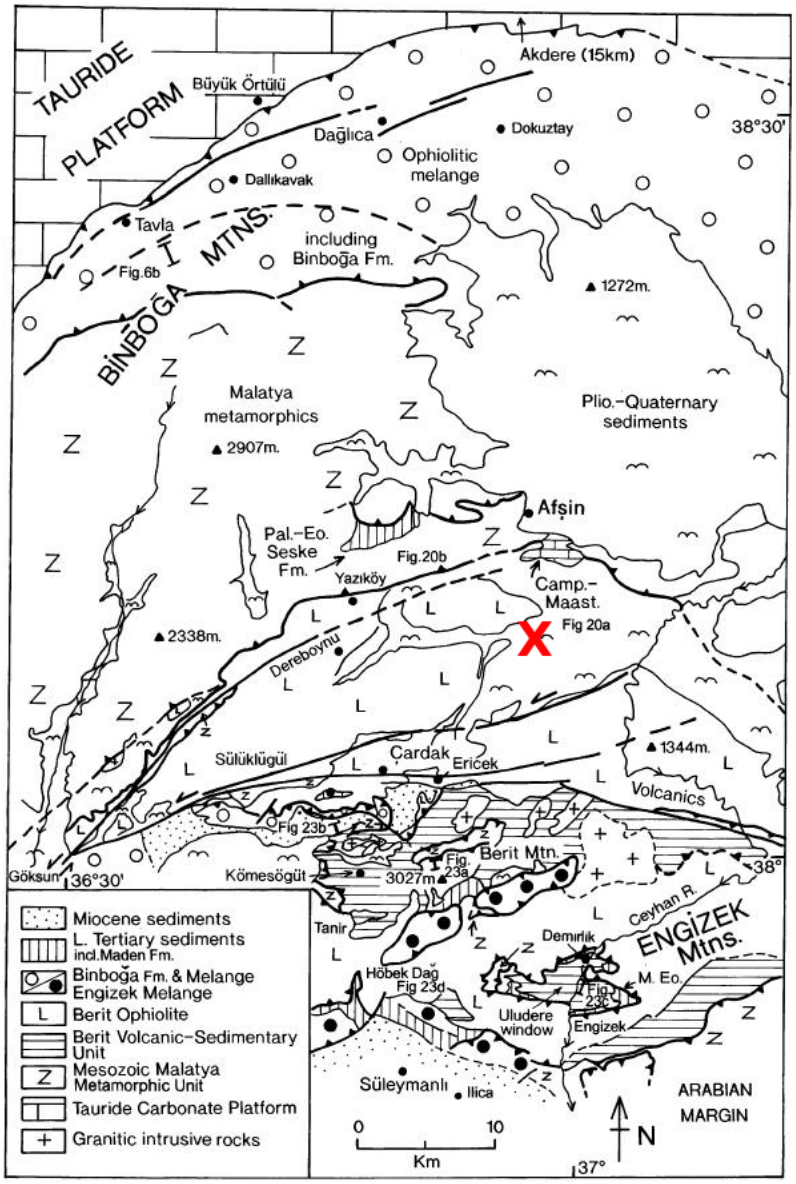

Figure 7.3.: *Geological overview of the Berit area. The survey area is indicated by a red cross; modified after (Robertson et al., 2006) (based on regional mapping by Perincek and Kozlu (1984)).*

The Isbendere Ophiolite is located near Sincik in Adiyaman, ca. 140 km east of the survey area (see Figure 7.1 and Figure 7.2-a). Similar to the Berit Ophiolite, it contains granitoid rocks like granodiorite (Karaoğlan et al., 2013). Near the Isbendere Ophiolite, several sulfide ores were detected in veins and in disseminated form including copper and iron mineralization such as chalcopyrite ($CuFeS_2$), bornite (Cu_5FeS_4), chalcosine (Cu_2S), covelline (CuS), pyrite (FeS_2), sphalerit (ZnS) and marcasite (FeS_2) (Yildirim et al., 2012).

These ores are typically found in oceanic crust where they are formed in hydrothermal deposits at oceanic arcs (Press and Siever, 2003). Where oceanic crust is subducted beneath continental crust, ore deposits are found in accreted fragments of the

oceanic crust (ophiolites), or they originate from melting and upward intrusion of the subsiding material (Press and Siever, 2003). The deposited ores are then found along veins or are disseminated (finely distributed) within the fractured, intruded material (Press and Siever, 2003; Yildirim et al., 2012). Disseminated copper ores are also referred to as porphyry copper ores which are the most important source for copper production worldwide (Press and Siever, 2003).

7.1.2. The Survey Area

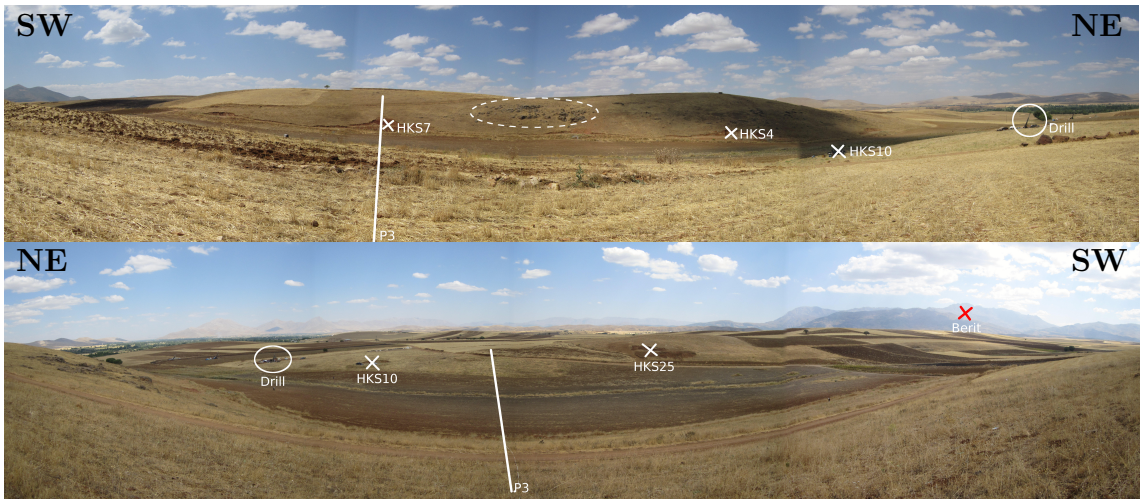

Figure 7.4.: *Panoramic overview of the survey area in Elbistan:* ***(top)*** *View towards northwestern direction;* ***(bottom)*** *View towards southeastern direction. The white line indicates Profile 3. Borehole locations are labeled with a white cross, the active drilling site by a white circle. Rock outcrops are indicated by a dashed white ellipse. The red cross denotes the Berit Mountain in distance.*

An overview of the survey area is shown in Figure 7.4. It lies in an altitude of 1170 m to 1200 m above mean sea level. In 2012, a copper ore deposit was discovered. The ore deposit is assumed to be elongated below the valley, that lies in the center of the survey area. According to the viewpoint of the panoramic pictures in Figure 7.4, the strike direction of the valley and the deposit is from left to right. During our survey, the area was still in the investigation phase by a mining company. Large-scale IP investigations had been conducted prior to the survey and drillings were driven prior and during our survey. The closest active drilling site is seen in Figure 7.4 and is denoted as "Drill" in Figure 7.5.

Due to the investigation status, only limited information about the results is available. Only some information based on borehole HKS 4 (cf. Figure 7.5) are at hand (Özyildirim et al. (2015), submitted for publication): The host rock is dacite, which is the fine grained equivalent to granodiorite. Beneath the top-soil with a thickness of 0.5 m, follows altered dacite (0.5 through 8 m depth), then filic dacite (8 m through 15 m depth) and potassic dacite (15 m through 50 m depth). Copper content is detected in depth below 8 m and is mainly of disseminated form.

We expect similar sulfide ore paragenesis as found close to the Isbendere Ophiolite because the near Berit Mountain in the Göksun Ophiolite belongs to the same tectonic system (cf. Chapter 7.1.1). Sulfides produce strong IP effects. Therefore, high chargeability values are expected. Several resistivity and chargeability values of selected minerals and rock types are given in Table A.2, Table A.3 and Table A.4 in the Appendix.

The survey area lies in an agricultural area. There were fields in the valley and on the hill coinciding with the viewpoint of the upper picture in Figure 7.4. But during our survey, all crops had been harvested already, and the topsoil was very dry. Outcrops of mineralized rocks are found at the northwestern hill, which is seen as dark spots in the center of Figure 7.4-top.

7.1.3. Geophysical Data Acquisition

We conducted a geophysical survey in collaboration with the Department of Geophysical Engineering of Ankara University, Ankara, Turkey in August 2013. The survey area covers a part of the copper ore deposit. The overview over the geophysical profiles and the assumed strike direction is shown in Figure 7.5. The assumed strike direction coincides with the valley in the center of the survey area. The orientation is roughly northeast to southwest.

Geophysical data was acquired on eight parallel profiles crossing the valley perpendicularly. The length of each profile is 300 m with an inter-profile distance of about 50 m. The lateral extension of the ore deposit is assumed to decrease from Profile 1 to Profile 8. Drilling locations are indicated by blue flags. We acquired DC/TDIP data and RMT data on all profiles.

DC/TDIP Data Acquisition

The DC/TDIP data were acquired using Equipment of *Zonge Engineering*: a combination of the transmitter *GGT30* and the receiver *GDP32-II* with eight channels (cf. Figure 7.6-c). Current injection was carried out using a stainless steel electrode (cf. Figure 7.6-a). The electrical potential was acquired using non-polarizable electrodes filled with Copper/Copper-sulfate as shown in Figure 7.6-b. The data was acquired in the Pole-Dipole configuration with a distant second source electrode (C2) as sketched in Figure 7.7. Each of the eight receiver channels was connected by a separate cable with one of the potential electrodes P1 through P8 (see also Figure 7.6-d). The potential electrodes formed a set of seven receiver pairs with dipole length a and distance $n \times a$ to the current electrode C1. So, during each measurement step, seven n-levels were recorded. After each measurement step, the whole electrode setup was moved along the profile. This procedure was done once with an electrode distance of $a = 10\,\text{m}$ and once with an electrode distance of $a = 20\,\text{m}$. Therefore, we obtained a dataset with 14 n-levels with overlapping pseudo-depths (see Table B.6).

At each station, several transmitting cycles were performed. The data obtained

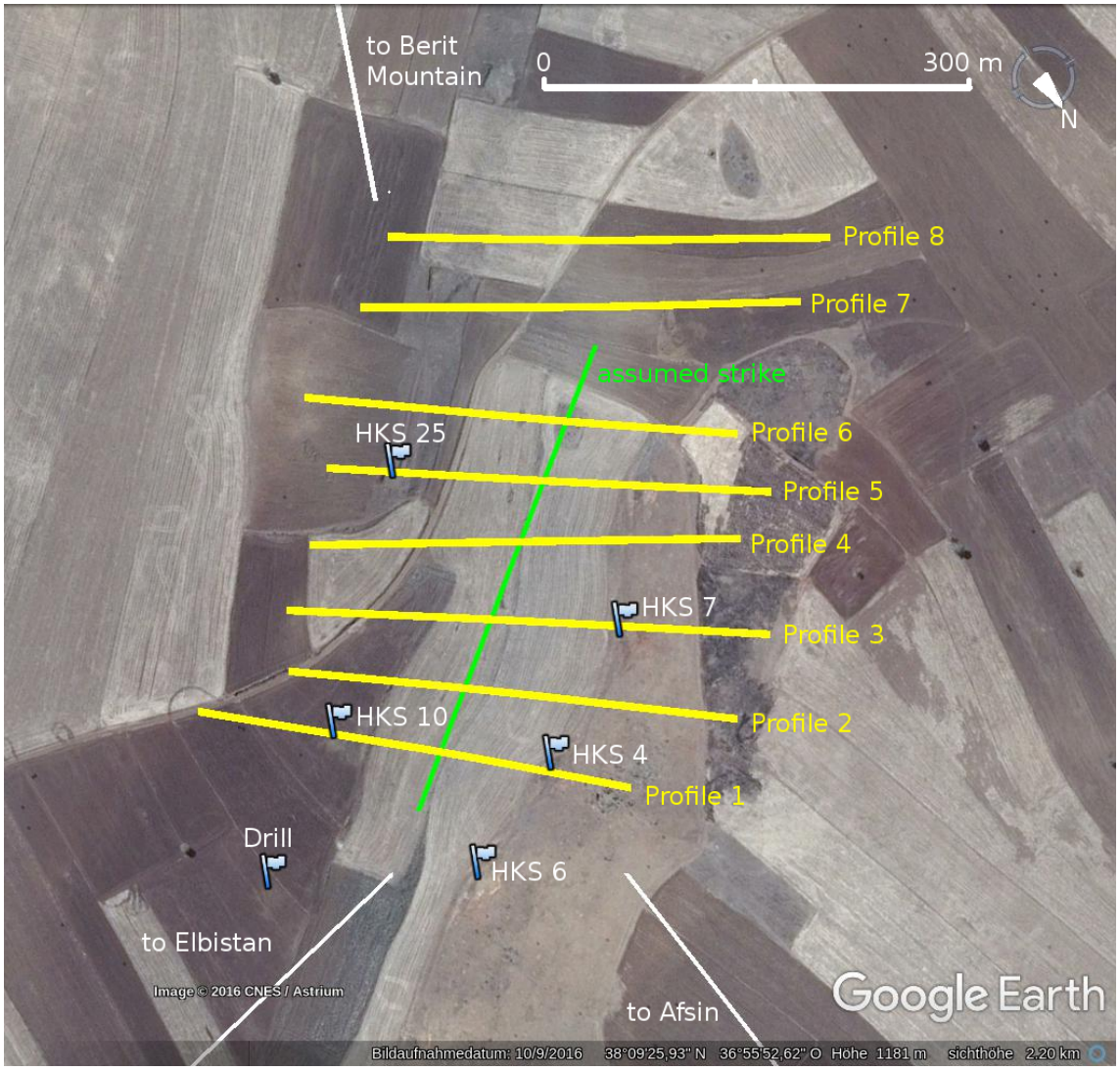

Figure 7.5.: *Location of the geophysical profiles (yellow) in the survey area. The assumed strike direction is indicated by a green line. Borehole locations are marked by blue symbols. The white lines indicate the directions towards the cities of Elbistan and Afşin and the Berit Mountain, respectively; Google Earth (2016)*

in each cycle are averaged afterwards, and a standard deviation is calculated. In each cycle, the potential data $V(t)$ is recorded and processed as follows. The duty cycle is 50%, so there is an on-time, off-time, negative on-time and off-time during one cycle with a time span of $T/4$ each. The cycle frequency is $f = 0.125\,\mathrm{Hz}$, so the cycle period is $T = 8\,\mathrm{s}$. 1024 data points are recorded per cycle, that yields a digitization period of $\Delta\tau = T/1024 = 7.8125\,\mathrm{ms}$. The primary potential is averaged from the last 64 data points before the current turn-off (see Figure 7.8). From that, the apparent DC-resistivity data is calculated. Instantly after the current turn-off, the first seven data-points are skipped. After that, the data points are grouped into sets of 19 data points that are averaged to one-time window. So, in each off-time, the secondary potential $V_s(t)$ is acquired in 13 time windows. The integrated

Figure 7.6.: *Photos made during the DC/TDIP survey in 2013:* ***a)*** *current injection through a steel electrode;* ***b)*** *potential measurement by a non-polarizable electrode filled with* $Cu/CuSO_4$*;* ***c)*** *utilized devices from Zonge Engineering;* ***d)*** *Each cable drum (white circle) represents the location of a potential electrode. The white cross denotes HKS10, outcropping rocks are indicated by a dashed white ellipse.*

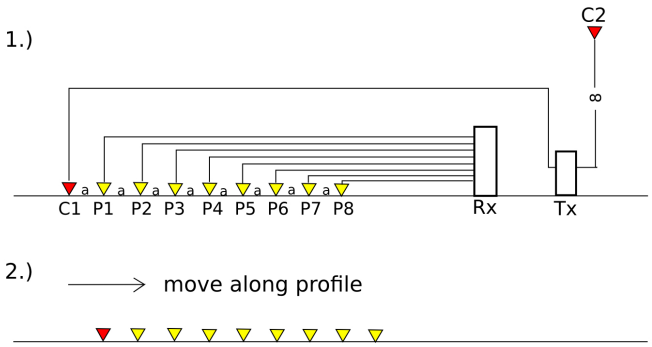

Figure 7.7.: *Schematic of the applied Pole-Dipole setup.* ***1.)*** *The current electrodes C1 and C2 are connected to the Transmitter Tx. Each potential electrode (P1-P8) is connected by a separate cable with the 8-channel receiver Rx.* ***2.)*** *After each measurement the whole setup is moved along the profile.*

chargeability is obtained after (Zonge, 2003)

$$M = \frac{T}{1024} \cdot \frac{1.87}{V_p} \cdot \int V_s(t)\,\mathrm{d}t \tag{7.10}$$

where the factor 1.87 is the swift constant (Swift Jr, 1973). For the Newmont Standard approximation, integration would be from 451.38 ms to 1097.32 ms. In terms of the given time windows, the closest approach of this integral is the summation of time windows 4-7, which actually refers to integration from 500 ms to 1100 ms. From that the "Zonge Standard" chargeability is obtained by (Zonge, 2003)

$$M_{\mathrm{Zonge}} = \frac{T}{1024} \cdot \frac{1.87}{V_p} \cdot 19 \sum_{i=4}^{7} W_i \tag{7.11}$$

where $W_i = \sum_j V_j/19$ is the normalized sum of the secondary voltages recorded in the 19 time steps of the according time window. The Newmont Standard approximation, given in msec or mV/V is then obtained by multiplication with 1.53 (Zonge, 2003):

$$M_{\mathrm{Newmont}} = 1.53 \cdot M_{\mathrm{Zonge}}\ . \tag{7.12}$$

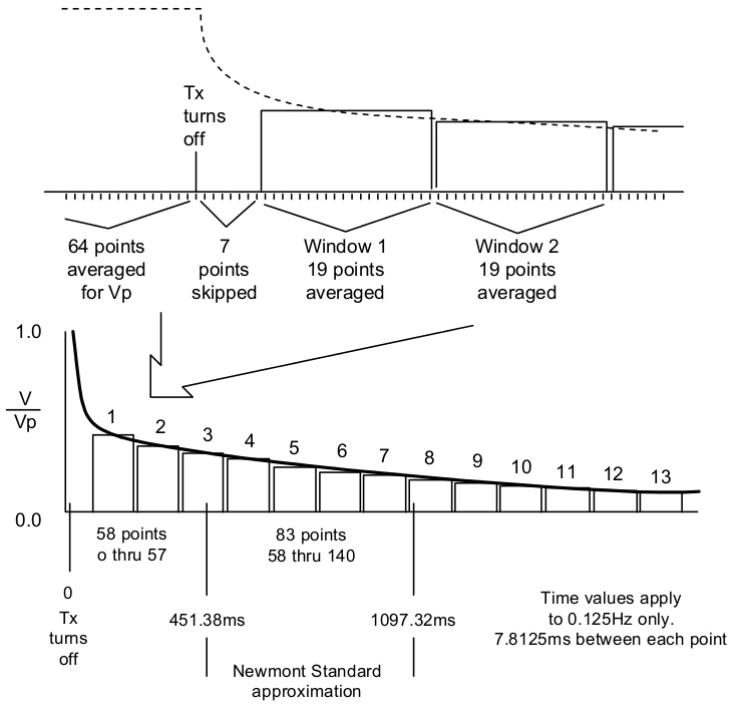

Figure 7.8.: *Time windows and integration times used to calculate the Newmont Standard approximation of the integrated chargeability at* 0.125 Hz *(Zonge, 2003).*

RMT Data Acquisition

The RMT data were recorded with the 4-channel RMT-F device of the University of Cologne (see Figure 7.9). The horizontal magnetic field components were recorded by two perpendicular coils. The horizontal electrical field components were obtained by capacitively coupled electrode cables with a length of 10 m in each direction (forming a length of 20 m in total for each component). The device records data in the frequency range of 10 kHz to 1 MHz. Unfortunately, the frequencies that were available in the survey area did not optimally cover this frequency range. This led to a rather poor data quality. The station distance was mainly 10 m and the locations coincide with the electrode locations. An exemplary RMT inversion result will be discussed in Chapter 7.1.7.

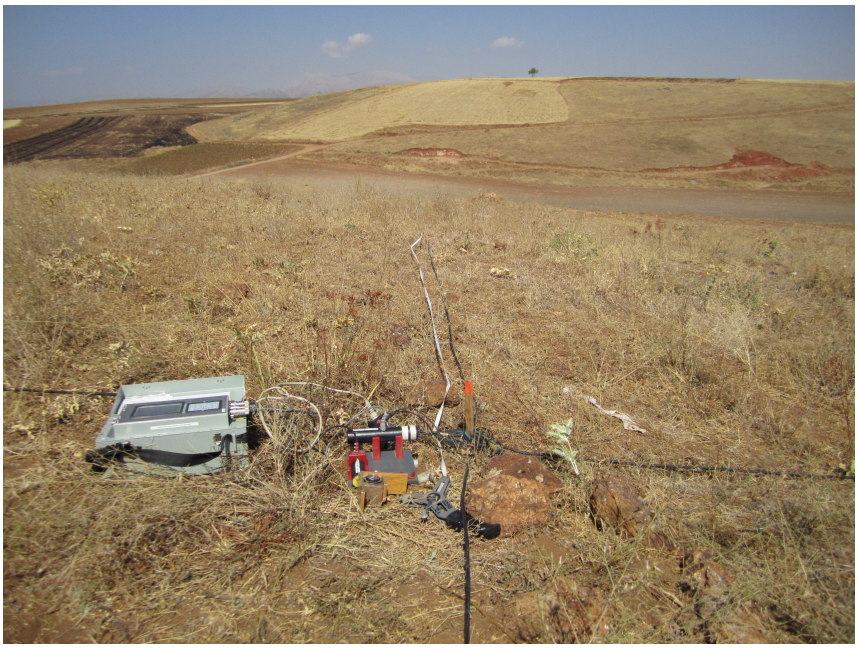

Figure 7.9.: *RMT-F device of the University of Cologne used in the field survey 2013.*

7.1.4. Topography Influence

The surface topography of the survey area was determined by GPS measurements at the electrode locations. For the generation of the inversion mesh, only the relative elevation of the locations is important. To reduce variations due to measuring inaccuracy, a moving average filter was applied to smooth the elevation data. Two examples of surface topography derived by this method are displayed in Figure 7.10-a,b. Profiles 3 and 7 are shown because they represent one of the most distinct and one of the smoothest topographies in the survey area.

The influence of topography on the apparent resistivity data in the survey area is evaluated by checking the pseudo-sections (cf. Figure 7.10-c,d) resulting from for-

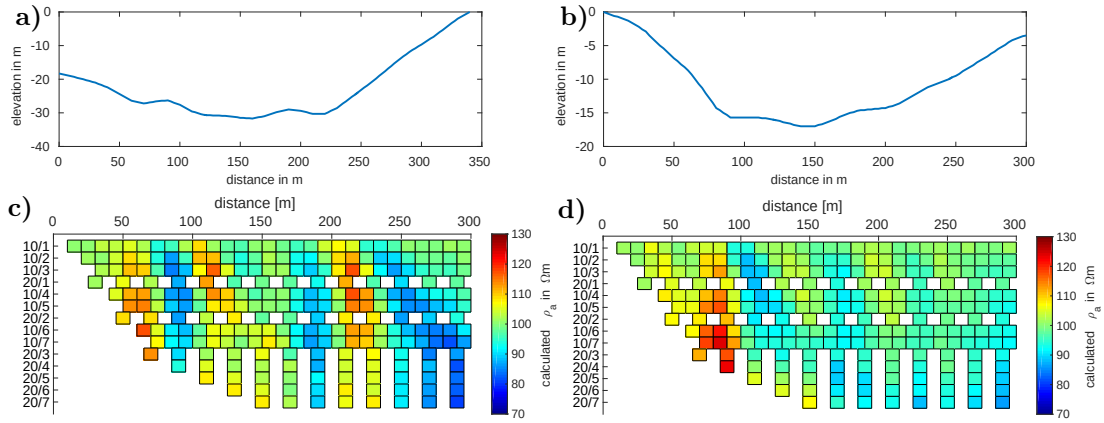

Figure 7.10.: *Topography influence. Surface topography of* **a)** *Profile 3 and* **b)** *Profile 7. Synthetic Pole-Dipole apparent resistivity calculated for a homogeneous subsurface resistivity of* 100 Ωm *beneath the topography according to* **c)** *Profile 3 and* **d)** *Profile 7. The used geometry factors are based on surface distances r_s.In the pseudo-sections, the electrode separation and the n-spacing are indicated on the y-axis in the form of a/n.*

ward calculation of a homogeneous resistivity of 100 Ωm below the given surface topography. This procedure has been introduced in Chapter 6. The Pole-Dipole pseudo-sections were calculated for the same electrode setup and protocol that were used in the field survey (see Table B.6). All following pseudo-sections are arranged as follows: Each rectangle represents a data-point according to one 3-electrode setup. The location on the x-axis represents the center of the receiving dipole. The corresponding electrode distances a (or dipole length) and the n-spacing is indicated as y-axis label. The n-levels are sorted according to the pseudo-depth as listed in Table B.6 calculated by the rule of thumb in Table 2.1. Since the electrode positions were determined by tape measures in the field, it is most suitable to also use surface distances in `ResIPIn2D` for the exemplary forward calculations shown here as well as for the inversion of field data.

From the comparison of surface topography and pseudo-sections shown in Figure 7.10, we can assign apparent resistivity anomalies to surface topography structures. Referring to Profile 3 (cf. Figure 7.10-c), there are e.g., two sequences of decrease, increase and decrease of apparent resistivity, once between profile distance 50-100 m and once between 180-250 m. These variations are mainly produced by the change in the downward slope around profile distance $x = 100$ m and the corner between valley trough and right slope at ca. $x = 200$ m. Overall, the topography influence results in a variation of up to 30%. This supports the importance of consideration of topography in the inversion of field data acquired in this area. Generally, the topography influence is not as strong in Profile 7 (cf. Figure 7.10-d). The only exception is the high apparent resistivity of about 120 Ωm in the left part of the profile which is related to the sharp bend between slope and trough at about $x = 90$ m. The topography influence of the remaining profiles is displayed in Appendix C.1.

7.1.5. Measured Data and Error Estimation

Due to the prominent topography effects discussed above, it is preferable to use the measured voltages as the basis of data interpretation instead of the apparent resistivity values calculated by the device (see also Chapter 6.2). This is because the device uses geometry factors on the assumption of a flat earth and constant electrode separations. This might lead to falsified measured apparent resistivity data. Furthermore, it might lead to erroneous resistivity models because the geometry factors utilized for the forward calculation during inversion are different than the geometry factors used by the device. Using different geometry factors when fitting two datasets, corresponds to different underlying resistivity models. Consequently, the measured voltages were used as basis of the preprocessing described in the following:

All field measurements were obtained using two or three transmitting cycles. From these, an average measured voltage U_{meas} and a standard deviation *std* (in %) is derived corresponding to every electrode combination. A short inversion procedure is started using a mesh with surface topography and surface distances for the geometry factor. When using measured voltages instead of measured apparent resistivity, `ResIPIn2D` internally calculates apparent resistivity values from the measured voltages using the same geometry factors as used in the forward calculations. The data is given in the final output-file. The data errors discussed at the beginning of Chapter 7 are based on measured apparent resistivity. Furthermore, it is more convenient to examine apparent resistivity pseudo-sections than voltage pseudo-sections. Therefore, the apparent resistivity data is extracted from the output-file and used for further processing. It is referred to as measured apparent resistivity in the following.

The relative geometry error $\left|\frac{\delta G}{G}\right|$ is approximated using Equation (7.2). A medium electrode misplacement of $\delta x = 15\,\text{cm}$ is assumed. The results for the applied electrode configurations are shown in Figure 7.11-a. The error is highest for small n-spacings and decreases with growing n-spacing. Overall, it is smaller for the larger dipole length ($a = 20\,\text{m}$). The relative voltage error $\left|\frac{\delta U}{U}\right|$ is approximated after Equation (7.8) estimating the voltage accuracy to be ca. $\delta U = 0.5\,\text{mV}$. The resulting errors are shown in Figure 7.11-b. The error increases with increasing n-level and increasing dipole length. Comparing e.g. n-level 10/7 and n-level 20/3 shows that the sum of relative errors is 5.19% for the 10/7 configuration but only 2.75% for the 20/3 configuration. Both levels have the same pseudo-depth, but the corresponding data is weighted differently during inversion due to varying geometry and voltage errors. However, the relative voltage error depends on the apparent resistivity value. For the example shown in Figure 7.11-b, a constant $\rho_a = 100\,\Omega\text{m}$ was assumed. For an apparent resistivity of $10\,\Omega\text{m}$, the voltage error increases by a factor of 10. In case of field data, the measured apparent resistivity is used.

According to Equation (7.9), the relative error on the measured apparent resistivity is estimated by building the sum of the geometry error, the voltage error and an additional noise floor of 3%. This seems to be reasonable because of the significant topography that complicates the exact positioning of electrodes and because only two to three stacks were used to determine the average voltage data. The standard deviation *std* (in %) is added to the final data error. The same data error is as-

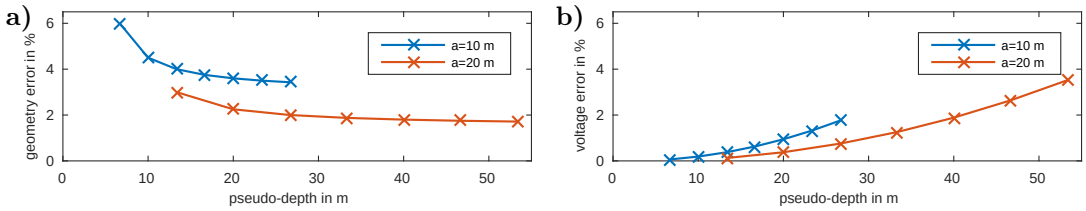

Figure 7.11.: ***a)*** *Relative geometry error* $\left|\frac{\delta G}{G}\right|$ *in % and* ***b)*** *relative voltage error* $\left|\frac{\delta U}{U}\right|$ *in % for a Pole-Dipole setup with* $a = 10\,\mathrm{m}$ *and* $a = 20\,\mathrm{m}$. *The electrode misplacement is* $\delta x = 15\,\mathrm{cm}$, *the voltage accuracy is* $\delta U = 0.5\,\mathrm{mV}$ *and the apparent resistivity is* $\rho_a = 100\,\Omega\mathrm{m}$.

signed to the corresponding measured chargeability. On the one hand, the error on apparent chargeability might be smaller because it is determined by a division of two potentials. On the other hand, the accuracy of the chargeability forward calculation depends on the accuracy of the resistivity forward calculation. The difference between the efficient resistivity ρ' and the intrinsic resistivity ρ is often small and might be of the same order as the inaccuracy of the resistivity model obtained by the resistivity inversion step. Therefore, the data error on apparent chargeability should not be smaller than that on apparent resistivity.

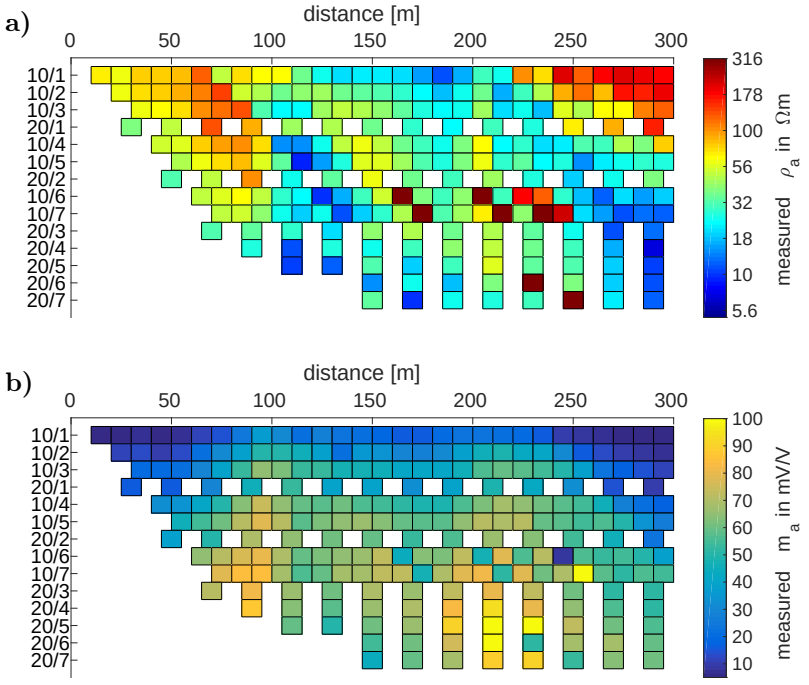

Figure 7.12.: ***a)*** *Apparent resistivity and* ***b)*** *apparent chargeability measured on Profile 3.*

As an example, the measured data acquired on Profile 3 is shown as apparent resistivity and apparent chargeability pseudo-sections in Figure 7.12. To check whether some anomalies are only induced by topography effect, the apparent resistivity data

was corrected after Fox et al. (1980) and shown in Figure 7.13. We see that the general resistivity distribution is similar. Only the amplitude of the anomalies differs. Both resistivity pseudo-sections show higher apparent resistivity values in the beginning and in the end of the profile than in the center. Therefore, we expect lateral resistivity changes close to the surface in the inversion result also if topography is considered in the inversion. In the center of the profile, the apparent resistivity is low close to the surface and increases downwards. So, a vertical change of resistivity is expected in the inversion models. The apparent chargeability pseudo-section shows rather low to intermediate chargeability values close to the surface. But there is a highly chargeable anomaly represented by growing apparent chargeability with growing pseudo-depth. The peak of about 100 mV/V is located at ca. $x = 200$ m in n-level 20/5 and the anomaly with max. 80 mV/V around $x = 90$ m in 10/7.

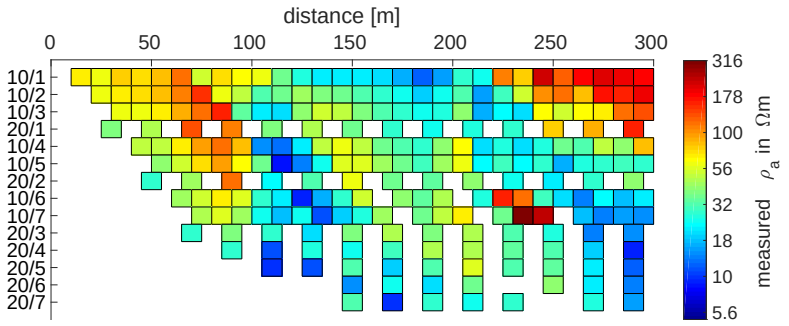

Figure 7.13.: *Apparent resistivity pseudo-section of the measured data of Profile 3 corrected for topography effects according to Fox et al. (1980). Outliers are already removed from the dataset.*

On close inspection, there are some single high resistive data points in levels 10/6 and 10/7. In order to decide which of these data points are outliers that can be removed from the dataset, an inversion is carried out, and the data-fit is evaluated by checking the difference between measured and calculated data normalized to the data error. When no data errors are considered in the inversion process, this might also be done by checking the relative difference of measured and calculated data. Here, the normalized difference is checked in two ways: First, it is visualized as a histogram in Figure 7.14. The bars represent the number of data points that have a certain normalized difference. The example shows that the normalized difference is below 5 for most data points. Only a few data points are poorly fitted, which corresponds to a large normalized difference. From that, an individual limit is set, and all data points that lie above this threshold are removed from the dataset. Besides the histogram, the normalized difference is also checked in the form of a pseudo-section as shown later in Figure 7.16-c,d. In this form, it is easy to connect poorly fitted data points directly to structures in the inversion models that are potentially only provoked by those data-points. Thus, it can be decided if such a data-point needs to be removed from the dataset because it disturbs the model or if it can remain in the dataset because it does not influence the model at all. However, it is usually worth to consider removing poorly fitted data points to allow for convergence within a few iterations. Keeping those data-points might lead to a

large number of iterations without reaching the desired data-fit in terms of $\chi = 1$. This procedure was applied to all measured datasets.

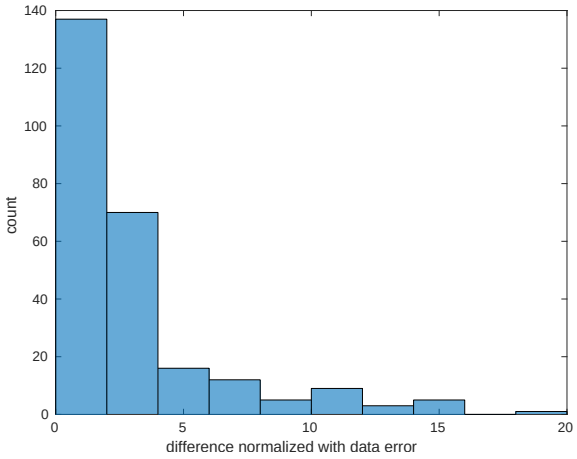

Figure 7.14.: *Profile 3: Histogram of the difference between measured and calculated data normalized on the data error.*

7.1.6. Inversion Results

Unless specified otherwise, all inversion results presented in this chapter are obtained by `ResIPIn2D` using the following settings: smoothness matrix C_b, initial and minimum regularization parameter $\lambda_{ini} = 100$ and $\lambda_{min} = 10$, stepwise reduction of λ when desired, parabola line-search for optimum step-length τ, a homogeneous initial model with $\rho^0 = 200\,\Omega$m and $m^0 = 10\,$mV/V, consideration of topography and surface distances. The shown resistivity models are the result the resistivity inversion step. Thus, they correspond to ρ' in terms of the definition in Equation (3.31). The approximate DOI_{app} is derived from the coverage isoline corresponding to $\text{cov}_t = -2.15$.

Figure 7.15 shows the inversion results for Profile 3 including models and normalized coverage. The measured data and the data-fit in terms of difference normalized to data error are shown in Figure 7.16. As expected according to the measured data, the resistivity close to the surface is with $> 100\,\Omega$m higher in the beginning and at the end of the profile than in the central valley where it is $< 15\,\Omega$m. The low resistive anomaly is located between profile distance 100-200 m and has a thickness of about 10 m. It is dipping downwards towards the end of the profile starting at $x = 200\,$m. Below this anomaly lies a high resistive structure of approximately $200\,\Omega$m with a thickness of about 40 m. All high resistive structures are followed by a transition to lower resistivity values. Since there are low resistive values in the lower n-levels of the measured data, this transition is produced by the data and are is not due to artifacts, particularly in the range $x = 70 - 120\,$m where the DOI_{app} lies below the high resistive structure. However, the DOI_{app} is shifted more towards the surface in the center of the profile. That indicates a lower sensitivity and with that less resolution below $z = 60\,$m in the center of the profile.

The chargeability model holds a highly chargeable structure below 20 m depth (below the surface) with $> 80\,\mathrm{mV/V}$. The lateral extension is about $x = 20 - 200\,\mathrm{m}$. The highest chargeabilities of $> 100\,\mathrm{mV/V}$ are confined to $x = 130 - 180\,\mathrm{m}$. This corresponds to the highest peak in measured apparent chargeability in the lower n-levels at similar profile distance. The structure corresponding to the weaker peak of measured apparent chargeability at the beginning of the profile is not as prominent. The lower boundary of the highly chargeable structure is not resolved. The coverage isoline indicates that the depth of investigation is larger than that for the resistivity model. The model responses and the normalized differences displayed in Figure 7.16 point out that the data is mostly fitted within the error bounds. There are only two outliers visible according to the apparent chargeability. But, according to the apparent resistivity, there are several badly fitted data-points especially at $x = 230 - 250\,\mathrm{m}$.

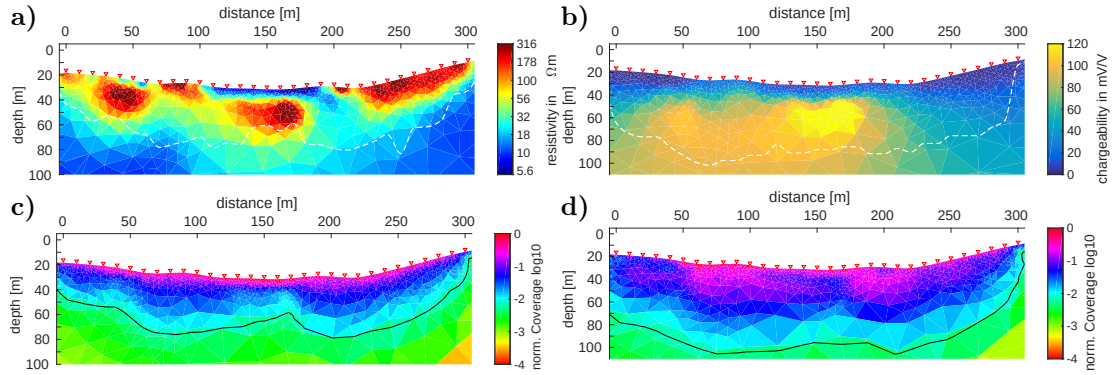

Figure 7.15.: *Inversion results Profile 3:* ***a)*** *Resistivity model, $\chi_{dc} = 2.5$,* ***b)*** *chargeability model, $\chi_{ip} = 0.98$,* ***c,d)*** *normalized coverage of the corresponding model at the top. The approximate DOI_{app} is represented by a dashed white line in the models and by a black line in the coverage plots. Electrode locations are indicated by red triangles.*

As an appraisal of the importance of topography consideration in the case of Profile 3, Figure 7.17 shows inversion results using a flat surface mesh. The models in Figure 7.17-a,b result from inversion of the data that were corrected for topography effects according to Fox et al. (1980) (see Figure 7.13) whereas the models in Figure 7.17-c,d result from the original data. For both, the resistivity and chargeability, the models are similar to each other. The shape of the resistivity structures are comparable, but the amplitudes differ slightly. In the case of the chargeability models, no differences are visible. However, in comparison to the inversion results obtained by using a topographic mesh some differences appear. The high resistive anomaly below the center, e.g., appears smaller and the amplitude is lower when using a flat surface mesh. The highly chargeable structure is more prominent with higher chargeability values in the case of a flat surface mesh. These findings are somewhat contradictory since it was shown in previous chapters that the chargeability is less influenced by the presence of topography.

Profile 8 lies at the end of our survey area. It does not cross the hill that was covered by Profiles 1-6 at the end of each profile which results in a rather flat topography.

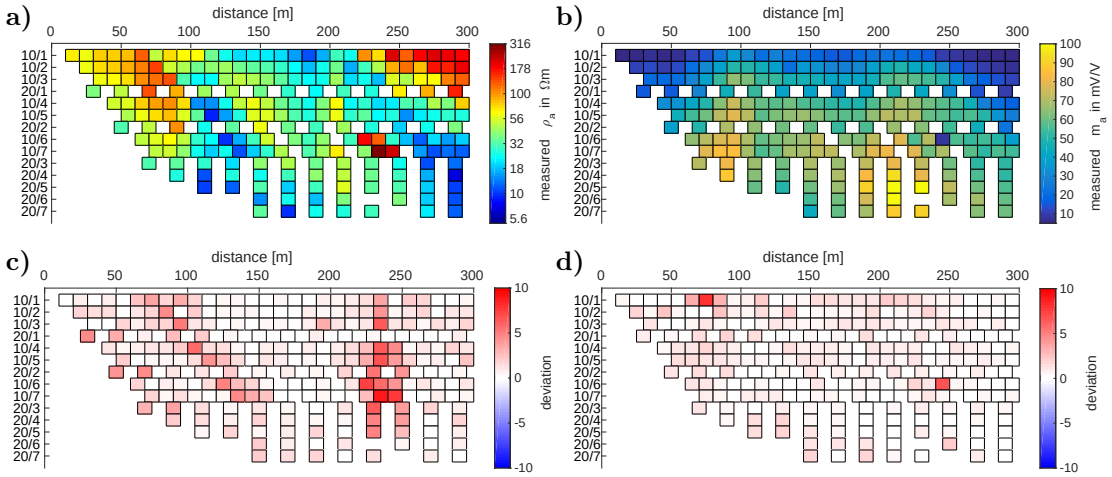

Figure 7.16.: *Inversion results Profile 3: Measured data as pseudo-sections* ***a)*** *apparent resistivity,* ***b)*** *apparent chargeability.* ***c,d)*** *Difference between the measured data and the corresponding calculated data shown above normalized to the data error.*

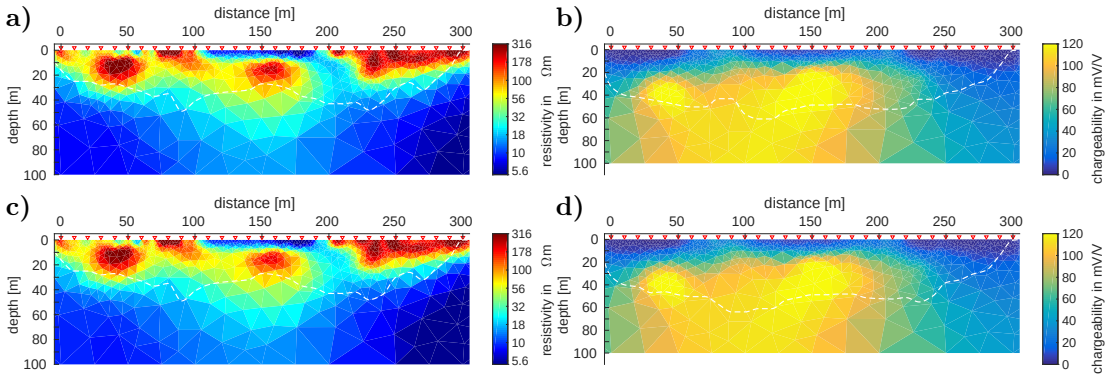

Figure 7.17.: *Profile 3:* ***a)*** *Resistivity (χ_{dc}=2.5) and* ***b)*** *chargeability (χ_{ip}=0.99) inversion result of the measured data corrected for topography effects according to Fox et al. (1980) using a flat surface inversion mesh.* ***c)*** *Resistivity (χ_{dc}=2.5) and* ***d)*** *chargeability (χ_{ip}=0.98) inversion result of the measured data without topography correction using a flat surface inversion mesh. Dashed whites lines represent the DOI_{app}. Electrode locations are indicated by red triangles.*

The resistivity and chargeability inversion models and corresponding normalized coverage are shown in Figure 7.18. The measured data and the normalized differences are shown in Figure 7.19. The models differ significantly from the models according to Profile 3, the high resistive structure close to the surface at the end of the profile is missing. Instead, the resistivities close to the surface (up to ca. 20 m below the surface) are mainly in a range between 5 Ωm and 50 Ωm. Below 20 m depth, a large high resistive structure (>150 Ωm) appears that extends from the beginning of the profile until ca. $x = 200$ m. Due to higher resistivity values, the approximate DOI is smaller than that of Profile 3, but nevertheless, the measured

data do not show a transition from high to low resistivity in depth. The measured apparent chargeability data do not contain anomalies as high as for Profile 3. However, a highly chargeable structure occurs in the chargeability model. But the lateral extension is decreased and it is located in deeper depth close to the coverage limits indicating the approximate DOI. The resistivity data-fit is generally close to the error bounds but a little higher than that according to the chargeability data-fit, both except a few outliers.

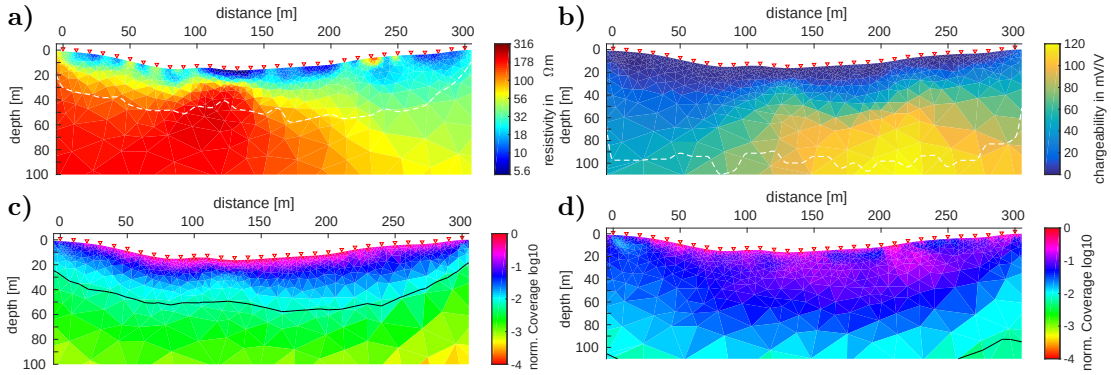

Figure 7.18.: *Inversion results Profile 8:* ***a)*** *Resistivity model, χ_{dc}=2.5,* ***b)*** *chargeability model, χ_{ip}=1.3,* ***c,d)*** *normalized coverage of the corresponding model at the top. The approximate DOI_{app} is represented by a dashed white line in the models and by a black line in the coverage plots. Electrode locations are indicated by red triangles.*

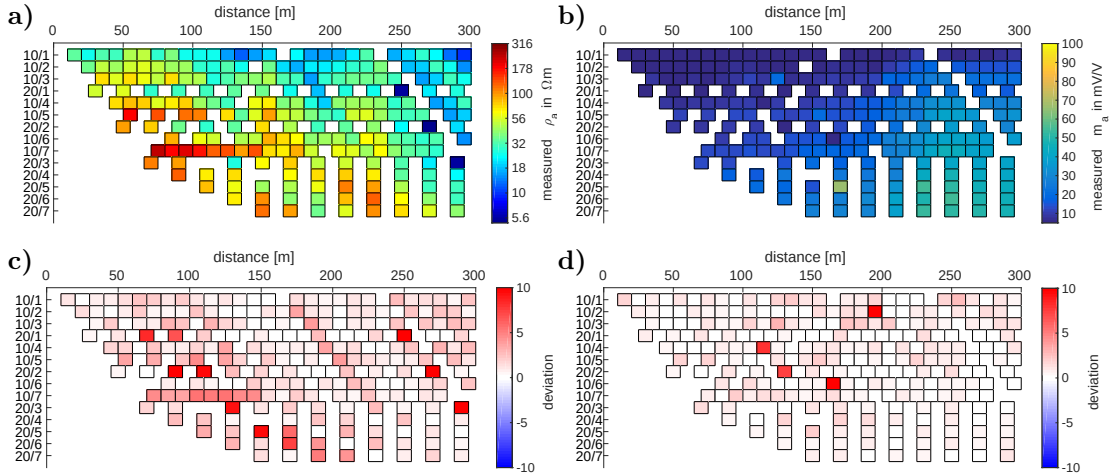

Figure 7.19.: *Inversion results Profile 8: Measured data as pseudo-sections* ***a)*** *apparent resistivity,* ***b)*** *apparent chargeability.* ***c,d)*** *Difference between the measured data and the corresponding calculated data shown above normalized to the data error.*

The individual inversion results of the remaining profiles are found in Appendix C.2. An overview over the resistivity and chargeability models of all eight profiles is shown in Figure 7.20. In this visualization, the parameters are interpolated onto a rectangular grid. Consequently, the shape of the structures appears different in comparison to the results shown before in which the distribution and shape of the inversion mesh are visible. Nevertheless, this visualization gives a good overview of all results.

The resistivity models (Figure 7.20-a) vary from profile to profile, but they have some features in common. The low resistive structure ($<15\,\Omega$m) that lies close to the surface appears in all profiles more or less in the center. It has a thickness of ca. 15 m. The dipping of this structure towards the bottom right is most prominent in Profile 3. But also in Profiles 1 and 2, there is a connection of the structure to rather low resistivity in deeper depth to the bottom right. Below this structure, the resistivity increases. The shape and size of the high resistive structure varies from profile to profile as well as the amplitude of resistivity. Overall it increases up to 100-300 Ωm. In most profiles, the structure continues from beneath the low resistive structure towards the beginning of the profiles. It is confined in depth by low resistivity in Profiles 2-5. There is another high resistive structure of 100-300 Ωm close to the surface at the end of the Profiles 1-4. This is where the profiles ascend a hill. The resistivity in this part of the models decreases from Profile 4 to Profile 8, where only ca. 10 Ωm are found. Profiles 7 and 8 do not ascend this hill.

In all chargeability models (Figure 7.20-b), the chargeability is below 10 mV/V close to the surface and a highly chargeable structure with amplitude of more than 100 mV/V appears in depth below ca. 10 m. The peak of this structure seems to be shifted from profile to profile. From that, the strike direction can be roughly approximated to be oriented from the beginning of Profile 1 to the end of Profile 8. In Profile 8, the upper boundary of the structure is lower than in the other profiles and lies close to the approximate DOI (cf. coverage limits in Figure 7.18).

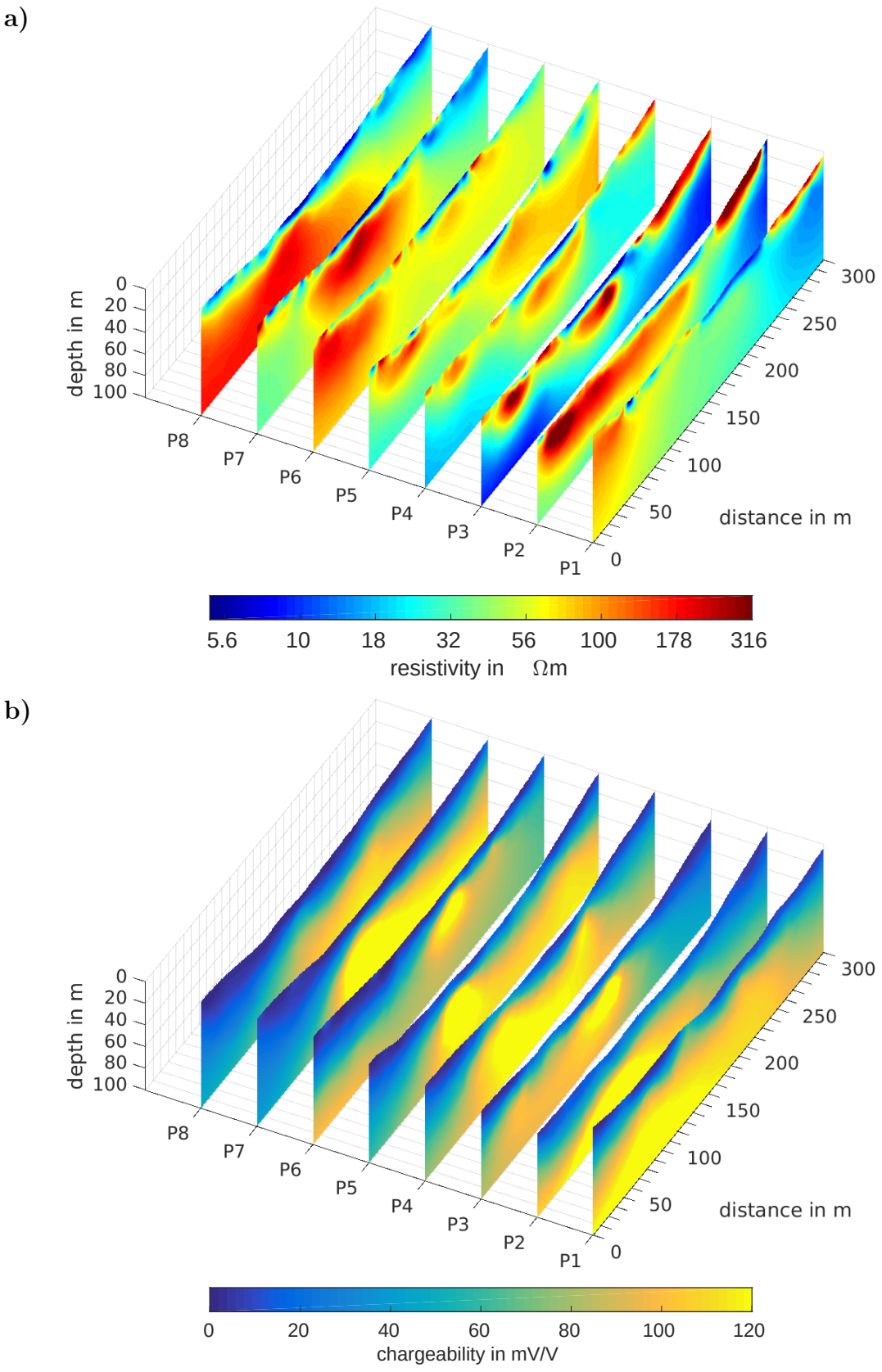

Figure 7.20.: *Overview of the inversion results:* **a)** *Resistivity models,* **b)** *Chargeability models.*

DOI index

To evaluate whether the inversion results of field data are influenced by the initial models, the DOI index according to Oldenburg and Li (1999) is displayed in Figure 7.21, exemplary for Profile 3. Since the DOI index is below 0.1 throughout both, the resistivity and the chargeability model, there is no significant influence of the initial models. This is an important information because the model update is only performed within the extension of the inversion mesh which is $-50\,\mathrm{m}$ through $350\,\mathrm{m}$ in lateral direction and $0\,\mathrm{m}$ through $200\,\mathrm{m}$ in vertical direction. The model parameters of the secondary mesh outside of this range are fixed during the iterations. Additionally to the findings in Chapter 5.3, the example with real field data proves that the applied procedure is adequate. Note that the inversion using $m_2^0 = 500\,\mathrm{mV/V}$ as initial model diverged. Therefore, the second chargeability initial model was set to $m_2^0 = 300\,\mathrm{mV/V}$ instead. However, the difference between m_{ini}^1 and m_{ini}^2 already covers a large range of chargeability.

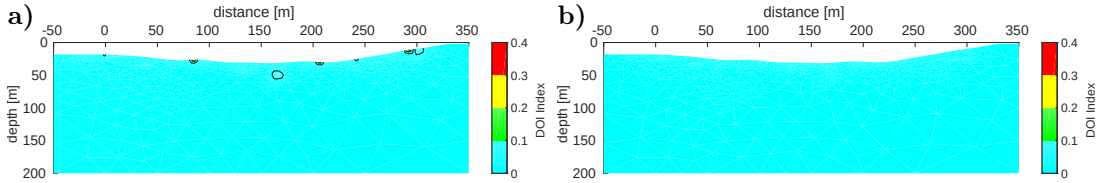

Figure 7.21.: *DOI index Profile 3:* ***a)*** *Resistivity inversion using initial parameters* $\rho_1^0 = 500\,\Omega\mathrm{m}$ *and* $\rho_2^0 = 5\,\Omega\mathrm{m}$. ***b)*** *Chargeability inversion using initial parameters* $m_1^0 = 300\,\mathrm{mV/V}$ *and* $m_2^0 = 5\,\mathrm{mV/V}$.

Approximation of the lower boundary of the chargeability anomaly

In Figure 7.22-a, the final chargeability model of the inversion of Profile 3 is displayed in a depth range of up to $z = 200\,\mathrm{m}$. In this model, no lower boundary of the highly chargeable structure is resolved. The corresponding calculated synthetic data is shown in Figure 7.22-b. In comparison to the original measured data (cf. Figure 7.16-b), the calculated data is mostly similar which is supported by the data-fit (χ). However, the apparent chargeability of the data points around profile distance $x = 150\,\mathrm{m}$ in the last n-levels is higher than the original data. This is emphasized by the relative difference between both datasets shown in Figure 7.24-a, where the overestimation of apparent chargeability is indicated by red colors (cf. n-levels 20/3 through 20/7). Note that the χ-values in Figure 7.24 are derived from linear parameters, in contrast to the χ-value in Figure 7.15-b.

In a modeling study, a lower boundary is simulated using simple models. It is evaluated whether the corresponding calculated data reproduces the measured data more adequately than the synthetic data shown in Figure 7.22-b. The chargeability model in Figure 7.22-a is used as basis. It is altered in the following way: Below a certain depth, the maximum chargeability is set to a certain limit (see Figure 7.23-a for an example). The resistivity model stays unchanged. Then, a forward calculation of

the altered chargeability models is conducted, and the resulting synthetic data is displayed in terms of relative difference with respect to the measured data (cf. Figure 7.24b-i). The left column refers to models with chargeability limit of maximum 10 mV/V. This is similar to the values that appear close to the surface. The right column refers to models with maximum chargeability of 50 mV/V which is similar to the values that appear in depth below 50 m in right part of the inversion model. The depth limit is set to 70 m in sub-figures (b,c), 80 m in (d,e), 90 m in (f,g) and 100 m in (h,i).

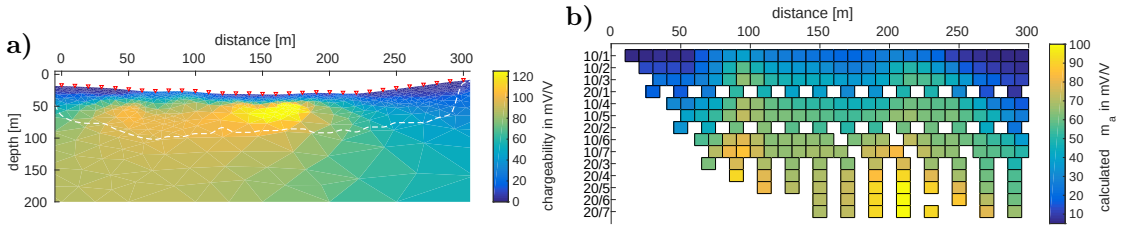

Figure 7.22.: *Profile 3:* ***a)*** *final chargeability inversion result displayed in a depth range from $z = 0 - 200$ m,* ***b)*** *calculated synthetic apparent chargeability data corresponding to the model in a).*

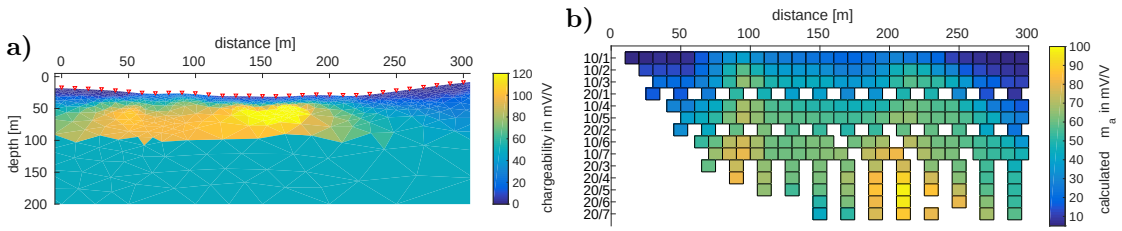

Figure 7.23.: ***a)*** *Chargeability model with maximum chargeability of* 50 mV/V *below* 100 m *depth.* ***b)*** *Calculated apparent chargeability corresponding to the model in a).*

According to the relative differences and χ-values that result from the chargeability limit of maximum 10 mV/V (left column), the following conclusions are made: When the boundary is located in 70 m or 80 m depth, the synthetic data is strongly influenced resulting in high (negative) relative difference with respect to the measured data beginning in the 3rd n-level downwards. Furthermore, the data-misfit is increased according to $\chi = 1.9$ and $\chi = 1.5$, respectively. Overall, relative difference and χ decreases with growing depth-limit, but even if the limit is located at $z = 100$ m, the negative relative difference indicates that the values of the synthetic data are smaller than the measured data in the last n-levels. Also, the χ-values are larger than that of the inversion model.

Referring to the relative differences according to the chargeability limit of maximum 50 mV/V (right column), the conclusions are: The relative differences are mostly negative, but not as strong as in the left column. When the depth limit is located in 70 m or 80 m, the relative difference of those data points, which were overestimated

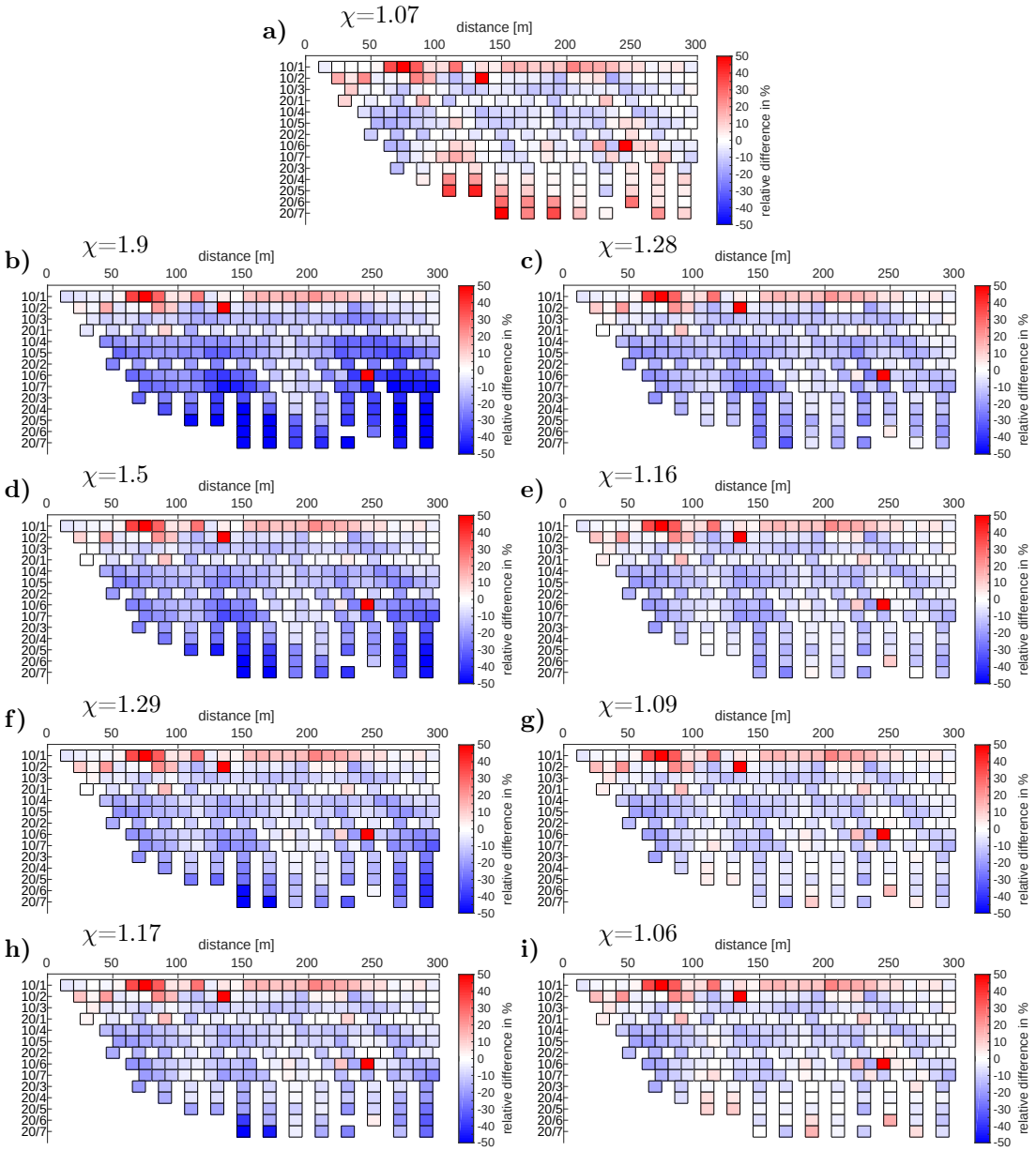

Figure 7.24.: *Profile 3: relative difference between measured data and the chargeability data calculated from models that were varied based on the final inversion model shown in Figure 7.22.* ***a)*** *Original inversion result,* ***b)*** *max.* 10 mV/V *below* $z = 70$ m, ***c)*** *max.* 50 mV/V *below* $z = 70$ m, ***d)*** *max.* 10 mV/V *below* $z = 80$ m, ***e)*** *max.* 50 mV/V *below* $z = 80$ m, ***f)*** *max.* 10 mV/V *below* $z = 90$ m, ***g)*** *max.* 50 mV/V *below* $z = 90$ m, ***h)*** *max.* 10 mV/V *below* $z = 100$ m, ***i)*** *max.* 50 mV/V *below* $z = 100$ m. *Here, the data misfit* χ *is determined using linear parameters.*

by the inversion model, are still clearly negative. The data-misfit is with $\chi = 1.28$ and $\chi = 1.16$ higher than that of the inversion model. In case of the limit in 90 m or 100 m depth, however, the relative difference in the lowest n-levels is still negative, but closer to zero than in (Figure 7.24-a). The smallest relative difference

corresponds to the model with lower boundary in 100 m depth. The corresponding data-fit is with $\chi = 1.06$ even slightly better than that of the inversion model ($\chi = 1.07$). The model and the corresponding calculated data is shown in Figure 7.23. Also, the visual comparison between the calculated data-sets (Figure 7.23-b) reveals that the data in the lower n-levels is in better agreement with the measured data.

According to this study, the boundary is assumed to be located between 90 m and 100 m depth. This is surely only a rough estimation because only a limited amount of altered models were investigated. Furthermore, no data errors were considered in this investigation. Therefore, single data points could be over-fitted. The deviation between measured and calculated data, normalized to the data error are displayed in Figure C.14.

7.1.7. Comparison of the Inversion Results

Exemplary for all field data discussed above, the inversion results of Profile 3 obtained with the newly developed algorithm `ResIPIn2D` are compared to results obtained by the algorithms `BERT` and `Res2DInv`. Furthermore, it is assessed whether the resistivity model resulting from the DC inversion conforms with the resistivity model resulting from inversion of RMT data.

Comparison with Inversion Results Obtained by Other Algorithms

As a comparison, the resistivity and chargeability inversion results for Profile 3 obtained by `BERT` and `Res2DInv` are displayed together with the results obtained by `ResIPIn2D` in Figure 7.25 and Figure 7.26, respectively. Referring to the resistivity results, generally, the same structures are resolved in all three models. However, also differences occur. The structures in the model obtained by `BERT` (Figure 7.25-b) are thicker and less resistive than in the `ResIPIn2D` model (Figure 7.25-a). The near surface high resistive structure does not continue towards the end of the profile. The `Res2DInv` resistivity model (Figure 7.25-c) shows a larger variation of resistivity than the other models. The color scale is exceeded in both directions (minimum and maximum value). Since `Res2DInv` uses rectangular model cells, the shape of structures appears more blocky. However, the thickness of the near-surface structures is comparable to the `ResIPIn2D` result. But, the high resistive block below 30 m depth in the center, is interrupted by lower resistivity.

The algorithms `ResIPIn2D` and `BERT` apply an error weighting scheme. The data-fit of the `ResIPIn2D` resistivity inversion in terms of χ is with $\chi = 2.5$ slightly better than that of the `BERT` inversion which is $\chi = 2.7$. `Res2DInv` does not apply error weighting. Thus, the according data-fit is given in terms of an RMS error which is 11.8%. In comparison, the data-fit of the `ResIPIn2D` model is slightly better with 7.4%.

The difference between the triangular mesh elements and the rectangular model blocks is more prominent in the chargeability models in Figure 7.26. The smoothness constraints lead to chargeability transitions over several triangular elements whereas

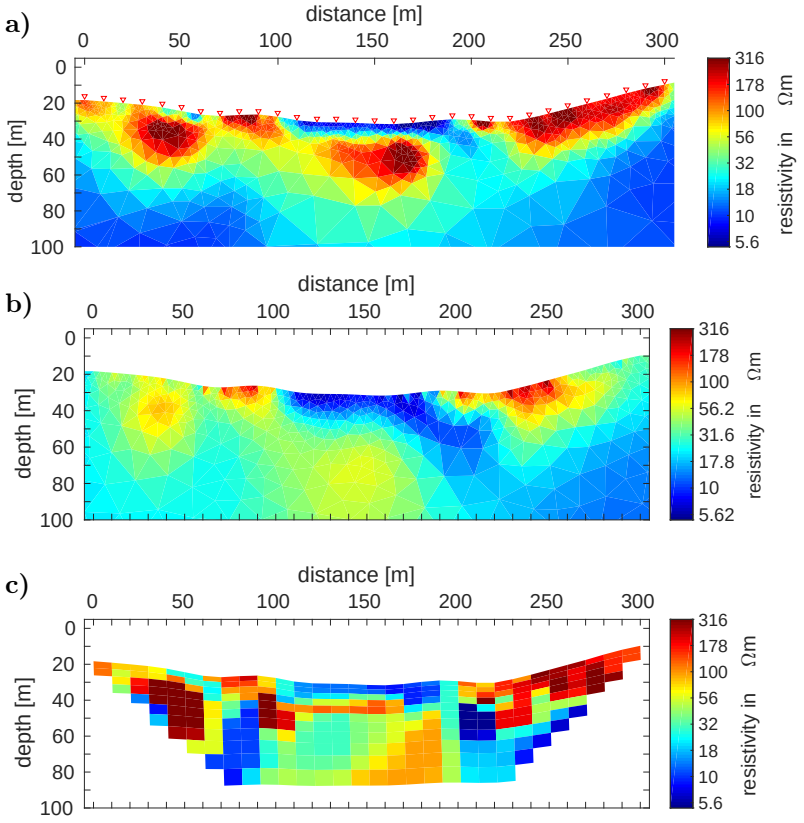

Figure 7.25.: *Profile 3: Resistivity model obtained by inversion using* **a)** `ResIPIn2D` $\chi = 2.5$, *RMS=7.4%,* **b)** `BERT` $\chi = 2.7$ *and* **c)** `Res2DInv` *RMS=11.8%.*

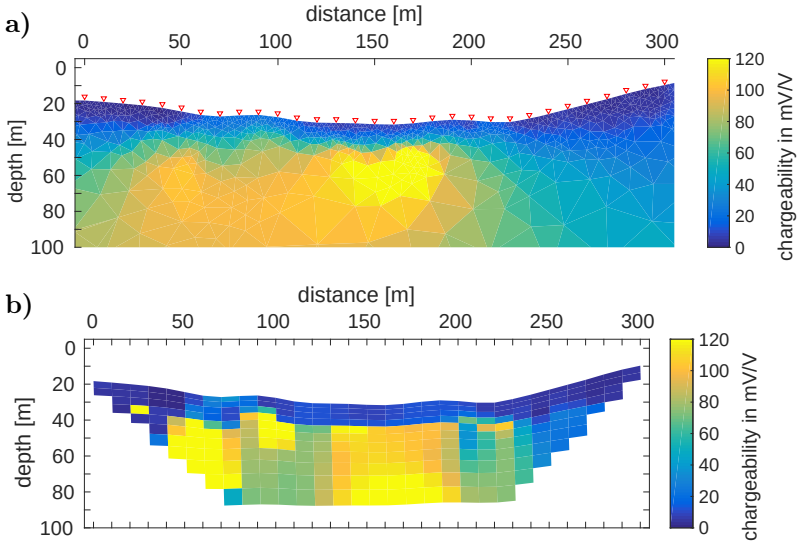

Figure 7.26.: *Profile 3: Chargeability model obtained by inversion using* **a)** `ResIPIn2D` $\chi = 0.98$, *RMS=6.3% and* **b)** `Res2DInv` *RMS=2.15%.*

the chargeability difference between neighboring rectangular blocks is abrupt. However, both models have several features in common, e.g. the chargeability close to the surface which is <15 mV/V and the thickness of this surface layer which is about 15 m. In the measured data (Figure 7.16-b), two peaks of increased apparent chargeability are visible. Referring to the `ResIPIn2D` model (Figure 7.26-a), this results in a wide structure with chargeability of >80 mV/V including two structures where the chargeability reaches a local maximum. The stronger anomaly is located between profile distance 130-180 m and has a chargeability of 120 mV/V and the weaker anomaly around $x = 50$ m has a chargeability of ca. 100 mV/V. These peaks are connected by a chargeability values of more than 80 mV/V. In the `Res2DInv` model (Figure 7.26-b), the chargeability difference between the peak structures and the area in between is larger, and the strong anomaly is located in deeper depth. Both models resolve the right boundary of the highly chargeable structure around profile distance $x = 200$ m. The lower boundary of the chargeable structure is resolved by neither algorithm. In terms of the RMS error, the data-fit of `Res2DInv` is with 2.15% better than that according to `ResIPIn2D`, which is 6.3%. But, due to the applied error weighting, the new algorithm terminated because the desired misfit of $\chi = 1$ was achieved. That means, for the estimated data errors, the `Res2DInv` result is actually over-fitted.

Comparison with RMT Results

Figure 7.27 shows the RMT inversion result of the TM mode data acquired on Profile 3. The inversion was carried out using the 2D FD inversion algorithm of Mackie et al. (1997). Topography was not considered during the inversion. However, the obtained resistivity model agrees with the DC inversion results, at least in the overlapping depth range. There is a low resistive area ($\rho < 10\,\Omega$m) close to the surface in the center of the profile which is dipping towards the end of the profile. The resistivity at the end of the profile is highest with values > 200 Ωm. Even though the amplitude of resistivity does not exactly fit that obtained by the DC data inversion, the overall structures and relative resistivity values of these structures are in good correspondence. According to the skin-depth, the depth of investigation of the RMT result is 20-30 m. However, beneath the low resistive structure in the center, the resistivity increases. This agrees with the DC model, although the RMT sensitivity is low.

7.1.8. Summary and Interpretation

In this chapter, it was shown, that the inversion of field data with `ResIPIn2D` results in reasonable resistivity and chargeability models that are comparable to the results obtained by the well-established algorithms `BERT` and `Res2DInv`. This is supported by the comparison with an RMT inversion result that resolved similar structures up to a depth of ca. 20 m.

The near surface high resistive structure that is visible in the resistivity models of Profiles 1-4 correlates with the appearance of outcropping rocky material on the hill

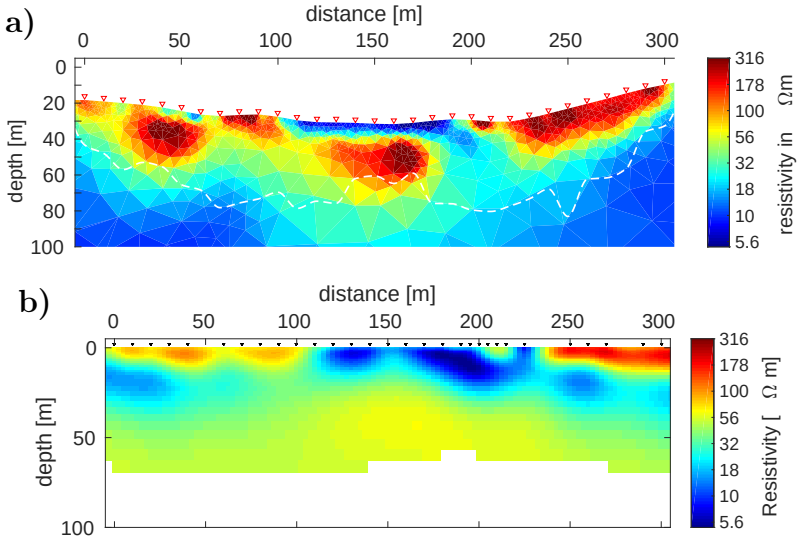

Figure 7.27.: *Profile 3:* ***a)*** *DC Resistivity inversion result.* ***b)*** *RMT inversion result of the TM mode obtained using the algorithm by Mackie et al. (1997); λ=25, RMS=4.4%. The location of RMT stations is indicated by black triangles.*

at the end of these profiles. The near surface low resistive structure in the center of all profiles corresponds to the trough of the valley and the location of agricultural fields. Thus, the low resistivity most likely indicates the presence of sediments in the valley. In Profiles 7 and 8, the near surface resistivity is low throughout the whole profile distance. This is reasonable because these profiles do not ascend the hill at the end, but are entirely located in a field. Below this low resistive structure, most models reveal a high resistive anomaly which stretches towards the beginning of the profiles. This structure has a similar resistivity as the structure that correlates to the near surface material below the hill. Thus it can be assumed to consist of similar material.

The presence of the ore deposit is not clearly revealed by the resistivity models alone which is certainly due to its disseminated form. However, the chargeability models show values of partly more than 100 mV/V below a depth of ca. 10 m below the surface. These values indicate the presence of sulfidic ore content. According to the inversion results, the lateral extension can be estimated, and the strike direction of the deposit is roughly oriented from the beginning of Profile 1 to the end of Profile 8. However, the lower boundary of this structure was not resolved by the inversion models. It was shown by a modeling study that the presence of a lower boundary enhances the data-fit of the lower n-levels. According to this study, it is approximated in depth between $z = 90 - 100$ m.

By the comparison of the resistivity and chargeability results with borehole information, the obtained physical parameters can be linked to the stratigraphy of earth material. Figure 7.28 shows the inversion models of Profile 1 together with a visualization of borehole information obtained from HKS4 (cf. Chapter 7.1.2), which is located at profile distance 250 m. The colors of the borehole stratigraphy refer to resistivity values derived from the inversion results. The dacite layers can be

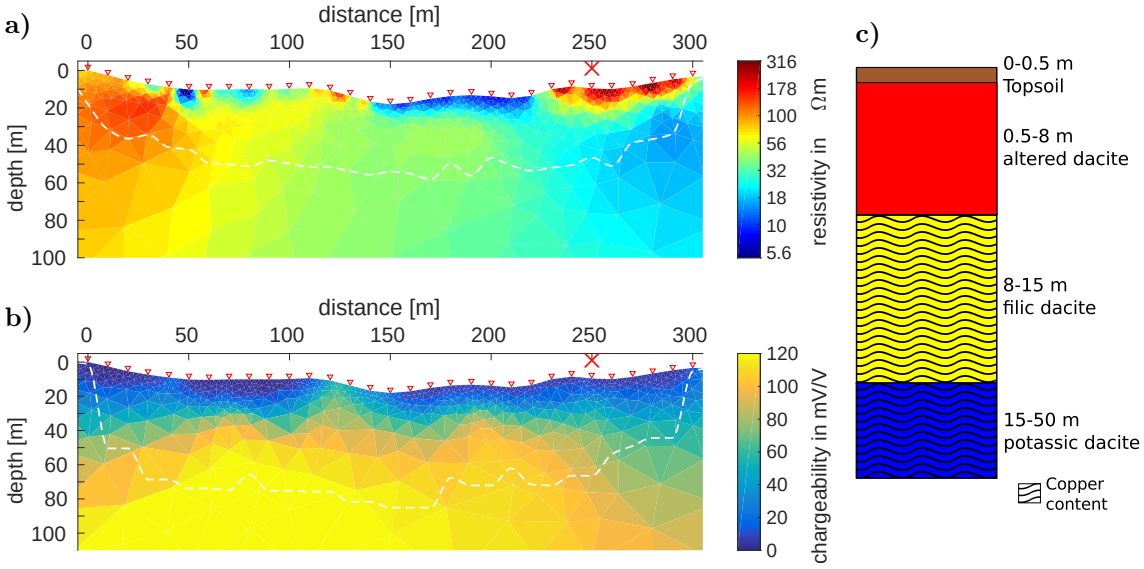

Figure 7.28.: *Profile 1:* ***a)*** *Resistivity ($\chi_{dc} = 1.6$) and* ***b)*** *chargeability inversion result ($\chi_{ip} = 0.95$). Electrode locations are indicated by red triangles. The dashed white line represents the DOI_{app}.* ***c)*** *Borehole information obtained from HKS4 (cf. Chapter 7.1.2) located at profile distance 250 m (red cross in a and b).*

associated with resistivity values of $> 200\,\Omega$m for the altered dacite, $50 - 100\,\Omega$m for the filic dacite and $< 50\,\Omega$m for the potassic dacite. These values are, however, in a smaller magnitude order than the resistivity of dacite listed in Table A.2. But surely, the texture and composition of the present dacites leads to altered resistivities. Furthermore, according to the simplified geological map in Figure 7.3, the surface layer in the survey area is covered by sediments of the Miocene-Pliocene. This fits to the low resistive surface layer in the center of the valley.

The copper and copper ore content below 8 m depth, identifies with increased chargeability values of partly $> 100\,$mV/V. Please refer to Table A.3 and Table A.4 in the Appendix for a list of chargeability values of sulfides and other materials. Note that the values are not given in Newmont Standard, therefore the chargeabilities are rather quantitative. The values in Table A.4 were determined after a charging time of 1 min. Thus, the values are generally increased in comparison to the field data. However, according to these literature values, a content of 2-8% leads to a significant IP effect. The chargeability increases with growing sulfide content. Furthermore, copper sulfides chalcocite, chalcopyrite and bornite, and copper produce a significant IP effect even for concentrations of 1%.

8. Discussion and Conclusions

The main focus of this thesis was the development of a 2D DC/TDIP inversion algorithm, denoted as `ResIPIn2D`, applying a smoothness constrained regularization approach on unstructured meshes. In contrast to established inversion algorithms, a new composition of finite element forward calculation and a locally constrained, error-weighted Gauss-Newton approach including a non-linear IP chargeability inversion was created. In particular, the employment of an unstructured inversion mesh with an incorporation of topography is to be mentioned. Due to the application of a non-linear IP inversion, the algorithm is capable of reproducing strong chargeability anomalies.

The implemented 2D finite element forward algorithm includes a Fourier-Cosine transformation of electrical potential from 3D to 2.5D wavenumber domain and a singularity removal by separation of potentials into a primary and secondary part. The calculation of the primary potential from a homogeneous half-space and the finite element solution of the secondary potential corresponding to a 2D conductivity distribution are conducted on separate unstructured triangular meshes to meet different requirements. Thus, the primary mesh is a locally refined version of the secondary mesh to increase accuracy in the direct vicinity of the electrodes. The extension of both meshes is sufficient to meet the boundary conditions. The advantage of unstructured meshes over structured meshes is that local refinement, where accuracy is needed, is possible without globally increasing the number of mesh elements significantly. Therefore, complex surface topography and subsurface structures can be reproduced well. Where sensitivity is small, mesh elements can be large to keep the number of DOF small.

It was shown that the forward calculation in `ResIPIn2D` produces accurate synthetic data. This was investigated by comparison of forward responses of 1D and 2D resistivity models with analytical solutions and FE and FD solutions of established algorithms namely `DC2DInvRes` and `Res2DMod`. Furthermore, it was shown that the effect of singularity removal is most positive for the synthetic data of the very first n-levels while subsequent n-levels are affected less by the singularity problem. Therefore, the use of the singularity removal technique is recommended whenever possible. However, the analytical solution of a homogeneous half-space is not valid for distinct surface topography models. Thus, modeling under topography requires calculation of the total potential. This might lead to noisy synthetic data corresponding to depths close to the surface.

The implemented IP perturbation model according to Seigel (1959) allows forward calculation of synthetic apparent chargeability data from double DC forward modeling. The solution obtained by `ResIPIn2D` is close to synthetic data calculated with `Res2DMod`.

The Gauss-Newton inversion scheme implemented in `ResIPIn2D` applies error weighting and local smoothness constraints on an unstructured triangular mesh. Due to insignificant sensitivity far from electrode locations, the inversion mesh is an excerpt of the secondary mesh. Therefore, unnecessary DOF are avoided. Inversion of DC resistivity and IP chargeability data is realized by a two-step inversion approach proposed by Oldenburg and Li (1994). After a DC inversion recovering a resistivity model, a non-linear IP inversion recovers a chargeability model. The method is slightly modified since it is assumed that the DC inversion step recovers the effective resistivity model instead of the intrinsic resistivity model as was noted in the practical considerations by Oldenburg and Li (1994). Therefore, the IP inversion step finds a chargeability model update and alters the intrinsic resistivity model in every iteration which is required for the calculation of the IP forward response. The applicability of inversion using `ResIPIn2D` was assessed by inversion of synthetic data and comparison to resistivity and chargeability models obtained by established algorithms, namely `BERT` and `Res2DInv`. At the same time, several computational and practical questions were investigated:

It was shown that chargeability structures are reproduced by inversion independent from the corresponding intrinsic or effective resistivity model. This is essential for the interpretation of field data because e.g. resistivity signatures of finely distributed chargeable material are often hard to detect while chargeability signatures are strong.

Furthermore, different approaches of smoothness constraint matrices were introduced and compared. Reasonable results are obtained by the matrix denoted as $\mathbf{C}_a$ that is the general form of the discrete approximation of first order derivatives. However, the employment of the matrix denoted as $\mathbf{C}_b$ is recommended because it includes the consideration of the varying length of triangle sides and element areas in the applied unstructured mesh. Moreover, it was shown that the application of a stepwise cooling produces promising results. This procedure starts with the (production) of a smooth model by using a rather large regularization parameter in the first inversion iterations. The regularization parameter is only decreased when the data-fit is not decreasing further. This procedure is continued until either the convergence criterion is met or a predefined minimum regularization parameter is reached. Moreover, it was shown that the application of an inexact line-search for an optimum model update step-length in the form of the two-point parabola technique serves to improve convergence and reduce the required number of iterations.

Another aspect that was investigated was the depth of investigation. Due to the applied local regularization, the DOI can not be determined from inversion models obtained using different initial models because the inversion results are merely independent of the choice of starting models. Consequently, an approximate DOI was derived from cumulative sensitivity. To do so, a coverage threshold is derived from the normalized coverage corresponding to a homogeneous half-space model: the coverage value that coincides with the depth of investigation according to the rule of thumb is defined as a threshold. Generally, a homogeneous half-space is used as the initial model. Thus, the coverage threshold is derived from the cumulative sensitivity of the first iteration, and the corresponding isoline is denoted as approximate DOI in the coverage plot of the final inversion iteration. The applicability of this approximation was tested by inversion of synthetic data calculated from block

models with lower boundaries in different depths. According to these examples, the approximate DOI sometimes underestimates the depth of investigation because the presence of the lower boundary of the model block was detected even below the defined isoline. However, the approximate DOI helps to limit well resolved model domains from poorly resolved domains. Furthermore, it signals sensitivity changes in 2D models in lateral direction.

The importance of consideration of effects caused by distinct surface topography was shown by forward modeling and inversion of synthetic data. Regarding the interpretation of field data, it is recommended to prefer measured voltage data over measured apparent resistivity. In any case, it is to make sure that the same electrode distances (surface distance or horizontal distance) are used for the geometry factor to prevent errors. It was shown that the newly developed algorithm is capable of reproducing original resistivity and chargeability models with surface topography to a reasonable extent. This was confirmed by comparison with inversion models obtained by `BERT` and `Res2DInv`. According to the presented examples, it is recommended to include the surface topography directly into the inversion mesh. However, the inversion of data that was corrected for topography effects according to Fox et al. (1980) using a flat surface inversion mesh also produces reasonable results. But since the distances between the electrodes and from the surface to subsurface structures vary, reproduced structures can be deformed or appear in a different depth. However, an inversion of data containing significant topography effects using a flat surface mesh are not recommended.

When distinct topography is present, the DOI according to the rule of thumb is not valid. In this case, the coverage threshold for the approximate DOI should be derived from a homogeneous half-space on a flat surface mesh using the same electrode setup. Undoubtedly, this represents only an estimation, but it still provides a clue about lateral and vertical sensitivity changes and a transition from well resolved to poorly resolved model domains.

The discussed chargeability models revealed that the chargeability data is not as affected by topography effects as the resistivity data. This is because the apparent chargeability is determined by a division of two electrical potentials that are superposed by the same topography effects. Nevertheless, the chargeability data is subject to the same drawbacks as the resistivity data that are corrected for topography effects.

Finally, the new algorithm was successfully applied to field data acquired on a copper ore deposit in Turkey. The ore deposit is mainly of disseminated form. Therefore, it was expected that the corresponding resistivity signature is ambiguous. But, due to sulfide content, a strong chargeability effect was expected. The obtained resistivity and chargeability inversion results fulfill these expectations. A highly chargeable structure is resolved with chargeability values of more than 100 mV/V. This structure does not coincide clearly with a corresponding resistivity structure. For an exemplary profile, the resistivity model was confirmed by inversion results obtained by `BERT` and `Res2DInv` and by an RMT inversion result. The corresponding chargeability model is similar to the model obtained by `Res2DInv`, although there are also deviations that are caused by different model parameterization and smoothing.

The lower boundary of the highly chargeable structure was not resolved by the applied Pole-Dipole field setup. Thus it was approximated by a forward modeling study.

The newly developed algorithm `ResIPIn2D` can be used as a standard tool for 2D DC/TDIP inversion at the IGM Cologne by future students. Possible further enhancements are e.g. an employment of adaptive grids that automatically refine locally where accuracy is required or where the gradient of electrical potential is high. This improves the reproduction of resistivity (or chargeability) structures. This is of special interest for field data when no apriori information is available. The applied IP chargeability inversion is suited best for strong IP effects. Especially in the case of noisy data, a weak chargeability effect is hard to detect. Furthermore, the implemented IP model is limited to the consideration of IP chargeability. In frequency domain IP, more detailed IP models exist, such as the Cole-Cole model. These models allow the appraisal of further parameters describing the texture of porous rocks. Approaches to retrieve this information from time-domain data were presented by Hönig (2002), Hördt et al. (2006), Hönig and Tezkan (2007) or Fiandaca et al. (2012).
The finite element forward solution, as well as the inverse problem, is solved by an iterative preconditioned conjugate gradient solver. The implementation of a direct solver could reduce the computational time. The new algorithm was tested only for local regularization schemes. The application of global regularization is still to be tested.

Bibliography

Archie, G. E. (1942). The electrical resistivity log as an aid in determining some reservoir characteristics. *Trans. Am. Inst. Min. Metal. and Petr. Eng.*, 146:54–62.

Bairlein, K., Hördt, A., and Nordsiek, S. (2014). The influence on sample preparation on spectral induced polarization of unconsolidated sediments. *Near Surface Geophysics*, 12(5):667–677.

Barker, R. (1989). Depth of investigation of collinear symmetrical four-electrode arrays. *Geophysics*, 54(8):1031–1037.

Beard, L. P., Hohmann, G. W., and Tripp, A. C. (1996). Fast resistivity/ip inversion using a low-contrast approximation. *Geophysics*, 61(1):169–179.

Broyden, C. (1972). *Quasi-Newton methods*. Academic Press, London.

Candansayar, M. (2008). Two-dimensional individual and joint inversion of three- and four-electrode array dc resistivity data. *Journal of Geophysics and Engineering*, 5(3):290.

Coggon, J. (1971). Electromagnetic and electrical modeling by the finite element method. *Geophysics*, 36(1):132–155.

Cole, K. S. and Cole, R. H. (1941). Dispersion and absorption in dielectrics i. alternating current characteristics. *The Journal of chemical physics*, 9(4):341–351.

Constable, S. C., Parker, R. L., and Constable, C. G. (1987). Occam's inversion: A practical algorithm for generating smooth models from electromagnetic sounding data. *Geophysics*, 52(3):289–300.

Dahlin, T. and Zhou, B. (2004). A numerical comparison of 2d resistivity imaging with 10 electrode arrays. *Geophysical Prospecting*, 52(5):379–398.

Dey, A. and Morrison, H. (1979). Resistivity modelling for arbitrarily shaped two-dimensional structures. *Geophysical Prospecting*, 27(1):106–136.

Dias, C. A. (1968). *A non-grounded method for measuring electrical induced polarization and conductivity*. PhD thesis, University of California, Berkeley, USA.

Dias, C. A. (2000). Developments in a model to describe low-frequency electrical polarization of rocks. *Geophysics*, 65(2):437–451.

Dilek, Y. and Flower, M. F. (2003). Arc-trench rollback and forearc accretion: 2. a model template for ophiolites in albania, cyprus, and oman. *Geological Society, London, Special Publications*, 218(1):43–68.

Erdoğan, E., Demirci, I., and Candansayar, M. E. (2008). Incorporating topography into 2d resistivity modeling using finite-element and finite-difference approaches. *Geophysics*, 73(3):F135–F142.

Farquharson, C. G. and Oldenburg, D. W. (2004). A comparison of automatic techniques for estimating the regularization parameter in non-linear inverse problems. *Geophysical Journal International*, 156(3):411–425.

Fiandaca, G., Ramm, J., Binley, A., Gazoty, A., Christiansen, A. V., and Auken, E. (2012). Resolving spectral information from time domain induced polarization data through 2-d inversion. *Geophysical Journal International*, page ggs060.

Fox, R. C., Hohmann, G. W., Killpack, T. J., and Rijo, L. (1980). Topographic effects in resistivity and induced-polarization surveys. *Geophysics*, 45(1):75–93.

Freund, R. W. and Nachtigal, N. M. (1994). An implementation of the qmr method based on coupled two-term recurrences. *SIAM Journal on Scientific Computing*, 15(2):313–337.

Freund, R. W. and Nachtigal, N. M. (1996). Qmrpack: a package of qmr algorithms. *ACM Transactions on Mathematical Software (TOMS)*, 22(1):46–77.

Friedel, S. (2003). Resolution, stability and efficiency of resistivity tomography estimated from a generalized inverse approach. *Geophysical Journal International*, 153(2):305–316.

Griffiths, D. and Barker, R. (1994). Electrical imaging in archaeology. *Journal of Archaeological Science*, 21(2):153–158.

Günther, T. (2004). *Inversion Methods and Resolution Analysis for the 2D/3D Reconstruction of Resistivity Structures from DC Measurements*. PhD thesis, Freiberg University of Mining and Technology, Germany, available from http://fridolin.tu-freiberg.de.

Günther, T., Rücker, C., and Spitzer, K. (2006). Three-dimensional modelling and inversion of dc resistivity data incorporating topography-ii. inversion. *Geophysical Journal International*, 166(2):506–517.

Hansen, P. C. and O'Leary, D. P. (1993). The use of the l-curve in the regularization of discrete ill-posed problems. *SIAM Journal on Scientific Computing*, 14(6):1487–1503.

Holcombe, H. T. and Jiracek, G. R. (1984). Three-dimensional terrain corrections in resistivity surveys. *Geophysics*, 49(4):439–452.

Hönig, M. (2002). *Entwicklung und Anwendung von Auswertealgorithmen für die induzierte Polarisation im Zeitbereich in bis zu drei Dimensionen: in German*. PhD thesis, University of Cologne, Germany.

Hönig, M. and Tezkan, B. (2007). 1d and 2d cole-cole-inversion of time-domain induced-polarization data. *Geophysical Prospecting*, 55(1):117–133.

Hördt, A., Blaschek, R., Kemna, A., and Zisser, N. (2007). Hydraulic conductivity estimation from induced polarisation data at the field scale-the krauthausen case history. *Journal of Applied Geophysics*, 62(1):33–46.

Hördt, A., Hanstein, T., Hönig, M., and Neubauer, F. M. (2006). Efficient spectral ip-modelling in the time domain. *Journal of Applied Geophysics*, 59(2):152–161.

Kang, S. and Oldenburg, D. W. (2016). On recovering distributed ip information from inductive source time domain electromagnetic data. *Geophysical Journal International*, 207(1):174–196.

Karaoğlan, F., Parlak, O., Klötzli, U., Koller, F., and Rızaoğlu, T. (2013). Age and duration of intra-oceanic arc volcanism built on a suprasubduction zone type oceanic crust in southern neotethys, se anatolia. *Geoscience Frontiers*, 4(4):399–408.

Karaoulis, M., Revil, A., Tsourlos, P., Werkema, D., and Minsley, B. (2013). Ip4di: A software for time-lapse 2d/3d dc-resistivity and induced polarization tomography. *Computers & Geosciences*, 54:164–170.

Keary, P., Brookes, M., and Hill, I. (2002). *An introduction to Geophysical exploration*. 3rd edn, Blackwell Scientific Publications.

Kemna, A. (1995). Tomographische inversion des spezifischen widerstandes in der geoelektrik: in german. Master's thesis, University of Cologne, Germany.

Kemna, A. (2000). *Tomographic inversion of complex resistivity: theory and application*. PhD thesis, Ruhr University Bochum, Germany, Der andere Verlag, Bochum, Germany.

Kemna, A., Binley, A., Cassiani, G., Niederleithinger, E., Revil, A., Slater, L., Williams, K. H., Orozco, A. F., Haegel, F.-H., Hoerdt, A., et al. (2012). An overview of the spectral induced polarization method for near-surface applications. *Near Surface Geophysics*, 10(6):453–468.

Kemna, A., Binley, A., and Slater, L. (2004). Crosshole ip imaging for engineering and environmental applications. *Geophysics*, 69(1):97–107.

Kemna, A., Vanderborght, J., Kulessa, B., and Vereecken, H. (2002). Imaging and characterisation of subsurface solute transport using electrical resistivity tomography (ert) and equivalent transport models. *Journal of Hydrology*, 267(3):125–146.

Kim, J.-H., Yi, M.-J., Park, S.-G., and Kim, J. G. (2009). 4-d inversion of dc resistivity monitoring data acquired over a dynamically changing earth model. *Journal of Applied Geophysics*, 68(4):522–532.

Knödel, K., Krummel, H., and Lange, G. (1997). *Handbuch zur Erkundung des Untergrundes von Deponien und Altlasten, Band3: Geophysik*. Springer Verlag, Berlin.

Kozlu, H., Prichard, H., Melcher, F., Fisher, P., Brough, C., and Stueben, D. (2014). Platinum group element (pge) mineralisation and chromite geochemistry in the berit ophiolite (elbistan/kahramanmaraş), se turkey. *Ore Geology Reviews*, 60:97–111.

LaBrecque, D. J., Miletto, M., Daily, W., Ramirez, A., and Owen, E. (1996). The effects of noise on occam's inversion of resistivity tomography data. *Geophysics*, 61(2):538–548.

Li, Y. and Oldenburg, D. W. (2000). 3-d inversion of induced polarization data. *Geophysics*, 65(6):1931–1945.

Li, Y. and Spitzer, K. (2002). Three-dimensional dc resistivity forward modelling using finite elements in comparison with finite-difference solutions. *Geophysical Journal International*, 151(3):924–934.

Loke, M. (2002). Res2dmod ver. 3.01: Rapid 2d resistivity forward modelling using the finite difference and finite-element methods. *Software manual*.

Loke, M. and Barker, R. (1996a). Practical techniques for 3d resistivity surveys and data inversion. *Geophysical prospecting*, 44(3):499–523.

Loke, M., Chambers, J., Rucker, D., Kuras, O., and Wilkinson, P. (2013). Recent developments in the direct-current geoelectrical imaging method. *Journal of Applied Geophysics*, 95:135–156.

Loke, M. and Dahlin, T. (2002). A comparison of the gauss–newton and quasi-newton methods in resistivity imaging inversion. *Journal of Applied Geophysics*, 49(3):149–162.

Loke, M. H. and Barker, R. (1996b). Rapid least-squares inversion of apparent resistivity pseudosections by a quasi-newton method. *Geophysical prospecting*, 44(1):131–152.

Lowry, T., Allen, M. B., and Shive, P. N. (1989). Singularity removal - a refinement of resistivity modeling techniques. *Geophysics*, 54:766–774.

Mackie, R., Rieven, S., and Rodi, W. (1997). Users manual and software documentation for two-dimensional inversion of magnetotelluric data, gsy-usa. *Inc., San Francisco, Calif.*

Marquardt, D. W. (1963). An algorithm for least-squares estimation of nonlinear parameters. *Journal of the society for Industrial and Applied Mathematics*, 11(2):431–441.

Marshall, D. J. and Madden, T. R. (1959). Induced polarization, a study of its causes. *Geophysics*, 24(4):790–816.

Martin, R. (2009). *Development and application of 2D and 3D transient electromagnetic inverse solutions based on adjoint Green functions: A feasibility study for the spatial reconstruction of conductivity distributions by means of sensitivities*. PhD thesis, University of Cologne, Germany.

Militzer, H., Rösler, R., and Lösch, W. (1979). Theoretical and experimental investigations for cavity research with geoelectrical resistivity methods. *Geophysical Prospecting*, 27(3):640–652.

Mufti, I. R. (1976). Finite-difference resistivity modeling for arbitrarily shaped two-dimensional structures. *Geophysics*, 41(1):62–78.

Okabe, M. (1981). Boundary element method for the arbitrary inhomogeneities problem in electrical prospecting. *Geophysical Prospecting*, 29(1):39–59.

Oldenburg, D. W. and Li, Y. (1994). Inversion of induced polarization data. *Geophysics*, 59(9):1327–1341.

Oldenburg, D. W. and Li, Y. (1999). Estimating depth of investigation in dc resistivity and ip surveys. *Geophysics*, 64(2):403–416.

Oldenburg, D. W., Li, Y., and Ellis, R. G. (1997). Inversion of geophysical data over a copper gold porphyry deposit: A case history for mt. milligan. *Geophysics*, 62(5):1419–1431.

Özyildirim, Ö., Candansayar, M. E., Demirci, I., and Tezkan, B. (2015). (Submitted for publication.) two dimensional inversion of mt/rmt data by using unstructured mesh. *Geophysical Journal International*.

Park, S. K. and Van, G. P. (1991). Inversion of pole-pole data for 3-d resistivity structure beneath arrays of electrodes. *Geophysics*, 56(7):951–960.

Pelton, W., Sill, W., and Smith, B. (1983). Interpretation of complex resistivity and dielectric data, part i. *Geophysical transactions*, 29(4):297–330.

Pelton, W., Ward, S., Hallof, P., Sill, W., and Nelson, P. H. (1978). Mineral discrimination and removal of inductive coupling with multifrequency ip. *Geophysics*, 43(3):588–609.

Pelton, W. H. (1977). *Interpretation of induced polarization and resistivity data*. PhD thesis, University of Utah, USA.

Perincek, D. and Kozlu, H. (1984). Stratigraphy and structural relations of the units in the afsin-elbistan-doganshehir region (eastern taurus). In Tekeli, O. and Goncuoglu, M., editors, *Proceedings of the International Symposium on the Geology of the Taurus Belt 1983*, pages 181–198. MTA, Ankara, Turkey.

Press, F. and Siever, R. (2003). *Allgemeine Geologie*. Elsevier, München, Germany, 3rd edition.

Pridmore, D., Hohmann, G., Ward, S., and Sill, W. (1981). An investigation of finite-element modeling for electrical and electromagnetic data in three dimensions. *Geophysics*, 46(7):1009–1024.

Queralt, P., Pous, J., and Marcuello, A. (1991). 2-d resistivity modeling: An approach to arrays parallel to the strike direction. *Geophysics*, 56(7):941–950.

Revil, A., Karaoulis, M., Johnson, T., and Kemna, A. (2012). Review: Some low-frequency electrical methods for subsurface characterization and monitoring in hydrogeology. *Hydrogeology Journal*, 20(4):617–658.

Reynolds, J. M. (1997). *An introduction to applied and environmental geophysics*. 2nd edition, John Wiley & Sons.

Robertson, A. H., Ustaömer, T., Parlak, O., Ünlügenç, U. C., Taşlı, K., and İnan, N. (2006). The berit transect of the tauride thrust belt, s turkey: Late cretaceous–early cenozoic accretionary/collisional processes related to closure of the southern neotethys. *Journal of Asian Earth Sciences*, 27(1):108–145.

Rodi, W. L. (1976). A technique for improving the accuracy of finite element solutions for magnetotelluric data. *Geophysical Journal International*, 44(2):483–506.

Roy, A. and Apparao, A. (1971). Depth of investigation in direct current methods. *Geophysics*, 36(5):943–959.

Rücker, C., Günther, T., and Spitzer, K. (2006). Three-dimensional modelling and inversion of dc resistivity data incorporating topography-i. modelling. *Geophysical Journal International*, 166(2):495–505.

Sasaki, Y. (1989). Two-dimensional joint inversion of magnetotelluric and dipole-dipole resistivity data. *Geophysics*, 54(2):254–262.

Sasaki, Y. (1994). 3-d resistivity inversion using the finite-element method. *Geophysics*, 59(12):1839–1848.

Schmutz, M., Ghorbani, A., Vaudelet, P., and Blondel, A. (2014). Cable arrangement to reduce electromagnetic coupling effects in spectral-induced polarization studies. *Geophysics*, 79(2):A1–A5.

Seigel, H. O. (1959). Mathematical formulation and type curves for induced polarization. *Geophysics*, 24(3):547–565.

Seigel, H. O., Vanhala, H., and Sheard, S. N. (1997). Some case histories of source discrimination using time-domain spectral ip. *Geophysics*, 62(5):1394–1408.

Shewchuk, J. R. (1996). Triangle: Engineering a 2d quality mesh generator and delaunay triangulator. In *Applied computational geometry towards geometric engineering*, pages 203–222. Springer.

Spitzer, K. (1995). A 3-d finite-difference algorithm for dc resistivity modelling using conjugate gradient methods. *Geophysical Journal International*, 123(3):903–914.

Spitzer, K. and Chouteau, M. (2003). A dc resistivity and ip borehole survey at the casa berardi gold mine in northwestern quebec. *Geophysics*, 68(2):453–463.

Spitzer, K. and Wurmstich, B. (1999). Speed and accuracy in 3d resistivity modeling. *Three-Dimensional Electromagnetics*, 7:161–176.

Sumner, J. S. (1976). *Principles of induced polarization for geophysical exploration.* Elsevier Scientific Pub.

Swift Jr, C. (1973). The l/m parameter of time-domain ip measurements-a computational analysis. *Geophysics*, 38(1):61–67.

Telford, W. M., Geldart, L. P., and Sheriff, R. E. (1990). *Applied Geophysics.* Cambridge University Press, 2nd edition.

Tikhonov, A. N. and Arsenin, V. Y. (1977). *Solutions of ill-posed problems.* Winston.

Titov, K., Kemna, A., Tarasov, A., and Vereecken, H. (2004). Induced polarization of unsaturated sands determined through time domain measurements. *Vadose Zone Journal*, 3(4):1160–1168.

Tong, L.-T. and Yang, C.-H. (1990). Incorporation of topography into two-dimensional resistivity inversion. *Geophysics*, 55(3):354–361.

Tripp, A., Hohmann, G., and Swift Jr, C. (1984). Two-dimensional resistivity inversion. *Geophysics*, 49(10):1708–1717.

Vanhala, H. and Peltoniemi, M. (1992). Spectral ip studies of finnish ore prospects. *Geophysics*, 57(12):1545–1555.

Ward, S. H. (1990). The resistivity and induced polarization methods. In *Geotechnical and Environmental Geophysics*, volume 1, chapter 6, pages 147–190. Society of Exploration Geophysicists.

Ward, S. H. and Fraser, D. C. (1967). Conduction of electricity in rocks. In *Mining Geophysics II, Theory*, pages 197–223. Society of Exploration Geophysicists.

Wilson, S., Ingham, M., and McConchie, J. (2006). The applicability of earth resistivity methods for saline interface definition. *Journal of Hydrology*, 316(1):301–312.

Xu, S.-z., Duan, B.-c., and Zhang, D.-h. (2000). Selection of the wavenumbers k using an optimization method for the inverse fourier transform in 2.5 d electrical modelling. *Geophysical Prospecting*, 48(5):789–796.

Yildirim, N., İlhan, S., Yildirim, E., and Dönmez, C. (2012). The geology, geochemistry and genetical features of the ormanbaşi hill (sincik, adiyaman) copper mineralization. *Bulletin Mineral Research and Exploration*, 144:75–104.

Yogeshwar, P. (2014). *A resistivity-depth model of the central Azraq basin area, Jordan: 2D forward and inverse modeling of time domain electromagnetic data.* PhD thesis, University of Cologne, Germany.

Yogeshwar, P., Tezkan, B., Israil, M., and Candansayar, M. (2012). Groundwater contamination in the roorkee area, india: 2d joint inversion of radiomagnetotelluric and direct current resistivity data. *Journal of Applied Geophysics*, 76:127–135.

Yuval, . and Oldenburg, D. (1996). Dc resistivity and ip methods in acid mine drainage problems: results from the copper cliff mine tailings impoundments. *Journal of Applied Geophysics*, 34(3):187–198.

Zhao, S. and Yedlin, M. J. (1996). Some refinements on the finite-difference method for 3-d dc resistivity modeling. *Geophysics*, 61(5):1301–1307.

Zhdanov, M. (2002). *Geophysical Inverse Theory and Regularization Problems*. Elsevier.

Zimmermann, E., Kemna, A., Berwix, J., Glaas, W., and Vereecken, H. (2008). Eit measurement system with high phase accuracy for the imaging of spectral induced polarization properties of soils and sediments. *Measurement Science and Technology*, 19(9):094010.

Zonge (2003). *Zonge GDP-32 II Multifunction Receiver Operation Manual*. Zonge Engineering and Research Organisation Inc., 3322 East Fort Lowell Road, Tucson, AZ 85716 USA.

List of Figures

2.1. Current injected at a point source C_1 within a homogeneous half-space ($\rho = \rho_0$). Dashed lines display equipotential surfaces, arrows display current flow lines. 10
2.2. Current injected at a point source C_1 at the surface of a homogeneous half-space ($\rho = \rho_0$). Dashed lines display equipotential surfaces, arrows display current flow lines. 11
2.3. Currents I and $-I$ injected at point sources C_1 and C_2 located at the surface of a homogeneous half-space ($\rho = \rho_0$). Dashed lines display equipotential surfaces, arrows display current flow lines. 11
2.4. Current flow through a boundary between Medium 1 with resistivity ρ_1 and Medium 2 with resistivity $\rho_2 > \rho_1$ (redrawn after Telford et al. (1990)). 12
2.5. Principle of a 4-electrode setup (redrawn after Knödel et al. (1997)). . 13
2.6. Conventional DC arrays: A direct current I is injected through electrodes C_1 and C_2, a potential difference $\Delta\Phi = U$ is measured between electrodes P_1 and P_2. Distances between electrodes are given in terms of the smallest electrode distance a and integer factors n and m. . . 15
2.7. Sensitivity patterns of different array types (Dahlin and Zhou, 2004). 16
2.8. Sketch of a multi-electrode setup and the positions of acquired data in the 2D pseudosection according to the involved 4-point electrode configuration (British Geological Survey (c) NERC 2013). 17
2.9. Schematic of the two main phenomena causing induced polarization effects. **Left:** Membrane polarization in a porous sandstone with clay content; **(a)** No DC voltage is applied, ions normally distributed in pore fluid, accumulation of positively charged ions near clay particles; **(b)** DC voltage is applied, membrane polarization occurs. After Ward and Fraser (1967); Sumner (1976). **Right:** electrode polarization in a porous rock with mineral content; DC voltage is applied. **c)** Electrolytic conductance is predominant and **d)** Electrode polarization occurs, caused by mineral grain blocking the pore; (Telford et al., 1990). 18
2.10. Voltage decay curve $U(t)$. The current is switched off at $t = t_0$. The primary voltage U_p is measured at $t < t_0$. At t_0 the voltage drops to the secondary voltage U_s. **a)** The area under the voltage decay curve is integrated from delay time t_d to last time point t_e. **b)** The voltage decay is averaged within several time intervals Δt_i (with $i = 1, 2, 3, \dots$) to approximate the area under the curve. The primary voltage is averaged within a time interval Δt_p. 19

2.11. IP response in terms of resistivity $|\rho|$ and phase φ dependent on the frequency modified after (Pelton et al., 1983; Reynolds, 1997). 22
2.12. Sketch of potential $\Phi(t)$ for a transmitter switch-on at $t_{0,\text{on}}$ and transmitter switch-off at $t_{0,\text{off}}$. When the transmitter is switched on, the potential increases instantly to Φ, then the potential increases slowly to a constant level Φ'. When the transmitter is switched off, the potential decreases instantly to Φ_s, then it decays to zero with time. . 23

3.1. **a)** Schematic of a triangular element i with constant conductivity σ_i and Potentials $\Phi_{i\tau}$ at the three edge nodes with coordinates $(x_{i\tau}, z_{i\tau})$ and $\tau = (1, 2, 3)$. **b)** Boundary element j with constant length L_j, conductivity $\sigma_j = \sigma_i$ and potentials Φ_{jl} at the two nodes with coordinates (x_{jl}, z_{jl}) with $l = (1, 2)$. **c)** Directions $\vec{r}$ from the source to the center of the boundary element and the normal direction $\vec{n}$ form the angle θ used in calculation of the boundary factor β_j. 30
3.2. Flowchart of the forward calculation within the inversion algorithm `ResIPIn2D`. 33
3.3. Different mesh types. **a)** structured rectangular, **b)** structured triangular, **c)** unstructured triangular. 34
3.4. Excerpts of the three meshes that are used for modeling of an exemplary array. The electrode distance is $a = 5\,\text{m}$ and the profile length is 100 m. **a)** The parameter mesh is indicated by blue elements. In this area, the parameter mesh and the secondary mesh coincide. Outside of the parameter mesh, the secondary mesh is indicated by red elements. It expands further in lateral and vertical directions than the presented excerpt. **b)** Detailed view of the secondary mesh. Constraints for the triangulation are nodes at the electrode positions (red triangles), three nodes in between (red dots) and $\alpha = 33.4°$. **c)** Detailed view of the primary mesh. Based on the nodes of the secondary mesh, the refined primary mesh is obtained by a further triangulation after introducing additional nodes (blue dots) in a depth of $1/10a$ below each electrode. 35
3.5. Dipole-dipole forward calculation (ρ_a in Ωm) of a homogeneous halfspace with $\rho_0 = 100\,\Omega\text{m}$; Left column is with singularity removal, right column is without singularity removal: **a,b)** n-level=1, **c,d)** n-level=3, **e,f)** n-level=12, blue represents $\rho_{a,\text{forward}}$ and red $\rho_{a,\text{reverse}}$, respectively. The utilized protocol is listed in Table B.2 in the Appendix. Note that the y-axes in the left and right column are different. 37
3.6. Two horizontal layers with resistivities $\rho_1 = 100\,\Omega\text{m}$ and $\rho_2 = 10\,\Omega\text{m}$ and thickness of the surface layer $d_1 = 1\,\text{m}$. Electrode positions are indicated by red triangles, smallest electrode distance is $a = 1\,\text{m}$. . . . 38

3.7. Forward calculation for the 2-layer model in Figure 3.6. Left: Dipole-dipole; Right: Schlumberger. **a,b)** Comparison of the sounding curve of apparent resistivity (in Ωm) between the analytical solution (green circles), $\rho_{a,\text{forward}}$ (blue line) and $\rho_{a,\text{reverse}}$ (red line). Note: the blue line is masked by the red line. **c,d)** Relative difference between $\rho_{a,\text{forward}}$ and the analytical solution. **e,f)** Reciprocity in % for $\rho_{a,\text{forward}}$ and $\rho_{a,\text{reverse}}$ numerical data. The applied electrode protocols are listed in Table B.2 and Table B.5 in the Appendix. 38
3.8. Vertical contact at $x = 10.5\,\text{m}$ between $\rho_1 = 100\,\Omega\text{m}$ on the left and $\rho_2 = 500\,\Omega\text{m}$ on the right. Electrode locations are indicated by red triangles and the smallest electrode distance is $a = 1\,\text{m}$. 39
3.9. Wenner forward calculation of the vertical contact shown in Figure 3.8. Left: n-level=1; Right: n-level=3. **a,b)** Comparison of apparent resistivity (in Ωm) between the analytical solution (green circles), $\rho_{a,\text{forward}}$ (blue line) and $\rho_{a,\text{reverse}}$ (red line). Note: the blue line is masked by the red line. **c,d)** Relative difference between $\rho_{a,\text{forward}}$ and the analytical solution. **e,f)** Reciprocity in % for $\rho_{a,forward}$ and $\rho_{a,\text{reverse}}$ numerical data. The Wenner protocol including the pseudo-depths is listed in Table B.7. 39
3.10. Dipole-Dipole forward calculation for the fault model in Figure 3.8. Left column: Apparent resistivity (in Ωm) for **a)** n-level=1, **c)** n-level=6 and **e)** n-level=12, shown as $\rho_{a,\text{forward}}$ (blue) and $\rho_{a,\text{reverse}}$ (red). Right column: Reciprocity in % for the corresponding data on the left. The applied electrode protocol is listed in Table B.2 in the Appendix. 40
3.11. Comparison of Dipole-Dipole forward calculations of a vertical contact at profile distance $x = 102.5\,\text{m}$ between $500\,\Omega\text{m}$ on the left and $100\,\Omega\text{m}$ on the right. The electrode distance is 5 m and the profile length is 200 m: Calculated apparent resistivity for **a)** the 1st n-level and **b)** the 5th n-level. RMS errors refer to the difference between synthetic data calculated by `ResIPIn2D` and the other corresponding algorithm. 41
3.12. Buried block with lateral extension of 80 m to 120 m and vertical extension of 10 m to 25 m. The resistivity of the block is $\rho_{\text{block}} = 500\,\Omega\text{m}$ and that of the surrounding half-space is $\rho_{hs} = 100\,\Omega\text{m}$. Electrode locations are indicated by red triangles and the smallest electrode spacing is $a = 5\,\text{m}$. 41
3.13. Dipole-Dipole forward calculation for the model including a buried block shown in Figure 3.12. Left column: Apparent resistivity (in Ωm) for **a)** n-level=1 and **b)** n-level=6, shown as $\rho_{a,\text{forward}}$ (blue) and $\rho_{a,\text{reverse}}$ (red). Right column: reciprocity in % for the corresponding data on the left. The applied electrode protocol is listed in Table B.2 in the Appendix. 42
3.14. Comparison of Dipole-Dipole forward calculations of the 2D model in Figure 3.12: Calculated apparent resistivity for **a)** n-level= 1 and **b)** n-level=5. RMS errors refer to the difference between synthetic data calculated by `ResIPIn2D` and the according other algorithm. 42

3.15. **a)** DC-resistivity and IP-chargeability model including a buried block with intrinsic resistivity $\rho_{\text{block}} = 100\,\Omega\text{m}$ and chargeability $m_{\text{block}} = 100\,\text{mV/V}$ within a half-space with $\rho_{hs} = 100\,\Omega\text{m}$ and $m_{hs} = 10\,\text{mV/V}$. Electrodes are indicated by red triangles. The applied Pole-Dipole configuration is listed in Table B.6 in the Appendix. **b)** Synthetic apparent resistivity $\rho'_a = f_{dc}(\rho')$, **c)** synthetic apparent resistivity $\rho_a = f_{dc}(\rho)$ and **d)** synthetic apparent chargeability m_a calculated by Equation (3.32). 43
3.16. Comparison with Res2DMod. **a)** Apparent chargeability pseudosection calculated with `Res2DMod` for the model in Figure 3.15-a. Left: Comparison of apparent chargeability for fixed n-levels 3 (**b**) and 11 (**c**). **d)** Comparison of apparent chargeability sounding curve at $x = 190\,\text{m}$. The label new algorithm refers to `ResIPIn2D`. The RMS errors refer to the difference between data calculated by `ResIPIn2D` and `Res2DMod`. 44

4.1. Flowchart of the inversion algorithm `ResIPIn2D`. 57
4.2. Line-search for the model update of the first iteration of **a)** a resistivity inversion and **b)** a chargeability inversion. Comparison between exact line-search (red), the two-point parabola (yellow line) and linear interpolation (blue). The sampling points of the two-point parabola are indicated by green circles and the minimum of the parabola by a pink cross. 60
4.3. Sketch of the triangular element i with neighboring elements n_1, n_2, n_3 and lengths of the element's sides $L(n_1)$, $L(n_2)$, $L(n_3)$ shared with the corresponding neighbors. 64
4.4. **a)** Normalized coverage of a Pole-Dipole array for a homogeneous half-space with resistivity $\rho_{hs} = 10\,\Omega\text{m}$. The red cross indicates the DOI_t. The coverage threshold cov_t=-2.15 is the coverage value coinciding with DOI_t. The approximate DOI_{app} (black line) is defined by the coverage isoline corresponding to cov_t. **b)** Normalized coverage according to an inhomogeneous model including a buried block with $\rho_{\text{block}} = 100\,\Omega\text{m}$ within a half-space with $\rho_{hs} = 10\,\Omega\text{m}$. The white line indicates the outline of the body. The black cov_t isoline denotes the approximate DOI_{app}. Electrode loactions are indicated by red triangles. 67

5.1. **a)** Original resistivity model $\rho(x, z)$, **b)** original chargeability model $m(x, z)$. The resistivity and chargeability values of the buried model blocks are listed in Table 5.1. The surrounding half space has a resistivity of $\rho = 100\,\Omega\text{m}$ and a chargeabilty of $m = 10\,\text{mV/V}$. Electrode locations are indicated by red triangles. **c)** Synthetic effective apparent resistivity pseudo-section (ρ'_a), **d)** synthetic apparent chargeability pseudo-section of the model in a and b calculated for the Dipole-Dipole protocol listed in Table B.3. **e,f)** Synthetic data including 3% noise. 72

5.2. Inversion results of the original synthetic data in Figure 5.1-e,f using $\mathbf{C}_b$, a fixed $\lambda = 79$ and a 2-point parabola line-search for τ. **a)** Resistivity model ρ' resulting from the DC inversion. The data-fit is $\chi_{dc} = 0.96$. **b)** Intrinsic resistivity model ρ and **c)** chargeability model m resulting from the 6th iteration of the IP inversion. The data-fit is $\chi_{ip} = 1.62$. **d)** Model response ρ'_a and **e)** model response m_a. **f,g)** Relative difference between the calculated data above and the original data. 74
5.3. Resistivity inversion: Data misfit χ^2_{dc} for different combinations of regularization parameter λ and step length τ. Each column refers to inversion using a different smoothness constraint matrix, such as $\mathbf{C}_a$ (**a,d,g**), $\mathbf{C}_b$ (**b,e,h**) and $\mathbf{C}_c$ (**c,f,i**). Each row refers to the according iteration number: **a,b,c)** iteration 1, **d,e,f)** iteration 2 and **g,h,i)** iteration 3. White cells represent that there is no entry. 75
5.4. Chargeability inversion: Data misfit χ^2_{ip} for different combinations of regularization parameter λ and step length τ. Each column refers to inversion using a different smoothness constraint matrix, such as $\mathbf{C}_a$ (**a,d,g**), $\mathbf{C}_b$ (**b,e,h**) and $\mathbf{C}_c$ (**c,f,i**). Each row refers to the according iteration number: **a,b,c)** iteration 1, **d,e,f)** iteration 2 and **g,h,i)** iteration 3. White cells represent that there is no entry. 76
5.5. Final chargeability data-fit χ_{ip} for different fixed regularization parameters. The optimum step-length τ was determined by the 2-point parabola technique. **a)** Using smoothness matrix $\mathbf{C}_a$ and **b)** using smoothness matrix $\mathbf{C}_b$. 77
5.6. Results of the 14th iteration of the chargeability inversion, additional to the results displayed in Figure 5.2 (using $\mathbf{C}_b$). After stepwise cooling, the final values are $\lambda = 2.5$ and $\chi_{ip} = 1.11$. **a)** Chargeability model m, **b)** intrinsic resistivity model ρ, **c)** calculated apparent chargeability m_a and **d)** relative difference between the data in (c) and the original data. **e)** Data misfit χ_{ip}, regularization parameter λ and step-length τ during iterations of chargeability inversion. 78
5.7. Inversion results of the synthetic data in Figure 5.2-e,f using C_b, a fixed $\lambda = 2.5$ and a 2-point parabola line-search for τ. **a)** Resistivity model ρ' resulting from DC inversion. **b)** Intrinsic resistivity model ρ and **c)** chargeability model m resulting from the 6th iteration of the chargeability inversion. The final data misfit is $\chi_{ip} = 1.12$. 79
5.8. Inversion results of the synthetic data in Figure 5.2-e,f using $\mathbf{C}_a$, $\lambda_{ini} = 8900$ and a 2-point parabola line-search for τ. **a)** Resistivity model ρ' resulting from the DC inversion. The data misfit is $\chi_{dc} = 0.95$. **b)** Chargeability model m resulting from the 5th iteration of IP inversion. The data-fit is $\chi_{ip} = 1.47$. **c)** Intrinsic resistivity model ρ and **d)** chargeability model m resulting from the 15th iteration. Final values are $\lambda = 35$, $\chi_{ip} = 1.21$. **e)** Data misfit χ_{ip}, regularization parameter λ and step-length τ during iterations of chargeability inversion. 80

5.9. **a)** Resistivity model ρ' resulting from DC inversion with initial resistivity of $\rho^0 = 100\,\Omega$m. **b)** Chargeability model m resulting from IP inversion with initial chargeability $m^0 = 30\,$mV/V. **c)** DOI index R after Oldenburg and Li (1999) for the resistivity model above determined from inversion using initial resistivity $\rho_1^0 = 1000\,\Omega$m and $\rho_2^0 = 10\,\Omega$m and **d)** DOI index R for the chargeability model above determined from inversion using initial chargeability $m_1^0 = 300\,$mV/V and $m_2^0 = 3\,$mV/V. Isolines of R are indicated by black lines in steps of 0.05. 81
5.10. Original resistivity models including a block with lateral extension $x = 95 - 205\,$m and vertical extension $z = 12 - 50\,$m. The resistivity of the block ρ_{block} and the half-space ρ_{hs} are **a)** ρ_{block}=10 Ωm, ρ_{hs}=100 Ωm and **b)** ρ_{block}=100 Ωm, ρ_{hs}=10 Ωm. 82
5.11. Apparent resistivity sounding curves at $x = 190\,$m **a)** calculated for the model in Figure 5.10-a and **b)** for the model in Figure 5.10-b, each with lower boundaries of the anomaly between 20 m and 100 m depth. The signatures are shown as relative difference to the signature of a dyke in %. The 5% limit is indicated by a dashed black line. 83
5.12. Resistivity models resulting from inversion of the original synthetic data based on the model in Figure 5.10-a with lower boundaries of the model block in different depth: **a)** 30 m, **b)** 50 m, **c)** 70 m and **d)** 90 m; and **e)** dyke model. The outline of the original block is indicated by a white line. The dashed white line represents the DOI$_{app}$. Electrode locations are indicated by red triangles. The initial model is a homogeneous half-space with resistivity $\rho^0 = 80\,\Omega$m. 84
5.13. Normalized coverage corresponding to the resistivity models resulting from inversion of synthetic data based on the model in Figure 5.10-a with lower boundaries of the anomaly in different depth: **a)** 30 m, **b)** 50 m, **c)** 70 m and **d)** 90 m; and **e)** dyke model. For all models, a $\chi \leq 1$ is achieved. The black isoline refers to the DOI$_{app}$. Electrode locations are indicated by red triangles. 84
5.14. Resistivity models resulting from inversion of the original synthetic data based on the model in Figure 5.10-b with lower boundaries of the anomaly in different depth: **a)** 30 m, **b)** 50 m, **c)** 70 m and **d)** 90 m; and **e)** dyke model. For all models, a $\chi \leq 1$ is achieved. The outline of the original block is indicated by a white line. The dashed white line represents the DOI$_{app}$. Electrode locations are indicated by red triangles. The initial model is a homogeneous half-space with resistivity $\rho^0 = 8\,\Omega$m. 85
5.15. Normalized coverage corresponding to the resistivity models resulting from inversion of synthetic data based on the model in Figure 5.10-b with lower boundaries of the anomaly in different depth: **a)** 30 m, **b)** 50 m, **c)** 70 m and **d)** 90 m; and **e)** dyke model. The black isoline refers to the DOI$_{app}$. Electrode locations are indicated by red triangles. 86

5.16. **a)** Original chargeability model m. The corresponding resistivity model ρ is a 100 Ωm homogeneous half-space. **b)** Apparent chargeability sounding curves at $x = 190\,\text{m}$ calculated for the model in a) with lower boundaries of the anomaly between 20 m and 100 m depth. The signatures are shown as relative difference to the signature of a dyke in %. The 5% limit is indicated by a dashed black line. 87
5.17. Chargeability models resulting from chargeability inversion of the original synthetic data based on the model in Figure 5.16 with lower boundaries of the anomaly in different depth: **a)** 30 m, $\chi = 0.97$, **b)** 50 m, $\chi = 0.97$,**c)** 70 m, $\chi = 1.05$ and **d)** 90 m, $\chi = 1.6$; and **e)** dyke model, $\chi = 1.5$. The outline of the original block is indicated by a white line. The dashed white line represents the DOI_{app}. Electrode locations are indicated by red triangles. The initial model is a homogeneous half-space with resistivity $\rho^0 = 80\,\Omega\text{m}$ and chargeability $m^0 = 8\,\text{mV/V}$. 88
5.18. Normalized Coverage for the corresponding chargeability models resulting from chargeability inversion of the original synthetic data based on the model in Figure 5.16 with lower boundaries of the anomaly in different depth: **a)** 30 m, **b)** 50 m, **c)** 70 m and **d)** 90 m; and **e)** dyke model. The black line refers to the DOI_{app}. Electrode locations are indicated by red triangles. 89
5.19. Resistivity models obtained by `BERT`: Inversion (using $\lambda = 30$) of synthetic data calculated from the models with lower boundary of the model block in 50 m depth and with **a)** a high resistive anomaly ($\chi_{dc} = 0.93$) and **b)** a low resistive anomaly ($\chi_{dc} = 0.95$) as shown in Figure 5.10-a,b. 89
5.20. Resistivity models obtained by `Res2DInv`: Inversion of synthetic data calculated from the models with lower boundary of the model block in 50 m depth and with **a)** a high resistive anomaly ($RMS_{dc} = 2.2\%$) and **b)** a low resistive anomaly ($RMS_{dc} = 2.1\%$) as shown in Figure 5.10-a,b. **c)** Chargeability model ($RMS_{ip} = 0.92\%$) of the synthetic data calculated from the model shown in Figure 5.16-a. 90

6.1. Effect of topography on the equipotential surfaces and current lines of a distant source electrode (Fox et al., 1980). 93
6.2. **a)** Hill model with 30° slope angle. Constant subsurface resistivity is $\rho_0 = 100\,\Omega\text{m}$. Electrode locations are indicated by red triangles. Calculated apparent resistivity pseudo-section for a Wenner (**b**) and Dipole-Dipole configuration (**c**). Topography factor t for different slope angles referring to the 4-th n-level of the Wenner configuration (**d**) and the 6-th level of the Dipole-Dipole configuration (**e**). The applied electrode protocols are listed in Table B.3 and Table B.4. . . 96
6.3. **a)** FE distorted mesh example as it is used by Erdoğan et al. (2008). **b)** Hill model with 30° slope angle. Surface resistivity is $\rho_0 = 100\,\Omega\text{m}$. Electrode locations are indicated by arrows. Synthetic apparent resistivity for a Schlumberger (**c**) and Dipole-Dipole configuration (**d**). All subfigures are extracted from Erdoğan et al. (2008). 97

6.4. **a)** Hill model with 30° slope angle. Constant subsurface resistivity is $\rho_0 = 100\,\Omega$m. Electrode locations are indicated by red triangles. Synthetic apparent resistivity for a Schlumberger (**b**) and Dipole-Dipole configuration (**c**) obtained by `ResIPIn2D`. 97
6.5. **a)** Valley model with 30° slope angle. Constant subsurface resistivity is $\rho_0 = 100\,\Omega$m. Electrode locations are indicated by red triangles. Calculated apparent resistivity pseudo-section for a Wenner (**b**) and Dipole-Dipole configuration (**c**). Topography factor t for different slope angles referring to the 4-th n-level of the Wenner configuration (**d**) and the 6-th n-level of the Dipole-Dipole configuration (**e**). The applied electrode protocols are listed in Table B.3 and Table B.4. . . 98
6.6. **a)** Hill-and-valley model with two high resistive anomalies with 500 Ωm (red) buried in 1 m depth below the trough and the summit. The surrounding resistivity is 100 Ωm. Electrode locations are indicated by red triangles. **Left column:** Schlumberger, **right column:** Dipole-Dipole. **b,c)** Synthetic apparent resistivity for the 2D model in (a) and **d,e)** for the topography model in (a) with homogeneous resistivity $\rho_0 = 100\,\Omega$m. 99
6.7. Forward modeling results using the FE distorted mesh for the hill-and-valley model with resistivity distribution as in Figure 6.6-a extracted from Erdoğan et al. (2008): **a)** Schlumberger, **b)** Dipole-Dipole. 100
6.8. **a)** Hill-and-valley model with two chargeable bodies with $m_{\text{body}} = 100\,$mV/V (yellow) buried in 1 m depth below the valley and the summit. The surrounding chargeability is $m_{hs} = 10\,$mV/V. The intrinsic resistivity is constant $\rho_0 = 100\,\Omega$m. Electrode locations are indicated by red triangles. **b,c)** Synthetic apparent chargeability data (in mV/V) for a constant chargeability $m^0 = 10\,$mV/V below the surface topography shown in a). Note the limited color scale. **d,e)** Synthetic apparent chargeability calculated for the model in a). **Left:** Schlumberger, **right:** Dipole-Dipole. 101
6.9. **a)** Flat surface model with two highly chargeable bodies with 100 mV/V buried in 1 m depth. The surrounding chargeability is 10 mV/V and the corresponding intrinsic resistivity is constant $\rho_0 = 100\,\Omega$m. Electrode locations are indicated by red triangles. Synthetic apparent chargeability data calculated for the model in a): **b)** Schlumberger, **c)** Dipole-Dipole. 101
6.10. **a,b)** Topography corrected synthetic data $\rho^c_{a,\text{topo}}$ corresponding to the model in Figure 6.6-a; **c,d)** Forward responses of the model in Figure 6.11-a; **e,f)** Forward responses of the model in Figure 6.11-b; **left:** Schlumberger, **right:** Dipole-Dipole. 103
6.11. Flat surface model with 2 buried bodies with resistivity ρ_{body}=500 Ωm within a half-space with ρ_{hs}=100 Ωm. **a)** Upper boundaries of both bodies lies in 1 m depth. **b)** The upper boundary of the left body is in 1.2 m depth and that of the right body in 0.8 m depth. Electrode locations are indicated by red triangles. 103

6.12. Sketch of two electrodes A and B at the surface of a topography structure: r_s refers to the electrode distance along the surface, r_d is the shortest distance between A and B and r_x is the x-component of the electrode distance. 105
6.13. Dipole-Dipole forward calculation of the 30° hill model (cf. Figure 6.2-a) with constant subsurface resistivity of $\rho_0 = 100\,\Omega$m using different geometry factors. Pseudo-sections shown as **a)** potential difference $\Delta\Phi$, **b)** apparent resistivity using electrode distances r_x, **c)** using surface distances r_s and **d)** using linear distances r_d. 106
6.14. **a)** Original resistivity model including a body with circular cross section (cf. Table 6.1) buried beneath a surface topography structure with 20° slope angle. Electrode locations are indicated by red triangles. **b)** Synthetic Pole-Dipole data calculated from the model in a). **c)** Synthetic Pole-Dipole data calculated for a constant resistivity of $\rho_0 = 100\,$m below the surface topography shown in a). **d)** Synthetic data shown in b) including 3% noise. 108
6.15. Final inversion models using a mesh including surface topography in the inversion: **a)** for the original data without noise (cf. Figure 6.14-b), the applied mesh includes the original boundaries of the buried body, χ=0.18, RMS=0.12%; **c)** for the original data including 3% noise (cf. Figure 6.14-d) using the same mesh as in a), χ=0.93 ; **e)** for the original data including 3% noise using an unbiased unstructured mesh, χ=0.93. Electrode locations are indicated by red triangles and the DOI_{app} by a dashed white line, respectively. **b,d,f)** Relative difference between the model response of the corresponding model on the left and the original data. The initial resistivity is $80\,\Omega$m. 109
6.16. Final inversion models using a mesh with flat surface in the inversion: **a)** for the original data including 3% noise (cf. Figure 6.14-d), χ=0.97; **c)** for the topography corrected data (cf. Figure 6.17-b) including 3% noise, χ=0.98; **e)** for the original data calculated for the model without surface topography (cf. Figure 6.17-a) including 3% noise, χ=0.97. Electrode locations are indicated by red triangles and the DOI_{app} by a dashed white line, respectively. **b,d,f)** Relative difference between the model response of the corresponding model on the left and the original data. The initial resistivity is $\rho^0 = 80\,\Omega$m. . . 110
6.17. **a)** Synthetic Pole-Dipole data calculated for the body specified in Table 6.1 buried beneath a flat surface. **b)** Synthetic data shown in Figure 6.14-b corrected for the topography effect by division with the signature of a homogeneous resistivity distribution (cf. Figure 6.14-c) according to Fox et al. (1980). **c)** Relative difference between the data shown in a) and b). 111
6.18. **a)** Original resistivity model buried beneath a surface topography structure with 20° slope angle. Electrode locations are indicated by red triangles. **b)** Synthetic Pole-Dipole apparent resistivity data calculated for the model in a). **c)** Synthetic Pole-Dipole data calculated for the same body buried beneath a flat surface. **d)** Relative difference between the data shown in b) and c). 112

6.19. Final resistivity inversion models: **a)** for the original data calculated with surface topography (cf. Figure 6.18-b) with 3% noise, the inversion mesh includes topography, χ=0.99; **c)** for the same data as in a), using a flat-surface inversion mesh, χ=0.99; **e)** for the original data calculated for the model without surface topography (cf. Figure 6.18-c) with 3% noise, χ=0.99. **b,d,e)** Relative difference between the model response of the corresponding model on the left and the original data. Red triangles indicate electrode locations, the dashed white line the DOI_{app}, respectively. The initial resistivity model is $\rho^0 = 8\,\Omega$m. 112
6.20. **a)** Original chargeability model including a body with circular cross section (cf. Table 6.2) buried beneath a surface topography structure with 20° slope angle. Electrode locations are indicated by red triangles. **b)** Synthetic Pole-Dipole apparent chargeability data calculated from the model in a). **c)** Synthetic Pole-Dipole apparent chargeability data calculated for the body specified in Table 6.2 buried beneath a flat surface. **d)** Relative difference between the data shown in b) and c). 114
6.21. Final chargeability inversion models: **a)** for the original data calculated with surface topography (cf. Figure 6.20-b) with 3% noise, the inversion mesh includes topography, χ=0.99; **c)** for the same data as in a) using a flat-surface inversion mesh, χ=0.99; **e)** for the original data calculated without topography (cf. Figure 6.20-c) with 3% noise using a flat-surface inversion mesh, χ=0.97. **b,d,f)** Relative difference between the model response of the corresponding model on the left and the original data. Red triangles indicate electrode locations, the dashed white line the DOI_{app}, respectively. The initial chargeability is $\rho^0 = 8\,$mV/V. 114
6.22. **a)** Original resistivity model buried beneath a surface topography structure with 20° slope angle. Electrode locations are indicated by red triangles. **b)** Synthetic Pole-Dipole apparent resistivity data calculated for the model in a). **c)** Synthetic Pole-Dipole data calculated for a homogeneous resistivity of 100 Ωm below the valley topography. **d)** Synthetic Pole-Dipole data calculated for the same body buried beneath a flat surface. **e)** Relative difference between the data shown in b) and d). 115
6.23. Final resistivity inversion models: **a)** for the original data calculated with surface topography (cf. Figure 6.22-b) with 3% noise, the inversion mesh includes topography, χ=0.99; **c)** for the same data as in a), using a flat-surface inversion mesh, χ=0.96; **e)** for the original data calculated without surface topography (cf. Figure 6.22-d) with 3% noise, χ=0.95. **b,d,f)** Relative difference between the model response of the corresponding model on the left and the original data. Red triangles indicate electrode locations, the dashed white line the DOI_{app}, respectively. The initial resistivity is $\rho^0 = 80\,\Omega$m. 116

6.24. **a)** Original resistivity model buried beneath a surface topography structure with 20° slope angle. Electrode locations are indicated by red triangles. **b)** Synthetic Pole-Dipole apparent resistivity data calculated for the model in a). **c)** Synthetic Pole-Dipole data calculated for the same body buried beneath a flat surface. **d)** Relative difference between the data shown in b) and c). 118
6.25. Final resistivity inversion models: **a)** for the original data calculated with surface topography (cf. Figure 6.24-b) with 3% noise, the inversion mesh includes topography, χ=0.97; **c)** for the same data as in a), using a flat-surface inversion mesh, χ=0.97; **e)** for the original data calculated for the model without surface topography (cf. Figure 6.24-c) with 3% noise, χ=1.00. **b,d,e)** Relative difference between the model response of the corresponding model on the left and the original data. Red triangles indicate electrode locations, the dashed white line the DOI_{app}, respectively. The initial resistivity is $\rho^0 = 8\,\Omega\text{m}$. 119
6.26. **a)** Original chargeability model buried beneath a surface topography structure with 20° slope angle. Electrode locations are indicated by red triangles. **b)** Synthetic Pole-Dipole apparent chargeability data calculated for the model in a). **c)** Synthetic Pole-Dipole data calculated for the same body buried beneath a flat surface. **d)** Relative difference between the data shown in b) and c). 119
6.27. Final chargeability inversion models: **a)** for the original data calculated with surface topography (cf. Figure 6.26-b) with 3% noise, the inversion mesh includes topography, χ=0.97; **c)** for the same data as in a), using a flat-surface inversion mesh, χ=1.00; **e)** for the original data calculated without surface topography (cf. Figure 6.26-c) with 3% noise, χ=1.03. **b,d,f)** Relative difference between the model response of the corresponding model on the left and the original data. Red triangles indicate electrode locations, the dashed white line the DOI_{app}, respectively. The initial chargeability is $m^0 = 8\,\text{mV/V}$. 120
6.28. Resistivity models obtained by `BERT` (using $\lambda = 30$): Inversion of synthetic data calculated from **a)** the hill model with low resistive anomaly in Figure 6.14-a ($\chi_{dc} = 0.98$), **b)** the hill model with high resistive anomaly in Figure 6.18-a ($\chi_{dc} = 0.98$), **c)** the valley model with low resistive anomaly in Figure 6.22-a ($\chi_{dc} = 5.2$) and **d)** the valley model with high resistive anomaly in Figure 6.24-a ($\chi_{dc} = 5.4$). 121
6.29. Resistivity and chargeability models obtained by `Res2DInv`: Inversion of original synthetic data calculated from **a)** the hill model with low resistive anomaly in Figure 6.14-a ($RMS_{dc} = 2.2\%$), **b)** the hill model with high resistive anomaly in Figure 6.18-a ($RMS_{dc} = 2.1\%$), **c)** the valley model with low resistive anomaly in Figure 6.22-a ($RMS_{dc} = 3.7\%$), **d)** the valley model with high resistive anomaly in Figure 6.24-a ($RMS_{dc} = 2.3\%$), **e)** the hill model with highly chargeable anomaly in Figure 6.20-a ($RMS_{ip} = 1.2\%$) and **f)** the valley model with highly chargeable anomaly in Figure 6.26-a ($RMS_{ip} = 0.37\%$). 121

7.1. Location of the survey area (green symbol), 20 km west of the city Elbistan in Turkey. The location of the Berit Mountain and the Isbendere Ophiolite are indicated by blue symbols; Google Earth (2016). 128
7.2. **a)** Major tectonic features and distribution of the Neotethyan ophiolites (green) in the eastern Mediterranean region; modified after (Dilek and Flower, 2003; Karaoğlan et al., 2013)). The Survey area is indicated by a red circle, the Göksun and the Isbendere Ophiolite by a red cross, respectively. **b,c)** Sketch of the development of SSZ-type ophiolites, granitoid intrusions and volcanic sediments, related to the arc, that were subducted or accreted during the late Cretaceous in the northern part of the southern Neotethys (Karaoğlan et al., 2013). 129
7.3. Geological overview of the Berit area. The survey area is indicated by a red cross; modified after (Robertson et al., 2006) (based on regional mapping by Perincek and Kozlu (1984)). 130
7.4. Panoramic overview of the survey area in Elbistan: **(top)** View towards northwestern direction; **(bottom)** View towards southeastern direction. The white line indicates Profile 3. Borehole locations are labeled with a white cross, the active drilling site by a white circle. Rock outcrops are indicated by a dashed white ellipse. The red cross denotes the Berit Mountain in distance. 131
7.5. Location of the geophysical profiles (yellow) in the survey area. The assumed strike direction is indicated by a green line. Borehole locations are marked by blue symbols. The white lines indicate the directions towards the cities of Elbistan and Afşin and the Berit Mountain, respectively; Google Earth (2016) 133
7.6. Photos made during the DC/TDIP survey in 2013: **a)** current injection through a steel electrode; **b)** potential measurement by a non-polarizable electrode filled with $Cu/CuSO_4$; **c)** utilized devices from Zonge Engineering; **d)** Each cable drum (white circle) represents the location of a potential electrode. The white cross denotes HKS10, outcropping rocks are indicated by a dashed white ellipse. 134
7.7. Schematic of the applied Pole-Dipole setup. **1.)** The current electrodes C1 and C2 are connected to the Transmitter Tx. Each potential electrode (P1-P8) is connected by a separate cable with the 8-channel receiver Rx. **2.)** After each measurement the whole setup is moved along the profile. 134
7.8. Time windows and integration times used to calculate the Newmont Standard approximation of the integrated chargeability at 0.125 Hz (Zonge, 2003). 135
7.9. RMT-F device of the University of Cologne used in the field survey 2013. 136

7.10. Topography influence. Surface topography of **a)** Profile 3 and **b)** Profile 7. Synthetic Pole-Dipole apparent resistivity calculated for a homogeneous subsurface resistivity of 100 Ωm beneath the topography according to **c)** Profile 3 and **d)** Profile 7. The used geometry factors are based on surface distances r_s.In the pseudo-sections, the electrode separation and the n-spacing are indicated on the y-axis in the form of a/n. 137
7.11. **a)** Relative geometry error $\left|\frac{\delta G}{G}\right|$ in % and **b)** relative voltage error $\left|\frac{\delta U}{U}\right|$ in % for a Pole-Dipole setup with $a = 10\,\text{m}$ and $a = 20\,\text{m}$. The electrode misplacement is $\delta x = 15\,\text{cm}$, the voltage accuracy is $\delta U = 0.5\,\text{mV}$ and the apparent resistivity is $\rho_a = 100\,\Omega\text{m}$. 139
7.12. **a)** Apparent resistivity and **b)** apparent chargeability measured on Profile 3. 139
7.13. Apparent resistivity pseudo-section of the measured data of Profile 3 corrected for topography effects according to Fox et al. (1980). Outliers are already removed from the dataset. 140
7.14. Profile 3: Histogram of the difference between measured and calculated data normalized on the data error. 141
7.15. Inversion results Profile 3: **a)** Resistivity model, $\chi_{dc} = 2.5$, **b)** chargeability model, $\chi_{ip} = 0.98$, **c,d)** normalized coverage of the corresponding model at the top. The approximate DOI_{app} is represented by a dashed white line in the models and by a black line in the coverage plots. Electrode locations are indicated by red triangles. 142
7.16. Inversion results Profile 3: Measured data as pseudo-sections **a)** apparent resistivity, **b)** apparent chargeability. **c,d)** Difference between the measured data and the corresponding calculated data shown above normalized to the data error. 143
7.17. Profile 3: **a)** Resistivity (χ_{dc}=2.5) and **b)** chargeability (χ_{ip}=0.99) inversion result of the measured data corrected for topography effects according to Fox et al. (1980) using a flat surface inversion mesh. **c)** Resistivity (χ_{dc}=2.5) and **d)** chargeability (χ_{ip}=0.98) inversion result of the measured data without topography correction using a flat surface inversion mesh. Dashed whites lines represent the DOI_{app}. Electrode locations are indicated by red triangles. 143
7.18. Inversion results Profile 8: **a)** Resistivity model, χ_{dc}=2.5, **b)** chargeability model, χ_{ip}=1.3, **c,d)** normalized coverage of the corresponding model at the top. The approximate DOI_{app} is represented by a dashed white line in the models and by a black line in the coverage plots. Electrode locations are indicated by red triangles. 144
7.19. Inversion results Profile 8: Measured data as pseudo-sections **a)** apparent resistivity, **b)** apparent chargeability. **c,d)** Difference between the measured data and the corresponding calculated data shown above normalized to the data error. 144
7.20. Overview of the inversion results: **a)** Resistivity models, **b)** Chargeability models. 146

7.21. DOI index Profile 3: **a)** Resistivity inversion using initial parameters $\rho_1^0 = 500\,\Omega$m and $\rho_2^0 = 5\,\Omega$m. **b)** Chargeability inversion using initial parameters $m_1^0 = 300\,$mV/V and $m_2^0 = 5\,$mV/V. 147
7.22. Profile 3: **a)** final chargeability inversion result displayed in a depth range from $z = 0 - 200\,$m, **b)** calculated synthetic apparent chargeability data corresponding to the model in a). 148
7.23. **a)** Chargeability model with maximum chargeability of 50 mV/V below 100 m depth. **b)** Calculated apparent chargeability corresponding to the model in a). 148
7.24. Profile 3: relative difference between measured data and the chargeability data calculated from models that were varied based on the final inversion model shown in Figure 7.22. **a)** Original inversion result, **b)** max. 10 mV/V below $z = 70\,$m, **c)** max. 50 mV/V below $z = 70\,$m, **d)** max. 10 mV/V below $z = 80\,$m, **e)** max. 50 mV/V below $z = 80\,$m, **f)** max. 10 mV/V below $z = 90\,$m, **g)** max. 50 mV/V below $z = 90\,$m, **h)** max. 10 mV/V below $z = 100\,$m, **i)** max. 50 mV/V below $z = 100\,$m. Here, the data misfit χ is determined using linear parameters. 149
7.25. Profile 3: Resistivity model obtained by inversion using **a)** `ResIPIn2D` $\chi = 2.5$, RMS=7.4%, **b)** `BERT` $\chi = 2.7$ and **c)** `Res2DInv` RMS=11.8%. 151
7.26. Profile 3: Chargeability model obtained by inversion using **a)** `ResIPIn2D` $\chi = 0.98$, RMS=6.3% and **b)** `Res2DInv` RMS=2.15%. 151
7.27. Profile 3: **a)** DC Resistivity inversion result. **b)** RMT inversion result of the TM mode obtained using the algorithm by Mackie et al. (1997); λ=25, RMS=4.4%. The location of RMT stations is indicated by black triangles. 153
7.28. Profile 1: **a)** Resistivity ($\chi_{dc} = 1.6$) and **b)** chargeability inversion result ($\chi_{ip} = 0.95$). Electrode locations are indicated by red triangles. The dashed white line represents the DOI_{app}. **c)** Borehole information obtained from HKS4 (cf. Chapter 7.1.2) located at profile distance 250 m (red cross in a and b). 154

B.1. Inversion results of the synthetic data in Figure 5.2-e,f using $\mathbf{C}_c$, $\lambda_{ini} = 113$ and a 2-point parabola line-search for τ. **a)** Resistivity model ρ' resulting from the 19th DC iteration. The final regularization parameter is $\lambda = 14$ and the data misfit is $\chi_{dc} = 0.99$. **b)** Intrinsic resistivity model ρ and **c)** chargeability model m resulting from the 25th IP iteration. Final values are $\lambda = 28$, $\chi_{ip} = 2.6$. **d,e)** Data misfit χ, regularization parameter λ and step-length τ during iterations of DC (d) and IP (e) inversion. 196

C.1. Topography influence. Surface topography of **a)** Profile 1 and **b)** Profile 2. Synthetic Pole-Dipole apparent resistivity calculated for a homogeneous subsurface resistivity of 100 Ωm beneath the topography according to **c)** Profile 1 and **d)** Profile 2. 197

C.2. Topography influence. Surface topography of **a)** Profile 4 and **b)** Profile 5. Synthetic Pole-Dipole apparent resistivity calculated for a homogeneous subsurface resistivity of 100 Ωm beneath the topography according to **c)** Profile 4 and **d)** Profile 5. 197
C.3. Topography influence. Surface topography of **a)** Profile 6 and **b)** Profile 8. Synthetic Pole-Dipole apparent resistivity calculated for a homogeneous subsurface resistivity of 100 Ωm beneath the topography according to **c)** Profile 6 and **d)** Profile 8. 198
C.4. Inversion results Profile 2: **a)** Resistivity model, χ_{dc}=3.6, **b)** chargeability model, χ_{ip}=2.4, **c,d)** normalized coverage of the corresponding model at the top. The approximate DOI_{app} is defined by the black isoline referring to cov_t=-2.15. Electrode locations indicated by red triangles. 199
C.5. Inversion results Profile 2: Measured data as pseudo-sections **a)** apparent resistivity, **b)** apparent chargeability. **c,d)** Difference between the measured data and the corresponding calculated data shown above normalized to the data error. 199
C.6. Inversion results Profile 4: **a)** Resistivity model, χ_{dc}=0.97, **b)** chargeability model, χ_{ip}=0.97, **c,d)** normalized coverage of the corresponding model at the top. The approximate DOI_{app} is defined by the black isoline referring to cov_t=-2.15. Electrode locations indicated by red triangles. 200
C.7. Inversion results Profile 4: Measured data as pseudo-sections **a)** apparent resistivity, **b)** apparent chargeability. **c,d)** Difference between the measured data and the corresponding calculated data shown above normalized to the data error. 200
C.8. Inversion results Profile 5: **a)** Resistivity model, χ_{dc}=1.36, **b)** chargeability model, χ=1.41, **c,d)** normalized coverage of the corresponding model at the top. The approximate DOI_{app} is defined by the black isoline referring to cov_t=-2.15. Electrode locations indicated by red triangles. 201
C.9. Inversion results Profile 5: Measured data as pseudo-sections **a)** apparent resistivity, **b)** apparent chargeability. **c,d)** Difference between the measured data and the corresponding calculated data shown above normalized to the data error. 201
C.10. Inversion results Profile 6: **a)** Resistivity model, χ_{dc}=1.90, **b)** chargeability model, χ_{ip}=1.5, **c,d)** normalized coverage of the corresponding model at the top. The approximate DOI_{app} is defined by the black isoline referring to cov_t=-2.15. Electrode locations indicated by red triangles. 202
C.11. Inversion results Profile 6: Measured data as pseudo-sections **a)** apparent resistivity, **b)** apparent chargeability. **c,d)** Difference between the measured data and the corresponding calculated data shown above normalized to the data error. 202

C.12. Inversion results Profile 7: **a)** Resistivity model, $\chi_{dc} = 2.04$, **b)** chargeability model, $\chi_{ip} = 0.99$, **c,d)** normalized coverage of the corresponding model at the top. The approximate DOI_{app} is defined by the black isoline referring to cov_t=-2.15. Electrode locations indicated by red triangles. 203
C.13. Inversion results Profile 7: Measured data as pseudo-sections **a)** apparent resistivity, **b)** apparent chargeability. **c,d)** Difference between the measured data and the corresponding calculated data shown above normalized to the data error. 203
C.14. Profile 3: deviation (normalized to data error) between measured data and the chargeability data calculated from models that were varied based on the final inversion model shown in Figure 7.22. **a)** Original inversion result, **b)** max. 10 mV/V below $z = 70$ m, **c)** max. 50 mV/V below $z = 70$ m, **d)** max. 10 mV/V below $z = 80$ m, **e)** max. 50 mV/V below $z = 80$ m, **f)** max. 10 mV/V below $z = 90$ m, **g)** max. 50 mV/V below $z = 90$ m, **h)** max. 10 mV/V below $z = 100$ m, **i)** max. 50 mV/V below $z = 100$ m. 204

List of Tables

2.1. Geometry factors and depth of investigation DOI_t according to Barker (1989) for conventional DC arrays. 15

5.1. Chargeability and resistivity values of the buried model blocks and the surrounding half-space (hs) in Figure 5.1. 72

6.1. Details of the buried body with circular cross-section. 107
6.2. Details of the buried body with circular cross-section with IP effect. . 113
6.3. Details of the buried block with rectangular cross-section. 115

A.1. Basic physical quantities of the electrical and electromagnetic theory. 185
A.2. Resistivity range of selected minerals and rock types. Values obtained from Telford et al. (1990). 186
A.3. Chargeability range of selected minerals with 1% vol. concentration, $T_{on} = 3\ s$, integration time 1 s. Values obtained from Telford et al. (1990). 186
A.4. Chargeability range of selected minerals and rock types. The charging time is ca. 1 min, integration is over the complete decay curve. Values obtained from Telford et al. (1990). 187

B.1. Wavenumbers k and weights g_k used in the Fourier Cosine Transformation (FCT) and Inverse FCT, respectively. Values are obtained from Erdoğan et al. (2008) and were calculated with the optimization approach after Xu et al. (2000). The values need to be divided by the smallest electrode spacing in order to be suitable for any electrode setup. 189
B.2. Dipole-Dipole protocol A: 12 n-level with fixed dipole length a. Please note, all measures refer to a smallest electrode distance of $a_0 = 1\,\mathrm{m}$. For other electrode distances (a_0), a and DOI need to be multiplied by a_0. 192
B.3. Dipole-Dipole protocol B: 22 n-level with varied dipole length a. Please note, all measures refer to a smallest electrode distance of $a_0 = 1\,\mathrm{m}$. For other electrode distances (a_0), a and DOI need to be multiplied by a_0. 193
B.4. Wenner protocol A: 12 n-level. Please note, all measures refer to a smallest electrode distance of $a_0 = 1\,\mathrm{m}$. For other electrode distances (a_0), a and DOI_t need to be multiplied by a_0. 194

B.5. Schlumberger protocol A: 9 n-level with fixed dipole length a. Please note, all measures refer to a smallest electrode distance of $a_0 = 1\,\mathrm{m}$. For other electrode distances (a_0), a and DOI need to be multiplied by a_0. 194
B.6. Pole-Dipole protocol A: 14 n-level with varied dipole length a. Please note, all measures refer to a smallest electrode distance of $a_0 = 1\,\mathrm{m}$. For other electrode distances (a_0), a and DOI need to be multiplied by a_0. 195
B.7. Wenner Protocol B: 8 n-level. Please note, all measures refer to a smallest electrode distance of $a_0 = 1\,\mathrm{m}$. For other electrode distances (a_0), a and DOI need to be multiplied by a_0. 195

A. Appendix Geophysical Methods

Table A.1.: *Basic physical quantities of the electrical and electromagnetic theory.*

Quantity	Symbol	Unit
Electric Field Intensity	$\vec{E}$	$\frac{\mathrm{V}}{\mathrm{m}}$
Electric Displacement Field	$\vec{D}$	$\frac{\mathrm{As}}{\mathrm{m}^2}$
Magnetic Flux Density	$\vec{B}$	$\mathrm{T} = \frac{\mathrm{Vs}}{\mathrm{m}}$
Magnetic Field Intensity	$\vec{H}$	$\frac{\mathrm{A}}{\mathrm{m}}$
Current Density	$\vec{j}$	$\frac{\mathrm{A}}{\mathrm{m}^2}$
Charge Density	q	$\frac{\mathrm{As}}{\mathrm{m}^3}$
Electrical Potential	Φ	V
Electrical Conductivity	σ	$\frac{\mathrm{S}}{\mathrm{m}}$
Electrical Resistivity	$\rho = \frac{1}{\sigma}$	Ωm
Apparent Resistivity	ρ_a	Ωm
Electrical Resistance	R	Ω
Voltage	U,V	V
Electrical Current	I	A
Geometry Factor	G	m
Chargeability	m	$\frac{\mathrm{mV}}{\mathrm{V}}$, ms
Apparent Chargeability	m_a	$\frac{\mathrm{mV}}{\mathrm{V}}$

Table A.2.: *Resistivity range of selected minerals and rock types. Values obtained from Telford et al. (1990).*

Rock Type/Mineral	Resistivity Range (Ωm)
Dacite (wet)	2×10^4
Diabase	$20 - 5 \times 10^7$
Granite porphyry	4.5×10^3-1.3×10^6
Feldspar porphyry	4×10^3
Diorite porphyry	1.9×10^3-2.8×10^4
Porphyry (various)	$60 - 10^4$
Andesite	4.5×10^4-1.7×10^2
Gabbro	10^3-10^6
Basalt	10-1.3×10^7
Sandstones	$1 - 6.4 \times 10^8$
Limestones	$50 - 10^7$
Hematite (Fe_2O_3)	$3.5 \times 10^{-3} - 10^7$
Chalcopyrite ($CuFeS_2$)	$10^{-4} - 1$
Chalcocite (Cu_2S)	3×10^{-2}
Bornite (Cu_5FeS_4)	3×10^{-3}

Table A.3.: *Chargeability range of selected minerals with 1% vol. concentration, $T_{on} = 3$ s, integration time 1 s. Values obtained from Telford et al. (1990).*

Mineral	Chargeability (ms)
Pyrite (FeS_2)	13.4
Chalcocite (Cu_2S)	13.2
Copper (Cu)	12.3
Graphite (C)	11.2
Chalcopyrite ($CuFeS_2$)	9.4
Bornite (Cu_5FeS_4)	6.3
Galena (PbS)	3.7
Magnetite (Fe_3O_4)	2.2
Malachite ($Cu_2CO_3(OH)_2$)	0.2
Hematite (Fe_2O_3)	0

Table A.4.: *Chargeability range of selected minerals and rock types. The charging time is ca. 1 min, integration is over the complete decay curve. Values obtained from Telford et al. (1990).*

Rock Type/Mineral	Chargeability Range (ms)
20% Sulfides	2000-3000
8-20% Sulfides	1000-2000
2-8% Sulfides	500-1000
Volcanic tuffs	300-800
Sandstone, siltstone	100-500
Dense volcanic rocks	100-500
Shale	50-100
Granite, granodiorite	10-50
Limestone, Dolomite	10-20

B. Appendix Forward Calculation

B.1. Wavenumbers and weights used in the FCT

Table B.1.: *Wavenumbers k and weights g_k used in the Fourier Cosine Transformation (FCT) and Inverse FCT, respectively. Values are obtained from Erdoğan et al. (2008) and were calculated with the optimization approach after Xu et al. (2000). The values need to be divided by the smallest electrode spacing in order to be suitable for any electrode setup.*

k	g_k
0.003694	0.007699
0.031109	0.028744
0.105288	0.071942
0.291071	0.181920
0.766626	0.468466
1.994081	1.210086
5.172940	3.147197
13.672040	8.763861

B.2. Element Matrices

The formulation of element matrices as they are implemented in `ResIPIn2D` is obtained from the work of A. Kemna (Kemna, 2000, 1995). For the sake of completeness they are listed in the following.

Rewriting the functional of Equation (3.22) in the form as in Equation (3.25) yields

$$
\begin{aligned}
F = \sum_{i=1}^{M_e} \Bigg\{ & \frac{1}{2}\sigma_i \iint\limits_{\Omega_i} \left[\left(\frac{\partial \tilde{\Phi}_s}{\partial x} \right)^2 + \left(\frac{\partial \tilde{\Phi}_s}{\partial z} \right)^2 \right] \mathrm{d}x\mathrm{d}z + \frac{1}{2}\sigma_i k^2 \iint\limits_{\Omega_i} \tilde{\Phi}_s^2 \, \mathrm{d}x\mathrm{d}z \\
& + \Delta\sigma_i \iint\limits_{\Omega_i} \left[\left(\frac{\partial \tilde{\Phi}_p}{\partial x} \right) \left(\frac{\partial \tilde{\Phi}_s}{\partial x} \right) + \left(\frac{\partial \tilde{\Phi}_p}{\partial z} \right) \left(\frac{\partial \tilde{\Phi}_s}{\partial z} \right) \right] \mathrm{d}x\mathrm{d}z + \Delta\sigma_i k^2 \iint\limits_{\Omega_i} \tilde{\Phi}_p \tilde{\Phi}_s \, \mathrm{d}x\mathrm{d}z \Bigg\} \\
& + \sum_{j=1}^{M_b} \left(\frac{1}{2}\beta_j \int\limits_{L_j} \tilde{\Phi}_s^2 \, \mathrm{d}L + \Delta\beta_j \int\limits_{L_j} \tilde{\Phi}_s^2 \, \mathrm{d}L \right)
\end{aligned}
\tag{B.1}
$$

The first term sums the contributions of all M_e triangular elements. For each triangle i integration is done over the element's area Ω_i. The integrals are rearranged into matrix syntax:

$$
\iint\limits_{\Omega_i} \left[\left(\frac{\partial \tilde{\Phi}}{\partial x} \right)^2 + \left(\frac{\partial \tilde{\Phi}}{\partial z} \right)^2 \right] \mathrm{d}x\mathrm{d}z = \vec{\tilde{\Phi}}_i^T \mathbf{S'}_{1,i} \vec{\tilde{\Phi}}_i \tag{B.2}
$$

$$
\iint\limits_{\Omega_i} \tilde{\Phi}^2 \, \mathrm{d}x\mathrm{d}z = \vec{\tilde{\Phi}}_i^T \mathbf{S'}_{2,i} \vec{\tilde{\Phi}}_i \tag{B.3}
$$

with potential vector $\vec{\tilde{\Phi}}_i = (\tilde{\Phi}_{l_1(i)}, \tilde{\Phi}_{l_2(i)}, \tilde{\Phi}_{l_3(i)})^T$ and indices $l_1(i)$, $l_2(i)$, $l_3(i)$ of the nodes at the three edges of the element. The 3x3-element matrices $\mathbf{S'}_{1,i}$ and $\mathbf{S'}_{2,i}$ are defined by

$$
\mathbf{S'}_{1,i} = u_1\mathbf{U}_1 + u_2\mathbf{U}_2 + u_3\mathbf{U}_3 \tag{B.4}
$$

$$
\mathbf{S'}_{2,i} = u_4\mathbf{U}_4 \tag{B.5}
$$

with scalars u_1, u_2, u_3, u_4 calculated from the coordinates $(x_{l_m(i)}, z_{l_m(i)})$ $(m \in \{1,2,3\})$ of the three edge nodes:

$$
u_1 = \left[(x_3 - x_1)^2 + (z_3 - z_1)^2 \right] / u_4 \tag{B.6}
$$

$$
u_2 = -\left[(x_3 - x_1)(x_2 - x_1) + (z_3 - z_1)(z_2 - z_1) \right] / u_4 \tag{B.7}
$$

$$
u_3 = \left[(x_2 - x_1)^2 + (z_2 - z_1)^2 \right] / u_4 \tag{B.8}
$$

$$
u_4 = (x_2 - x_1)(z_3 - z_1) - (x_3 - x_1)(z_2 - z_1) \tag{B.9}
$$

and matrices

$$\mathbf{U}_1 = \frac{1}{2}\begin{pmatrix} 1 & -1 & 0 \\ -1 & 1 & 0 \\ 0 & 0 & 0 \end{pmatrix} \tag{B.10}$$

$$\mathbf{U}_2 = \frac{1}{2}\begin{pmatrix} 2 & -1 & -1 \\ -1 & 0 & 1 \\ -1 & 1 & 0 \end{pmatrix} \tag{B.11}$$

$$\mathbf{U}_3 = \frac{1}{2}\begin{pmatrix} 1 & 0 & -1 \\ 0 & 0 & 0 \\ -1 & 0 & 1 \end{pmatrix} \tag{B.12}$$

$$\mathbf{U}_4 = \frac{1}{24}\begin{pmatrix} 2 & 1 & 1 \\ 1 & 2 & 1 \\ 1 & 1 & 2 \end{pmatrix} \tag{B.13}$$

Matrices $\mathbf{S'}_{1,i}$ and $\mathbf{S'}_{2,i}$ are extended into NxN-matrices $\mathbf{S}_{1,i}$ and $\mathbf{S}_{2,i}$ by filling the entries with zeros that refer to node indices not belonging to the element. N is the number of nodes in the computational area. For the entries $(s_{1,i})_{mn}$ of $\mathbf{S}_{1,i}$ this means

$$(s_{1,i})_{mn} = \begin{cases} (s'_{1,i})_{\kappa\lambda} & \text{, if } \kappa, \lambda \in \{1,2,3\} \text{ with } m = l_\kappa(i),\ n = l_\lambda(i) \\ 0 & \text{, else} \end{cases} \tag{B.14}$$

Matrices $\mathbf{S}_{2,i}$ is created analogously.

The element matrices $\mathbf{S}_{3,j}$ regarding the boundary elements are created in a similar way. Since the boundary elements are one-dimensional and are defined by two indices the linear shape functions have the form

$$\tilde{\Phi}(L) = a_j + b_j L \tag{B.15}$$

The second sum in Equation (B.1) adds the contributions of all M_b boundary elements. In this term, the integration for every boundary element j is done over the element's length L_j. The integrals are rearranged into matrix syntax:

$$\int_{L_j} \tilde{\Phi}^2 \,\mathrm{d}L = \vec{\tilde{\Phi}}_j^T \mathbf{S'}_{3,j} \vec{\tilde{\Phi}}_j \tag{B.16}$$

with 2x2-element matrices $\mathbf{S'}_{3,j}$

$$\mathbf{S'}_{3,j} = \frac{L_j}{6}\begin{pmatrix} 2 & 1 \\ 1 & 2 \end{pmatrix} \tag{B.17}$$

Analogue to the element matrices of the triangular elements, matrices $\mathbf{S'}_{3,j}$ are extended into NxN-matrices $\mathbf{S}_{3,j}$ by filling the entries of the matrix with zeros for

node indices that do not belong to the according boundary element. The matrix entries $(s_{3,j})_{mn}$ are

$$(s_{3,j})_{mn} = \begin{cases} (s'_{3,j})_{\kappa\lambda} & \text{, if } \kappa, \lambda \in \{1,2\} \text{ with } m = l_\kappa(j),\ n = l_\lambda(j) \\ 0 & \text{, else} \end{cases} \tag{B.18}$$

The matrices $\mathbf{S}_{1,i}$, $\mathbf{S}_{2,i}$ and $\mathbf{S}_{3,j}$ are used to build the linear system of equations in chapter 3.2.

B.3. Electrode Protocols

Table B.2.: *Dipole-Dipole protocol A: 12 n-level with fixed dipole length a. Please note, all measures refer to a smallest electrode distance of $a_0 = 1\,\mathrm{m}$. For other electrode distances (a_0), a and DOI need to be multiplied by a_0.*

n-level	a	n	DOI_t in m
1	1	1	0.75
2	1	2	1.00
3	1	3	1.25
4	1	4	1.50
5	1	5	1.75
6	1	6	2.00
7	1	7	2.25
8	1	8	2.50
9	1	9	2.75
10	1	10	3.00
11	1	11	3.25
12	1	12	3.50

Table B.3.: *Dipole-Dipole protocol B: 22 n-level with varied dipole length a. Please note, all measures refer to a smallest electrode distance of* $a_0 = 1\,\mathrm{m}$*. For other electrode distances (*a_0*), a and DOI need to be multiplied by* a_0*.*

n-level	a	n	DOI_t in m
1	1	1	0.75
2	1	2	1.00
3	1	3	1.25
4	1	4	1.50
5	1	5	1.75
6	1	6	2.00
7	1	7	2.25
8	2	3	2.50
9	2	4	3.00
10	2	5	3.50
11	3	3	3.75
12	2	6	4.00
13	3	4	4.25
14	3	5	5.25
15	3	6	6.00
16	4	4	6.00
17	5	3	6.25
18	4	5	7.00
19	4	6	8.00
20	5	5	8.75
21	4	7	9.00
22	5	6	10.0

Table B.4.: *Wenner protocol A: 12 n-level. Please note, all measures refer to a smallest electrode distance of $a_0 = 1\,\mathrm{m}$. For other electrode distances (a_0), a and DOI_t need to be multiplied by a_0.*

n-level	a	DOI in m
1	1	0.51
2	2	1.02
3	3	1.53
4	4	2.04
5	5	2.55
6	6	3.06
7	7	3.57
8	8	4.08
9	9	4.59
10	10	5.10
11	11	5.61
12	12	6.12

Table B.5.: *Schlumberger protocol A: 9 n-level with fixed dipole length a. Please note, all measures refer to a smallest electrode distance of $a_0 = 1\,\mathrm{m}$. For other electrode distances (a_0), a and DOI need to be multiplied by a_0.*

n-level	a	n	DOI_t in m
1	1	1	0.57
2	1	2	0.95
3	1	3	1.33
4	1	4	1.71
5	1	5	2.09
6	1	6	2.47
7	1	7	2.85
8	1	8	3.23
9	1	9	3.61

Table B.6.: *Pole-Dipole protocol A: 14 n-level with varied dipole length a. Please note, all measures refer to a smallest electrode distance of $a_0 = 1\,\mathrm{m}$. For other electrode distances (a_0), a and DOI need to be multiplied by a_0.*

n-level	a	n	DOI_t in m
1	1	1	0.66
2	1	2	1.00
3	1	3	1.33
4	1	4	1.67
5	1	5	2.00
6	1	6	2.33
7	1	7	2.67
8	2	1	1.33
9	2	2	2.00
10	2	3	2.67
11	2	4	3.33
12	2	5	4.00
13	2	6	4.67
14	2	7	5.33

Table B.7.: *Wenner Protocol B: 8 n-level. Please note, all measures refer to a smallest electrode distance of $a_0 = 1\,\mathrm{m}$. For other electrode distances (a_0), a and DOI need to be multiplied by a_0.*

n-level	a	DOI_t in m
1	1	0.51
2	2	1.02
3	3	1.53
4	4	2.04
5	5	2.55
6	6	3.06
7	7	3.57
8	8	4.08

B.4. Appendix Inversion of Synthetic Data

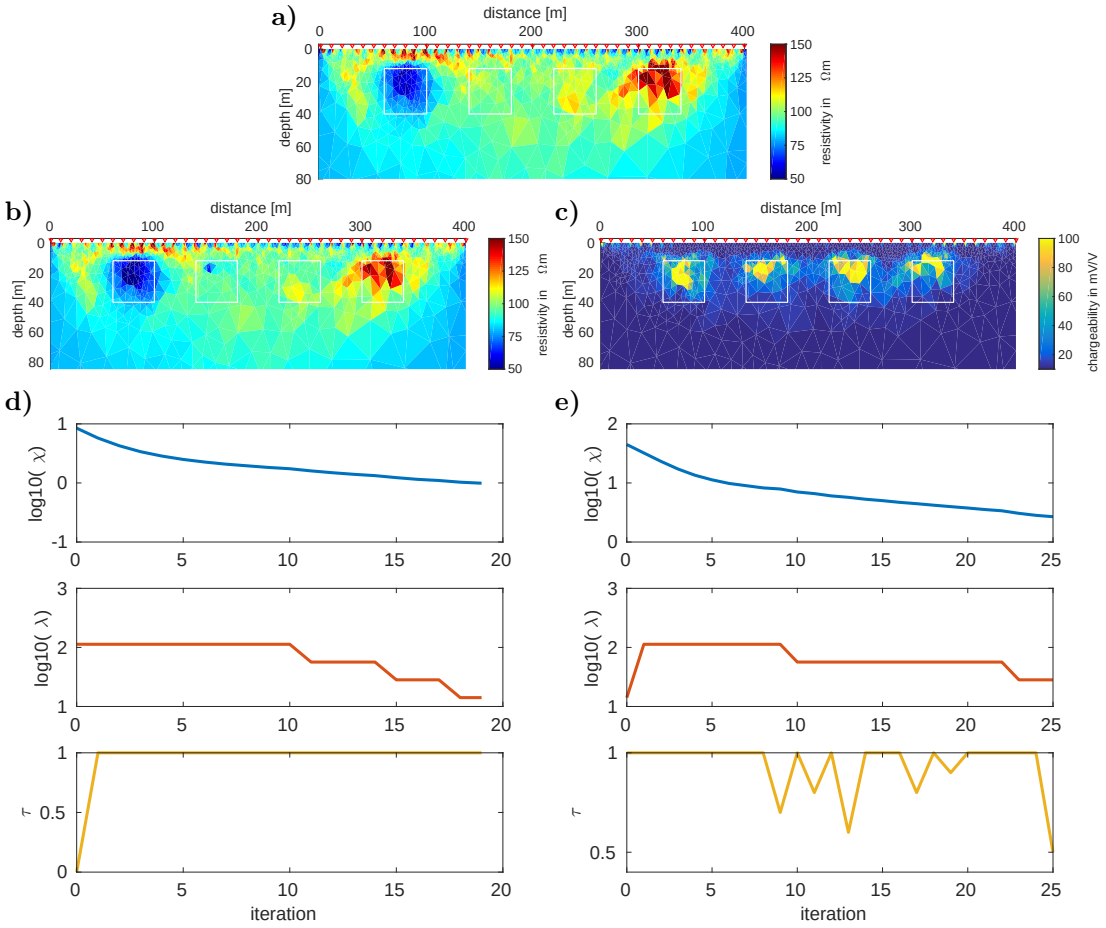

Figure B.1.: *Inversion results of the synthetic data in Figure 5.2-e,f using* $\mathbf{C}_c$, $\lambda_{ini} = 113$ *and a 2-point parabola line-search for* τ. ***a)*** *Resistivity model* ρ' *resulting from the 19th DC iteration. The final regularization parameter is* $\lambda = 14$ *and the data misfit is* $\chi_{dc} = 0.99$. ***b)*** *Intrinsic resistivity model* ρ *and* ***c)*** *chargeability model* m *resulting from the 25th IP iteration. Final values are* $\lambda = 28$, $\chi_{ip} = 2.6$. ***d,e)*** *Data misfit* χ, *regularization parameter* λ *and step-length* τ *during iterations of DC (d) and IP (e) inversion.*

C. Appendix Survey Results

C.1. Topography Influence

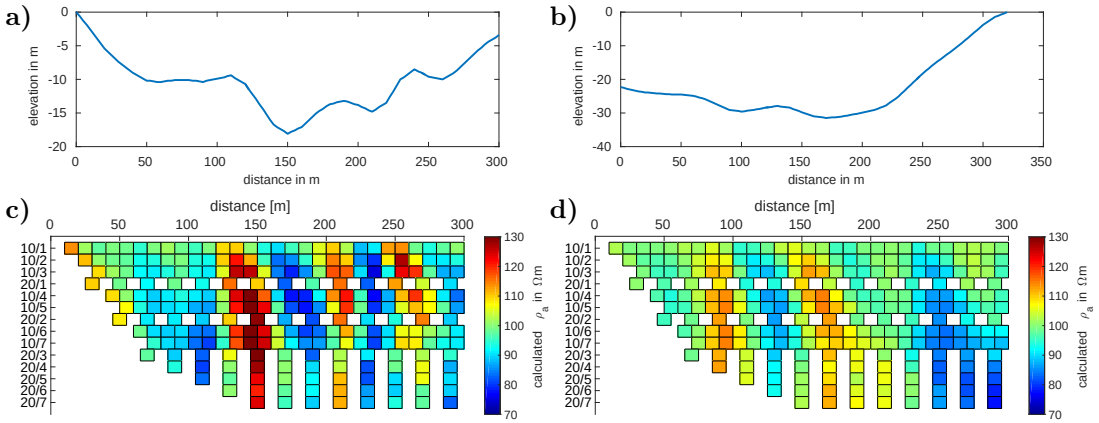

Figure C.1.: *Topography influence. Surface topography of* **a)** *Profile 1 and* **b)** *Profile 2. Synthetic Pole-Dipole apparent resistivity calculated for a homogeneous subsurface resistivity of* 100 Ωm *beneath the topography according to* **c)** *Profile 1 and* **d)** *Profile 2.*

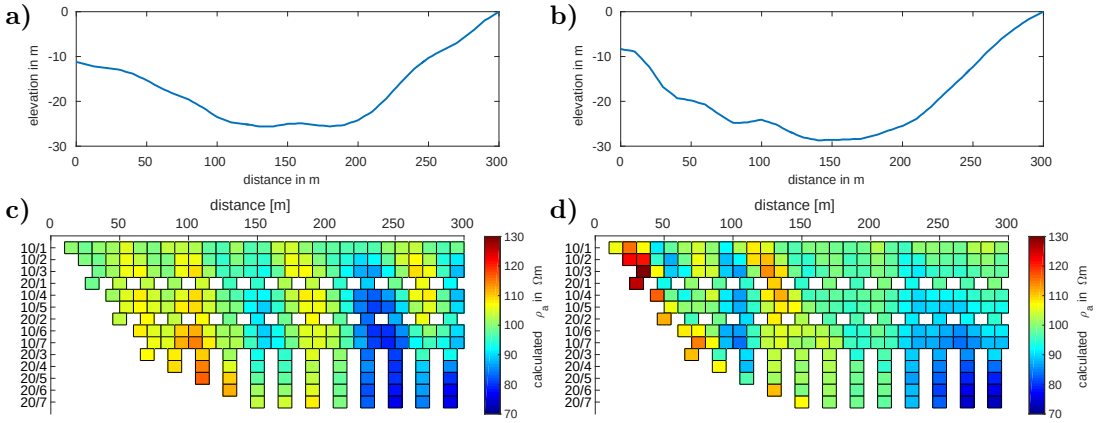

Figure C.2.: *Topography influence. Surface topography of* **a)** *Profile 4 and* **b)** *Profile 5. Synthetic Pole-Dipole apparent resistivity calculated for a homogeneous subsurface resistivity of* 100 Ωm *beneath the topography according to* **c)** *Profile 4 and* **d)** *Profile 5.*

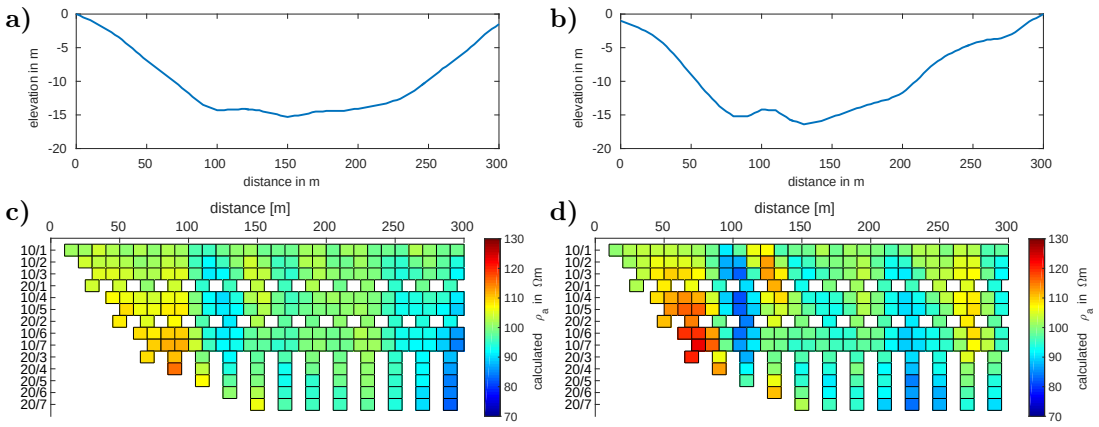

Figure C.3.: *Topography influence. Surface topography of* **a)** *Profile 6 and* **b)** *Profile 8. Synthetic Pole-Dipole apparent resistivity calculated for a homogeneous subsurface resistivity of* $100\,\Omega\mathrm{m}$ *beneath the topography according to* **c)** *Profile 6 and* **d)** *Profile 8.*

C.2. Inversion Results

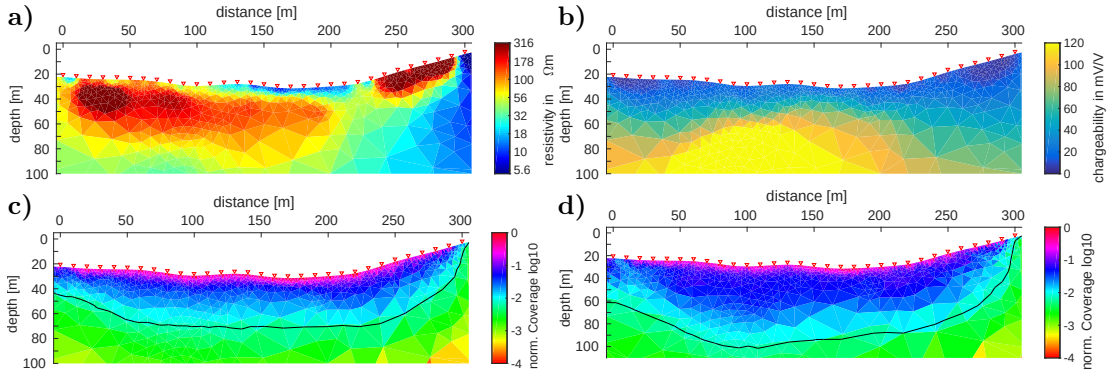

Figure C.4.: *Inversion results Profile 2:* **a)** *Resistivity model,* χ_{dc}*=3.6,* **b)** *chargeability model,* χ_{ip}*=2.4,* **c,d)** *normalized coverage of the corresponding model at the top. The approximate* DOI_{app} *is defined by the black isoline referring to* cov_t*=-2.15. Electrode locations indicated by red triangles.*

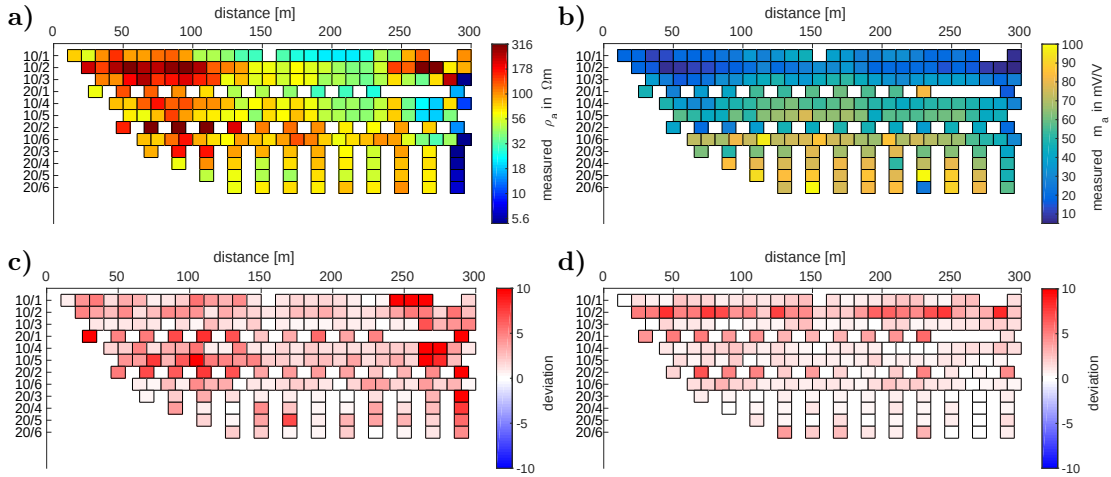

Figure C.5.: *Inversion results Profile 2: Measured data as pseudo-sections* **a)** *apparent resistivity,* **b)** *apparent chargeability.* **c,d)** *Difference between the measured data and the corresponding calculated data shown above normalized to the data error.*

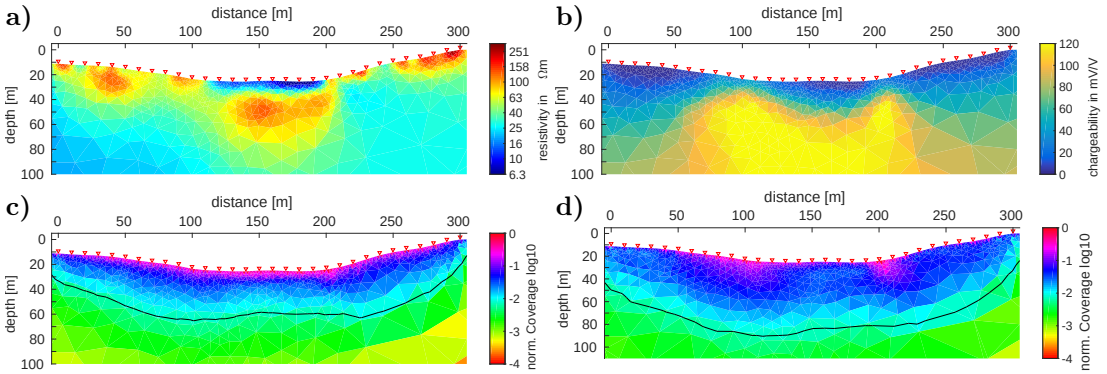

Figure C.6.: *Inversion results Profile 4:* ***a)*** *Resistivity model, χ_{dc}=0.97,* ***b)*** *chargeability model, χ_{ip}=0.97,* ***c,d)*** *normalized coverage of the corresponding model at the top. The approximate DOI_{app} is defined by the black isoline referring to cov_t=-2.15. Electrode locations indicated by red triangles.*

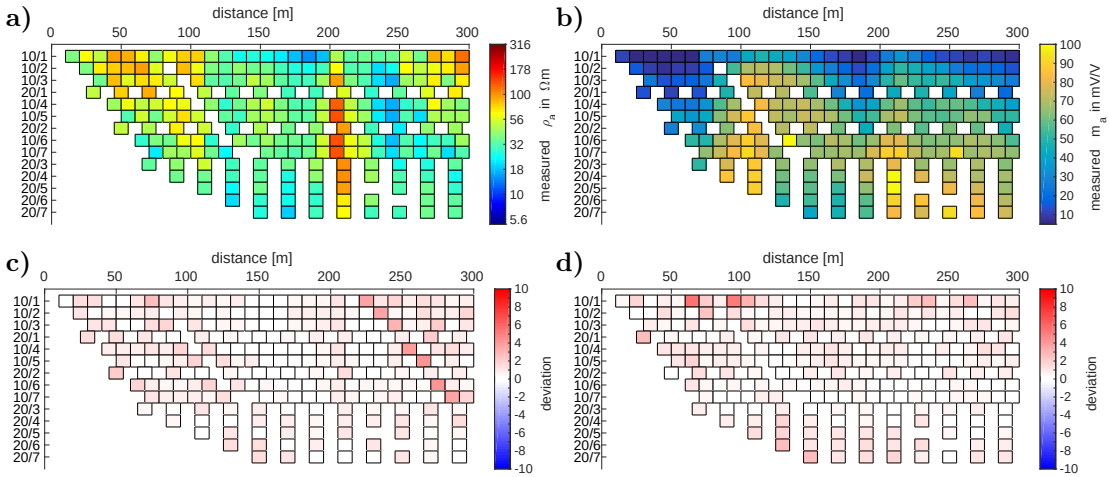

Figure C.7.: *Inversion results Profile 4: Measured data as pseudo-sections* ***a)*** *apparent resistivity,* ***b)*** *apparent chargeability.* ***c,d)*** *Difference between the measured data and the corresponding calculated data shown above normalized to the data error.*

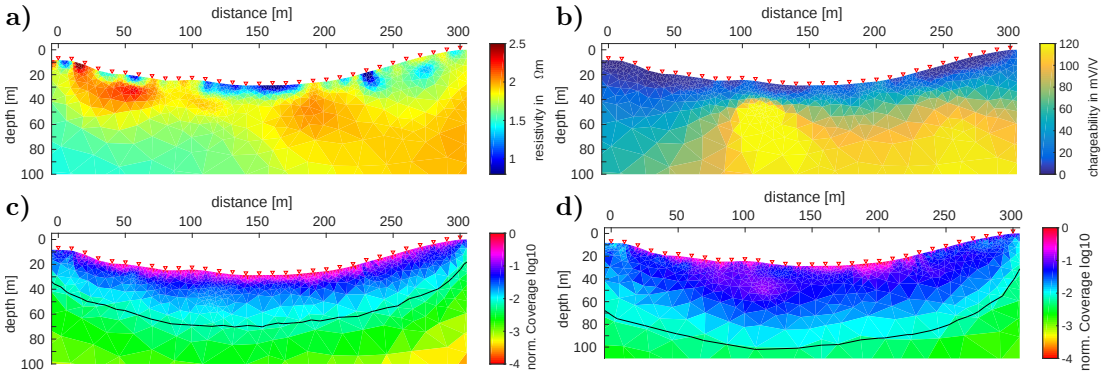

Figure C.8.: *Inversion results Profile 5:* ***a)*** *Resistivity model, χ_{dc}=1.36,* ***b)*** *chargeability model, χ=1.41,* ***c,d)*** *normalized coverage of the corresponding model at the top. The approximate DOI_{app} is defined by the black isoline referring to cov_t=-2.15. Electrode locations indicated by red triangles.*

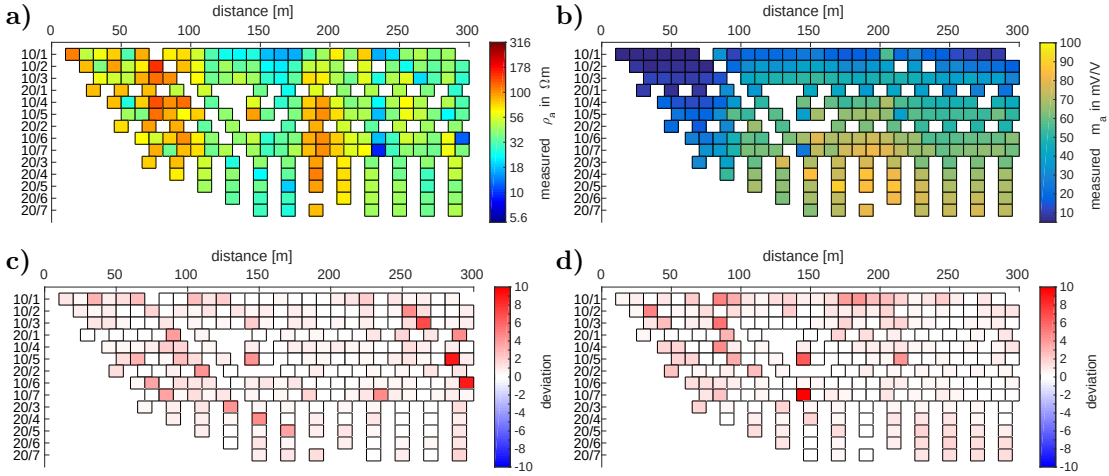

Figure C.9.: *Inversion results Profile 5: Measured data as pseudo-sections* ***a)*** *apparent resistivity,* ***b)*** *apparent chargeability.* ***c,d)*** *Difference between the measured data and the corresponding calculated data shown above normalized to the data error.*

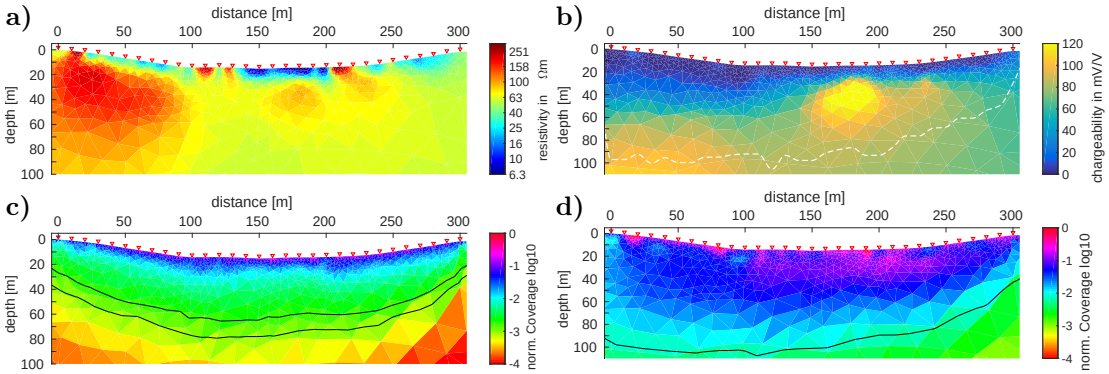

Figure C.10.: *Inversion results Profile 6:* ***a)*** *Resistivity model, χ_{dc}=1.90,* ***b)*** *chargeability model, χ_{ip}=1.5,* ***c,d)*** *normalized coverage of the corresponding model at the top. The approximate DOI_{app} is defined by the black isoline referring to cov_t=-2.15. Electrode locations indicated by red triangles.*

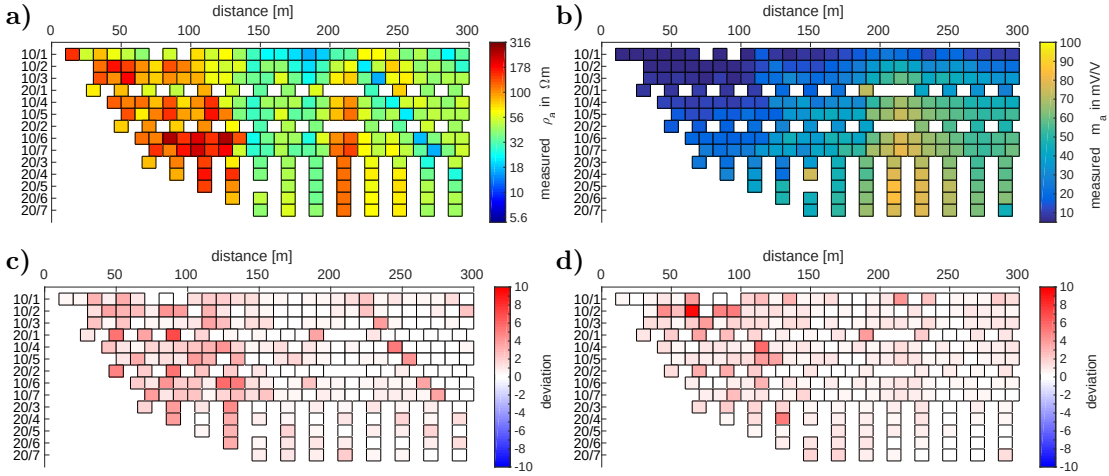

Figure C.11.: *Inversion results Profile 6: Measured data as pseudo-sections* ***a)*** *apparent resistivity,* ***b)*** *apparent chargeability.* ***c,d)*** *Difference between the measured data and the corresponding calculated data shown above normalized to the data error.*

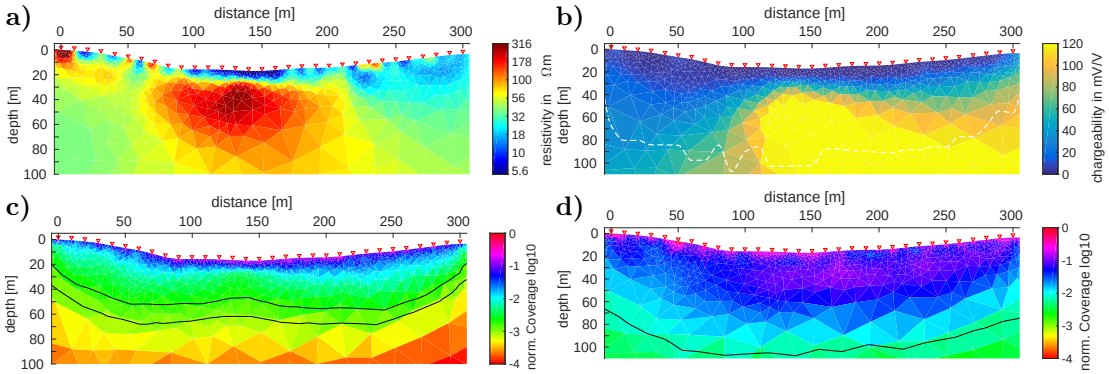

Figure C.12.: *Inversion results Profile 7:* ***a)*** *Resistivity model, $\chi_{dc} = 2.04$,* ***b)*** *chargeability model, $\chi_{ip} = 0.99$,* ***c,d)*** *normalized coverage of the corresponding model at the top. The approximate DOI_{app} is defined by the black isoline referring to cov_t=-2.15. Electrode locations indicated by red triangles.*

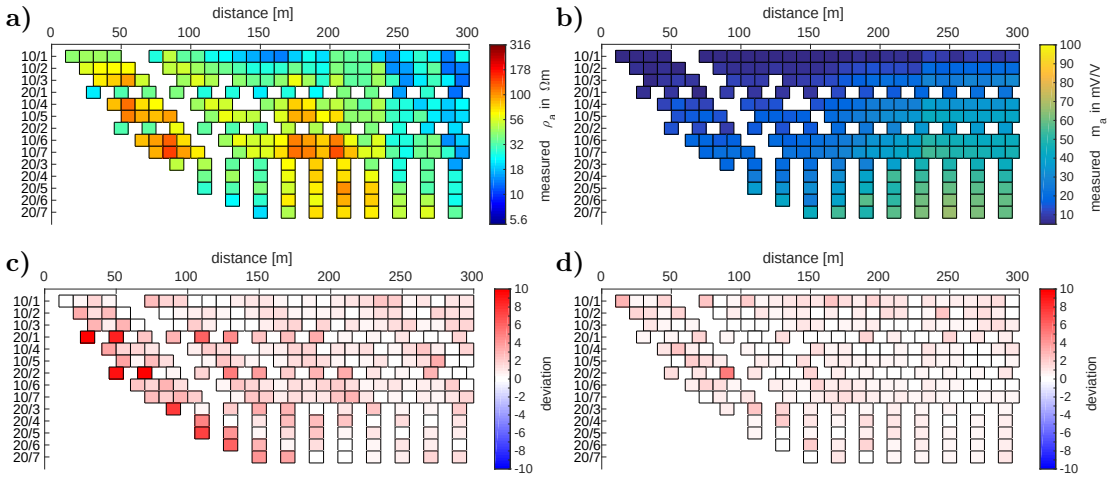

Figure C.13.: *Inversion results Profile 7: Measured data as pseudo-sections* ***a)*** *apparent resistivity,* ***b)*** *apparent chargeability.* ***c,d)*** *Difference between the measured data and the corresponding calculated data shown above normalized to the data error.*

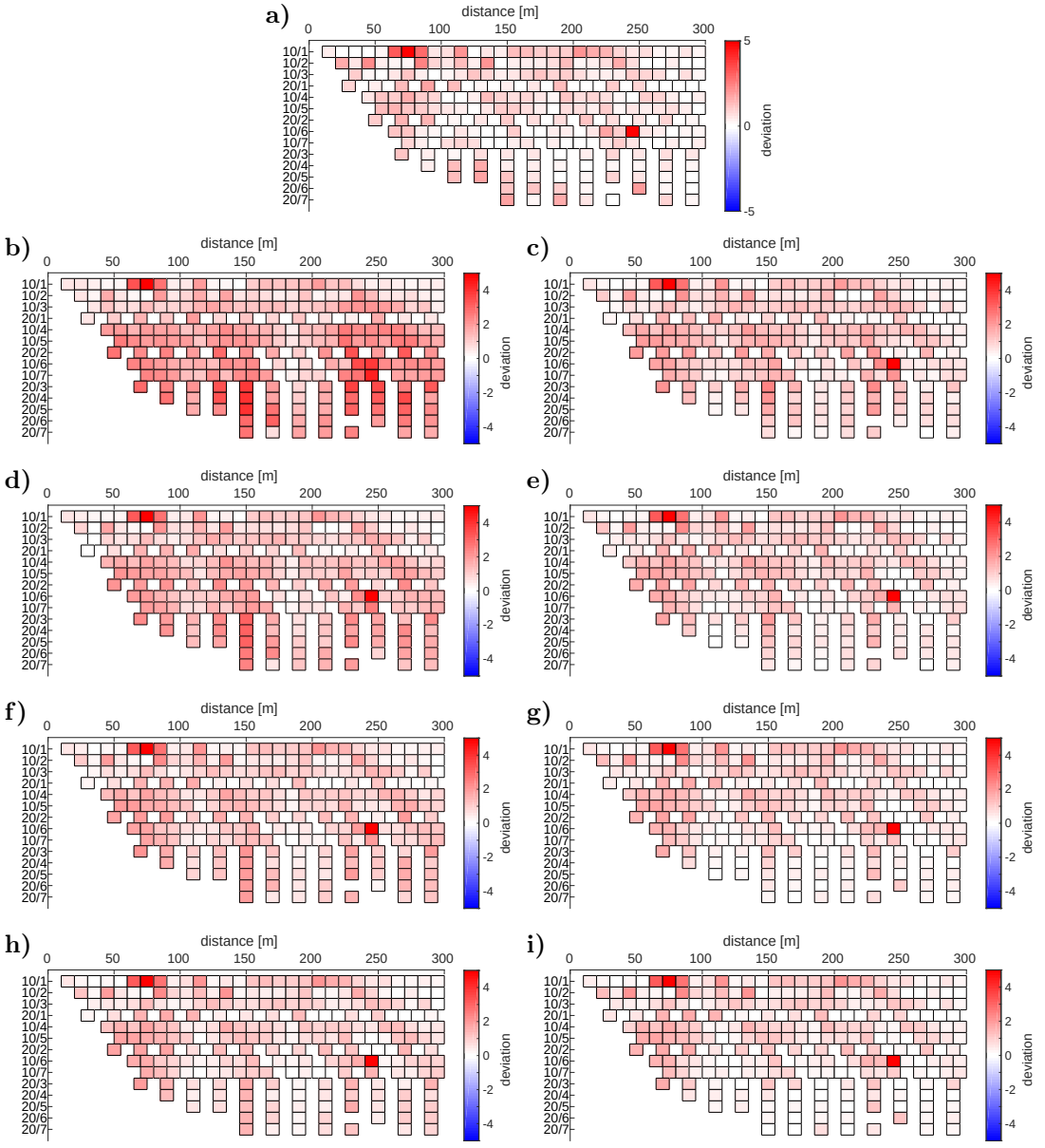

Figure C.14.: *Profile 3: deviation (normalized to data error) between measured data and the chargeability data calculated from models that were varied based on the final inversion model shown in Figure 7.22.* ***a)*** *Original inversion result,* ***b)*** *max.* $10\,\mathrm{mV/V}$ *below* $z = 70\,\mathrm{m}$, ***c)*** *max.* $50\,\mathrm{mV/V}$ *below* $z = 70\,\mathrm{m}$, ***d)*** *max.* $10\,\mathrm{mV/V}$ *below* $z = 80\,\mathrm{m}$, ***e)*** *max.* $50\,\mathrm{mV/V}$ *below* $z = 80\,\mathrm{m}$, ***f)*** *max.* $10\,\mathrm{mV/V}$ *below* $z = 90\,\mathrm{m}$, ***g)*** *max.* $50\,\mathrm{mV/V}$ *below* $z = 90\,\mathrm{m}$, ***h)*** *max.* $10\,\mathrm{mV/V}$ *below* $z = 100\,\mathrm{m}$, ***i)*** *max.* $50\,\mathrm{mV/V}$ *below* $z = 100\,\mathrm{m}$.

Danksagung

An dieser Stelle möchte ich mich bei allen herzlich bedanken, die mich auf meinem Weg als Doktorandin begleitet und mich unterstützt haben. Mein Dank gilt:

Prof. Dr. Bülent Tezkan für die Betreuung dieser Arbeit und für die Unterstützung während meiner Jahre als studentische Hilfskraft und Doktorandin,

Prof. Dr. Andreas Hördt für die Zweitkorrektur dieser Arbeit,

Prof. Dr. J. Saur für die Betreuung im Rahmen der Graduate School for Geosciences (GSGS),

Prof. Dr. Emin Candansayar und seiner Arbeitsgruppe am Department of Geophysical Engineering der Universität Ankara für die gemeinsamen Feldmessungen in der Türkei und die Zusammenarbeit in dem gemeinsamen BMBF/TÜBITAK Projekt,

Marc Seidel und *Natalie Pickartz* für die gemeinsamen Reisen und die Hilfe bei den Feldmessungen,

Amir Haroon, *Hannah Langenbach* und *Wiebke Mörbe* für viele hilfreiche Tipps und Anregungen beim Anfertigen dieser Arbeit,

Hannah Langenbach, *Anne Schreiner* und *Amir Haroon* für die unvergessliche Zeit, in denen wir uns ein Büro geteilt haben,

allen Kollegen der beiden Geophysik Arbeitsgruppen (*AGeos* und *Eties*), neben den schon genannten besonders: Jan, Pritam, Klaus, Diego, Mitch, Fabrizio, Oliver und Rudi,

dem Bundeministerium für Bildung und Forschung (*BMBF*) für die finanzielle Unterstützung im Rahmen des Projektes "Zweidimensionale Interpretation von Radiomagnetotellurik-, Geoelektrik- und Induzierten Polarisationsdaten: Ein Beispiel aus der Erzexploration",

der *GSGS* für die finanzielle Unterstützung im Rahmen eines Travel Grants und eines Fellowships (No. GSGS-2017A-F04),

und zu guter Letzt geht natürlich ein riesiges Dankeschön an *meine Familie und Freunde*, die mich während der Zeit der Doktorarbeit unterstützt, aber zum Ende hin kaum zu Gesicht bekommen haben.

Und zu allerletzt, gilt ein besonderer Dank *Thomas*, für die vielen gemeinsamen Jahre!

Versicherung

Ich versichere, dass ich die von mir vorgelegte Dissertation selbstständig angefertigt, die benutzten Quellen und Hilfsmittel vollständig angegeben und die Stellen der Arbeit - einschließlich Tabellen, Karten und Abbildungen-, die anderen Werken im Wortlaut oder dem Sinn nach entnommen sind, in jedem Einzelfall als Entlehnung kenntlich gemacht habe; dass diese Dissertation noch keiner anderen Fakultät oder Universität zur Prüfung vorgelegen hat; dass sie - abgesehen von unten angegebenen Teilpublikationen - noch nicht veröffentlicht worden ist sowie, dass ich eine solche Veröffentlichung vor Abschluss des Promotionsverfahrens nicht vornehmen werde. Die Bestimmungen der Promotionsordnung sind mir bekannt. Die von mir vorgelegte Dissertation ist von Prof. Dr. Bülent Tezkan betreut worden.

Köln, 17.09.2017

Teilpublikationen

Adrian, J. & Tezkan, B., 2017. *Exploration of an ore deposit in Turkey using time-domain IP: A newly developed 2D inversion algorithm.* Near Surface Geophysics. Submitted for publication.

Adrian, J. & Tezkan, B., 2016. *2D DCR/TDIP Two-step Inversion: Detectability of ore deposits and Depth of Investigation*, 4th International Workshop on Induced Polarization, Aarhus, Denmark.